CONTENTS

Jan Slota, Ivan Gajdos, Emil Spišák, Marek Šiser
Springback Prediction of Stretching Process using Finite Element Analysis for DP600 Steel Sheet 5

Tadeusz Pała, Ihor Dzioba, Jarosław Gałkiewicz
Verification of Strength of the Welded Joints by using of the Aramis Video System 9

Ryszard Sygulski, Michał Guminiak, Łukasz Polus
Stability of a Steel Welded Girder with Bending and Shear Forces Included 14

Najeeb Alam Khan, Shahnila Aziz, Saif Ullah
Entropy Generation on MHD Flow of Powell-Eyring Fluid Between Radially Stretching Rotating Disk with Diffusion-Thermo and Thermo-Diffusion Effects 20

Maciej Słowik, Daniel Ołdziej, Zdzisław Gosiewski
Integration and In-Field Gains Selection of Flight and Navigation Controller for Remotely Piloted Aircraft System 33

Czesław Janusz Jermak
Discussion on Flow-Through Phenomena in the Air Gauge Cascade 38

Paweł Sidun, Andrzej Łukaszewicz
Verification of Ram-Press Pipe Bending Prosses using Elasto-Plastic FEM Model 47

Dariusz Urban, Marek Jałbrzykowski, Maria Gołębiewska
Fatigue Testing of Dental Bridges on Selected Examples 53

Volodimyr Kalchenko, Andrij Yeroshenko, Sergiy Boyko, Nataliia Sira
Determination Of Cutting Forces In Grinding With Crossed Axes Of Tool And Workpiece 58

Wojciech Horak, Bogdan Sapiński, Marcin Szczęch
Analysis of Force in MR Fluids during Oscillatory Compression Squeeze 64

Peter Kaššay, Jaroslav Homišin, Matej Urbanský, Robert Grega
Transient Torsional Analysis of a Belt Conveyor Drive with Pneumatic Flexible Shaft Coupling 69

Adam Łapiński, Dariusz Butrymowicz, Mirosława Kołodziejczyk
Measurement Approach of Mean Heat Transfer Coefficient for Packed Bed of Vegetables 73

Abstracts 81

DE GRUYTER
OPEN

DOI 10.1515/ama-2017-0001 acta mechanica et automatica, vol.11 no.1 (2017)

SPRINGBACK PREDICTION OF STRETCHING PROCESS USING FINITE ELEMENT ANALYSIS FOR DP600 STEEL SHEET

Jan SLOTA[*], Ivan GAJDOS[*], Emil SPIŠÁK[**], Marek ŠISER[*]

[*]Department of Computer Support of Technology, Technical University of Košice, Mäsiarska 74, 040 01 Košice, Slovakia
[**]Department of Technology and Materials, Technical University of Košice, Mäsiarska 74, 040 01 Košice, Slovakia

jan.slota@tuke.sk, ivan.gajdos@tuke.sk, emil.spisak@tuke.sk, marek.siser@tuke.sk

received 3 December 2015, revised 12 December 2016, accepted 10 December 2016

Abstract: Springback phenomenon is well predicted for some mild steel materials, but not for steels with higher strength. One of the most used tools to stamping optimization is usage of finite element analysis. In order to accurate describe the real behaviour of the materials for stamping of vehicle panels, the application of proper hardening rule seems to be crucial. Due to higher accuracy of predicted results, high strength steel sheets are usually modelled by means of kinematic or mixed isotropic-kinematic hardening models. In this paper the springback prediction of advanced high strength steel DP600 by numerical simulation was investigated. Through cyclic tension-compression tests, the material characterization has been performed for DP600 steel sheet. Different hardening models (isotropic, kinematic and mixed isotropic-kinematic) used in the simulations were compared with expreriment. The Yoshida–Uemori model succesfully describe the kinematic behaviour of the material and provided more accurate results than others.

Key words: Sheet Metal Forming, Springback, Simulation

1. INTRODUCTION

Stamping process is the most commonly used manufacturing process to produce thin vehicle panels. The biggest challenge in stamping process is to ensure satisfying design specifications without causing defect as splits, wrinkling, skid lines, surface distortions and springback issues (Slota et al., 2015). The springback phenomenon is still the current issue in automotive industry, considering mainly materials which have higher strength (Slota et al., 2012). Numerical simulation by finite element method (FEM) is widely used as a tool for engineers to improve the part design taking into account the process limitations. Finite element analysis (FEA) is a well-established tool for analyzing and predicting sheet forming strains for various materials and test conditions. FE simulation of springback, however, is much more sensitive to numerical tolerances and to material model than forming simulations. Numerical procedures that must be considered more critical for springback simulation include the spatial integration scheme, element type and time integration scheme (implicit, explicit, one-step). Various material representations affect springback simulations significantly such as the unloading scheme, strain hardening rule, evolution of elastic properties, plastic anisotropy, Bauschinger effect, etc. (Wagoner et al., 2013).

During the forming operations, the sheet metal often undergoes to bending-unbending and stretching processes. For example, when a sheet is drawn over a tool radius or draw bead. In these cases, the material is subjected to complex strain paths which make it difficult to accurately predict the final shape of the part after forming. Because of this, the accuracy of the implemented product is dependent on the accuracy of the implemented material constitutive model amongst others.

Complex material models are presented increasingly in FEM codes to provide accurate predictions of material behaviour. These models take into account different phenomena, such as the Bauschinger Effect, the transient behaviour and the permanent softening. Predictions of all these effects which affect the final shape are connected to the hardening rule. Hardening models describe the evolution of the initial yield surface. It is recommended to use various types of hardening models, according to their ability to explain and exact predict plastic behaviour during the given deformation process (Silvestre, 2015). With the increased complexity of hardening model, it is able to increase the accuracy of the predictions (Eggertsen and Mattiasson, 2010).

There are four types of hardening models which may arise during sheet metal forming processes: isotropic models, kinematic models, rotational and distortional hardening models (Bruschi et al., 2014). Isotropic hardening models are used for simple applications. They are able to express the proportional expansion of the initial yield surface (Slota et al., 2014; Bruschi et al., 2014). The advantage of these models is that are able to predict hardening behaviour of a high range of different materials and they are widely used due to their simplicity. However, FEM simulation of new advanced materials, such as advanced high strength steels (AHSS) or ultra high strength steels (UHSS), need more complex formulation of hardening. The use of isotropic hardening models overestimates the hardening in reversal loading under reverse strain paths. This is due to the occurrence of different phenomena during reversal loading which occur commonly in high strength materials, especially as: the Bauschinger effect, the transient behaviour and the permanent softening (Bruschi et al., 2014). Kinematic hardening laws offer more sophisticated models than isotropic. These models assume, that the yield surfaces preserve their shape and size but translate through the stress space. Due to their ability to predict some phenomena mentioned above, kinematic hardening models have received special attention in the

DOI 10.1515/ama-2017-0001

last years (Eggertsen and Mattiasson, 2010). The Bauschinger effect is a clear illustration of how the mechanical response of a metallic material depends not only on its current stress state but also on its history of plastic deformation. A combination of the isotropic and a non-linear kinematic hardening rule (also called mixed hardening models) gives a uniform expansion and translation in shape of the yield surface. Mixed hardening models can predict properly material behaviour of AHSS (Lemoine et al., 2011). According to Kim et al. (2012) the hardening behaviour including the transient behaviour and Bauschinger effect was well described by a modified mixed Chaboche model for dual phase steels. Based on the Yoshida combined isotropic-kinematic hardening model, the constitutive parameters for several AHSS, such as DP780 and DP980 was determined by Shi et al. (2008). Yoshida model was able to determine the stress and strain behaviours in various cycle tension and compression tests. The complexity and accuracy of models depend on the number of material parameters and history variables. Every model has its precise requirements in terms of experimental data and testing needed to identify its parameters. However, in the characterization of stamping operations, cyclic loading experimental tests are generally used in order to analyse kinematic hardening (Lemoine et al., 2011). Several authors have proposed several reverse loading tests (Cao et al., 2009; Silvestre et al., 2015; Eggertsen and Mattiasson, 2010; Slota et al., 2014; Yoshida and Uemori, 2002; Boger et al., 2005; Chongthairungruang et al., 2013; Kuwabra et al., 2009; Piao et al., 2012). Rotational hardening model assumes that the yield locus rotates and distortional hardening model assumes that the yield locus distorts. Nevertheless, the capabilities of isotropic and kinematic hardening models to fully describe the hardening curve upon opposite load, it cannot describe the anisotropic and distortional hardening behaviour. It is due to the change of the sheet metal plastic anisotropy at increasing level of deformation as a result of the texture evolution (Bruschi et al., 2014).

Advanced high strength steels represent special challenges because in general they have higher strength and ductility combinations than conventional steels for vehicle panels and they make use of either very coarse microstructures (DP steels) or strain-induced transformations and complex hardening behaviour (TRIP and TWIP steels). These differences manifest themselves in large changes of elastic "modulus" following plastic deformation, very large hardening transients following a stress reversal, and high temperatures attained by the plastic work in areas of large deformation. Much of the current research on springback focuses just on these aspects (Wagoner et al., 2013).

The goal of this research is to study springback effects of dual phase steel grade DP600 by both, experimentally and numerically. To verify the predicted results of investigated steel, experimental tests were carried out. FE simulations of the forming with stretching were performed in explicit FE code. Accurate springback prediction requires knowing the stress state through the part before unloading, which is controlled by the plastic response of the material during stamping. Parameters of material model that can often be put aside in satisfactory stamping simulations must be included for springback simulations (Yoshida and Uemori, 2003). Among these features belong: Bauschinger effect, hardening stagnation, permanent softening and early re-yielding in the compression phase of the cycle. These features can be revealed performing cyclic tension-compression test. Not all of new material models describing this features. Yoshida–Uemori kinematic hardening material model (Mahmoudi et al., 2011) describes kinematic hardening of the loading surface, combined isotropic-kinematic hardening for the bounding surface, Bauschinger transient similar to a general two surface model and work hardening stagnation at large plastic strain. First step in process of implementation these features is to perform cyclic test under tension-compression load. Next step is fit the experimental curves by means of optimization technique. Experimental and numerical results concerning springback after stamping were compared.

2. EXPERIMENTAL PROCEDURE

2.1. Experimental material

The material investigated in this work was the high strength dual phase steel grade DP600 with a thickness of 1.0 mm. Mechanical properties of this steel sheet obtained from uniaxial tensile test are shown in Tab. 1. The data shown in the table represents mean values.

Tab. 1. Mechanical properties of DP600 steel sheet

Material	Re [MPa]	Rm [MPa]	A80 [%]	K [MPa]	n [-]
DP 600	383	620	26.1	1008	0.179

In order to characterizing the Bauschinger effect during reverse deformation including the transient Bauschinger strain, early re-yielding, work-hardening stagnation and permanent softening behaviour of investigated steel, cyclic tests under tension-compression load were performed. The cyclic tests were carried out using TiraTest testing machine. Elongation of the specimen (Fig.1) was controlled by crosshead displacement of the testing machine.

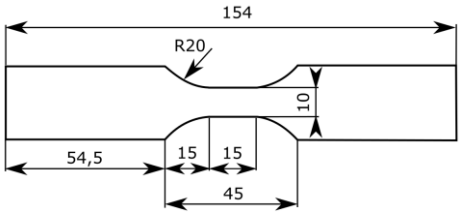

Fig. 1. Dimensions of specimen used for cyclic tension-compression test

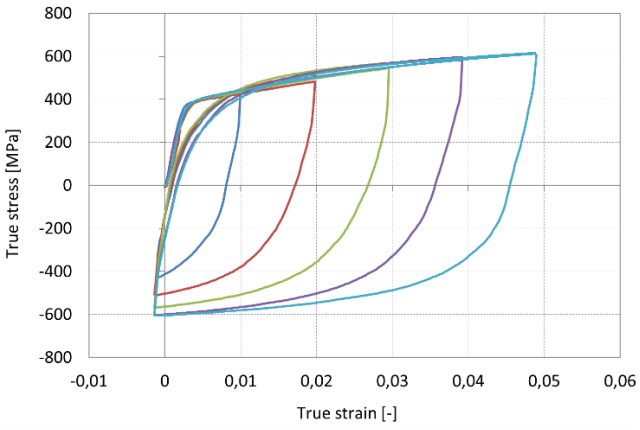

Fig. 2. Tension-compression experimental curve of DP600

DOI 10.1515/ama-2017-0001

Tension-compression test was started by tension load as first part of full cycle. After a specific crosshead stroke corresponding to a defined pre-strain level, load was reversed to compression until reaching crosshead displacement according to a given compression strain. Next, re-loading in tension direction was introduced until the crosshead stroke being equal to that in the first tension. The pre-strain levels between 1 and 5 percent were studied (Fig. 2). It should be noted that higher pre-strain levels could lead to a buckling of the sample.

2.2. FEM simulation

Springback effect of the investigated steel by means of numerical simulation and the final resulted shapes of the sample after tool removal were predicted. Numerical simulation was performed in explicit FE code and the input parameters are presented in Tab. 2.

Tab. 2. Input parameters of FE analysis

Parameter	Value	Parameter	Value
Time integration scheme	Explicit	Element type	Shell
Mesh type	Rectangle	Refinement	0
Mesh size	1.5 mm	Holding force	10 kN
Nr. of integration points	5	Friction coefficient	0.15

The stamping simulation was consisting of two stages. The first stage was the deep-drawing process and the second stage was springback after the tool release process. The FE model with boundary conditions were generated according to experimental setup. The shell elements were used to mesh the sample.

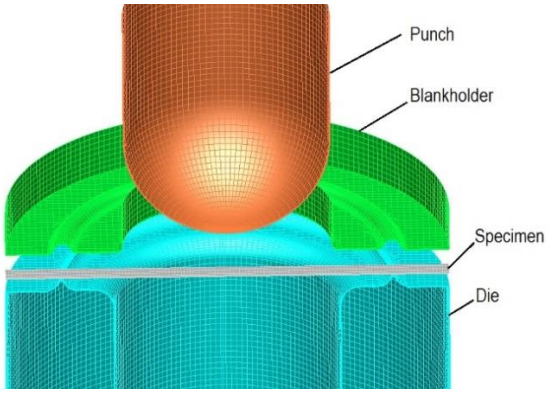

Fig. 3. Experimental setup used in experiment

Fig. 4. Formed sample for springback analysis

All parts of the tool were setup as a rigid body. The friction coefficient of 0.15 was set for every contact surface of the tool. The springback profiles of the deformed samples calculated by FE simulations were compared with experimental results.

For this research was selected tool which is used into the Nakajima test. Geometry of the tool is showed in Fig. 3. This experiment was performed on the universal testing machine Erichsen 145-60. Blankholder force was set to the values of 10 kN. Experimentally stamped specimen of investigated high strength steel is presented in Fig. 4. The geometry was selected due to existence of drawbeads and great diameter of punch what may have influence to the diminishing problems associated with the problems of numerical modeling.

2.3. Results

To compare experiments with numerical material models, both analyses were performed using the same process conditions. When advanced material models which consider kinematic hardening were obtained, numerical simulation of tensile-compression test was performed and the strain paths were plotted. For this purpose, the mixed isotropic-kinematic hardening model of Chaboche and Yoshida-Uemori kinematic hardening model were used. The true stress-strain curves obtained from the numerical tension-compression cyclic tests compared with experiment are presented in Fig. 5. When Yoshida-Uemori kinematic hardening material model was used, it can be observed, that transient Bauschinger effect is described preferably. The stress-strain curve illustrated in Fig. 5 shows, that the material behaviour is described with higher accuracy than isotropic or mixed hardening models.

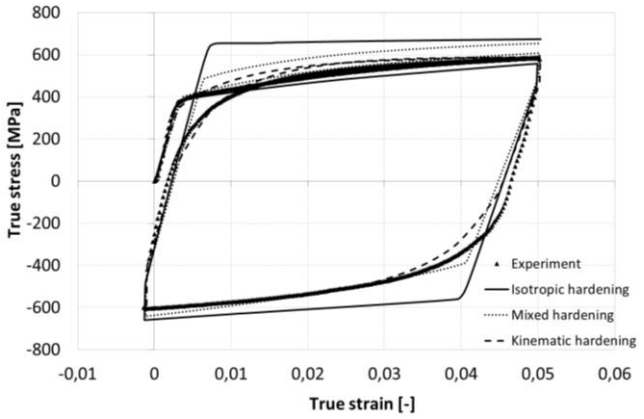

Fig. 5. True stress-strain curves obtained from cyclic T-C test from numerical simulation and the real experiment of DP600 steel sheet

In Fig. 6 is illustrated course of the contact force between punch and the sheet metal. From this graph implies that the drawing stroke was the same in the case of numerical simulation and real experiment. The load-displacement curves were calculated by FE simulations using different materials models and compared with the experimental results. From these three curves implies, that the Yoshida-Uemori kinematic hardening material model predicts experimental course more accurate than others.

DOI 10.1515/ama-2017-0001

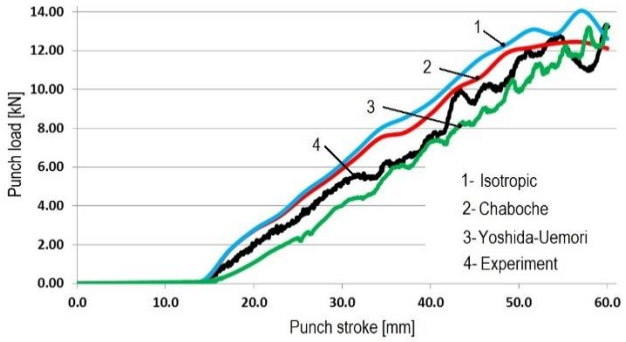

Fig. 6. Experimentally measured punch load curve during stamping in comparison with FE simulation results using different hardening models for the DP600 steel

The final shape of the stamped part after springback obtained from simulation and the real experiment is shown in Fig. 7. It is shown, that the predicted profiles of the part after springback better agreed with measured data of investigated material when the Yoshida-Uemori kinematic hardening material model was used. This result is confirmed by the course of stress-strain curve shown in the Fig. 5. Cross-section profile predictions from Yoshida-Uemori model most fairly agreed with the experimental results, whereas the isotropic provided the least accurate predictions. The springback prediction of high strength steels by FE simulation with using isotropic hardening model seems to be inadequate.

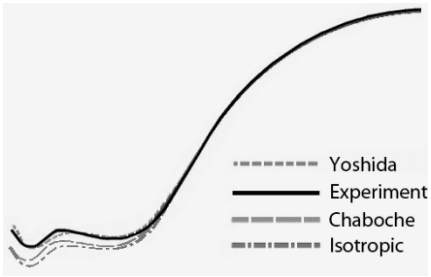

Fig. 7. Cross-section profiles of the sample after springback calculated by FEM using different hardening models in comparison with experimental results for DP600 steel

3. CONCLUSIONS

From the research presented in this paper implies, that the hardening models which consider kinematic hardening are more accurate within springback simulation. Implementation of advanced hardening material models presented in this research is associated with the need of an appropriate experimental test to obtain stress-strain curve from cyclic tension – compression test. In compression phase of the cycle, this test is associated with the problem of buckling. Therefore, it is necessary to use a special fixture to prevent buckling. Designed fixture allows reliably measure stress-strain curves. Subsequently, hardening models which describe springback issue with great accuracy can be implemented. Yoshida-Uemori kinematic hardening model was successfully fitted to the experimental stress-strain curves obtained from cyclic test. The numerical prediction of springback with this hardening model agreed well with experimental data. The application of conventional isotropic hardening model for materials such advanced high strength steels is unsatisfactory.

REFERENCES

1. **Boger R.K., Wagoner, R.H., Barlat F., Lee M.G., Chung K.** (2005), Continous, large strain, tension/compression testing of sheet material, *International Journal of Plasticity*, 21, 2319–2343.
2. **Bruschi S., Altan T., Banabic D., Bariani P.F., Brosius A., Cao J., Tekkaya A. E.** (2014), Testing and modelling of material behaviour and formability in sheet metal forming, *CIRP Annals-Manufacturing Technology*, 63(2), 727–749.
3. **Cao J., Lee W., Cheng H.S., Seniw M., Wang H., Chung K.** (2009), Experimental and numerical investigation of combined isotropic-kinematic hardening behavior of sheet metals, *International Journal of Plasticity*, 25, 942-972.
4. **Chongthairungruang B., Uthaisangsuk V., Suranuntchai S., Jirathearanat S.** (2013), Springback prediction in sheet metal forming of high strength steels, *Materials & Design*, 50, 253-266.
5. **Eggertsen P., Mattiasson K.** (2010), On constitutive modeling for springback analysis, *International Journal of Mechanical Sciences*, 52(6), 804–818.
6. **Kim J.H., Kim D., Barlat F., Lee M.** (2012) Crystal plasticity approach for predicting the Bauschinger effect in dual-phase steels. *Materials Science and Engineering: A*, 539, 259–270.
7. **Kuwabara T., Kumano Y., Ziegelheim J., Kurosaki I.** (2009), Tension–compression asymmetry of phosphor bronze for electronic parts and its effect on bending behavior, *International Journal of Plasticity*, 25(9), 1759–1776.
8. **Lemoine X., Durrenberger L., Zhu H., Kergen R.** (2011), *Mixed hardening models: parameters identification on AHSS steels*, IDDRG Conference Proceedings.
9. **Mahmoudi A.H., Pezeshki-Najafabadi, S.M., Badnava, H.** (2011), Parameter determination of Chaboche kinematic hardening model using a multi objective Genetic Algorithm, *Computational Materials Science*, 50, 1114-1122.
10. **Piao K., Lee J.K., Kim J.H., Kim H.Y., Chung K., Barlat F., Wagoner R.H.** (2012), A sheet tension/compression test for elevated temperature, *International Journal of Plasticity*, 38, 27- 49.
11. **Shi M., Zhu X., Xia C., Stoughton T.** (2008) *Determination of nonlinear isotropic/kinematic hardening constitutive parameters for AHSS using tension and compression tests*, Numisheet Conference, 137–142.
12. **Silvestre E., Mendiguren J., Galdos L., Sáenz de Andragona E.** (2015), Comparison of the hardening behaviour of different steel families: From mild and stainless steel to advanced high strength steels, *International Journal of Mechanical Sciences*, 101-102, 10-20.
13. **Slota J., Jurčišin M., Spišák E.** (2012), Numerical and experimental springback determination of sheet metals in an air bending process, *Acta Metallurgica Slovaca*, 18(4), 200-209.
14. **Slota J., Jurčišin M., Spišák E., Sleziak, T.** (2014), An investigation of springback in sheet metal forming of high strength steels, *Applied Mechanics and Materials*, 693, 370-375.
15. **Wagoner R.H., Lim H., Lee M.G.** (2013), Advanced issue on springback, *International Journal of Plasticity*, 45, 3-20.
16. **Yoshida, F., Uemori, T.** (2002), A model of large-strain cyclic plasticity describing the Bauschinger effect and workhardening stagnation, *International Journal of Plasticity*,18, 661–686.
17. **Yoshida, F., Uemori, T.** (2003), A model of large-strain cyclic plasticity and its application to springback simulation, *International Journal of Mechanical Sciences*, 45(10), 1687–1702.

The work has been accomplished under the research project No. APVV-0273-12: "Supporting innovations of autobody components from the steel sheet blanks oriented to the safety, the ecology and the car weight reduction" financed by the Slovak Research and Development Agency and VEGA 1/0872/14 supported by the Scientific Research Committee".

DE GRUYTER
OPEN

DOI 10.1515/ama-2017-0002 acta mechanica et automatica, vol.11 no.1 (2017)

VERIFICATION OF STRENGTH OF THE WELDED JOINTS BY USING OF THE ARAMIS VIDEO SYSTEM

Tadeusz PAŁA*, Ihor DZIOBA*, Jarosław GAŁKIEWICZ*

*Department of Machine Design Fundamentals, Faculty of Mechatronics and Machine Design, Kielce University of Technology, Al. 1000-lecia PP 7, 25-314 Kielce, Poland

tadeusz.pala@gmail.com, pkmid@tu.kielce.pl, jgalka@tu.kielce.pl

received 8 October 2015, revised 22 February 2017, accepted 6 March 2017

Abstract: In the paper are presented the results of strength analysis for the two types of the welded joints made according to conventional and laser technologies of high-strength steel S960QC. The hardness distributions, tensile properties and fracture toughness were determined for the weld material and heat affect zone material for both types of the welded joints. Tests results shown on advantage the laser welded joints in comparison to the convention ones. Tensile properties and fracture toughness in all areas of the laser joints have a higher level than in the conventional one. The heat affect zone of the conventional welded joints is a weakness area, where the tensile properties are lower in comparison to the base material. Verification of the tensile tests, which carried out by using the Aramis video system, confirmed this assumption. The highest level of strains was observed in HAZ material and the destruction process occurred also in HAZ of the conventional welded joint.

Keywords: High-Strength Steel, Laser Welded Joints, Tensile Properties, Fracture Toughness

1. INTRODUCTION

With the development of steel production technology on the market appear high-strength ferritic steels, which yield strength reaches 1000 MPa. The weldability pays an important role in a broad applicability of the high-strength steels. The selection of the appropriate method and welding parameters has an influence on the quality of the resulting joints. The aim of making the welded joints is to obtain level of strength characteristics, which is not lower than in the base material (BM). It is a difficult task when high-strength steels are welded, because the welding process causes changes in the original microstructure, which may lead to a reduction of the mechanical properties of the base material in zones near the weld - in the heat affect zone (Dzioba and Pała, 2011; Hakansson, 2002; Keehan et al., 2010; Lambert-Perlade et al., 2010; Lillemae et al., 2016; Lisiecki, 2014; Liu et al., 2015; Mazanek et al., 2013). Thus, making a welded joint of high-strength ferritic steels, one may pay attention to quality and strength of the weld material (WM) and also to the material of heat affect zone (HAZ).

Two welded joints were tested in the research: joint made by a traditional conventional type of welding and the joint welded by an advanced laser technology. The high-strength ferritic steel S960QC was used as a base material for both welded joints (Tab. 1). Both material strength and fracture toughness characteristics of different welded joints zones were determined. Based on these results was assessed a zone, in which failure would happened. This prevision was verified during tensile test of the welded joints, in which were analyzed strain distributions obtained by using of the Aramis video systems (Aramis v6.1).

2. TEST METHODS AND RESULTS

The authors of the paper did not participate in the development of the welding technologies. They performed the studies on the supplied joints only. The thickness of the two type welded plates was identical – 6 mm. However, it is an important notice, that the linear welding energy (LWE) for laser welding is significantly lower (LWE = 0.175 kJ/mm), in comparison with the traditional MIG/MAG technology (LWE = 0.7 kJ/mm).

The standard test procedures were used for determination of the hardness distributions, mechanical properties and fracture toughness of the material in different zones of both welded joints (ASTM E 1820-05; PN-EN ISO 6507-1:2006, PN-EN ISO 6892-1:2010). The details of cut out and preparation the specimens for tensile and fracture toughness tests were presented in the paper [6]. The principle of measuring the fields of the strains by using the Aramis video system is described in the user manual (Aramis v6.1) and was presented in Pała et al. (2016).

The high level of strength properties of S960QC steel are reached using the control heat-rolling treatment during a production process. The tensile characteristics of the S960QC steel according to the standard are: $R_e \geq 960$ MPa, $R_m \geq 1000$ MPa (Dzioba et al., 2014). The chemical composition is presented in the Tab. 1.

Tab. 1. Chemical composition (in wt.%) [5]

	C	Si	Mn	P	S	Ti	Cr	Ni	Mo	V	Cu
S960-QC	0.11	0.25	1.20	0.020	0.010	0.07	CEV=C+Mn/6+(Cr+Mo+V)/5+ (Cu+Ni)/15				

DOI 10.1515/ama-2017-0002

2.1. Hardness distributions

Hardness measurements were carried out on the hardness tester of *Wolpert Wilson Instruments Company*, according to the Vicker's method with a load of 10 N. Hardness distributions in welded joints were determined in the cross-sections of the welded plates (Fig. 1, Fig. 2). The point "0 mm'' on the horizontal axis corresponds to hardness of a weld material in its axis. From the hardness distribution graphs, as it can be seen that the laser joint of LWE = 0.175 kJ/mm (Fig. 1) has a narrower weld and heat affected zone (HAZ) than the conventional joint of LWE = 0.7 kJ/mm (Fig. 2). In the cross-section of the laser joint, width of the weld material area and heat affected zone decreases with an increase of the distance from the weld face. Weld shape is symmetrical. From the weld face has a width of ~2 mm and HAZ ~0.7 mm. Then, in the middle part of thickness of smelting, is greatly reduced to ~ 1 mm and a constant width HAZ, reaching around the root, the width of ~ 0.4 mm and HAZ ~ 0.3.

a)

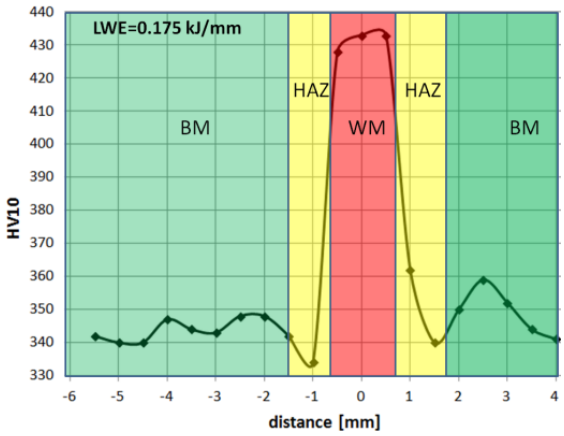

b)

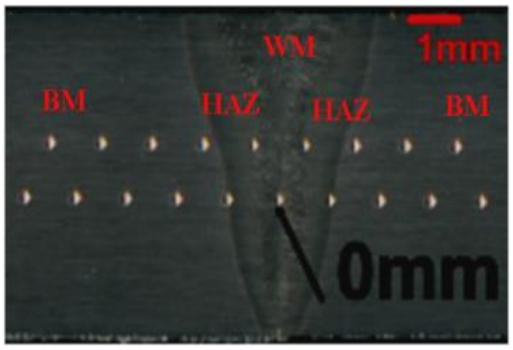

Fig. 1. The hardness distribution (a) and cross-section (b) the laser welded joint

In the case of the joint of LWE = 0.7 kJ/mm the weld material and HAZ take more complex shapes and larger sizes (Fig. 2b). At the weld face has a width of ~ 9 mm and HAZ ~ 1 mm, then there is a local narrowing. In the middle part of the weld, thickness has a width of ~7 mm, HAZ ~ 4 mm. At a distance of ~ 1.7 mm from the surface to the side of the root joint, the zones are narrowing to the equal value of ~ 4 mm to finally reach the width of ~ 6 mm and ~ 2.4 mm on the joint surface, respectively for the weld and HAZ.

From hardness distribution graphs (Fig. 1a), one may observe that hardness in the weld material in the laser joint (~435 HV10) and in the welded joint by a conventional method (Fig. 2a) (~400 HV10) are higher than the values that the base material has (~350-370 HV10). However, the conventionally welded joint is characterized by a significant reduction in hardness in the HAZ, of about 35-40% compared to the base material. This is a disadvantage, because one may expect that it will be an area of reduced strength properties. In the case of the laser joint, the local reduction of hardness does not occur.

a)

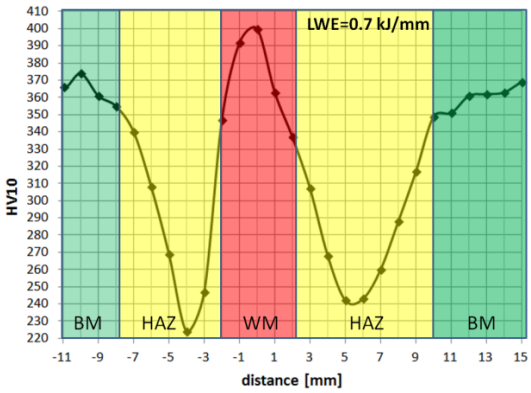

b)

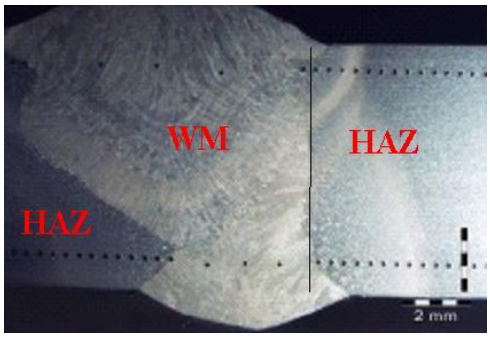

Fig. 2. The hardness distribution (a) and cross-section (b) the conventional welded joint

2.2. Strength properties

Strength properties of the analyzed welded joints were determined in the uniaxial tensile test on the modernized tensile testing machine *UTS-100*, equipped with a test control and results record system. Signal strength and elongation of the measuring part of the specimens were recorded during carried out uniaxial tensile tests. Flat type specimens were taken from the proper areas of the welded joints: weld material (WM), heat affected zone material (HAZ) and base material (BM) [6]. The obtained results of the yield strength (R_e), ultimate strength (R_m), hardness (HV10) and Young modulus (E) for both joints are presented in the Table 2. For the laser joint the mechanical properties were determined in the middle part of the HAZ material, because to the small sizes of the HAZ zone. In the case of the joint made by the conventional method the width of the HAZ zone is bigger, the specimens were taken from three areas: HAZFL (in the vicinity of the fusion line), HAZN (in the vicinity of end normalization area of the material) and HAZE (near the end of the HAZ. The specimens taken from particular zones of the conventional joint to determine strength characteristics had the cross-section of 2x4 mm^2.

The weld material in the laser joint has very high strength characteristics: R_e = 1071 MPa, R_m = 1358 MPa and hardness of 448 HV10. In HAZ the tensile properties and hardness of the material decrease evenly to level, which corresponds to the char-

DOI 10.1515/ama-2017-0002

acteristics of the base material. Analyzing setting of the true tensile curves for the particular laser joint zones, one can observe that the lowest is situated the curve representing the specimen taken from the BM (Fig. 3a). It is an advantageous situation, because the joint welded by laser can provide a loading equal to the element made of BM.

Tab. 2. Mechanical properties of the materials taken from the areas of the welded joints

		LWE = 0.175 kJ/mm		LWE = 0.7 kJ/mm			
Joint zone	BM	WM	HAZ	WM	HAZFL	HAZN	HAZE
E, (GPa)	185	193	192	178	187	185	191
R_e, (MPa)	1005	1071	1014	850	678	963	1183
R_m, (MPa)	1090	1358	1056	1090	912	975	1208
HV10	350	448	355	368	306	294	371

In the conventional joint the lowest tensile characteristics occur in the HAZFL: R_e = 678 MPa and R_m = 912 MPa. Also, lower than in BM tensile characteristics are in HAZN: R_e = 963 MPa and R_m = 978 MPa. The true tensile curve for specimens taken from the HAZ material sets significantly lower, than the one for BM (Fig. 3b). This is a disadvantageous situation, because the welded joint is not able to provide the loading on the BM level.

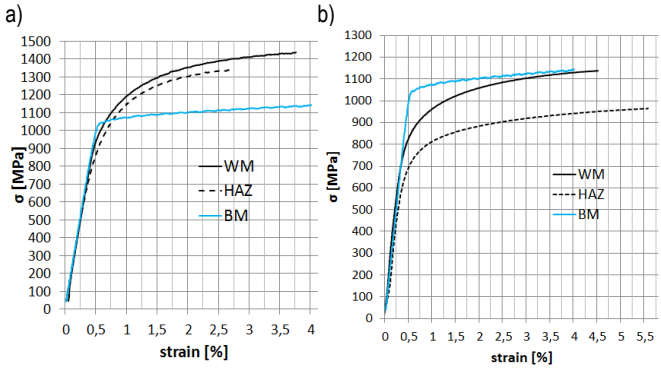

Fig. 3. The true tensile curves for the particular zones of the joint LWE = 0.175 kJ/mm (a) and LWE = 0.7 kJ/mm (b)

2.3. Fracture toughness

Fracture toughness characteristics were determined on the *MTS-250* testing machine, equipped with an automated test control and results record system. The tests were carried out at room temperature on the three point bend specimens with a single-edge notch that were mechanically cut in the WM, HAZ and BM. During fracture toughness determination the signals of force, P, sample bending at a load point, u_{ext}, crack opening, u_{COD}, and change potential, U, at time were recorded. In a case of ductile extension of crack fracture toughness critical values were determined according to the ASTM E1820-05 standard [2]. In the case of brittle fracture, preceded by plasticizing of the area at front of the crack, the critical values of J_{IC} were calculated by the formula:

$$J_{IC} = \frac{2A_C}{B(W-a_0)} \quad (1)$$

where: A_C - strain energy at the moment of cracking, computed on the basis of $P = f(u_{ext})$ graph, W - specimen height, B - specimen thickness, $a_0 \approx 0.5W$.

Critical values of J integral, J_C, were converted into units of stress intensity factor according to:

$$K_{JC} = \sqrt{\frac{J_{IC}E}{(1-\nu^2)}} \quad (2)$$

where: E - Young's modulus, ν - Poisson's ratio.

The critical values of fracture toughness for the laser joints and the joints welded by a conventional method are presented in the Table 3. The fracture toughness critical values were determined in WM, HAZ and BM. Next, in the HAZ area the values of the K_{JC} were determined in three locations: HAZFL - vicinity of the fusion line; HAZ_0.5 - at the distance 0.5 mm from a fusion line; HAZN - in the vicinity of end the normalization area. A sample specimen of notched in the weld material for the laser joint presented in the Fig. 4.

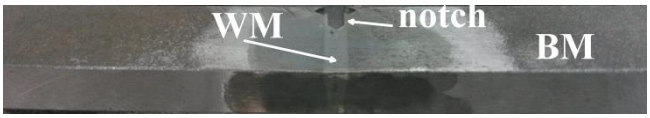

Fig. 4. A sample specimen notched in the laser weld material

Tab. 3. Fracture toughness in the zones of the laser and conventional joint

	Joint zones				
	WM	HAZFL	HAZ_05	HAZN	BM
Conventional joint (LWE = 0.7 kJ/mm)					
K_{JC} [MPa*m$^{1/2}$]	**155**; 160	**168**; 188	**160**; 170; 260	**290**; 310	**260**; 280
Laser joint (LWE = 0.175 kJ/mm)					
K_{JC} [MPa*m$^{1/2}$]	**159**; 162	**152**; 159	**244**; 250	**297**; 299	**269**; 288

The lowest values of the fracture toughness for both welded joints were obtained for the WM. For conventional welded joints was observed the level K_{JC} similar to WM for the material of the HAZFL and HAZ_0.5. An increase of the distance from a fusion line leads to an increase of the material fracture toughness values to the level proper for the BM. For laser welded joints the level K_{JC} similar to WM was obtained only in HAZFL area. In the areas more away from the fusion line, the fracture toughness reaches the level similar for BM. Base on these results we can state, that laser joints have higher fracture toughness in comparison to joints welded conventionally.

2.4. The microstructure studies of the welded joints material

The base material, steel S960QC, as a result of the thermo-mechanical treatment performed in a controlled manner directly at the production line, has a fine-grained bainite-martensite microstructure (Fig. 5) and a high level of tensile properties and fracture toughness that were shown above. The obtained results are confirmed with data received for similar steels, which has fine-grained bainite-martensite microstructure (Bhadeshia, 2001; Dzioba, 2011).

DOI 10.1515/ama-2017-0002

As a welding result the weld material has of martensite-bainite types (Fig. 6) with small laths of 0.5-2.0 mm width. The increase of LWE level is caused by more numerous and larger carbide precipitates which are occurred in WM.

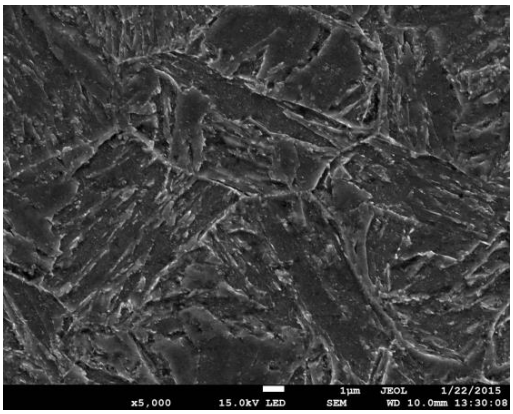

Fig. 5. Bainite-martensite microstructure of the S960QC steel

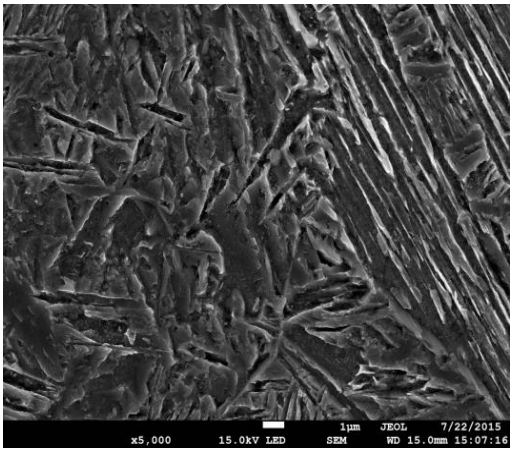

Fig. 6. Martensite-bainite microstructure the WM of the joints

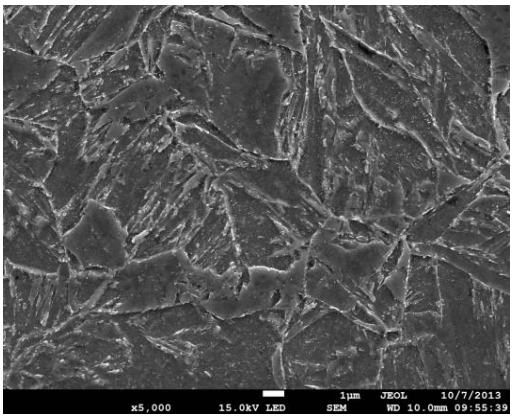

Fig. 7. Bainite-martensite microstructure in the HAZ of the joint welded with LWE = 0.175 kJ/mm

The significant differences in types of microstructure are observed in HAZ. The welding process made with lower LWE level has an insignificant influence on the microstructure of a base material. Only more numerous carbide precipitates in comparison to BM were observed in HAZ after welding with LWE = 0.175 kJ/mm (Fig. 7). The welding with a high level of LWE lead to significant changes in the microstructure of BM. As a result welding with LWE = 0.7 kJ/mm in HAZ is observed fine-grained ferrite microstructure with numerous carbide precipitates (Fig. 8). This type of microstructure is characterized by a lower level of tensile and fracture toughness properties (Bhadeshia, 2001; Dzioba, 2011; Lambert-Perlade et al., 2004; Tweed and Knott, 1987; Yang et al., 2015).

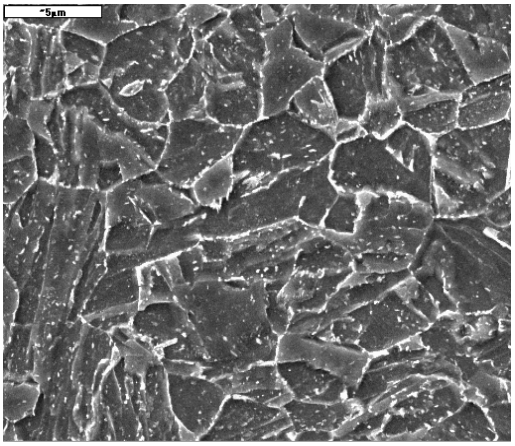

Fig. 8. The fine-grain ferrite with carbides precipitates microstructure in the HAZ of the joint welded with LWE = 0.7 kJ/mm

2.5. Uniaxial loading the welded joints carried out by using the Aramis video system

In the next stage was performed verification of the joints strength. The flat specimens, which contained welded joints were loaded by uniaxial tensile. The verification was done on the base results from the strain maps obtained using the Aramis video system. The strain maps on the surface loaded element measured were received in current time by using the video system.

a)

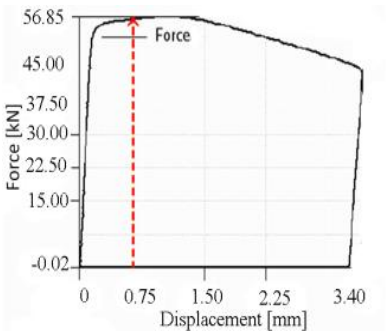

b)

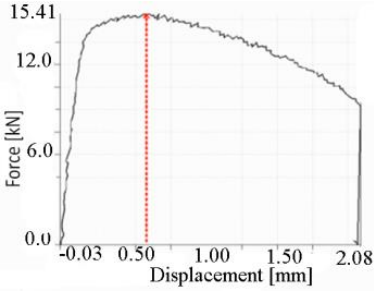

Fig. 9. Plots of force-displacement for a laser (a) and conventional (b) joints

DOI 10.1515/ama-2017-0002

In the Fig. 9a and 9b are shown the force-displacement curves recorded during uniaxial tensile loading of the welded joints. The strain maps, which correspond to the maximum loading, for the laser joint and the conventional joint, are presented in figures 10a and 10b. At following loading in the laser welded joint the region, where the maximal strain occurs and creating a neck, performed in the BM, which means that the BM is the weakest in this welded joint. In the conventional joint, by contrast, the weakest area exposed in HAZ. Following loading leaded to destruction in the corresponding areas of the joints. The results obtained by using the Aramis video system confirm the results of strength and fracture toughness properties of the material from different zones the welded joints.

a)

b)

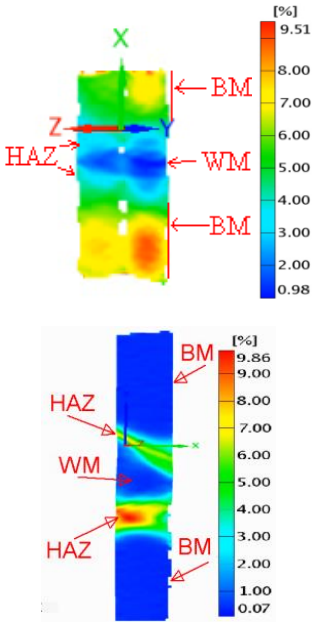

Fig. 10. The corresponding strain maps at the moment of acting of the maximum load for a laser (a) and conventional (b) joints, respectively

3. CONCLUSION

The presented study clearly shows that the laser joints of high-strength steel S960QC have more advantageous mechanical properties, than joints welded by the conventional technology. The geometry sizes of laser welded joints are less than ones made of conventional technology. In the laser welded joints reduction hardness and tensile properties in WM and HAZ of the laser welded joints does not occur, as opposed to the joints conventionally welded. The fracture toughness the material in different areas of the laser welded joints is no less than in the conventional joints.

Verification tests carried out for the both welded joints by using the Aramis video system validated previous assumption according to the weakness areas in the welded joints. In the conventional welded joints the weakness area is the HAZ, what is not advantageous, because the mechanical properties in the HAZ are lower than of the BM, so the joint is not able to resists load such as the BM. In the laser welded joints the weakness area is the BM, what is favorable, because the joint is able to resist load as the BM.

REFERENCES

1. Aramis v6.1 User Manual, GOM Gmbh, 2009.
2. ASTM E 1820-05, Standard Test Method for Measurement of Fracture Toughnes,. *ASTM*, Philadelphia; 2000.
3. **Bhadeshia H.K.D.H.** (2001), *Bainite in Steels*, Institute of Materials, London.
4. **Dzioba I.** (2011), The influence of the microstructural components on fracture toughness of 13HMF steel, *Materials Science*, 47(5), 357-364.
5. **Dzioba I., Pała T.** (2014), Mechanical properties of welded joints made of high-strength steel S960-QC by laser method, *Logistyka,* 6, 3458-3464 (in Polish).
6. **Dzioba I., Pała T., Valkonen I.** (2013), Strength and fracture toughness of the welded joints made of high-strength ferritic steel, *Acta Mechanica et Automatica*, 7(4), 226-229.
7. **Gałkiewicz J., Pała T., Dzioba I.** (2012), Mechanical properties of the welded joints of ultra-strength ferritic steels, *XXIII Symposium on Fatigue and Fracture Mechanics Bydgoszcz– Pieczyska*, 63-72 (in Polish).
8. **Górka J.** (2015), Weldability of Thermomechanically Treated Steels Having a High Yield Point, *Archives of Metallurgy and Materials,* 60(1), 469-475.
9. **Hakansson K.**, Weld Metal Properties for Extra High Strength Steels, Report 2002 – August, Division of Welding, Department of Production Engineering, The Royal Institute of Technology, 1-36.
10. **Keehan E., Zachrisson J., Karlsson L.** (2010), Influence of cooling rate on microstructure and properties of high strength steel weld metal, *Science and Technology of Welding and Joining,* 15, 233-238.
11. **Lambert-Perlade A., Gourgues A.F., Besson J., Sturel T., Pineau A.** (2004), Mechanisms and modeling of cleavage fracture in simulated heat-affected zone microstructures of a high-strength low alloy steel, *Metall Mater Trans A*; 35(13):1039-53.
12. **Lillemäe I., Remes H., Liinalampi S., Itävuo A.** (2016), Influence of weld quality on the fatigue strength of thin normal and high strength steel butt joints, *Welding in the World,* 4, 1-10.
13. **Lisiecki A.** (2014), Weldability of Thermomechanically Treated Steels Having a High Yield Point, *Archives of Metallurgy and Materials,* 59(4), 1625-1631.
14. **Liu F., Yu X., Huang C., He L., Chen Y., Bu W.** (2015), Microstructure and mechanical properties of AerMet 100 ultra-high strength steel joints by laser welding, *Journal of Wuhan University of Technology-Mater. Sci. Ed.*, 8/2015, 30, 827-830.
15. **Mazanek K., Sniezek I., Slezak T.** (2013), Fatigue research of welded joints of high strength S960QL steel, *Bulletin of the Military University of Technology*, 42(1), 253-269 (in Polish).
16. **Pała T., Gałkiewicz J., Dzioba I.** (2016), Determination of Strain and Stress Fields in Laser Welded Joints by Means of the Aramis Video System, *Solid State Phenomena,* 250, 151-156.
17. PN-EN ISO 6507-1:2006. *Metals, toughness measurement by the Vicker's method*, part 1, testing method (in Polish).
18. PN-EN ISO 6892-1:2010. *Metals, tensile test, part 1: Testing method at room temperature* (in Polish).
19. **Tweed J.R., Knott J.F.** (1987), Micromechanisms of failure in C-Mn weld metal, *Acta Metallurgica*, 35(7), 1401-1414.
20. **Yang Y., Shi L., Xu Z., Lu H., Chen X., Wang X.** (2015), Fracture toughness of the materials in welded joints of X80 pipeline steel, *Engineering Fracture Mechanics*, 148, 337-349.

Acknowledgments: Financial support from the Grant of the Polish National Centrum of Research and Development (NCBiR) PBS1/B5/13/2012 and the Polish Ministry of Science and Higher Education under contracts NN 01.0.08.00/2.01.01.01.0035 are gratefully acknowledged.

DOI 10.1515/ama-2017-0003

THE STABILITY OF A STEEL WELDED GIRDER WITH BENDING AND SHEAR FORCES INCLUDED

Ryszard SYGULSKI[*], Michał GUMINIAK[**], Łukasz POLUS[**]

[*]Polytechnic Faculty, The President Stanisław Wojciechowski Higher Vocational State School in Kalisz, Poznańska 201-205, Kalisz, Poland
[**]Institute of Structural Engineering, Poznan University of Technology, Piotrowo 5, 60-965 Poznan, Poland

ryszard.sygulski@gmail.com, michal.guminiak@put.poznan.pl, lukasz.polus@put.poznan.pl

received 14 October 2015, revised 22 February 2017, accepted 6 March 2017

Abstract: The stability of the element of a steel welded girder subjected to bending and shear forces is considered. The considered element is a rectangular plate supported on boundary. The type of a plate boundary conditions depend on the types (thickness) of the stiffeners. Considered plate is loaded by in-plane forces causing bending and shear effects. The Finite Element Method was applied to carry out the analysis. Additionally the Boundary Element Method in terms of boundary-domain integral equation was applied to evaluate the critical shear loading.

Key words: Buckling Analysis, the Finite Element Method, the Boundary Element Method

1. INTRODUCTION AND PROBLEM FORMULATION

The correct determination of the critical load is essential in the design process. This issue was investigated and solved in an analytical way by Timoshenko et al. (1962). The Finite Element Method (FEM) is applied to a numerical investigation of the stability of the steel welded girder with the bending and the shear forces included. Suitable numerical algorithms of FEM were presented e.g. by Rakowski and Kacprzyk (2005). Others e.g. Shi (1990), Chinnaboon et al. (2007)have used the Boundary Element Method (BEM) to solve the buckling problem of thin plates of any shape including plates with holes. Garstecki and Rzeszut (2009) solved the stability problem of thin walled cold formed sigma profiles with geometrical imperfection. Marcinowski (2007) analysed stability of relatively deep segments of spherical shells loaded by external pressure. The non-linear stability of elastic thin walled structures considering unilateral constraints was investigated by Rzeszut and Garstecki (2011). The direct non-singular formulation of the boundary element method using the fundamental solutions given by Ganowicz and its application to a static analysis of plates with intermediate thickness was presented by Litewka and Sygulski (2010). The analysis of the influence of the fire load on the class of cross-section of steel structural elements was presented by Rzeszut and Polus (2013). The stability problem of thin walled girders considering initial imperfections was investigated by Rzeszut and Garstecki (2013) and Chybinski et al. (2013). Biegus and Kowal (2013) presented that the insufficient buckling strength may lead to disaster. Gosowski (1999) analysed spatial buckling of thin-walled steel-construction beam-columns with discrete bracings. Load capacity and the stability of steel thin-walled beams with local stiffening elements were analysed by Chybiński (2015).

The stability of steel welded girders subjected to in-plane complex loading is presented in the paper. The part of the main structure is indicated in the Fig. 1. The element being a part of the steel welded girder is considered as the square plate, simply-supported with a clamped edge (Fig. 2a) and simply-supported (Fig 2b).

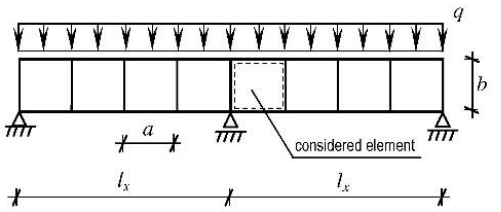

Fig. 1. Steel girder with vertical stiffeners

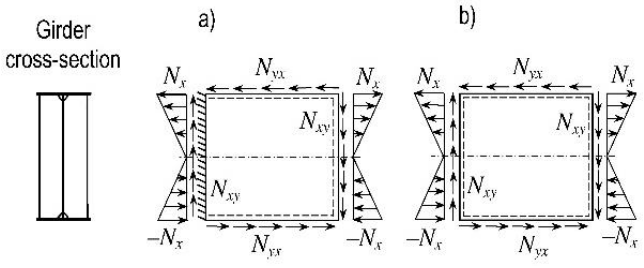

Fig. 2. Considered element

It usually works as a part of the structure under bending and shear load. It is assumed that the material is linear-elastic. The considered plates are subjected to N_x and N_{xy} in-plane forces with linear and constant distributions respectively (Fig. 2a and 2b).

2. AN APPLICATION OF THE FEM

The differential equation qoverning of plate initial stability has the form:

DOI 10.1515/ama-2017-0003

$$D \cdot \nabla^4 w = -\bar{p}, \tag{1}$$

where $\bar{p}$ is the substitute load

$$\bar{p} = N_x \cdot \frac{\partial^2 w}{\partial x^2} + 2N_{xy} \cdot \frac{\partial^2 w}{\partial x\, \partial y}. \tag{2}$$

The Finite Element Method is applied to solve the initial stability problem described by equation (1). In the current analysis four types of finite elements are applied: (i) the rectangular four node shell elements with three degrees of freedom (DOF) per node (deflection and angle of rotations in two perpendicular directions); (ii) the triangular three node shell elements with three DOF per node; (iii) the rectangular eight node shell elements with three DOF per node (deflection and angle of rotations in two perpendicular directions); (iv) and the triangular six node shell elements with three DOF per node. The reduced integration of all shape functions will be applied too. Applying the FEM in pure form leads to the generalized eigenvalue problem (Rakowski and Kacprzyk, 2005)

$$\left(K - \lambda \cdot K_G\right) \cdot \tilde{q} = 0, \tag{3}$$

where: $\lambda = N_{cr}$ is critical multiplier, K is the stiffness matrix, K_G is the geometric stiffness matrix and $\tilde{q}$ is the vector of nodal displacement with non-zero elements.

The finite element analysis was carried out using the Abaqus system (Abaqus, 2005).

3. AN APPLICATION OF THE BEM

The Boundary Element Method in terms of the boundary – domain integral equations is introduced. The initial stability problem of the plate subjected only to N_{xy} in-plane forces is solved as the simple benchmark test in reference to the FEM. The solution of differential equation (1) can be expressed as the integral representation of two boundary-domain integral equations formulated according to the simplified approach (Guminiak and Sygulski, 2003; Guminiak, 2014):

$$\begin{aligned} &c(\mathrm{x}) \cdot w(\mathrm{x}) + \int_\Gamma [T_n^*(\mathrm{y},\mathrm{x}) \cdot w(\mathrm{y}) + \\ &-M_{ns}^*(\mathrm{y},\mathrm{x}) \cdot \frac{dw(\mathrm{y})}{ds} - M_n^*(\mathrm{y},\mathrm{x}) \cdot \varphi_n(\mathrm{y})\Big] \cdot d\Gamma(\mathrm{y}) = \\ &= \int_\Gamma [\tilde{T}_n(\mathrm{y}) \cdot w^*(\mathrm{y},\mathrm{x}) - M_n(\mathrm{y}) \cdot \varphi_n^*(\mathrm{y},\mathrm{x})] \cdot d\Gamma(\mathrm{y}) + \\ &+ \int_\Omega 2N_{xy} \cdot \frac{\partial^2 w}{\partial x\, \partial y} \cdot w^*(\mathrm{y},\mathrm{x}) \cdot d\Omega(\mathrm{y}), \end{aligned} \tag{4}$$

$$\begin{aligned} &c(\mathrm{x}) \cdot \varphi_n(\mathrm{x}) + \int_\Gamma [\bar{T}_n^*(\mathrm{y},\mathrm{x}) \cdot w(\mathrm{y}) + \\ &-\bar{M}_{ns}^*(\mathrm{y},\mathrm{x}) \cdot \frac{dw(\mathrm{y})}{ds} - \bar{M}_n^*(\mathrm{y},\mathrm{x}) \cdot \varphi_n(\mathrm{y})\Big] \cdot d\Gamma(\mathrm{y}) = \\ &= \int_\Gamma [\tilde{T}_n(\mathrm{y}) \cdot \bar{w}^*(\mathrm{y},\mathrm{x}) - M_n(\mathrm{y}) \cdot \bar{\varphi}_n^*(\mathrm{y},\mathrm{x})] \cdot d\Gamma(\mathrm{y}) + \\ &+ \int_\Omega 2N_{xy} \cdot \frac{\partial^2 w}{\partial x\, \partial y} \cdot \bar{w}^*(\mathrm{y},\mathrm{x}) \cdot d\Omega(\mathrm{y}), \end{aligned} \tag{5}$$

where the fundamental solution of biharmonic equation:

$$\nabla^4 w^*(\mathrm{y},\mathrm{x}) = \frac{1}{D} \cdot \delta(\mathrm{y},\mathrm{x}) \tag{6}$$

is given as:

$$w^*(\mathrm{y},\mathrm{x}) = \frac{1}{8\pi D} \cdot r^2 \cdot \ln(r) \tag{7}$$

for a thin isotropic plate, $r = |y - x|$, δ is the Dirac delta, $D = Eh^3/\left(12(1-v^2)\right)$ is the plate stiffness, x is the source point and y is a field point. The coefficient $c(x)$ is taken as: $c(x) = 1$, when x is located inside the plate domain, $c(x) = 0.5$, when x is located on the smooth boundary and $c(x) = 0$, when x is located outside the plate domain. The second boundary-domain integral equation (3) can be obtained by replacing the unit concentrated force $P^* = 1$ with the unit concentrated moment $M_n^* = 1$. Such a replacement is equivalent to the differentiation of the first boundary integral equation (4) with respect to the co-ordinate n at the source point *x*. The expression $\tilde{T}_n(y)$ denotes shear force for clamped and for simply-supported edges: $\tilde{T}_n(y) = T_n(y)$ is the shear force (distributed reaction of the support) on the boundary far from the plate corner or $\tilde{T}_n(y) = R_n(y)$ the distributed reaction along the small fragment of the boundary close to the corner. Because the relation between $\varphi_s(y)$ and the deflection is known: $\varphi_s(y) = dw(y)/ds$, the angle of rotation $\varphi_s(y)$ can be evaluated using a finite difference scheme of the deflection with two or more adjacent nodal values (Guminiak and Sygulski, 2003; Guminiak, 2014).

3.1. Construction of set of algebraic equations

The plate boundary is discretized by elements of the constant type. Two approaches of constructing the boundary-domain integral equations are considered. According to the first approach, singular, the collocation points are located exactly on the plate boundary. According to the second approach, non-singular, the collocation points are located outside of the plate boundary (Abaqus, 2005). The plate domain is divided by rectangular subdomains associated with a single collocation point. The set of algebraic equations has the following form:

$$\begin{bmatrix} \mathrm{G_{BB}} & -\lambda \cdot \mathrm{G_{B\kappa}} \\ \mathrm{G_{\kappa B}} & -\lambda \cdot \mathrm{G_{\kappa\kappa}} + \mathrm{I} \end{bmatrix} \cdot \begin{Bmatrix} \tilde{\mathrm{B}} \\ \kappa \end{Bmatrix} = \begin{Bmatrix} 0 \\ 0 \end{Bmatrix}, \tag{8}$$

where: the critical force $\mathrm{N_{cr}}$ is expressed by eigenvalue multiplier $\lambda = N_{xy} = N_{cr}$.

Integration of suitable fundamental functions is done in a local coordinate system ni, si connected with ith boundary element and next, these integrals must be transformed to nk, sk coordinate system, connected with kth element (Guminiak and Sygulski, 2003; Guminiak, 2014). For a non-singular approach, the localization of a collocation point is defined by the parameter $\tilde{\delta}$ which determines the distance from a plate edge or by non-dimensional parameter $\varepsilon = \tilde{\delta}/d$ where d is the element length (Guminiak and Sygulski, 2003; Guminiak, 2014).

The vector of unknowns consist: $\tilde{B} = \{B, \varphi_s\}$ – the vector of boundary independent variables, φ_s – the vector of additional parameters of the angle of rotation in the tangential direction, which depends on the boundary deflection in case of the free edge and κ – the vector specifying curvatures κ_{xy} inside a plate domain. The matrix G_{BB} groups boundary integrals dependent on the type of boundary. The matrix $G_{B\kappa}$ includes values of fundamental functions w^* and $\bar{w}^*$ established in internal collocation points associated with internal rectangular sub-domains. The matrix $G_{\kappa B}$ groups boundary integrals dependent on the type of boundary (integration from internal collocation points over boundary elements), the matrix $G_{\kappa\kappa}$ groups values of fundamental functions w^* and $\bar{w}^*$ established in internal collocation points associated with internal rectangular sub-domains (integration from internal collocation points over internal sub-domains) and I is the unit matrix. The second matrix equation (8)2 can be derived by double

DOI 10.1515/ama-2017-0003

differentiation of the equation (4).

In the present examples only supported plate edges (clamped or simply-supported) are considered, hence the vector φ_s has all elements equal to zero thus $\tilde{B} = B$. The analysis of plates with external in-plane loading acting directly along free edges (edges without any constraints) requires a broader analysis. Elimination of boundary variables B and from matrix equation (8) allows to obtain the standard eigenvalue problem (Guminiak and Sygulski, 2003; Guminiak, 2014):

$$\{\mathrm{A} - \tilde{\lambda} \cdot \mathrm{I}\} \cdot \kappa = 0, \tag{9}$$

where: $\tilde{\lambda} = 1/\lambda$ and

$$\mathrm{A} = \{\mathrm{G}_{\kappa\kappa} - (\mathrm{G}_{\kappa\mathrm{B}}) \cdot [\mathrm{G}_{\mathrm{BB}}]^{-1} \cdot \mathrm{G}_{\mathrm{B}\kappa}\} \quad . \tag{10}$$

3.2. Modes of buckling

The set of the algebraic equations indispensable to calculate the elements of eigenvector w has the form

$$\begin{bmatrix} \mathrm{G}_{\mathrm{BB}} & 0 \\ \mathrm{G}_{\mathrm{wB}} & \mathrm{I} \end{bmatrix} \cdot \begin{Bmatrix} \mathrm{B} \\ \mathrm{w} \end{Bmatrix} = \begin{Bmatrix} \lambda \cdot \mathrm{G}_{\mathrm{Bw}} \cdot \kappa \\ \lambda \cdot \mathrm{G}_{\mathrm{ww}} \cdot \kappa \end{Bmatrix}, \tag{11}$$

where elements of the eigenvector κ are obtained after solution of the standard eigenvalue problem (9). The first equation (11)1 is obtained from the first equation of (8) and the second equation (11)2 is got by construction of the boundary integral equations for calculating the plate deflection in internal collocation points. The displacement vector w can be calculated directly by elimination of boundary variables B (Guminiak and Sygulski, 2003; Guminiak, 2014):

$$\mathrm{w} = \lambda \cdot [\mathrm{G}_{\mathrm{ww}} - (\mathrm{G}_{\mathrm{wB}}) \cdot [\mathrm{G}_{\mathrm{BB}}]^{-1} \cdot \mathrm{G}_{\mathrm{Bw}}] \quad \cdot \kappa. \tag{12}$$

4. NUMERICAL EXAMPLES

The initial stability problem of square plates with various boundary and load conditions is considered. The critical value of the external loading is investigated. The plate properties are: Young modulus E = 205 GPa, Poisson ratio v = 0.3. The following notations are assumed: BEM I – singular formulation of governing boundary-domain integral equations (4) and (5); BEM II – non-singular formulation of governing boundary-domain integral equations (4) and (5), the collocation point of single boundary element is located outside, near the plate edge, $\varepsilon = \tilde{\delta}/d = 0.001$ (Guminiak and Sygulski, 2003); FEM – ABAQUS system with finite elements of the S4R and S8R types are applied (for square plates without holes). The critical force N_{cr} is expressed using non-dimensional term: $\tilde{N}_{cr} = N_{cr} \cdot a^2/D$, where D is the plate stiffness and a is dimension of the plate edge.

4.1. Example 1

The square plate of dimensions a = 2.0 m, clamped along one edge and simply-supported along other edges (Fig. 3) is considered. The plate are subjected to N_{xy} in-plane forces. Plate edges were divided into 128 boundary elements and the number of internal square sub-domains is equal 256. The number of finite element is equal 1600. The results of calculation are presented in Tab. 1 in column a). The first buckling mode is shown in Fig. 4. Column b) contains resuts of calculation for the plate simply supported along all edges.

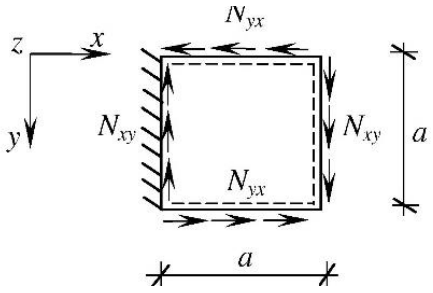

Fig. 3. The plate subjected to in-plane tangential loading

Tab. 1. Critical loading values $\tilde{N}_{\mathrm{cr}}$

$\tilde{N}_{\mathrm{cr}} = \tilde{N}_{xy}$	a)	b)
BEM I	106.971	93.009
BEM II	106.996	93.051
FEM (S4R)	100.601	92.601
FEM (S8R)	101.323	92.799
[1]	–	92.182

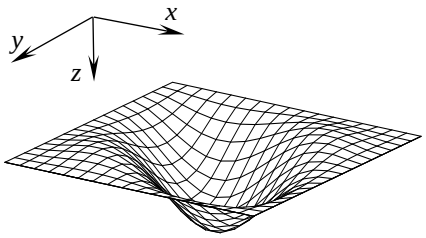

Fig. 4. The first buckling mode for square plate clamped along one edge and simply-supported along other edges

4.2. Example 2

The element of the steel welded girder is considered and modelled as the square simply-supported plate. The plate edge dimensions is a = 2.0 m. The plate is subjected to N_x and N_{xy} in-plane forces with linear and constant distributions respectively (Fig. 5). The finite element discretization is the same as in Example 1. The results of the calculation are presented in Tab. 2. The first buckling mode is shown in Fig. 6.

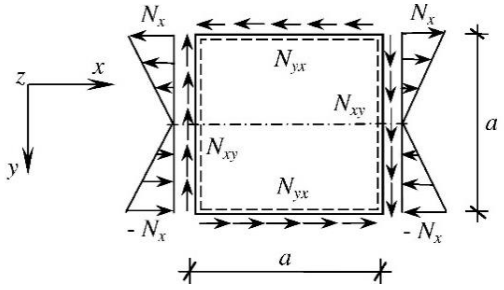

Fig. 5. Considered element of the steel welded girder

DOI 10.1515/ama-2017-0003

Tab. 2. Critical loading value $\tilde{N}_{cr}$. Assumed the comparative compressing loading: $\tilde{N}_x$

$\tilde{N}_{xy}/\tilde{N}_x$	0.0	0.025	0.05	0.1	0.15
S4R	251.837	250.498	247.032	236.685	224.229
S8R	250.069	248.705	245.227	235.037	222.884

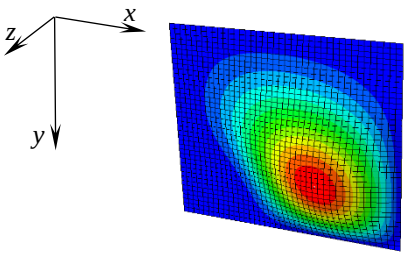

Fig. 6. The first buckling mode for simply-supported square plate ($\tilde{N}_{xy}/\tilde{N}_x$ = 0.1)

4.3. Example 3

The square element of the steel welded girder is considered and modelled as the square plate clamped along one edge and simply-supported along other edges. The plate egde dimension is a = 2.0 m. The plate is subjected to N_x and N_{xy} in-plane forces with linear and constant distributions respectively (Fig. 7). The finite element discretization is the same as in Example 1.

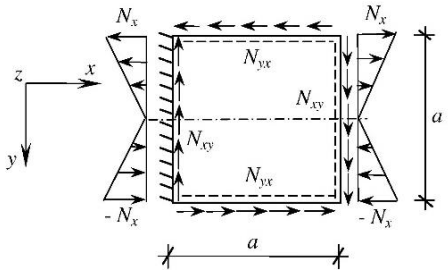

Fig. 7. Considered element of the steel welded girder

The results of the calculation are presented in Tab. 3. The first buckling mode for $\tilde{N}_{xy}/\tilde{N}_x$ = 0.1 is shown in Fig. 8.

Tab. 3. Critical loading value $\tilde{N}_{cr}$. Assumed the comparative compressing loading: $\tilde{N}_x$

$\tilde{N}_{xy}/\tilde{N}_x$	0.0	0.025	0.05	0.1	0.15
S4R	259.794	256.013	251.596	241.294	229.720
S8R	261.093	257.527	253.306	243.324	231.972

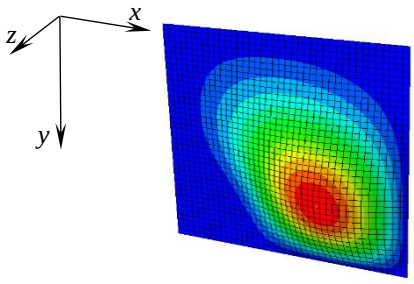

Fig. 8. The first buckling mode for square plate clamped along one edge and simply-supported along other edges ($\tilde{N}_{xy}/\tilde{N}_x$ = 0.1)

4.4. Example 4

The square element of a steel welded girder with the symmetrically square hole is considered and modelled as the square plate. The plate edge dimension is *a* = 2.0 m. The plate is subjected to N_x and N_{xy} in-plane forces with linear and constant distributions respectively (Fig. 9).

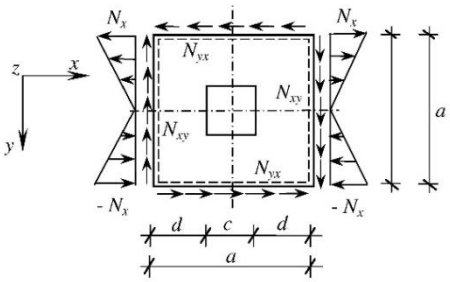

Fig. 9. Considered element of the steel welded girder with square hole

Dimensions of the hole are: *c* = 0.25·a, *d* = 0.375·a. The total number of finite elements is equal 1745 (Fig. 10).

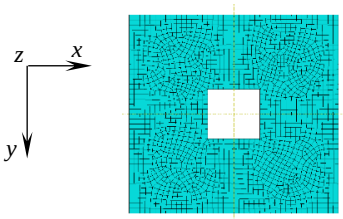

Fig. 10. Considered element of steel welded girder with square hole

The results of the calculation are presented in Tab. 4. The first buckling mode for $\tilde{N}_{xy}/\tilde{N}_x$ = 0 is shown in Fig. 11.

Tab. 4. Critical loading value $\tilde{N}_{cr}$. Assumed the comparative compressing loading: $\tilde{N}_x$

$\tilde{N}_{xy}/\tilde{N}_x$	0.0	0.025	0.05	0.1	0.15
FEM1	116.411	114.277	110.584	101.183	91.164
FEM2	115.047	112.654	108.589	98.601	88.266

The following designations are assumed: FEM1 - four node rectangular finite elements (S4R) and three node triangle finite elements, with three degrees of freedom per node; FEM2 - eight node rectangular finite elements (S8R) and six node triangle finite elements, with three degree of freedom per node.

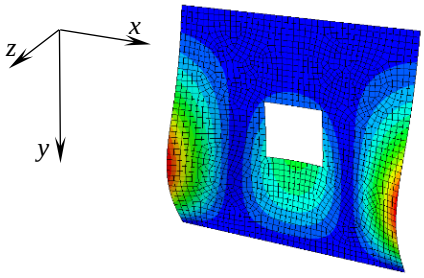

Fig. 11. The first buckling mode for simply-supported square plate with square hole ($\tilde{N}_{xy}/\tilde{N}_x$ = 0)

DOI 10.1515/ama-2017-0003

The first buckling mode for $\tilde{N}_{xy}/\tilde{N}_x$ = 0.025 is shown in Fig. 12.

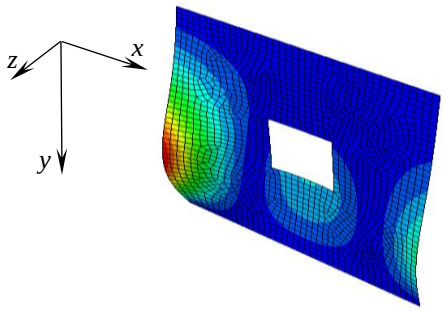

Fig. 12. The first buckling mode for simply-supported square plate with square hole ($\tilde{N}_{xy}/\tilde{N}_x$ = 0.025)

4.5. Example 5

The square element of a steel welded girder with the symmetrically hexagonal hole is considered and modeled as the simply-supported plate. The plate edge dimension is a = 2.0 m. The plate is subjected to tensile N_x in-plane forces with constant distributions respectively (Fig. 13).

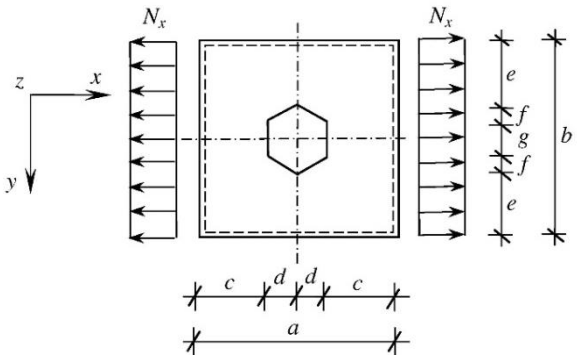

Fig. 13. Considered element of steel welded girder with hexagonal hole

Dimensions of the hole are: c = 0.3268·a, d =0.1732·a, e = 0.3·a, f = 0.1·a, g = 0.2·a. The total number of finite elements equals 1685 (Fig. 14).

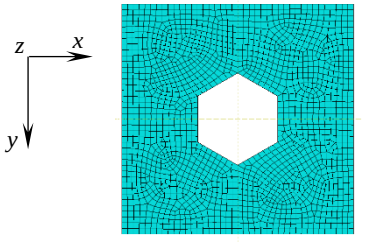

Fig. 14. Considered element of steel welded girder with hexagonal hole

The results of the calculation are presented in Tab. 5.

Tab. 5. Critical loading value $\tilde{N}_{cr} = \tilde{N}_x$

FEM1	FEM2
488.371	479.810

The first buckling mode is shown in Fig. 15.

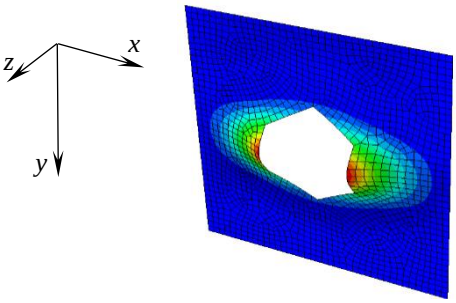

Fig. 15. The first buckling mode for simply-supported square plate with hexagonal hole

4.6. Example 6

The 2-meter-long part of the web of the two-span beam was analysed (Fig. 16). It was assumed that the beam was under continuous restraint and was not susceptible to lateral-torsional buckling. There was no shear lag effect. However, the web was with cross section of class 4 (Fig. 17), in which local buckling may occur.

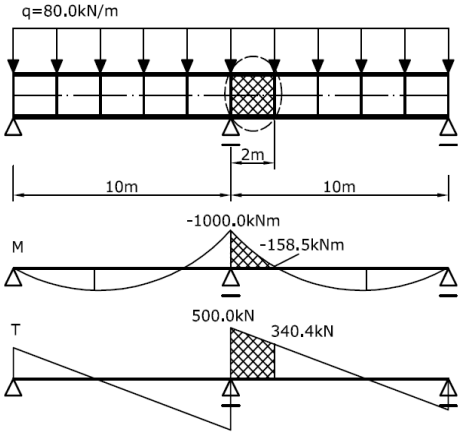

Fig. 16. Analysed steel welded-girder

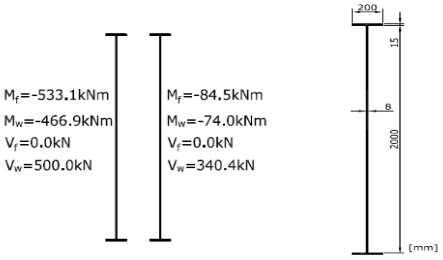

Fig. 17. Analysed steel welded-girder cross-section

For this reason, transverse stiffeners were used every two meters. In this example, the steel square plate was checked for local buckling using the Abaqus finite element system.

The analysed part of the steel welded girder is loaded by bending and shear forces according to Fig. 18. The proportion between shear and bending loading are assumed similarly.

DOI 10.1515/ama-2017-0003

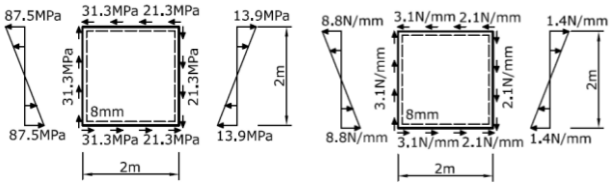

Fig. 18. Analysed steel welded-girder cross-section

This part was divided into 1600 finite elements of S8R type. The boundary conditions are as indicated in Fig. 19.

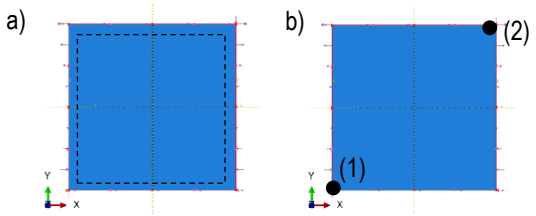

Fig. 19. Boundary conditions: a) blocked transverse displacement u3=0 and b) blocked in plane displacements u1=0 and u2=0 at selected points (1) and (2)

The results of the calculation are presented in Tab. 6.

Tab. 6. Critical loading value N_{cr} [kN/m]

Only shear	Only bending	Shear and bending
119.53	87.533	77.407

Due to transverse stiffeners, local buckling did not occur. One can find that there was influence of the shear forces on the eigenvalue.

5. FINAL CONCLUSIONS

The analysis of initial stability of steel welded girders was carried out in this paper. The BEM was proposed to solve the simple benchmark test of the plate subjected to shear in-plane forces with constant distribution. The FEM was applied to the complex analysis. The impact of additional tangential in-plane loading cannot be avoided which is confirmed by numerical experiment. Special attention should also be paid to girders with holes. In this case tensile in-plane forces (Example 5) cause compressing in the area near the hole. Note that the problem of plate stability is sensitive on the type of finite element and modeling of boundary conditions. The stress singularities in hole vertices were not specifically considered. The boundary conditions of considered plates are conventional to some extent. It depends on the thickness of the stiffeners, as well as lower and upper flange plates. Example 6 demonstrates the significant effect of shear on the value of critical loading N_{cr} which is shown in Tab. 6 (the critical load was reduced by more than 10 percent). Therefore good estimation of critical force is primary importance for the reasonable designing of the plane girder.

REFERENCES

1. Abaqus, Abaqus Manuals. (2005), Inc. Providence.
2. **Biegus A.**, **Kowal A.** (2013), Collapse of halls made from cold-formed steel sheets, *Engineering Failure Analysis*, 31, 189–194.
3. **Chinnaboon B., Chucheepsakul S., Katsikadelis J.T.** (2007), A BEM-bases Meshless Method for Buckling Analysis of Elastic Plates with Various Boundary Conditions, *Journal of Structural Stability and Dynamics*, 1(7), 81–89.
4. **Chybiński M. (2015)**, *Load capacity and stability of steel thin-walled beams with local stiffening elements*, The Poznan University of Technology Publishing House, Poznan (in Polish).
5. **Chybinski M., Rzeszut K., Garstecki A.** (2013), Snap-through phenomenon of imperfect steel structures, *Proceedings of International Conference Design, Fabrication and Economy of Metal Structures*, Miskolc, Hungary, Springer-Verlag.
6. **Garstecki A., Rzeszut K.** (2009), Modeling of initial geometrical imperfections in stability analysis of thin-walled structures, *Journal of Theoretical and Applied Mechanics*, 47(3), 667–684.
7. **Gosowski B.** (1999), Spatial bucling of thin-walled steel-construction beam-columns with discrete bracings, *Journal of Constructional Steel Research*, 52(3), 293–317.
8. **Guminiak M.** (2014), An Alternative Approach of Initial Stability Analysis of Kirchhoff Plates by the Boundary Element Method, *Engineering Transactions*, 62(1), 33–59.
9. **Guminiak M., Sygulski R.** (2003), Initial stability of thin plates by the Boundary Element Method, *Stabililty of Structures X Symposium*, Zakopane, Poland, eds.: K. Kowal-Michalska, Z. Kołakowski.
10. **Litewka B.**, **Sygulski R.** (2010), Application of the fundamental solutions by Ganowicz in a static analysis of Reissner's plates by the boundary element method, *Engineering Analysis with Boundary Elements*, 34(12), 1072–1081.
11. **Marcinowski J.** (2007), Stability of relatively deep segments of spherical shells loaded by external pressure, *Thin-Walled Structures*, 45(10–11), 906-910.
12. **Rakowski G., Kacprzyk Z.** (2005), *The Finite Element Method in Stuctural Mechanics*, The Warsaw University of Technology Publishing House, Warsaw (in Polish).
13. **Rzeszut K., Garstecki A.** (2011), Thin-walled structures with slotted connections in stability problems,*Thin-Walled Structures*, 49, 674–681.
14. **Rzeszut K., Garstecki A.** (2013), Stability of thin-walled structures accounting for initial imperfections and clearances, in.: *Statics, dynamics and stability of structures*, Vol. 3, 127–146.
15. **Rzeszut K., Polus Ł.** (2013), Classes of Cross-Sections of Steel Structrural Elements in the Fire Situation, *Procedia Engineering*, 57, 967–976.
16. **Shi G.** (1990), Flexural vibration and buckling analysis of orthotropic plates by the Boundary Element Method, *Journal of Thermal Stresses*, 26(12), 1351–1370.
17. **Timoshenko S., Woynowsky-Krieger S.** (1962), *Theory of elstic stability*, Arkady, Warszawa.

ENTROPY GENERATION ON MHD FLOW OF POWELL-EYRING FLUID BETWEEN RADIALLY STRETCHING ROTATING DISK WITH DIFFUSION-THERMO AND THERMO-DIFFUSION EFFECTS

***Najeeb Alam KHAN, *Shahnila AZIZ, **Saif ULLAH**

*Department of Mathematics, University of Karachi, Karachi 75270, Pakistan
**Department of Mathematics, Government College University Lahore, 54000, Pakistan.

najeeb@uok.edu.pk, shahnilaaziz@yahoo.com, dr.saifullah@gcu.edu.pk

received 30 July 2015, revised 23 February 2017, accepted 6 March 2017

Abstract: An investigation is performed for an alyzing the effect of entropy generation on the steady, laminar, axisymmetric flow of an incompressible Powell-Eyring fluid. The flow is considered in the presence of vertically applied magnetic field between radially stretching rotating disks. The Energy and concentration equation is taking into account to investigate the heat dissipation, Soret, Dufour and Joule heating effects. To describe the considered flow non-dimensionalized equations, an exact similarity function is used to reduce a set of the partial differential equation into a system of non-linear coupled ordinary differential equation with the associated boundary conditions. Using homotopy analysis method (HAM), an analytic solution for velocity, temperature and concentration profiles are obtained over the entire range of the imperative parameters. The velocity components, concentration and temperature field are used to determine the entropy generation. Plots illustrate important results on the effect of physical flow parameters. Results obtained by means of HAM are then compared with the results obtained by using optimized homotopy analysis method (OHAM). They are in very good agreement.

Keywords: Axisymmetric flow, Entropy generation, Stretching disk, Powell-Eyring fluid, Diffusion

1. INTRODUCTION

Energy flux or diffusion of energy is produced by a composition gradient termed as Dufour effect or the diffusion-thermo effect, though mass flux or species differentiation emerging in an initially homogeneous mixture can be caused by a temperature gradient, embodies the Soret or thermal-diffusion effect. Whenever the transfer of heat and mass occurs then there exists density differences in the flow regime, abovementioned effects are momentous for the separation of isotope and mixture amongst gases of very light molecular weight such as hydrogen and helium and of medium molecular weight such as nitrogen and air. Due to the simultaneous occurrence of heat and mass transfer in a moving fluid, the association among the fluxes and the driving potentials might be of more complicated in nature. These effects substantially cover the areas, for instance, geothermal energy, nuclear waste disposal, hydrology etc. and deliberated as second-order phenomena. Many researchers considered the combined effect of Soret and Dufour effects as they are not of the smaller order of magnitude than the effect defined by Fourier's and Fick's laws. Diverse situations have been deliberated by modern researchers to gain insight regarding the non-Newtonian fluid flow rate and heat transfer on the stretching, rotating surfaces. Flow over inextensible moving surface was first proposed and investigated by Sakiadas (1961). In recent times a large number of researchers have been further extending the work of Sakiadas (1961) by considering various physical situations. Exact solution for two-dimensional viscous boundary layer flow affected by linear stretching of the elastic flat surface was presented by Crane (1970). Later Wang (1984) and Banks (1983) generalized the same problem for three-dimensional flows due to stretching sheet and to a power law stretching velocity respectively, the acquired result was no longer exact in such cases. In addition, Gupta and Gupta (1977) continued the Crane's problem by including mass suction and injection at the wall. Bataller (2007) observed the flow and heat transfer characteristics of the homogeneous second-grade fluid over a non-isothermal stretching sheet in the presence of non-uniform internal heat generation. While the flow over stretching surface subject to an unvarying heat flux along with the temperature field was discussed by Grubka and Bobba (1985). On the other hand, Wang (1988) talked about the rotating fluid flow over the stretching surface. Fang (2007) further extended the problem of stretching surface to the combine effects of stretching and disk rotation. Fang and Zhang (2008) found the exact solution of Navier-Stokes equations for the flow between two stretching disks. A numerical study was conducted by Ashraf and Batool (2013) for the analysis of the axisymmetric steady flow of an electrically conducting micropolar fluid and heat transfer in the presence of magnetic field over a stretching disk. Turkyilmazoglu (2012) employed an extremely accurate spectral numerical integration scheme to examine the flow due to radially stretchable rotating disk of an electrically conducting fluid under the influence of vertically applied magnetic field. Moreover, for the first time power-law stretching rotating disk in the radial direction was pondered by Asghar et al. (2014). He used Lie group theory to calculate the symmetries of governing equations and then Munawar et al. (2011) presented analytic solution using optimal homotopy analysis method for the viscous fluid flow sandwiched between two stretching disks with slip boundaries and the effects of materi-

DOI 10.1515/ama-2017-0004

al parameters on the quantities of physical interest. Ariel (2001) studied the viscoelastic fluid flow over a radially stretching disk wherein he obtained the perturbation and asymptotic solution for small and large Deborah number respectively. The considered flow is axisymmetric for both cases. The Unsteady axisymmetric flow over a radially stretching sheet has been obtained by Sajid et al. (2008) and he also found the series solution of considered flow and observed the heat transfer effect. A number of cases had been presented by Eckert and Drake (1097) wherein thermal-diffusion and diffusion-thermo effect cannot be neglected. Linear and non-linear stability analysis were carried out by Gaikwad (2007) for double diffusive convection with Soret and Dufour effects in a two component couple stress fluid layer. A numerical model to study the combined effect of Soret and Dufour effects and also the influence of hydromagnetic effect on convective slip flow, viscous dissipation, Ohmic heating, heat and mass transfer, the flow induced by a rotating disk was developed by Osalusi et al. (2008). Additionally, Afify (2009) worked for free convective heat and mass transfer characteristics over a stretching surface and also considered the suction or injection with Soret and Dufour effects. Tsai et al. (2009) presented heat and mass transfer analysis which had been designed for steady stagnation point flow through a porous medium over a uniform stretching surface by solving of continuity, momentum, energy and concentration equations using the numerical procedure. A numerical analysis using fourth order Runge-Kutta based on shooting method was conducted, on MHD slip flow of an electrically conducting Newtonian fluid over a porous rotating infinite disk with the consideration of thermal radiation effect, Soret and Dufour effects by Anjali et al. (2011). With the aim of reporting, Hayat et al. (2010) observed heat and mass transfer characteristics of the viscoelastic fluid, in consideration of Soret and Dufour diffusion effects on mixed convection boundary layer flow over a linearly stretching vertical surface in a porous medium. Rashidi et al. (2011) considered the thermal-diffusion and diffusion-thermo effects, viscous dissipation, Ohmic heating, MHD convective and partial slip effects due to rotating disk flow of homogeneous fluid. He derived solution in the form of exponentially-decaying series functions via homotopy analysis method. Khan et al. (2014) have discussed the unsteady flow of couple stress fluid over a rotating disk in which they observed the different behavior of couple stresses. Powell and Eyring (1944) proposed the mechanism for the relaxation theory of viscosity. Khan et al. (2014) presented MHD flow of Powell-Eyring fluid due a rotating disk under the influential external magnetic field and discussed analytically using the semi-analytical method.

In thermodynamical systems, flow and heat transfer process losses useful energy which can cause great disorder and controlling of this disorder is the core interest of modern engineers and scientists. Analysis of second law of thermodynamics is a useful tool by which one can secure wastage of energy, predict the performance and fully utilize energy resources by minimizing the irreversibility, measured by entropy generation and get the optimal and improved efficiency of the thermal system. Many researchers employed the approach of minimizing entropy generation by taking diverse geometrical arrangements and many engineers have designed a thermal system to optimize, for instance, Butt et al. (2012) showed that entropy generation rate can be abridged and precise as the slip which is present over a vertical plate. Guo et al. (2011) numerically investigated laminar flow in a microchannel. Li et al. (2011) conducted local entropy generation analysis based on two-dimensional, two-phase fuel cells. For more recent studies see ref. (Butt and Ali, 2014, Rashidi et. Al., 2014, Torabi and Zhang, 2015,Parvin and Chamkha, 2014, Mahian et. Al., 2013, Shateyi et. Al., 2015, Abolbashari et. Al., 2014, Bhatti et. Al., 2016).

The flow of non-Newtonian fluid over stretching and rotating surfaces has been focused by scientists and engineers as it has extensively important applications. Phenomena's in which such type of flows occur are designing cooling systems for liquid metals, thermal-power-generating systems, flow meters, gas turbines, medical equipment, metallurgical and polymer extrusion of sheet materials, rolling of plastic films etc. Furthermore, the spinning of fibers, glass blowing, crystalline materials and continuous casting of metals, involve the flow above the stretching surfaces.

Stimulated by the aforementioned reference works and the various industrial and engineering applications of MHD flow of non-Newtonian fluids over a stretching rotating disk, the current article aims at investigating the Soret and Dufour effect on steady MHD flow of Powell-Eyring fluid in the presence of uniformly applied magnetic field. We propose to extend the problem of Gorder et al. (2010) and consider the electrically conducting non-Newtonian Powell-Eyring fluid between two stretching disks with heat and mass transfer. Moreover, we are taking entropy generation analysis into account in order to discuss the second law of thermodynamics. Invoking suitable similarity transformations, the system of nonlinear partial differential equations reduced into nonlinear ordinary differential equations and then deciphered analytically for the velocity, temperature and the concentration distributions by employing a powerful, easy-to-use technique, namely homotopy analysis method presented by Liao (2003, 2004) . Firstly we computed the series solution and discussed its convergence. Obtained results using HAM are compared with results of optimized homotopy analysis method (OHAM). Lastly, the graphs are sketched for the variations of different flow governing parameters on the velocity, temperature and concentration profiles are addressed.

2. FLOW ANALYSIS OF THE PROBLEM

Effects of Soret and Dufour on steady, laminar, hydromagnetic, axisymmetric flow of non-Newtonian Powell-Eyring fluid in between stretching rotating disks studied. Disks are separated vertically by distance c and both of the disks are stretched outwardly with the velocity proportional to the radius of the disk. Considered flow is defined in non-rotating cylindrical polar coordinates $(\mathrm{r}, \psi, \mathrm{z})$ with z is chosen as the vertical axis, and as r and ψ are radial and tangential axes. $(\mathrm{u}, \mathrm{v}, \mathrm{w})$ are assumed to be the velocity components in the direction of cylindrical polar coordinates $(\mathrm{r}, \psi, \mathrm{z})$ respectively. At the plane, $\mathrm{z} = 0$ the lower disk is fixed, while the upper disk is fixed at the plane $\mathrm{z} = \mathrm{c}$. A transverse uniformly distributed magnetic field with a constant magnetic flux density B is applied vertically to the surface of the disk as shown in Fig. 1.

The external electric field and the electric field due to the polarization of charges are assumed to be negligible. Furthermore, the magnetic Reynolds number Re for the considered flow is a number much smaller than the fluid Reynolds number Re_m as the induced magnetic field is neglected. The continuity, momentum, energy and concentration equations governing the magneto-hydrodynamics flow of Powell-Eyring fluid for the problem with the related boundary condition can be written in the form:

Najeeb Alam Khan, Shahnila Aziz, Saif Ullah DOI 10.1515/ama-2017-0004

$$\frac{\partial u}{\partial r}+\frac{u}{r}+\frac{\partial w}{\partial z}=0 \tag{1}$$

$$u\frac{\partial u}{\partial r}-\frac{v^2}{r}+w\frac{\partial u}{\partial z}=-\frac{1}{\rho}\frac{\partial p}{\partial r}+\frac{1}{\rho}\left(\frac{\partial S_{rr}}{\partial r}+\frac{\partial S_{zr}}{\partial z}+\left(\frac{S_{rr}-S_{\psi\psi}}{r}\right)\right)-\sigma B u \tag{2}$$

$$u\frac{\partial v}{\partial r}-\frac{u v}{r}+w\frac{\partial v}{\partial z}=\frac{1}{\rho}\left(\frac{\partial S_{r\psi}}{\partial r}+\frac{\partial S_{z\psi}}{\partial z}+2\frac{S_{r\psi}}{r}\right)-\sigma B v \tag{3}$$

$$u\frac{\partial w}{\partial r}+w\frac{\partial w}{\partial z}=-\frac{1}{\rho}\frac{\partial p}{\partial z}+\frac{1}{\rho}\left(\frac{\partial S_{rz}}{\partial r}+\frac{\partial S_{zz}}{\partial z}+\frac{S_{rz}}{r}\right) \tag{4}$$

$$u\frac{\partial T}{\partial r}+w\frac{\partial T}{\partial z}=\frac{k}{\rho\, Cp}\left(\frac{\partial^2 T}{\partial r^2}+\frac{1}{r}\frac{\partial T}{\partial r}+\frac{\partial^2 T}{\partial z^2}\right)+\frac{Dm\, Kt}{\rho\, Cs\, Cp}\left(\frac{\partial^2 C}{\partial r^2}+\frac{1}{r}\frac{\partial C}{\partial r}+\frac{\partial^2 C}{\partial z^2}\right)+\frac{\sigma B^2}{\rho\, Cp}(u^2+v^2)+\frac{1}{\rho\, Cp}\begin{pmatrix} S_{rr}\left(\frac{\partial u}{\partial r}\right)+S_{\psi\psi}\left(\frac{u}{r}\right)+S_{zz}\left(\frac{\partial w}{\partial z}\right)\\ +S_{rz}\left(\frac{\partial u}{\partial z}+\frac{\partial w}{\partial r}\right)+S_{r\psi}\left(\frac{\partial v}{\partial r}-\frac{v}{r}\right)\\ +S_{\psi z}\left(\frac{\partial v}{\partial z}\right)\end{pmatrix} \tag{5}$$

$$u\frac{\partial C}{\partial r}+w\frac{\partial C}{\partial z}=Dm\left(\frac{\partial^2 C}{\partial r^2}+\frac{1}{r}\frac{\partial C}{\partial r}+\frac{\partial^2 C}{\partial z^2}\right)+\frac{Dm\, Kt}{Tm}\left(\frac{\partial^2 T}{\partial r^2}+\frac{1}{r}\frac{\partial T}{\partial r}+\frac{\partial^2 T}{\partial z^2}\right) \tag{6}$$

$$u(r,0)=l\,r,\qquad u(r,c)=l\,r\,\varepsilon,\qquad v(r,0)=v(r,c)=0,\qquad w(r,0)=w(r,c)=0,\qquad p(r,0)=\frac{l\,\rho\,\upsilon\,\beta}{4}\frac{r^2}{c^2} \tag{7}$$

where:

$$V(r,z)=\begin{pmatrix}u\\ v\\ w\end{pmatrix},\quad S_{ij}=\mu\,\nabla V+\frac{1}{\varepsilon}\left(\frac{1}{b}\nabla V-\frac{1}{6}\left(\frac{1}{b}\nabla V\right)^3\right),$$

$$i,j=r,\psi,z,\qquad \left|\frac{1}{b}\nabla V\right|\ll 1$$

S_{ij} is the extra stress tensor for the Powell-Eyring model, V is the velocity, ε and b are the material constant of the Powell-Eyring fluid model, ρ σ and υ are the density, electric conductivity and viscosity of the fluid, l is a stretching disk parameter, η is an unknown parameter to be determined later. Using suitable similarity transformation:

$$u=l\,r\,F(\Lambda),\qquad v=0,\qquad w=l\,c\,H(\Lambda),\qquad p=l\,\mu\left(P(\Lambda)+\frac{\eta}{4}\frac{r^2}{c^2}\right),\qquad \Lambda=\frac{z}{c},\qquad T=T_0+(T_1-T_0)\theta(\Lambda),\qquad C=C_0+(C_1-C_0)\phi(\Lambda) \tag{8}$$

As we see that the equation of continuity is identically satisfied by using Eq. (8) and yields the relation:

$$2F(\Lambda)+H'(\Lambda)=0 \tag{9}$$

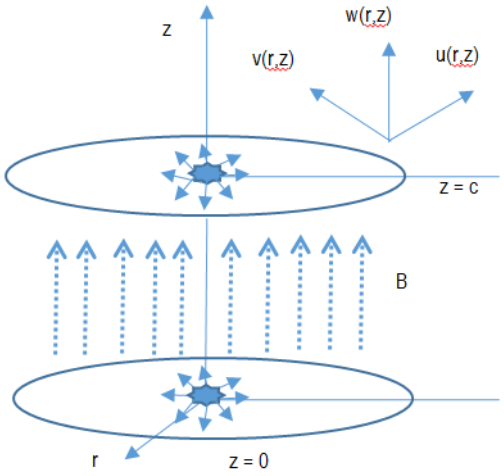

Fig. 1. Physical model of considered flow

Now using Eqs. (6) and (7) in momentum, energy and concentration equations we get:

$$\frac{\eta}{2}+\mathrm{Ha}\,F(\Lambda)+\mathrm{Re}\left(\left(F(\Lambda)\right)^2-H(\Lambda)F'(\Lambda)\right)+(1+N)F''(\Lambda)-2\,N\,L\begin{pmatrix}6F(\Lambda)\left(F'(\Lambda)\right)^2\\ +2\,c\,F''(\Lambda)\\ +\left(H'(\Lambda)\right)^2F''(\Lambda)\\ +2\,F'(\Lambda)H'(\Lambda)H''(\Lambda)\\ +\frac{3}{2}\delta\left(F'(\Lambda)\right)^2F''(\Lambda)\end{pmatrix}=0 \tag{10}$$

$$P'(\Lambda)+\mathrm{Re}\,H(\Lambda)\,H'(\Lambda)-2(1+N)\left(F'(\Lambda)+H''(\Lambda)\right)+2\,N\,L\begin{pmatrix}4\left(F(\Lambda)\right)^2F'(\Lambda)+8F(\Lambda)F'(\Lambda)H'(\Lambda)\\ +2F(\Lambda)\left(H'(\Lambda)\right)^2+H''(\Lambda)\left(F(\Lambda)\right)^2\\ +6H''(\Lambda)\left(H'(\Lambda)\right)^2+\delta\left(F'(\Lambda)\right)^3\\ +F'(\Lambda)H'(\Lambda)F''(\Lambda)\end{pmatrix}=0 \tag{11}$$

$$\theta''(\Lambda)-\mathrm{Pr}\,\mathrm{Re}\,H(\Lambda)\theta'(\Lambda)-\mathrm{Ha}\,\mathrm{Br}\,\mathrm{Re}\left(F(\Lambda)\right)^2+\mathrm{Du}\,\mathrm{Pr}\,\phi''(\Lambda)-(1+N)\mathrm{Br}\begin{pmatrix}\frac{4}{\delta}\left(F(\Lambda)\right)^2+\left(F'(\Lambda)\right)^2\\ +\frac{2}{\delta}\left(H'(\Lambda)\right)^2\end{pmatrix}+N\,L\,Br\begin{pmatrix}8\left(F(\Lambda)\right)^2\left(F'(\Lambda)\right)^2+4\left(F'(\Lambda)\right)^2\left(H'(\Lambda)\right)^2\\ +\frac{16}{\delta}\left(F(\Lambda)\right)^4+\delta^2\left(F'(\Lambda)\right)^4\\ +16\left(H'(\Lambda)\right)^2\left(F(\Lambda)\right)^2+4\left(F'(\Lambda)\right)^4\end{pmatrix}=0 \tag{12}$$

$$\phi''(\Lambda)+\mathrm{Sr}\,\mathrm{Sc}\,\theta''(\Lambda)-\mathrm{Re}\,\mathrm{Le}\,\mathrm{Pr}\,H(\Lambda)\phi(\Lambda)=0 \tag{13}$$

with boundary conditions:

$$H(0)=H(1)=0,\qquad F(0)=1,\qquad F(1)=\gamma \tag{14}$$

and:

$$P(0)=0,\quad \theta'(0)=0,\quad \theta(1)=1,\quad \phi'(0)=0,\quad \phi(1)=1 \tag{15}$$

DOI 10.1515/ama-2017-0004

Using Eq. (9) in Eq. (10) and by taking Eq. (14) with that, it can be seen that the system is overdetermined, so differentiation of Eq. (10) produces more compact expression:

$$(1+N)H''''(\Lambda) - \mathrm{Ha}\,\mathrm{Re}\,H''(\Lambda) - \mathrm{Re}\,H(\Lambda)H'''(\Lambda) - N\,L\begin{pmatrix} 7\big(H''(\Lambda)\big)^3 + 20\,H'(\Lambda)H''(\Lambda)H'''(\Lambda) \\ +3\big(H'(\Lambda)\big)^2H''''(\Lambda) + \frac{3}{2}\delta\big(H'''(\Lambda)\big)^2H''(\Lambda) \\ +\frac{3}{4}\delta\big(H''(\Lambda)\big)^2H''''(\Lambda) \end{pmatrix} = 0 \quad (16)$$

which is still subjected to the boundary conditions:

$$H(0) = H(1) = 0, \quad H'(0) = -2, \quad H'(1) = -2\gamma \quad (17)$$

where $Br = Pr\,Ec$ is the Brinkman number, $Du = \frac{Dm\,Kt\,(C_1-C_0)}{\upsilon\,Cp\,Cs\,(T_1-T_0)}$ is the Dufour number, $Ec = \frac{l^2\,r^2}{Cp\,(T_1-T_0)}$ is the Eckert number, $Ha = \frac{\sigma\,B^2}{\rho\,l}$ is the Hartman number, $Le = \frac{k}{\rho\,Cp\,Dm}$ is the Lewis number, $L = \frac{l^2}{6\,b^2}$ and $\mathrm{N} = \frac{1}{\mu\,\varepsilon\,\mathrm{b}}$ are non-Newtonian Powell-Eyring parameters, $Pr = \frac{\mu\,Cp}{k}$ is the Prandtl number, $Re = \frac{l\,c^2}{\upsilon}$ is the wall stretching Reynolds number, $Sc = \frac{l\,c^2}{Dm}$ is the Schmidt number, $Sr = \frac{Dm\,Kt\,(T_1-T_0)}{\upsilon\,Tm\,(C_1-C_0)}$ is the Soret number, Ratio of the stretching velocity of the upper disk to the lower disk is considered to be γ and $\delta = \frac{\mathrm{r}^2}{\mathrm{c}^2}$ is the dimensionless ratio of the disk to the distance between them.

The local skin-friction coefficients $\mathrm{C_f}$ at lower and upper disk and the heat transfer coefficient in terms of local Nusselt number Nu are defined as under:

$$C_f = -\frac{1}{2}\frac{1}{\sqrt{\mathrm{Re}}}H''(\Lambda)\begin{pmatrix} 1+N-3N\,L\big(H''(\Lambda)\big)^2 \\ -\mathrm{Re}N\,L\begin{pmatrix}\frac{1}{4}\big(H''(\Lambda)\big)^2 \\ +\big(G'(\Lambda)\big)^2\end{pmatrix}\end{pmatrix}\Bigg|_{\Lambda=0,c} \quad (18)$$

$$\mathrm{Nu} = -\frac{r\left(\frac{\partial T}{\partial z}\right)\Big|_{z=0}}{(T_1-T_0)} \quad (19)$$

An unknown parameter can be determine using calculated value of $\mathrm{F}(\Lambda)$ and $\mathrm{H}(\Lambda)$.

$$\eta = -2\Big(HaF(\Lambda) + Re\Big(\big(F(\Lambda)\big)^2 - H(\Lambda)F'(\Lambda)\Big)\Big) - 2(1+N)F''(\Lambda) + 4\,N\,L\begin{pmatrix} 6F(\Lambda)\big(F'(\Lambda)\big)^2 \\ +2F''(\Lambda)\big(F(\Lambda)\big)^2 \\ +F''(\Lambda)\big(H'(\Lambda)\big)^2 \\ +2F'(\Lambda)H'(\Lambda)H''(\Lambda) \\ +\frac{3}{2}\delta F''(\Lambda)\big(F'(\Lambda)\big)^2 \end{pmatrix} \quad (20)$$

3. ENTROPY GENERATION

Entropy is a decisive physical concept originated from this law. The substantial consequence of altercation of momentum and energy as the fluid flows within the boundary is entropy generation succeeding the thermodynamic irreversibility of the system. This is the decisive concept, whose origin is second order law of thermodynamics. One part of entropy generation is due to heat transfer in the direction of temperature gradients, whereas others may be due to fluid friction irreversibility, Joule heating, viscous heating. Conferring to (Bejan, 1982, 1996, Arikoglu and Ozkol, 2008) the volumetric entropy generation rate for the considered axisymmetric flow of Powell-Eyring fluid in the presence of magnetic field is given by:

$$S_G = \frac{1}{T_0}\begin{pmatrix}\left(\frac{\partial u}{\partial r}\right)S_{rr} + \left(\frac{u}{r}\right)S_{\psi\psi} + \left(\frac{\partial w}{\partial z}\right)S_{zz} \\ +\left(\frac{\partial u}{\partial z}+\frac{\partial w}{\partial r}\right)S_{rz} + \left(\frac{\partial v}{\partial r}-\frac{v}{r}\right)S_{r\psi} + \left(\frac{\partial v}{\partial z}\right)S_{\psi z}\end{pmatrix} + \frac{k}{(T_0)^2}\left(\left(\frac{\partial T}{\partial r}\right)^2 + \left(\frac{\partial T}{\partial z}\right)^2\right) + \frac{\sigma\,B}{T_0}(u^2+v^2) \quad (21)$$

As seen in above equation that the entropy generation equation consists of three parts. The first and second part refer the local entropy generation caused by fluid friction irreversibility and heat transfer irreversibility while the third part signifies magnetic field effects.

In terms of dimensionless variable, entropy generation number defines as the ratio between the actual entropy generation rate and the characteristic entropy generation rate. By using the transformation function, defined in Eq. (8), the entropy generation number for the considered flow problem turn out to be:

$$N_G = \frac{S_G}{S_{G0}} = \frac{4\,\mathrm{Br}}{\delta}\big(F(\Lambda)\big)^2 + \frac{2\,\mathrm{Br}}{\delta}\big(H'(\Lambda)\big)^2 + \mathrm{Br}\big(F'(\Lambda)\big)^2 + \lambda\big(\theta'(\Lambda)\big)^2 + \mathrm{Ha}\,\mathrm{Re}\,\mathrm{Br}\big(F(\Lambda)\big)^2 \quad (22)$$

where: $\lambda = \frac{T_1-T_0}{T_0}$ and $S_{G0} = \frac{k(T_1-T_0)}{c^2\,T_0}$.

It can be seen from Eq. (18) that raise in the Brinkman number will result in the increase in entropy generation due to fluid friction irreversibility. Similarly as α and Hartmann number increases in the entropy generation due to heat transfer and the magnetic effect increases respectively. Bejan number provides information regarding irreversibility mechanism which plays a vital role in analyzing entropy generation. For the considered problem this dimensionless parameter ratio can be written as:

$$\mathrm{Be} = \frac{\lambda\big(\theta'(\Lambda)\big)^2}{\begin{pmatrix}\frac{4\,\mathrm{Br}}{\delta}\big(F(\Lambda)\big)^2 + \frac{2\,\mathrm{Br}}{\delta}\big(H'(\Lambda)\big)^2 \\ +\mathrm{Br}\big(F'(\Lambda)\big)^2 + \lambda\big(\theta'(\Lambda)\big)^2 \\ +\mathrm{Ha}\,\mathrm{Re}\,\mathrm{Br}\big(F(\Lambda)\big)^2\end{pmatrix}} \quad (23)$$

Najeeb Alam Khan, Shahnila Aziz, Saif Ullah DOI 10.1515/ama-2017-0004

4. HOMOTOPY ANALYTIC SOLUTION

In the past two decades, for analytical solution of lots of non-linear problems in science and engineering, many researchers have applied Homotopy analysis method (HAM) successfully. HAM is employed to solve Eqs. (12), (13) and (16) subject to the boundary conditions (15) and (17). HAM solutions are an infinite power series for suitable initial approximation, which can be in turn, expressed in a closed form. Initial approximations and auxiliary linear operators have been selected as follows:

$$H(\Lambda) = -2\Lambda + 2(2+\gamma)\Lambda^2 - 2(1+\gamma)\Lambda^3, \quad \theta_0(\Lambda) = \Lambda^2 \text{ and } \theta_0(\Lambda) = \Lambda^2 \tag{24}$$

$$\mathcal{L}_1(\mathrm{H}) = \frac{d^4H}{d\Lambda^4}, \mathcal{L}_2(\theta) = \frac{d^2\theta}{d\Lambda^2} \text{ and } \mathcal{L}_3(\mathrm{H}) = \frac{d^2\phi}{d\Lambda^2} \tag{25}$$

which was found to be quite efficient and has the property that:

$$\begin{cases} \mathcal{L}_1[C_1 + C_2\Lambda + C_3\Lambda^2 + C_4\Lambda^3] = 0 \\ \mathcal{L}_2[C_5 + C_6\Lambda] = 0 \\ \mathcal{L}_3[C_7 + C_8\Lambda] = 0 \end{cases} \tag{26}$$

With $\mathrm{C_n}$, $\mathrm{n} = 1,2 \ldots 8$ are arbitrary constants. Now we construct system of zeroth order deformation equation associated with the considered flow which is respectively, given by:

$$\begin{aligned} &(1-x)\mathcal{L}_1[H(\Lambda,x) - H_0(\Lambda)] = x\,\hbar\,N_H\,[H(\Lambda,x)], \\ &(1-x)\mathcal{L}_2[\theta(\Lambda,x) - \theta_0(\Lambda)] = x\,\hbar\,N_\theta[H(\Lambda,x), F(\Lambda,x), \phi(\Lambda,x)], \\ &(1-x)\mathcal{L}_3[\phi(\Lambda,x) - \phi_0(\Lambda)] = x\,\hbar\,N_\phi\,[H(\Lambda,x), \theta(\Lambda,x)]. \end{aligned} \tag{27}$$

Subject to the boundary conditions:

$$\begin{aligned} &H(0,x) = 0, H(1,x) = 0, H'(0,x) = -2, H'(1,x) = -2\gamma, \\ &\theta'(0,x) = 0, \theta(1,x) = 1, \phi'(0,x) = 0, \phi(1,x) = 1 \end{aligned} \tag{28}$$

in which the nonlinear operators $\mathrm{N_H}, \mathrm{N_\theta}$ and $\mathrm{N_\phi}$ are defined as:

$$\begin{aligned} N_H[H(\Lambda,x)] &= (1+N)H''''(\Lambda) - \mathrm{Ha\,Re}\,H''(\Lambda) \\ &-\mathrm{Re}\,H(\Lambda)H'''(\Lambda) \\ &-N\,L\begin{pmatrix} 7\big(H''(\Lambda)\big)^3 + 20\,H'(\Lambda)H''(\Lambda)H'''(\Lambda) \\ +3\,\big(H'(\Lambda)\big)^2H''''(\Lambda) + \frac{3}{2}\delta\big(H'''(\Lambda)\big)^2H''(\Lambda) \\ +\frac{3}{4}\delta\,\big(H''(\Lambda)\big)^2H''''(\Lambda) \end{pmatrix} \end{aligned} \tag{29}$$

$$\begin{aligned} N_\theta[\mathrm{H}(\Lambda,x), F(\Lambda,x), \phi(\Lambda,x)] &= \theta''(\Lambda) - \mathrm{Pr\,Re}\,H(\Lambda)\theta'(\Lambda) \\ &-\mathrm{Ha\,Br\,Re}\big(F(\Lambda)\big)^2 + Du\,\mathrm{Pr}\,\phi''(\Lambda) \\ &-(1+N)\,Br\left(\frac{4}{\delta}\big(F(\Lambda)\big)^2 + \big(F'(\Lambda)\big)^2 + \frac{2}{\delta}\big(H'(\Lambda)\big)^2\right) \\ &+N\,L\,Br\begin{pmatrix} 8\big(F(\Lambda)\big)^2\big(F'(\Lambda)\big)^2 + 4\big(F'(\Lambda)\big)^2\big(H'(\Lambda)\big)^2 \\ +\frac{16}{\delta}\big(F(\Lambda)\big)^4 + \delta^2\big(F'(\Lambda)\big)^4 \\ +16\big(H'(\Lambda)\big)^2\big(F(\Lambda)\big)^2 + 4\big(F'(\Lambda)\big)^4 \end{pmatrix} \end{aligned} \tag{30}$$

$$N_\phi[H(\Lambda,x), \theta(\Lambda,x)] = \phi''(\Lambda) + \mathrm{Sr\,Sc}\,\theta''(\Lambda) - \mathrm{Re\,Le\,Pr}\,H(\Lambda)\phi'(\Lambda) \tag{31}$$

Where parameter x x in above equations represents an embedding parameter defined in the regime $[0,1]$. We have

$$\begin{aligned} &H(\Lambda,0) = H_0(\Lambda), \quad H(\Lambda,1) = H(\Lambda), \\ &\theta(\Lambda,0) = \theta_0(\Lambda), \quad \theta(\Lambda,1) = \theta(\Lambda), \\ &\phi(\Lambda,0) = \phi_0(\Lambda), \quad \phi(\Lambda,1) = \phi(\Lambda) \end{aligned} \tag{32}$$

Therefore as x varies from 0 to 1, $\mathrm{H}(\Lambda,\mathrm{x}), \theta(\Lambda,\mathrm{x})$ and $\phi(\Lambda,\mathrm{x})$ continuously vary from $\mathrm{H_0}(\Lambda)$ to $\mathrm{H}(\Lambda)$, $\theta_0(\Lambda)$ to $\theta(\Lambda)$ and $\phi_0(\Lambda)$ to $\phi(\Lambda)$. This continuous variation is known as deformation in topology. By Taylor's theorem and equation (32) yields the relations.

$$\begin{aligned} H(\Lambda;x) &= H_0(\Lambda) + \sum_{i=1}^{\infty} H_j(\Lambda)\,x^j, \\ \theta(\Lambda;x) &= \theta_0(\Lambda) + \sum_{i=1}^{\infty} \theta_j(\Lambda)\,x^j, \\ \phi(\Lambda;x) &= \phi_0(\Lambda) + \sum_{i=1}^{\infty} \phi_j(\Lambda)\,x^j. \end{aligned} \tag{33}$$

where:

$$H_j(\Lambda) = \frac{1}{j!}\frac{\partial^j H(\Lambda;x)}{\partial x^j}\bigg|_{x=0}, \quad \theta_j(\Lambda) = \frac{1}{j!}\frac{\partial^j \theta(\Lambda;x)}{\partial x^j}\bigg|_{x=0}, \quad \phi_j(\Lambda) = \frac{1}{j!}\frac{\partial^j \phi(\Lambda;x)}{\partial x^j}\bigg|_{x=0}.$$

The convergence of the series presented in Eqs. (33) is contingent only on auxiliary parameter i.e. $\hbar$ as mentioned by Liao (2004), and assumed that this auxiliary parameter is carefully chosen such that the series (33) converges at $\mathrm{x} = 1$ then by reason of Eq. (32) we have:

$$\begin{aligned} H(\Lambda;x) &= H_0(\Lambda) + \sum_{i=1}^{\infty} H_j(\Lambda), \\ \theta(\Lambda;x) &= \theta_0(\Lambda) + \sum_{i=1}^{\infty} \theta_j(\Lambda), \\ \phi(\Lambda;x) &= \phi_0(\Lambda) + \sum_{i=1}^{\infty} \phi_j(\Lambda). \end{aligned} \tag{34}$$

Now for the j[th] order deformation equations, differentiating Eq. (27) j-times with respect to x divided by $j!$ and then set $x = 0$ one obtain

$$\begin{aligned} &\mathcal{L}_1\big[H_j(\Lambda) - \zeta H_{j-1}(\Lambda)\big] = \hbar\,\mathcal{R}_H^j(\Lambda), \\ &\mathcal{L}_2\big[\theta_j(\Lambda) - \zeta\theta_{j-1}(\Lambda)\big] = \hbar\,\mathcal{R}_\theta^j(\Lambda), \\ &\mathcal{L}_3\big[\phi_j(\Lambda) - \zeta\phi_{j-1}(\Lambda)\big] = \hbar\,\mathcal{R}_\phi^j(\Lambda). \end{aligned} \tag{35}$$

with boundary condition:

$$\begin{aligned} &H(0,x) = 0, \quad H(1,x) = 0, \quad H'(0,x) = -2, \\ &H(1,x) = -2\gamma, \quad \theta'(0,x) = 0, \quad \theta(1,x) = 1, \\ &\phi'(0,x) = 0, \quad \phi(1,x) = 1 \end{aligned} \tag{36}$$

DOI 10.1515/ama-2017-0004

Here $\zeta_j = \begin{cases} 0, & j \geq 1 \\ 1, & j > 1 \end{cases}$ and $\mathcal{R}_H^j, \mathcal{R}_\theta^j$ and $\mathcal{R}_\phi^j$ are respectively given:

$$\mathcal{R}_H^j = (1+N)H_{j-1}''' - Ha\,Re\,H_{j-1}'' - Re\sum_{i=0}^{j-1} H_i\,H_{j-1-i}'''$$

$$-L\,N\left(\begin{array}{l} 7\sum_{i=0}^{j-1} H_{j-1-i}''\sum_{m=0}^{i} H_{i-m}''\,H_m'' \\ +20\sum_{i=0}^{j-1} H_{j-1-i}'\sum_{m=0}^{i} H_{i-m}''\,H_m'' \\ +3\sum_{i=0}^{j-1} H_{j-1-i}''''\sum_{m=0}^{i} H_{i-m}'\,H_m' \\ +\frac{3}{2}\delta\sum_{i=0}^{j-1} H_{j-1-i}''\sum_{m=0}^{i} H_{i-m}'''\,H_m''' \\ +\frac{3}{4}\delta\sum_{i=0}^{j-1} H_{j-1-i}''''\sum_{m=0}^{i} H_{i-m}''\,H_m'' \end{array}\right)$$

$$\mathcal{R}_\theta^j = \theta_{j-1}'' - \Pr Re\sum_{i=0}^{j-1} H_i\,\theta_{j-1-i}' + \mathrm{Du}\,\Pr\,\phi_{j-1}''$$

$$-\frac{1}{4}\mathrm{Ha}\,\mathrm{Br}\,\mathrm{Re}\sum_{i=0}^{j-1} H_i'\,H_{j-1-i}'$$

$$-\mathrm{Br}(1+N)\left(\frac{3}{\delta}\sum_{i=0}^{j-1} H_i'\,H_{j-1-i}' + \frac{1}{4}\sum_{i=0}^{j-1} H_i''\,H_{j-1-i}''\right)$$

$$+L\,N\,\mathrm{Br}\left(\begin{array}{l} \frac{3}{2}\sum_{i=0}^{j-1} H_{j-1-i}''\sum_{m=0}^{i} H_{i-m}'\,H_m' \\ +\frac{9}{\delta}\sum_{i=0}^{j-1} H_{j-1-i}'\sum_{m=0}^{i} H_{i-m}'\sum_{y=0}^{m} H_{m-y}'\,H_y' \\ +\frac{\delta}{16}\sum_{i=0}^{j-1} H_{j-1-i}''\sum_{m=0}^{i} H_{i-m}''\sum_{y=0}^{m} H_{m-y}''\,H_y'' \end{array}\right)$$

$$\mathcal{R}_\phi^j = \phi_{j-1}'' + \mathrm{Sr}\,\mathrm{Sc}\,\theta_{j-1}'' - \mathrm{Re}\,\mathrm{Le}\,\Pr\sum_{i=0}^{j-1} H_i\,\phi_{j-1-i}'$$

On solving Eq. (35) along with Eq. (36), the analytical solution for velocity, temperature and concentration profiles are obtained. Unlike all other analytic methods, the HAM make available a simple mode to regulate the rate of approximations and control the convergence region of the series solution, ensured by taking the most suitable value of the non-zero auxiliary parameter $\hbar$. Consequently, the auxiliary parameter shows vital role in the frame of the HAM which can be defined by the so-called $\hbar$-curves. For this purpose $\hbar$ -curves are plotted in Fig. (2) which shows the admissible range.

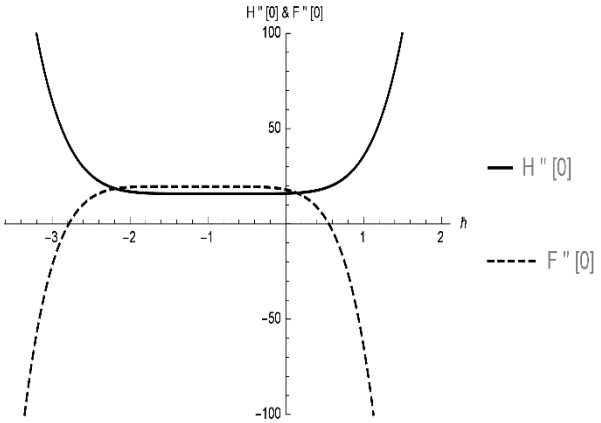

Fig. 2. $\hbar$ curves

5. DISCUSSION OF RESULTS

In this section, we present our findings i.e. the influence of pertinent parameters on velocity, temperature, pressure and concentration fields, in graphical form along with their interpretation. Also, graphical representations of entropy generation and Bejan number have presented to see the behavior of involved parameters. The considered mathematical flow problem has been defined in Eqs. (12), (13) and (16) together with the boundary conditions Eq. (15) and (17) have been solved analytically via HAM. Obtained results of the velocity and temperature fields have been used to compute the entropy generation and Bejan number. Exhibited results showing a comparison between HAM solutions with those generated by using optimized HAM. To validate the results comparison was made. An excellent correspondence between two methods is achieved, as seen in Figures 3-6.

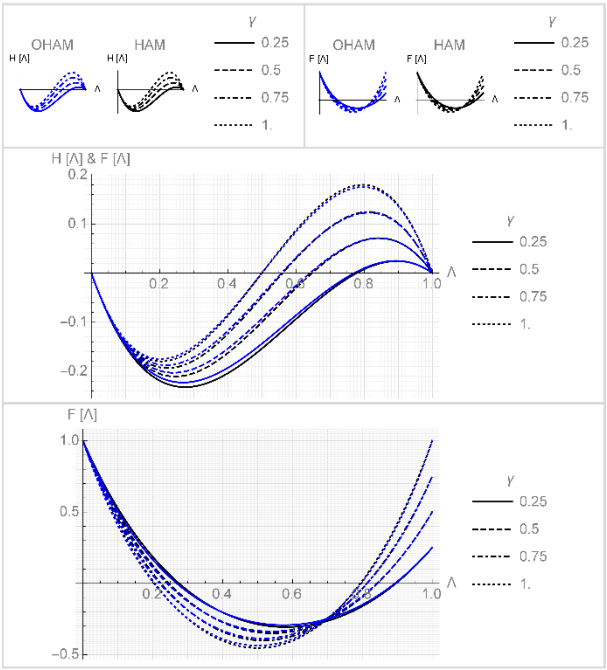

Fig. 3. Effect of γ on $\mathrm{F}(\Lambda)$ and $\mathrm{H}(\Lambda)$ with $\delta = 0.1, Ha = 2, Re = 5, L = 0.1, N = 0.1$

Najeeb Alam Khan, Shahnila Aziz, Saif Ullah
DOI 10.1515/ama-2017-0004

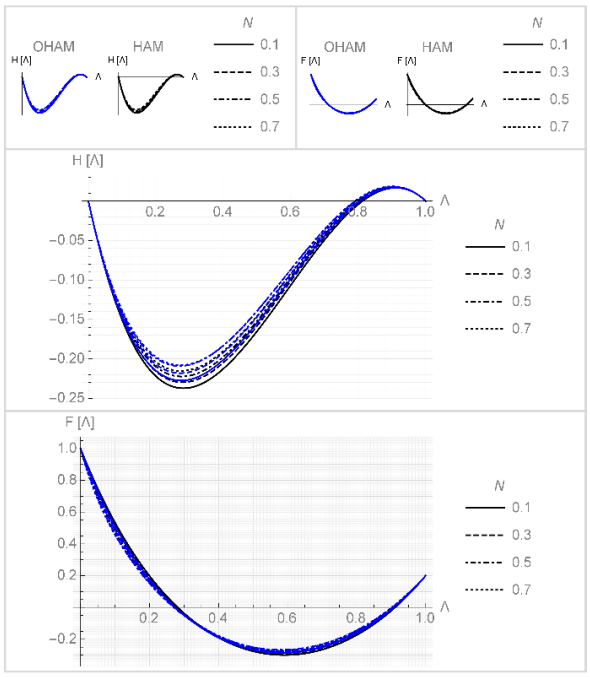

Fig. 4. Effect of N on $F(\Lambda)$ and $H(\Lambda)$ with
$\delta = 0.1, Ha = 2, Re = 5, L = 0.1, \gamma = 0.2$

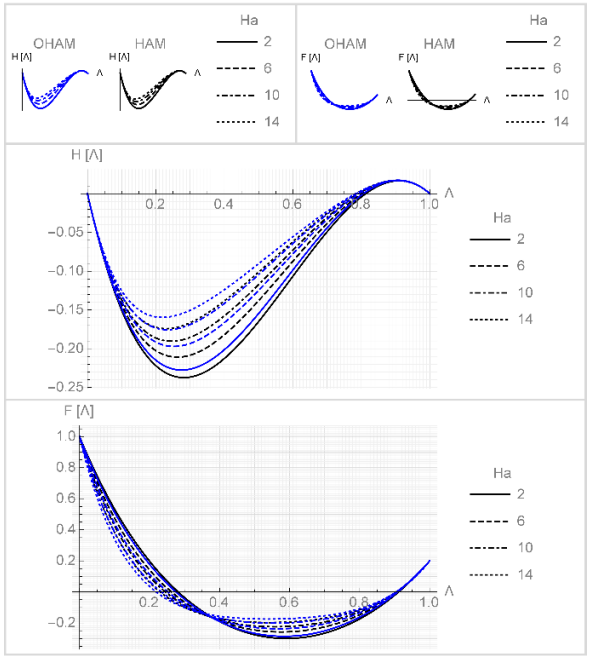

Fig. 5. Effect of Ha on $F(\Lambda)$ and $H(\Lambda)$ with
$\delta = 0.1, \gamma = 0.2, Re = 5, L = 0.1, N = 0.1$

Figs. 3-6 are sketched to see the variations of the Powell-Eyring parameter N, stretching disk parameter γ, Hartmann number Ha and Reynolds number Re on dimensionless velocity profiles in radial $F(\Lambda)$ and axial direction $H(\Lambda)$. Fig. 3 clarifies that dimensionless $H(\Lambda)$ declines first and then starts to increase due to increase in N and at upper disk it gets vanish, after attaining certain values while dimensionless $F(\Lambda)$ decreases and it increases gradually. For γ Fig. 4 elucidates that the increment in γ declines first and then rapidly rises $H(\Lambda)$ and at the upper disk it dies out, however, diminutions near lower disk and maximum amplification nearby upper disk in $F(\Lambda)$ can be seen. Fig. 5 depicts that the magnitude of $H(\Lambda)$ gets weakens adjacent to the lower disk as the Ha increases. Behind this Lorentz force is the reason, which opposes the motion of fluid. Further, it slowly increases and approaches to zero. $F(\Lambda)$ decreases with the rise in Ha and after getting some point it starts increasing. As the increase in Re results the increase in $H(\Lambda)$, therefore the viscosity of Powell-Eyring fluid decreases and stretching of disks have not been considerably influential for a less viscous fluid. Whereas $F(\Lambda)$ decreases first and when the Re increase enough it starts increasing (see Fig. 6). It is quite obvious from all the graphs of $H(\Lambda)$ that axial velocity at lower disk decreases and it turns into a radial component of the disk and also it disappears at the upper disk.

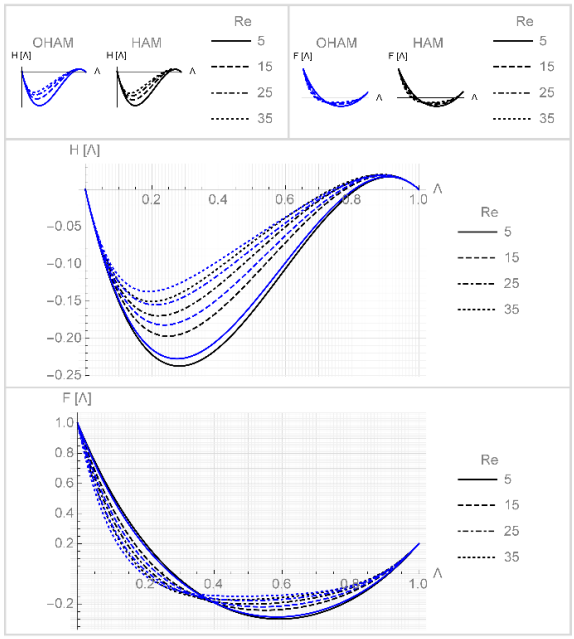

Fig. 6. Effect of Re on $F(\Lambda)$ and $H(\Lambda)$ with
$\delta = 0.1, Ha = 2, \gamma = 0.2, L = 0.1, N = 0.1$

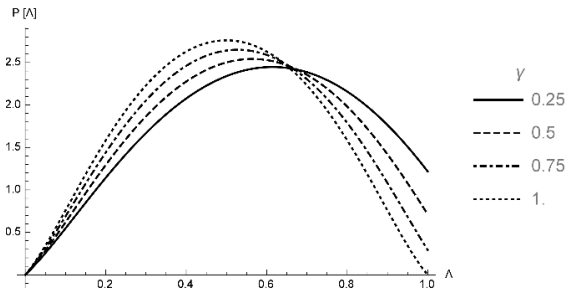

Fig. 7. Effect of γ on $P(\Lambda)$ with
$\delta = 0.1, Ha = 2, Re = 5, L = 0.1, N = 0.1$

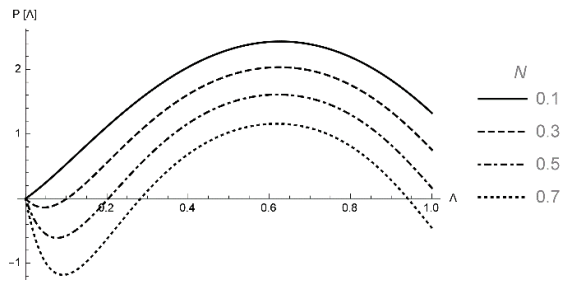

Fig. 8. Effect of N on $P(\Lambda)$ with
$\delta = 0.1, Ha = 2, Re = 5, L = 0.1, \gamma = 0.2$

DOI 10.1515/ama-2017-0004

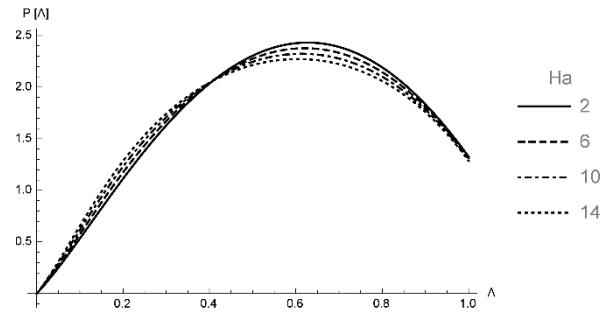

Fig. 9. Effect of Ha on $\mathrm{P}(\Lambda)$ with
$\delta = 0.1, \gamma = 0.2, Re = 5, L = 0.1, N = 0.1$

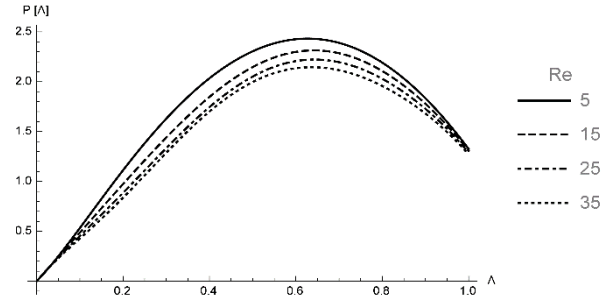

Fig. 10. Effect of Re on $\mathrm{P}(\Lambda)$ with
$\delta = 0.1, Ha = 2, \gamma = 0.2, L = 0.1, N = 0.1$

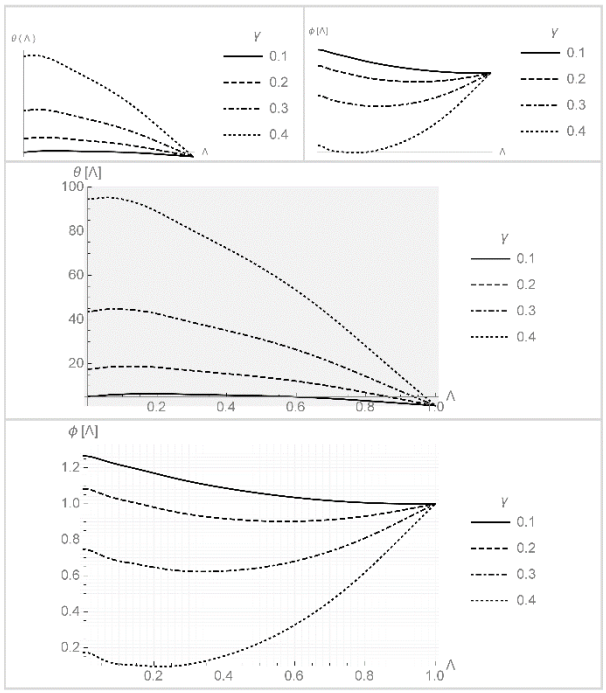

Fig. 11. Effect of γ on $\theta(\Lambda)$ and $\phi(\Lambda)$ with
$\delta = 0.1, \mathrm{Du} = 0.5, \mathrm{Le} = 1, \mathrm{Ha} = 2, \mathrm{Sc} = 0.3, \mathrm{Sr} = 0.4,$
$\mathrm{Re} = 1, \mathrm{Pr} = 0.7, \mathrm{Br} = 0.14, L = 0.1, N = 5$

Fig. 7-10 reveals the effects of the various parameter against pressure profile (Λ). It is illustrated by Figs. 7-8 that $\mathrm{P}(\Lambda)$ becomes strengthen as γ and Ha enhances but after reaching the particular point it comes to drop. An increase in N and Re, $\mathrm{P}(\Lambda)$ turn out to be diminished as shown in Figs. 9-10.

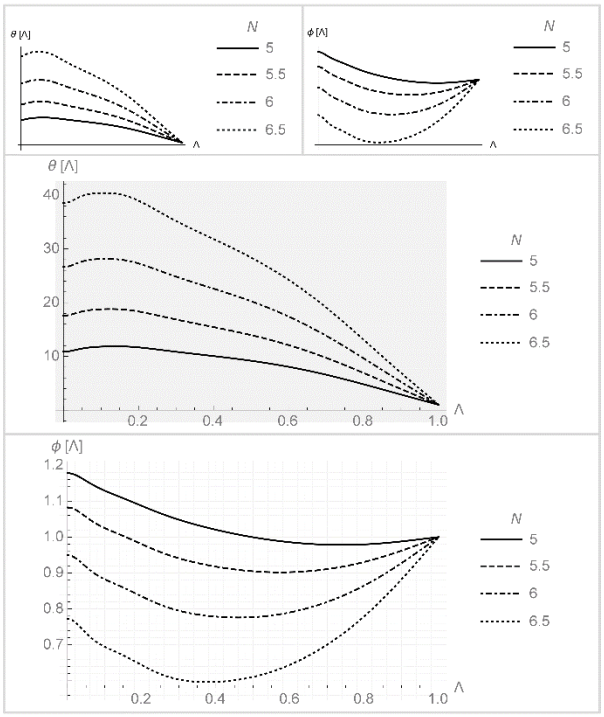

Fig. 12. Effect of N on $\theta(\Lambda)$ and $\phi(\Lambda)$ with
$\delta = 0.1, Du = 0.5, Le = 1, Ha = 2, Sc = 0.3, Sr = 0.4,$
$Re = 1, Pr = 0.7, Br = 0.14, L = 0.1, \gamma = 0.2$

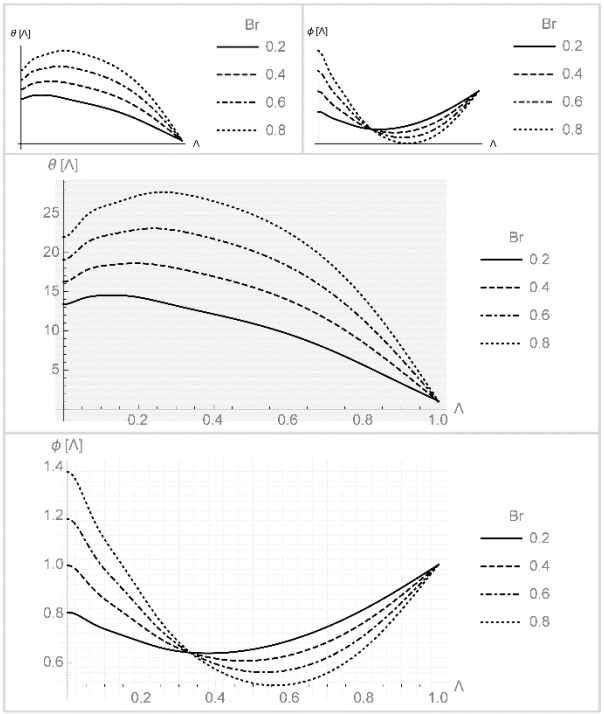

Fig. 13. Effect of Br on $\theta(\Lambda)$ and $\phi(\Lambda)$ with
$\delta = 0.1, Du = 0.5, Le = 1, Ha = 2, Sc = 0.3, Sr = 0.4,$
$Re = 5, Pr = 0.7, N = 5, L = 0.1, \gamma = 0.2$

Effects of flow parameters on temperature $\theta(\Lambda)$ and concentration $\phi(\Lambda)$ fields are displayed in Figs. 11-20. The effect of γ and N on $\theta(\Lambda)$ and $\phi(\Lambda)$ are given in Figs. 11 and 12. These figures illustrate that an increment in N and γ accelerates $\theta(\Lambda)$ and decelerates $\phi(\Lambda)$. According to Figs. 13 as Brinkman number intensifies $\theta(\Lambda)$ also intensify on the other hand $\phi(\Lambda)$ first

increases near the lower disk and then starts to decline and at the upper disk it gets constant. In Fig. 14-15 it can be observed that due to increase in Pr and Re, $\theta(\Lambda)$ rises due to this thickness of thermal boundary layer and reduces $\phi(\Lambda)$.

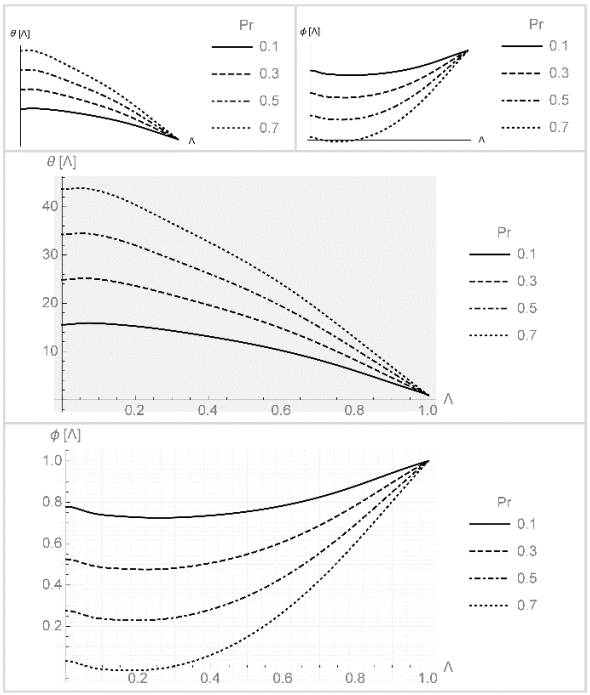

Fig. 14. Effect of Pr on $\theta(\Lambda)$ and $\phi(\Lambda)$ with
$\delta = 0.1, Du = 0.5, Le = 1, Ha = 2, Sc = 0.3, Sr = 0.4,$
$Re = 5, \gamma = 0.5, Br = 0.14, L = 0.1, N = 5$

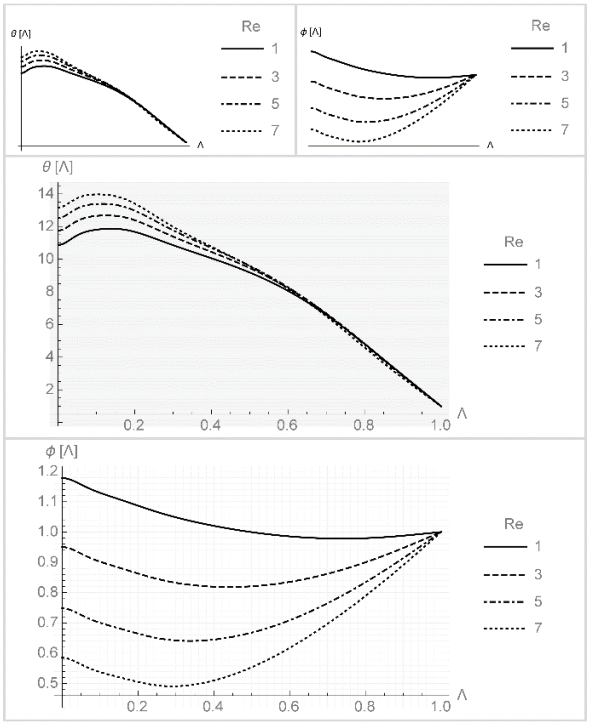

Fig. 15. Effect of Re on $\theta(\Lambda)$ and $\phi(\Lambda)$ with
$\delta = 0.1, Du = 0.5, Le = 1, Ha = 2, Sc = 0.3, Sr = 0.4,$
$\gamma = 0.2, Pr = 0.7, Br = 0.14, L = 0.1, N = 5$

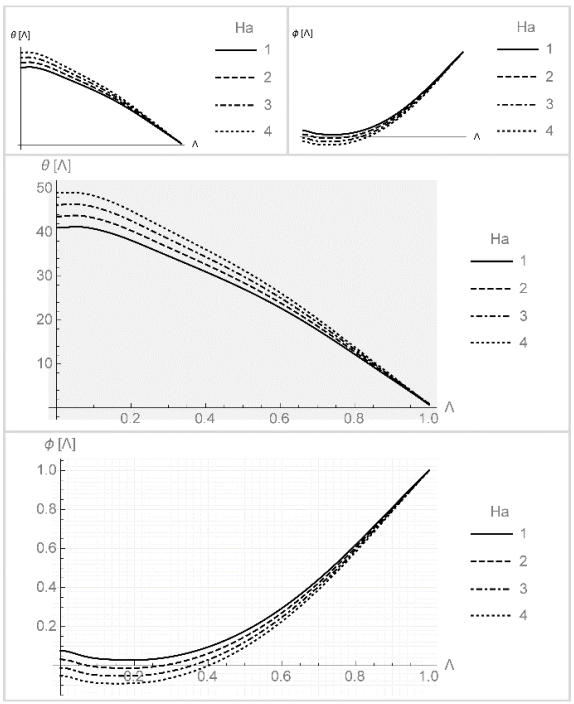

Fig. 16. Effect of Ha on $\theta(\Lambda)$ and $\phi(\Lambda)$ with
$\delta = 0.1, Du = 0.5, Le = 1, \gamma = 0.5, Sc = 0.3, Sr = 0.4,$
$Re = 5, Pr = 0.7, Br = 0.14, L = 0.1, N = 5$

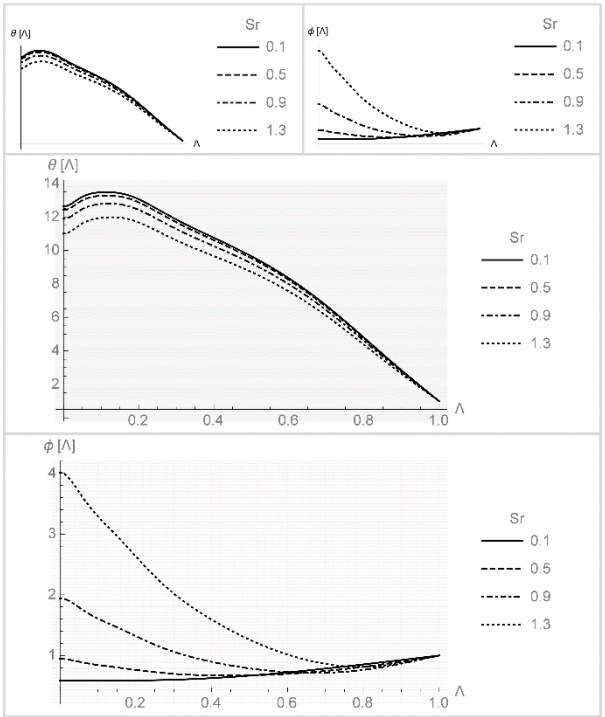

Fig. 17. Effect of Sc on $\theta(\Lambda)$ and $\phi(\Lambda)$ with
$\delta=0.1, Du=0.5, Le=1, Ha=2, \gamma=0.2, Sr=0.3,$
$Re = 5, Pr = 0.7, Br = 0.14, L = 0.1, N = 5$

Since a drag force has the effect of decay and ultimately thickening of the thermal boundary layer and reduction in $\phi(\Lambda)$ having noticed as the Ha gets stronger (see Fig. 16). Similar effects have been observed for Soret and Schmidt number from Figs. 17 and 18. For large amounts of Soret and Schmidt number $\theta(\Lambda)$ is larger and these numbers have the thickening effect on

DOI 10.1515/ama-2017-0004

thermal boundary layer, however, $\phi(\Lambda)$ has its maximum value at the lower disk and drops near the upper disk. Fig. 19 and 20 depict that the effect of Dufour and Lewis number are alike. With the increase in Dufour and Lewis number $\theta(\Lambda)$ come to enhance and $\phi(\Lambda)$ becomes depreciated.

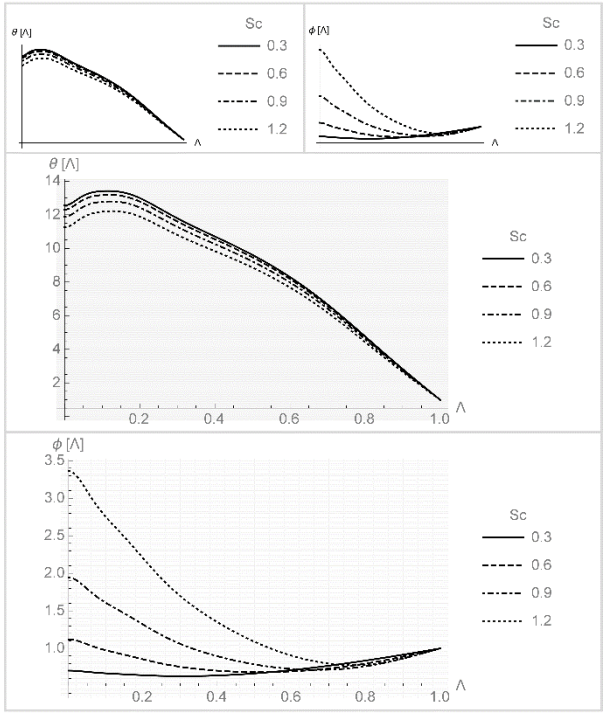

Fig. 18. Effect of Re on $\theta(\Lambda)$ and $\phi(\Lambda)$ with
$\delta = 0.1, Du = 0.5, Le = 1, Ha = 2, Sc = 0.3, Sr = 0.4,$
$\gamma = 0.2, Pr = 0.7, Br = 0.14, L = 0.1, N = 5$

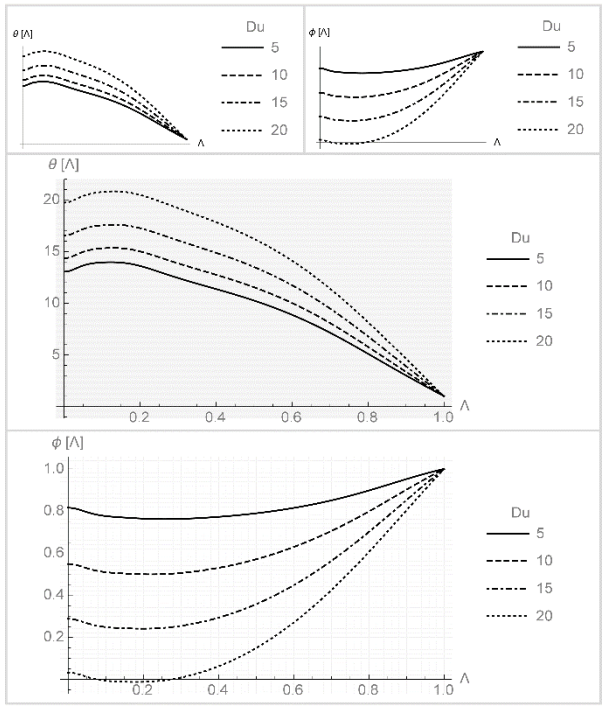

Fig. 19. Effect of Le on $\theta(\Lambda)$ and $\phi(\Lambda)$ with
$\delta = 0.1, Du = 0.5, \gamma = 0.2, Ha = 2, Sc = 0.3, Sr = 0.4,$
$Re = 5, Pr = 0.7, Br = 0.14, L = 0.1, N = 5$

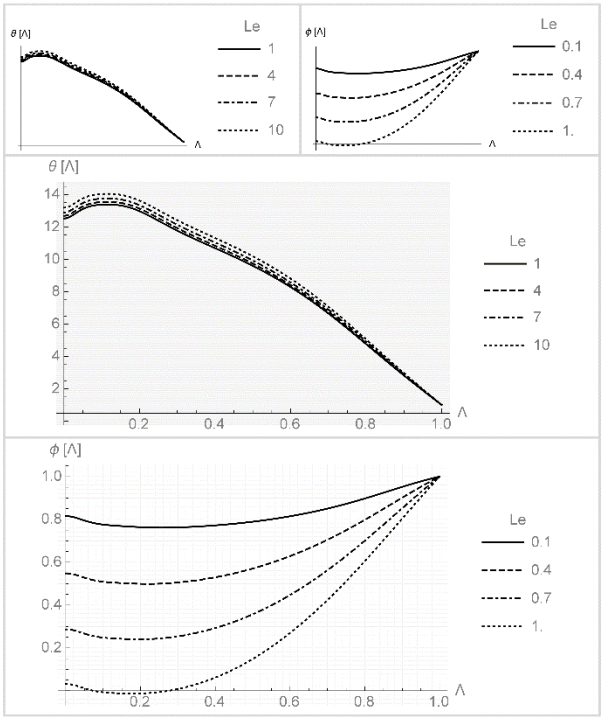

Fig. 20. Effect of Du on $\theta(\Lambda)$ and $\phi(\Lambda)$ with
$\delta = 0.1, \gamma = 0.2, Le = 1, Ha = 2, Sc = 0.3, Sr = 0.4,$
$Re = 5, Pr = 0.7, Br = 0.14, L = 0.1, N = 5$

The variation in entropy generation number N_G and Bejan number Be are plotted in Fig. 21-25.

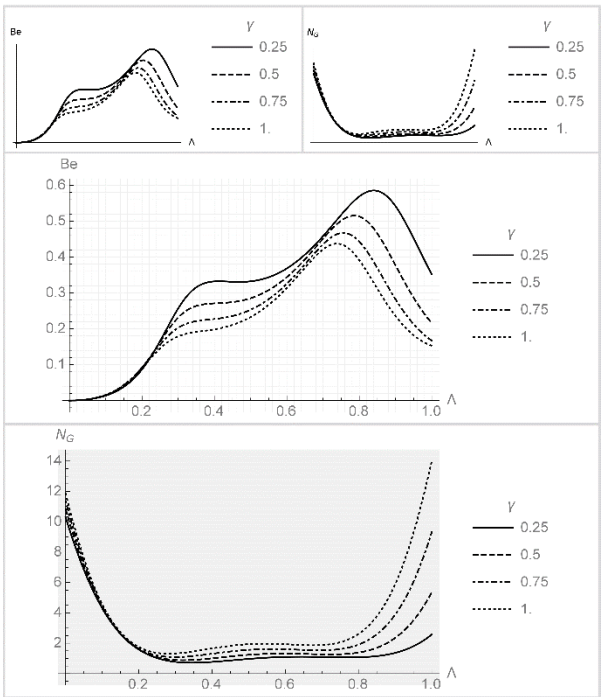

Fig. 21. Effect of γ on N_G and Be with
$\delta = 0.3, \lambda = 0.4, Du = 0.5, Le = 0.1, Sc = 0.1, Sr = 0.2,$
$Br = 0.14, Pr = 0.7, Ha = 2, Re = 5, L = 0.1, N = 0.1$

Najeeb Alam Khan, Shahnila Aziz, Saif Ullah DOI 10.1515/ama-2017-0004

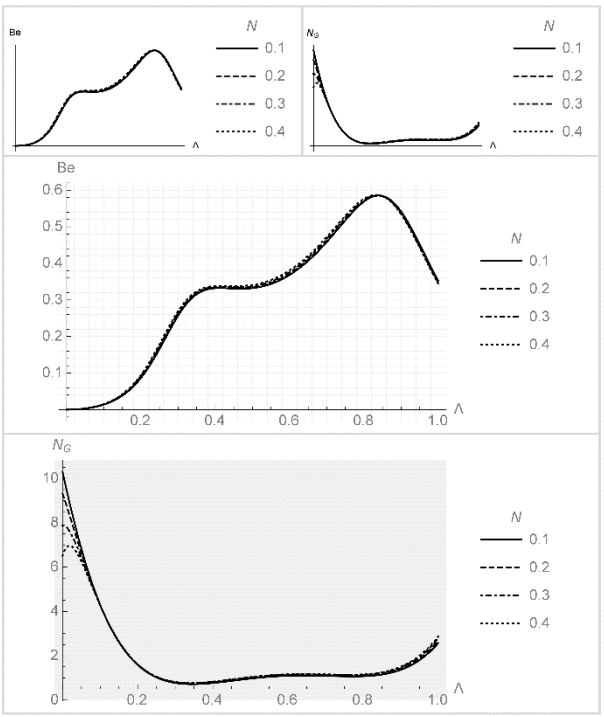

Fig. 22. Effect of N on N_G and Be with
$\delta = 0.3, \lambda = 0.4, Du = 0.5, Le = 0.1, Sc = 0.1, Sr = 0.2,$
$Br = 0.14, Pr = 0.7, Ha = 2, Re = 5, L = 0.1, \gamma = 0.25$

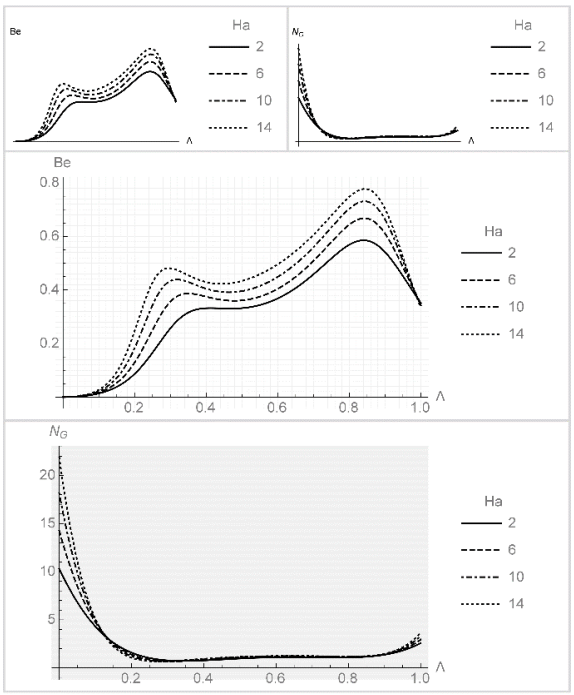

Fig. 23. Effect of Ha on N_G and Be with
$\delta = 0.3, \lambda = 0.4, Du = 0.5, Le = 0.1, Sc = 0.1, Sr = 0.2,$
$Br = 0.14, Pr = 0.7, \gamma = 0.25, Re = 5, L = 0.1, N = 0.1$

As γ gets stronger, entropy generation also gets stronger and energy loss is maximized at the lower and upper disk but flatten in between the disk. Although the Bejan number increases as γ augments and declines as one goes downstream. Near the lower disk variation in Be due to γ are negligible but farther than in the flow regime entropy effect due to fluid friction and magnetic field becomes fully dominant (see Fig. 21). Fig. 22 shows N_G is maximum at lower disk due to stretching of the disk, and decreases as the N increases far away but at the upper disk, it slowly increases. Further, Be gradually increases thus entropy effect due to heat transfer gets strong and near the upper disk, it comes to weak. Fig. 23 illustrates that as Ha gets stronger, energy loss is maximum at the lower disk and far away the disk energy loss steadily decreases but at the upper disk it increases a little bit. Moreover, from the same figure, it can be seen that due to Ha intensification effect of entropy due to heat transfer becomes clearly prominent.

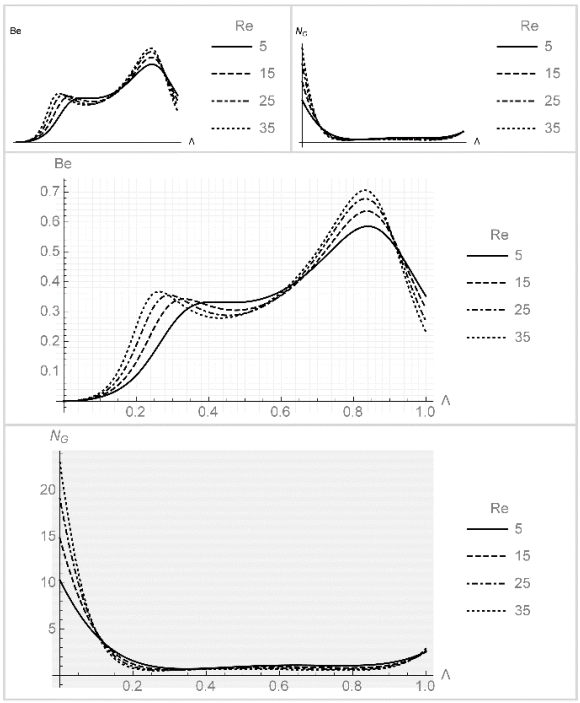

Fig. 24. Effect of Re on N_G and Be with
$\delta = 0.3, \lambda = 0.4, Du = 0.5, Le = 0.1, Sc = 0.1, Sr = 0.2,$
$Br = 0.14, Pr = 0.7, Ha = 2, \gamma = 0.25, L = 0.1, N = 0.1$

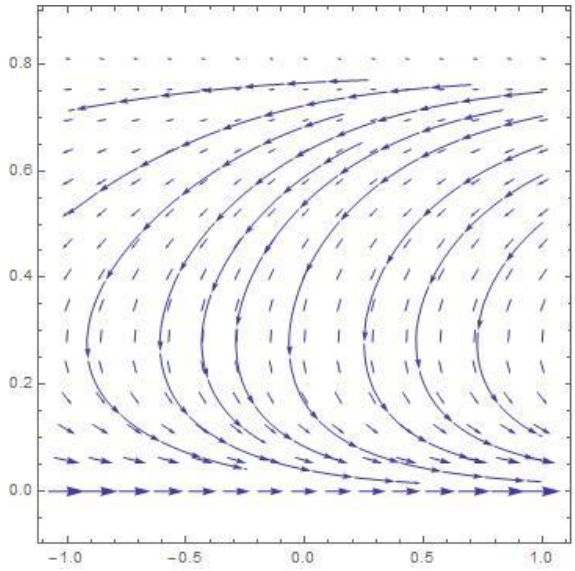

Fig. 25. Velocity vector u for $= 0.25, 0.50,$
$\delta = 0.3, \lambda = 0.4, Du = 0.5, Le = 0.1, Sc = 0.1, Sr = 0.2,$
$Br = 0.14, Pr = 0.7, Re = 5, L = 0.1, N = 0.1$

DOI 10.1515/ama-2017-0004

Due to an increase in Re entropy generation has larger value at the lower disk, but as it moves farther from the lower disk it shows the reverse behavior as portray in Fig.24. The effects of Re on Be are also shown in Fig. 24 for large Re two different trends are noticed. The effect of fluid heat transfer irreversibility dominates over fluid friction and magnetic field irreversibility near the surface of the lower disk as the Re increases while far away in the flow regime, the heat transfer irreversibility lessen. Furthermore, fluid friction and magnetic field irreversibility again become stronger whereas at upper disk the heat transfer irreversibility becomes strong and fully dominant. Fig. 25 and 26 are depicted for velocity components u, w for different stretching parameters $\gamma = 0.25, 0.5$ respectively.

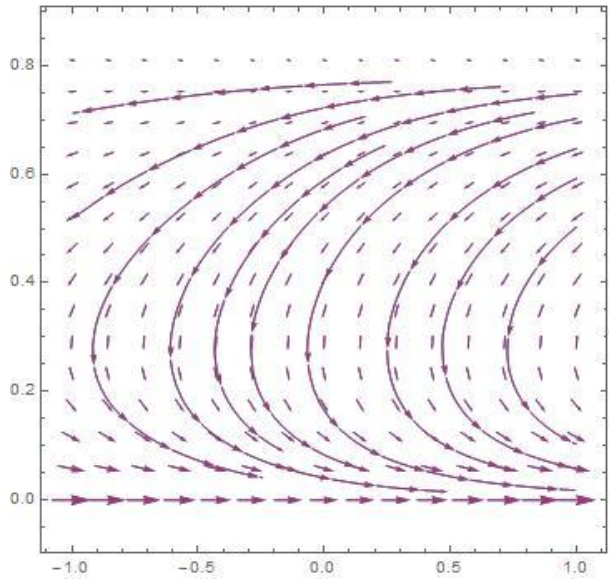

Fig. 26. Velocity vectors $\mathrm{w}$for γ = 0.25, 0.50, $\delta = 0.3, \lambda = 0.4, Du = 0.5, Le = 0.1, Sc = 0.1, Sr = 0.2, Br = 0.14, Pr = 0.7, Re = 5, L = 0.1, N = 0.1$

The comparison between our results and the results reported by Gorder et al. (2009). When we put $N = 0, L = 0$ Eq. (16) it will reduces for the Newtonian fluid as Gorder et al. (2009) have presented.

6. CONCLUSION

The present study is focused on the analytical exploration of the flow and entropy generation characteristics associated with the steady laminar incompressible flow of Powell-Eyring fluid between two stretching rotating disks in the presences of applied magnetic field. The magnetic field is taken as constant and acting only in the axial direction. The system of the nonlinear ordinary differential equation derived after using appropriate similarity functions. HAM has applied to solve the arising nonlinear ODEs and a comparison with the results obtained from OHAM have been made to corroborate the results which were obtained by HAM. An excellent confirmation of results has observed. Acquired results were sketched graphically and the effects of pertinent parameters discussed thoroughly. For the considered problem Skin friction coefficient and local Nusselt number were represented mathematically. Entropy generation and Bejan number were also rendered and presented explicitly for the different values of involved parameters.

In this study acquired results concluded in such a manner that these will use to improve the optimality and efficiency of a thermally designed flow system and to reduce the energy loss within the system by taking the suitable values of flow parameters.

REFERENCES

1. **Abolbashari M.H., Freidoonimehr N., Nazari F., Rashidi M.M.** (2014), Entropy analysis for an unsteady MHD flow past a stretching permeable surface in nano-fluid, *Powder Technology*, 267, 256–267.
2. **Afify A.A.** (2009), Similarity solution in MHD: effects of thermal diffusion and diffusion thermo effects on free convective heat and mass transfer over a stretching surface considering suction or injection, *Communications in Nonlinear Science and Numerical Simulation*, 14, 2202–2214.
3. **Anjali Devi S.P., Uma Devi R.** (2011), Soret and Dufour effects on MHD slip flow with thermal radiation over a porous rotating infinite disk, *Communications in Nonlinear Science and Numerical Simulation*, 16, 1917–1930.
4. **Ariel P.D.** (2001), Axisymmetric Flow of a Second Grade Fluid Past a Stretching Sheet, *International Journal of Engineering Science*, 39, 529-553.
5. **Arikoglu A., Ozkol I.** (2008), Komurgoz G. Effect of slip on entropy generation in a single rotating disk in MHD flow, *Appl. Energy*, 85, 1225-1236.
6. **Asghar S., Jalil M., Hussan M., Turkyilmazoglu M.** (2014), Lie group analysis of flow and heat transfer over a stretching rotating disk, *International Journal of Heat and Mass Transfer*, 69, 140–146.
7. **Ashraf M., Batool K.** (2013), MHD flow and heat transfer of a micropolar fluid over a stretchable disk, *Journal of Theoretical and Applied Mechanics*, 51, 25-38.
8. **Banks W.** (1983), Similarity solutions of the boundary-layer equations for a stretching wall, J*ournal de. Mécaniqe, Théorique et Appliquee*, 2, 375–392.
9. **Bataller R.C.** (2007), Viscoelastic fluid flow and heat transfer over a stretching sheet under the effects of a non-uniform heat source, viscous dissipation and thermal radiation, *International Journal of Heat and Mass Transfer*, 50, 3152–3162.
10. **Bejan A.** (1982), *Entropy generation through heat fluid flow*, 2nd ed., New York, Wiley.
11. **Bejan A.** (1996), *Entropy generation minimization: the method of thermodynamic optimization of finite-size systems and finite-time processes*, CRC Press.
12. **Bhatti M.M., Abbas T., Rashidi M.M., Ali M.E.S.** (2016), Numerical Simulation of Entropy Generation with Thermal Radiation on MHD Carreau nanofluid towards a Shrinking Sheet, *Entropy*, 18(6), 200.
13. **Butt A.S., Ali A.** (2014), Entropy analysis of magnetohydrodynamic flow and heat transfer due to a stretching cylinder, *Journal of Taiwan institute of chemical engineers*, 45, 780-786.
14. **Butt A.S., Munawar S., Ali A., Mehmood A.** (2012), Entropy generation in hydrodynamic slip flow over a vertical plate with convective boundary, *Journal of Mechanical Science and Technology*, 26, 2977-2984
15. **Crane L.J.** (1970), Flow past a stretching plate, *ZAMP*, 21, 645-647.
16. **Eckert E.R.G., Drake R.M.** (1972), *Analysis of heat and mass transfer*, New York: McGraw-Hill.
17. **Fang T.** (2007), Flow over a stretchable disk, *Physics of Fluids*, 19, 128105.
18. **Fang T., Zhang J.** (2008), Flow between two stretchable disks-an exact solution of the Navier–Stokes equations, *International Communication of Heat and Mass Transfer*, 35, 892–895.
19. **Gaikwad S.N., Malashetty M.S., Prasad Rama K.** (2007), An analytical study of linear and nonlinear double diffusive convection with Soret and Dufour effects in couple stress fluid, *International Journal of Non-Linear Mechanics*, 42, 903-913.

20. **Gorder R.V., Sweet E., Vajravelu K.** (2010), Analytical solutions of a coupled nonlinear system arising in a flow between stretching disks, *Applied Mathematics and Computation*, 216, 1513–1523.
21. **Grubka L.J., Bobba K.M.** (1985), Heat transfer characteristic of a continuous stretching surface with variable temperature, *International Journal of Heat and Mass Transfer*, 107, 248–250.
22. **Guo J., Xu M., Cai J., Huai X.** (2011), Viscous dissipation effect on entropy generation in curved square microchannels, *Energy*, 36, 5416-5423.
23. **Gupta P., Gupta A.** (1977), Heat and mass transfer on a stretching sheet with suction or blowing, *Candian Journal of Chemical Engineers*, 55, 744–746.
24. **Hayat T., Mustafa M., Pop I.** (2010), Heat and mass transfer for Soret and Dufour's effect on mixed convection boundary layer flow over a stretching vertical surface in a porous medium filled with a viscoelastic fluid, *Communications in Nonlinear Science and Numerical Simulation*, 15, 1183–1196.
25. **Khan N.A., Aziz S., Khan N.A.** (2014), MHD flow of Powell-Eyring fluid over a rotating disk, *Journal of the Taiwan Institute of Chemical Engineers*, 45, 2859-2867.
26. **Khan N.A., Aziz S., Khan N.A.** (2014), *Numerical Simulation for the Unsteady MHD Flow and Heat Transfer of Couple Stress Fluid over a Rotating Disk*, Plos One..
27. **Li X., Faghri A.** (2011), Local entropy generation analysis on passive high-concentration DMFCs (direct methanol fuel cell) with different cell structures, *Energy*, 36, 403-414.
28. **Liao S.J.** (2003), *Beyond Perturbation: Introduction to the Homotopy Analysis Method*, Chapman & Hall CRC Press, Boca Raton.
29. **Liao S.J.** (2004), On the Homotopy Analysis Method for nonlinear problems, *Applied Mathematics and Computation*, 147, 499–513.
30. **Mahian O., Oztop H., Pop I. Mahmud S., Wongwises S.** (2013), Entropy generation between two vertical cylinders in the presence of MHD flow subjected to constant wall temperature, *International Communications in Heat and Mass Transfer*, 44, 87-92.
31. **Munawar S., Mehmood A., Ali A.** (2011), Effects of slip on flow between two stretchable disks using optimal homotopy analysis method, *Canadian Journal of Applied Sciences*, 1, 50-68.
32. **Osalusi E., Side J., Harris R.** (2008), Thermal-diffusion and diffusion-thermo effects on combined heat and mass transfer of a steady MHD convective and slip flow due to a rotating disk with viscous dissipation and Ohmic heating, *International Journal of Heat and Mass Transfer*, 35, 908–915.
33. **Parvin S., Chamkha A.J.** (2014), An analysis on free convection flow, heat transfer and entropy generation in an odd-shaped cavity filled with nanofluid, *International Communications in Heat and Mass Transfer*, 54, 8-17.
34. **Powell R.E., Eyring H.** (1944), Mechanism for the relaxation theory of viscosity, *Nature*, 154, 427–428.
35. **Rashidi M.M., Hayat T., Erfani E., Mohimanian Pour S.A., Awatif Hendi A.** (2011), Simultaneous effects of partial slip and thermal-diffusion and diffusion-thermo on steady MHD convective flow due to a rotating disk, *Communications in Nonlinear Science and Numerical Simulation*, 16, 4303–4317.
36. **Rashidi M.M., Kavyani N., Abelman S.** (2014), Investigation of entropy generation in MHD and slip flow over a rotating porous disk with variable properties, *International Journal of Heat and Mass Transfer*, 70, 892-917.
37. **Sajid M., Hayat T., Ayub M.** (2008), Series Solution for Unsteady Axisymmetric Flow and Heat Transfer over a Radially Stretching Sheet, *Communications in Nonlinear Science and Numerical Simulation*, 13, 2193-2202.
38. **Sakiadis B.C.** (1961), Boundary layer behavior on continuous solid surfaces: I boundary layer on a continuous flat surface, *AICHE J.*, 7, 221-225.
39. **Shateyi S., Motsa S.S., Makukula Z.** (2015), On Spectral Relaxation Method for Entropy Generation on a MHD Flow and Heat Transfer of a Maxwell Fluid, *Journal of Applied Fluid Mechanics*, 8, 21-31.
40. **Torabi M., Zhang K.** (2015), Heat transfer and thermodynamic performance of convective- radiative cooling double layer walls with temperature-dependent thermal conductivity and internal heat generation, *Energy Conversion and Management*, 89, 12-23
41. **Tsai R., Huang J.S.** (2009), Heat and mass transfer for Soret and Dufour's effects on Hiemenz flow through porous medium onto a stretching surface, *International Journal of Heat and Mass Transfer*, 52, 2399–2406.
42. **Turkyilmazoglu M.** (2012), MHD fluid flow and heat transfer due to a stretching rotating disk, International Journal of Thermal Science, 51, 195–201.
43. **Wang C.Y.** (1984), The three-dimensional flow due to a stretching flat surface, *Physics of Fluids*, 27, 1915.
44. **Wang C.Y.** (1988), Stretching a surface in a rotating fluid, *Journal of Applied Mathematics and Physics, ZAMP*, 39, 177–185.

Nomenclature: B – Magnetic flux density (T), Be – Bejan number, Br – Brinkman number, C – Concentration of fluid $(\mathrm{m}^{-3}\,\mathrm{mol})$, $\mathrm{C}_1, \mathrm{C}_2, \ldots \mathrm{C}_8$ – Arbitrary constants, $\mathrm{C_f}$ – Coefficient of skin friction, Cp – Specific heat at constant pressure $(\mathrm{N\,m\,kg^{-1}K^{-1}})$, Cs – Concentration susceptibility of fluid, Dm – Molecular diffusion coefficient, Du – Dufour number, Ec – Eckert number, F, G, H – Dimensionless radial, tangential and axial velocities, Ha – Hartmann number, Kt – Thermal diffusion ratio, L – Powell-Eyring parameter, $\mathcal{L}$ – Auxiliary linear operator, Le – Lewis number, N – Powell-Eyring Parameter, N_G – Entropy generation number, $\mathrm{N_u}$ – Nusselt number, P – Dimensionless pressure, Re – Wall stretching Reynolds number, Re_m – Magnetic Reynolds number, S_{ij} – Extra stress tensor of Powell-Eyring fluid, Sc – Schmidt number, Sr – Soret number, S_G – Volumetric entropy generation rate $\mathrm{J\,K^{-1}}$, $\mathrm{S_{G0}}$ – Characteristic entropy generation rate $(\mathrm{J\,K^{-1}})$, T – Temperature of fluid (K), $\mathrm{T_m}$ – Mean fluid temperature (K), $\boldsymbol{V}$ – Velocity of fluid $(\mathrm{m\,s^{-1}})$, b – Material constant for Powell-Eyring fluid, c – Distance between two disks (m), k – Thermal conductivity of fluid $(\mathrm{W\,m^{-1}\,K^{-1}})$, l – Stretching disk parameter, p – Pressure of fluid (Pa), q – Embedding parameter, r, ψ, z – Coordinate axes, u, v, w – Dimensional r, ψ and z components of velocity $(\mathrm{m\,s^{-1}})$, α – Fluid thermal diffusivity $(\mathrm{m^2\,s^{-1}})$, ε – Material constant for Powell-Eyring fluid, γ – Ratio of stretching velocity of the upper disk to the lower disk, δ – Dimensionless ratio of the radius of the disk to the distance between them, $\hbar$ – Auxiliary non-zero operator, η – Unknown parameter, μ – Dynamic viscosity of fluid $(\mathrm{Kg\,m^{-1}\,s^{-1}})$, ν – Kinematic viscosity $(\mathrm{m^2\,s^{-1}})$, Ω – Angular velocity of disk $(\mathrm{s^{-1}})$, ϕ – Dimensionless concentration of fluid, θ – Dimensionless temperature of fluid, ρ – Density of fluid $(\mathrm{Kg\,m^{-3}})$, σ – Electric conductivity $(\Omega^{-1}\,\mathrm{m^{-1}})$.

DE GRUYTER
OPEN

DOI 10.1515/ama-2017-0005

acta mechanica et automatica, vol.11 no.1 (2017)

INTEGRATION AND IN-FIELD GAINS SELECTION OF FLIGHT AND NAVIGATION CONTROLLER FOR REMOTELY PILOTED AIRCRAFT SYSTEM

Maciej SŁOWIK[*], Daniel OŁDZIEJ[**], Zdzisław GOSIEWSKI[**]

[*]Moose sp z. o.o., Żurawia 71 Street, 15-540 Bialystok, Poland
[**]Bialystok University of Technology, Faculty of Mechanical Engineering, Wiejska 45C Street, 15-351 Bialystok, Poland

maciej.slowik@mooseinc.eu, d.oldziej@pb.edu.pl, z.gosiewski@pb.edu.pl

received 10 October 2015, revised 23 February 2017, accepted 6 March 2017

Abstract: In the paper the implementation process of commercial flight and navigational controller in own aircraft is shown. The process of autopilot integration were performed for the fixed-wing type of unmanned aerial vehicle designed in high-wing and pull configuration of the drive. The above equipment were integrated and proper software control algorithms were chosen. The correctness of chosen hardware and software solution were verified in ground tests and experimental flights. The PID controllers for longitude and latitude controller channels were selected. The proper deflections of control surfaces and stabilization of roll, pitch and yaw angles were tested. In the next stage operation of telecommunication link and flight stabilization were verified. In the last part of investigations the preliminary control gains and configuration parameters for roll angle control loop were chosen. This enable better behavior of UAV during turns. Also it affected other modes of flight such as loiter (circle around designated point) and auto mode where the plane executed a pre-programmed mission.

Key words: Remotely Piloted Aircraft System, Unmanned Aerial Vehicle, Autopilot, Flight Controller, Navigation Controller

1. INTRODUCTION

In the last five years rapid development of different technologies such as formation flight (Kownacki and Ołdziej, 2016; Gosiewskia and Ambroziak, 2013) or launchers for take-off (Kondratiuk and Gosiewski, 2013), connected with unmanned aerial vehicles (UAVs) can be observed. They become standard in different military and civilian applications. Among them, assessment of crisis situations, monitoring of mass ventures, recording videos and taking photos from the air can be distinguished (Marconi et al., 2011; Erdos et al., 2013). But still there is a constant need for the human operator who control air vehicle. It force the investigations connected with replacing of the operator by automatic control system (Koszewnik, 2014; Spinka et al., 2011). Used autopilots consist of sensor modules which provide stabilization of flight (such as gyroscopes, accelerometers and magnetometers) and facilitate the navigation (such as global navigational satellite signals (GNSS) receivers and compasses). These elements are the basis for calculating the orientation and position in space (Walendziuk et al., 2015). Among available solutions two groups of autopilots can be distinguished: the first one have closed firmware, the second one – have open-source code which is almost always supported by hobbyist and science community (Mahony et al., 2012; Arifianto and Farhood, 2015; Meier et al., 2012; HaiYang, 2010).

A methodology of the integration of market available component of UAV to prepare it for the autonomous flight is considered in the paper (Fig. 1). The properties of used aircraft equipment are described. After that the simulations of flight modes and control algorithms were tested by software in the loop (SITL). Next ground control station (GCS) adjusted to the aircraft was described. It allow for C2 (Communication and Control) mode of operation what allows to view, analyse and setting parameters of flight. It also enable control the mission of UAV, changing modes of flight, changes of waypoints and their altitude (Wang et al., 2006). Above mentioned simulations were used for correctness testing of algorithms and flight modes without risk of damaging of a real aircraft model. In the next stage of investigations the flight field tests were conducted, whereas trim and communication link tests were made. The experimental choice of controller gains for roll angle were performed. Next the impact of different gains on the aircraft during flight were shown.

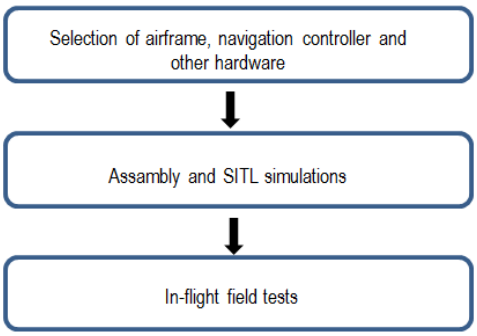

Fig. 1. Methodology scheme of the UAV integration

2. HARDWARE

As the vehicle for the whole system, aircraft in high wing configuration was used. The chosen airplane (Multiplex Mentor) is a micro class airframe – which MTOM (Maximum Take-Off Mass) is below 2 [kg] (Fig. 2) (Multiplex Mentor Assambly Manual – Tab. 1).

Maciej Słowik, Daniel Ołdziej, Zdzisław Gosiewski
DOI 10.1515/ama-2017-0005

Fig. 2. Multiplex Mentor

The expanded polypropylene foam known as Elapor is structure material. Three-phase electrical engine is a propulsion drive. This type of drive for UAV allows for the distribution of power to all components of onboard systems such as autopilot, sensors, communication modules and drives of control surfaces.

Tab. 1. UAV fuselage specification (Multiplex Mentor Assambly Manual)

Fuselage	Elapor foam
Airfoil	High-wing placement
Wingspan	1650 [mm]
Wing area	45 [dm^2]
Wing loading	44,5 [g/dm^2]
Length	1170 [mm]
Fuel type	electric
Weight (with 3s LiPo 3,2Ah recommended battery)	1950 [g]

The drive and power elements shown in Tab. 2 are also constant elements of UAV.

Tab. 2. UAV components

Main drive	BLDC motor	DUALSKY XM3548CA-4
	Propeller	APC 11x5,5
	Motor speed controller	Emax ESC 50A
Control surfaces drives	Servo motors	Hitec HS 311
	Servo motors	Hitec HS 82MG
Power source	Rechargeable battery	LiPo 3S 3,6Ah
Communication link	Pair of radiomodems	3DR 433 [MHz]

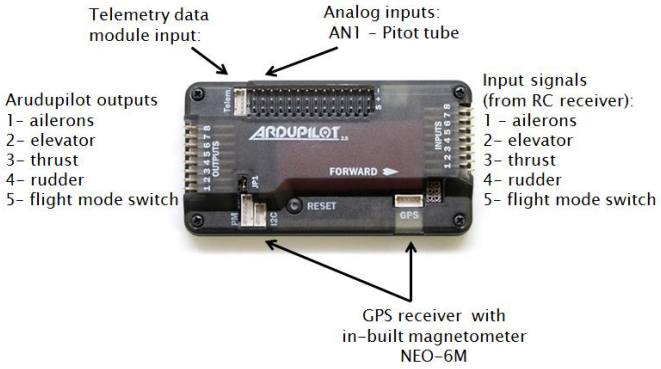

Fig. 3. The scheme of the autopilot inputs/outputs

In order to build fully efficient and functional unnamed system there is a need for use autopilot unit which can stabilize flight and control navigation. Ardupilot 2.6 shown in Fig. 3 (http://plane.ardupilot.com/) is a chosen autopilot.

Full functionality of autopilot can be achieved by using of the dedicated peripheral elements such as GPS receiver with magnetometer, static and dynamic pressure sensor, power module with current sensor and radio modem for communication with ground control station. Implementation of autopilot with above modules is shown in Fig. 4.

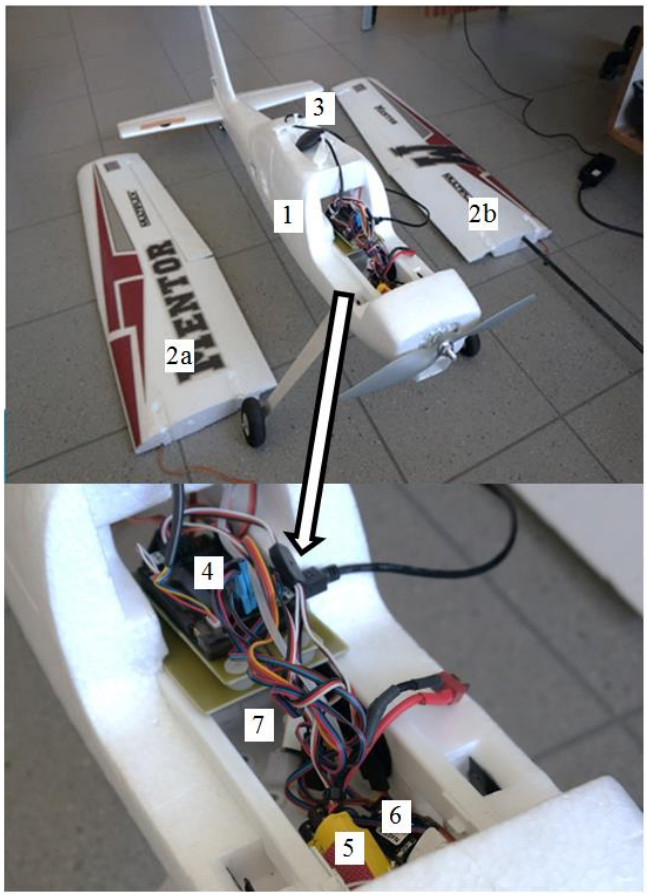

Fig. 4. Hardware assamblied on board of Mentor airframe. 1 – fuselage; 2a – right part of wing, 2b – left part of wing 3 – GPS receive, 4 – flight and navigation controller, 5 – motor speed controller, 6 – RC receiver, 7 – battery chamber

3. SITL SIMULATIONS

After configuration completion, the proper work of software and flight modes in software in the loop simulation have been tested. For this purpose the software package for emulation of autopilot, communication system (Mavlink protocol (Crespo et al., 2014)) and application for ground control station were chosen (http://planner.ardupilot.com/). For assembly of above mentioned the Cygwin package which enable utilities and compilers from GNU/Linux environment was installed. Next, compilation process was configured for firmware dedicated for planes – ArduPlane. Afterwards Mission Planner GCS was set for sending and receiving telemetry data frames (under TCP/UDP protocol) from and to virtual ArduPilot controller. Final version of software in the loop simulation consist of the following applications: mavproxy, console, map and mission planner.

DOI 10.1515/ama-2017-0005

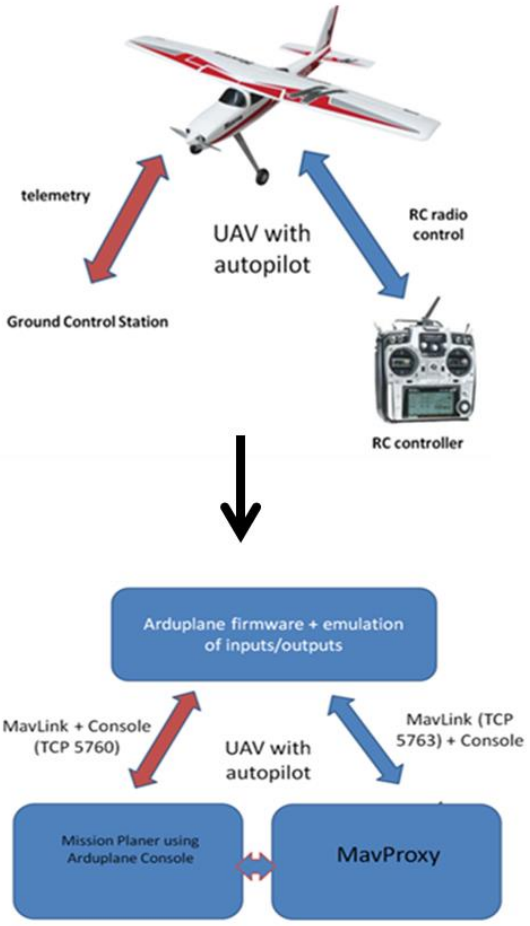

Fig. 5. Schematic diagram showing classic approach for control UAV with use of ArduPilot (up) and transition to SITL simulation (down) where functions of human operator with RC controller and GCS are executed by assembly of simulation programs with dedicated interfaces

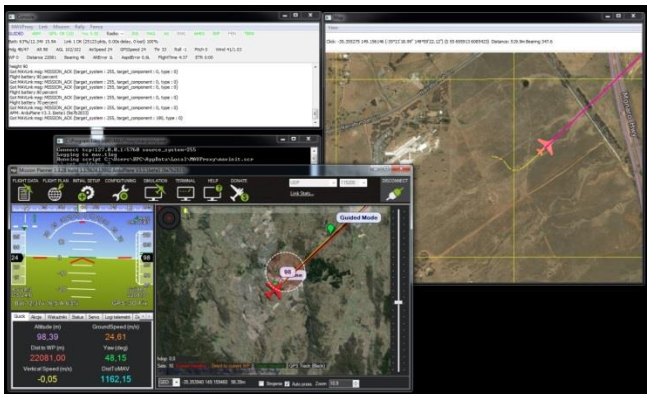

Fig. 6. The print screen showing SITL simulation. In the upper right corner - MavProxy, on the right side in the background the console application, in the lower right corner – GCS Mission Planner, on the left side – the map application – which allow view of current position of UAV on the map

During the investigations the different flight modes such as manual, stabilize, fly by wire, loiter and auto were checked. The schematic diagram of transforming from classical UAV control to SITL simulation was shown below in Fig. 5. The control link of RC controller and communication and control link from GCS were substituted by software solution. It enable use of MavProxy applications, which are proxy between elements of simulation system. Additionally in described simulation one can view and change low-level parameters of control surfaces deflection and engine throttle in the same way as in RC controller. With this solution, there exist a possibility of modification of flight parameters such as roll, pitch and yaw angle, geographical latitude and longitude or altitude. The simulation allows for setting waypoints for automatic flight and tuning gains of PID controllers responsible for flight stabilization and navigation (Fig. 6). Realization of above simulations faciliate the inflight field tests.

Currently the PID control is not the best control method, but is relevantly simple which impact on its implementation ability. It also allow for finding out object dynamic, which further open posibiity to use more complex and advanced controllers of flight parameters (Koslosky, 2015; Kownacki, 2015; Mystkowski, 2014).

4. IN-FLIGT FIELD TESTS

During the field experiments series of flight tests were made. At the beginning the final trimming of Mentor UAV was done. Further, modes of assisted manual flight were tested to ensure proper setting of controller parameters. The stabilize mode in which autopilot ensure limited level of deflection of control surfaces set by operator and stabilization based on IMU information was then tested.

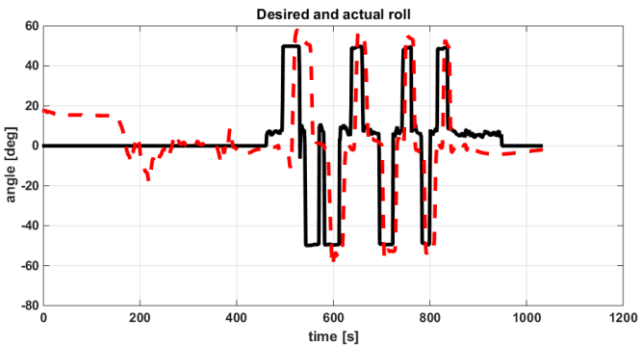

Fig. 7. Changes of roll angle during flight in FBWA mode with proportional gain of PID roll angle controller equals 0.4. After 470 [s] the manual flight mode was changed for FBWA and rapid changes of bank angle (up to 50 [°] in both sides) was commanded – solid line desired value, dashed line – actual value

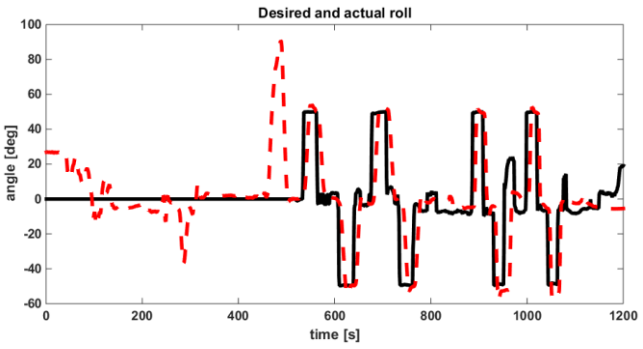

Fig. 8. Changes of roll angle during flight in fly by wire A mode with proportional gain of PID roll angle controller equals 1.4. After 530 [s] the manual flight mode was changed for FBWA and rapid changes of bank angle (up to 50 [°] in both sides) was commanded – solid line desired value, dashed line – actual value. – solid line desired value, dashed line – actual value

DOI 10.1515/ama-2017-0005

The next FBWA (fly by wire type A) mode, where flight controller hold roll angle to maximal value of LIM_CD_ROLL parameter was tested. This enable safe manual turning in the air without risk of loss of altitude during this maneuver. The stall prevention parameter, which limited bank angle to 25 [°] was disabled to ensure possibility of narrower turns. The preliminary in-flight tuning of PID controller for roll was made. The proportional gain was changed increasingly from 0.4, which was default value in tests, but object was under-steer. The parameter was changes up to 1.9 value, then object was over-steer and highly overshooted which complicated fluenty turning after course changes, especcialy over 30 degrees. Finally the gain was decreased to value 1.4. It caused faster reaction of airplane for commanded bank angle (shown in Fig. 7 and Fig. 8) which enable narrower turns and better behavior in different modes of flight.

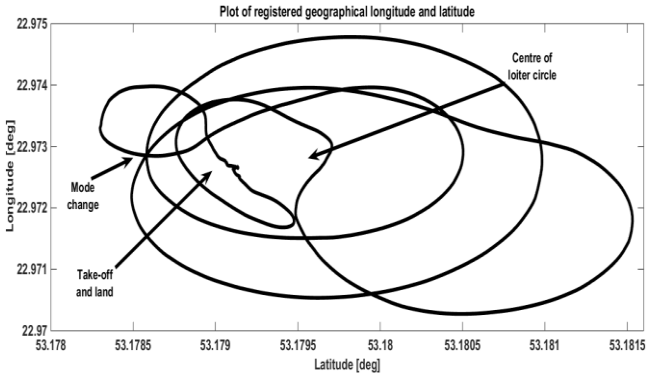

Fig. 9. Plot of registered geographical longitude and latitude for loiter mode of flight. The outer (the biggest) circle was made first, after that wind gusts (around 10 [m/s]) affected UAV in way shown above

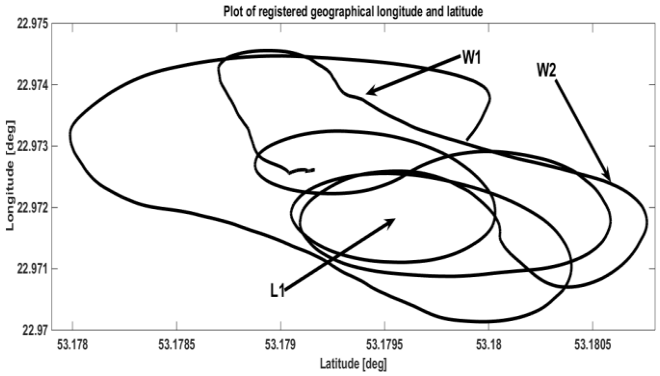

Fig. 10. Plot of registered geographical longitude and latitude for auto and loiter mode. W1 and W2 are waypoints for auto flight mode, L1 mean center of the circle for loiter mode

In the next part of investigations the loiter mode of flight was tested (Fig. 9). It allows for flying in circle of desired radius (in this case 30 [m]), where the center of circle is determined by geographical longitude and latitude of point where mode setting (by RC controller or GCS application) is done. Also investigations of the auto flight mode in which the autopilot fly between waypoints and altitude (60 [m]) were done (Fig. 10). Take-off and landing were done in manual mode, after reaching safe altitude the mode of flight was changed for ones of described above.

5. CONCLUSIONS

The process of preparation and integration of micro airplane platform, flight controller unit and peripheral equipment for realization of different flight modes dedicated for UAV was shown in the paper. Adopted scheme of integration and testing expedite and arrange preparation to UAV to flight. After proper assambly of airplane model with control deflections servos and proppeler drive, the control unit with neccesery equipment was installed on board. Next phase of investigations considered simulation of different modes of flight in software in the loop. During these tests the investigations of chosen flight modes, modification of low-level parameters of flight and ground control station applications were made. Afterwards the field tests of proper autopilot integration and communication systems in flight were made. The more aggressive gain and configuration parameters for roll angle control loop were chosen. In the result more precisely flight on the desired trajectory in loiter mode was achieved. To summarize the integration process of chosen flight control unit on board of micro airplane platform is described in the paper. Used methodology accelerate the whole process and increase safety of field flight tests by performed software in the loop simulations.

REFERENCES

1. **Ambroziak, L., Gosiewski, Z.** (2015), Two stage switching control for autonomous formation flight of unmanned aerial vehicles, *Aerospace Science and Technology*, 46, 221- 226.
2. **Crespo G., Glez-de-Rivera G., Garrido J., Ponticelli R.**(2014): "Setup of a communication and control systems of a quadrotor type Unmanned Aerial Vehicle", *Proceedings of Conference on Design of Circuits and Integrated Circuits (DCIS)*, Madrid, Spain, 1-6.
3. **Erdos D., Erdos A., Watkins S.E.** (2013), An experimental UAV system for search and rescue challenge, *Aerospace and Electronic Systems Magazine*, 28, 32-37.
4. **HaiYang C. , YongCan C., YangQuan C.** (2010), Autopilots for small unmanned aerial vehicles: A survey, International Journal of Control, Automation and Systems, 8(1), 36-44.
5. http://plane.ardupilot.com/ (access 30.08.2016)
6. http://planner.ardupilot.com/ (access 30.08.2016)
7. **Kondratiuk M., Gosiewski Z.** (2013), Simulation model of an electromagnetic multi-coil launcher for micro aerial vehicles, *Solid State Phenomena: Mechatronic Systems and Materials IV*, 406-411.
8. **Koslosky E., Wehrmeister M.A., Fabro J.A., Oliveira A.S. (**2015), On Using Fuzzy Logic to Control a Simulated Hexacopter Carrying an Attached Pendulum, *2015 Latin America Congress on Computational Intelligence (LA-CCI)*, 1-6.
9. **Koszewnik A.** (2014), The Parrot UAV controlled by PID controllers, *Acta Mechanica et Automatica*, 8(2), 65-69.
10. **Kownacki C.** (2015), Design of an adaptive Kalman filter to eliminate measurement faults of a laser rangefinder used in the UAV system, *Aerospace Science and Technology*, 41, 81-89.
11. **Kownacki C., Ołdziej D.** (2016), Fixed-wing UAVs Flock Control through Cohesion and Repulsion Behaviours Combined with a Leadership, *International Journal of Advanced Robotic Systems*, 13, 1-10.
12. **Mahony R. , Kumar V., Corke P.** (2012), Multirotor Aerial Vehicles: Modeling, Estimation, and Control of Quadrotor", *IEEE Robotics & Automation Magazine*, 19(3), 20-32.
13. **Marconi L., Naldi R., Gentili L.** (2011), Modelling and control of a flying robot interacting with the environment, *Automatica*, 47, 2571-2583.

DOI 10.1515/ama-2017-0005

15. **Meier L., Tanskanen P., Heng L., Lee G. H., Fraundorfer F., Pollefeys M.** (2012), PIXHAWK: A micro aerial vehicle design for autonomous flight using onboard computer vision, *Autonomous Robots*, 33(1-2), 21-39.
16. Multiplex Mentor Assambly Manual http://hitecrcd.com/files/md_mentor_5sp.pdf (access 30.08.2016)
17. **Mystkowski A.** (2014), Implementation and investigation of a robust control algorithm for an unmanned micro-aerial vehicle, *Robotics and Autonomous Systems*, 62, 1187-1196.
18. **Orifianto O., Farhood M.** (2015), Development and Modeling of a Low-Cost Unmanned Aerial Vehicle Research Platform, *Journal of Intelligent & Robotic Systems*, 80(1), 139-164.
19. **Spinka O., Holub O., Hanzalek Z.** (2011) Low-Cost Reconfigurable Control System for Small UAVs, *Transactions on Industrial electronics*, 58(3), 880-889.
20. **Walendziuk W., Sawicki A., Idźkowski A.** (2015), Estimation of the object orientation and location with the use of MEMS sensors, *SPIE Proceedings*, 9662, 1-6.
21. **Wang D., Xu J., Yao R.** (2006), Simulation system of telemetering and telecontrol for unmanned aerial vehicle, *Aerospace and Electronic Systems Magazine*, 21, 3-5.

The work has been accomplished under the research project No. MB/WM/15/2016 and S/WM/1/2016 financed by the Ministry of Science and Higher Education

DE GRUYTER
OPEN

DOI 10.1515/ama-2017-0006

DISCUSSION ON FLOW-THROUGH PHENOMENA IN THE AIR GAUGE CASCADE

Czesław Janusz JERMAK*

*Division of Metrology and Measurement Systems, Faculty of Mechanical Engineering and Menagement, Poznan University of Technology, Piotrowo 3, 61-138 Poznań, Poland

czesław.jermak@put.poznan.pl

received 3 November 2015, revised 27 February 2017, accepted 6 March 2017

Abstract: In the paper, the flow-through phenomena in the air gauge are under discussion form the thermodynamic and gasodynamic perspective. The main elements of the cascade are considered the inlet nozzle (restriction), measuring chamber and the measuring nozzle with the measuring slot (displacement between the nozzle head and measured surface). The purpose of the analysis was to point out the impact on the metrological characteristics of the air gauge. In particular, attention was paid to the airflow through the measuring slot. Here, the complex phenomena take place, among others the supersonic areas and a "bubble ring," which cause discontinuity and hysteresis in the static characteristic. On the other hand, the air stream expansion after the restriction (inlet nozzle) is observed in the measuring chamber. The point of the above discussion was to work out some recommendation on the nozzles geometry and the localization of the back-pressure measuring point in the chamber.

Key Words: air gauges, static metrological properties, flow-through phenomena, pressure fluctuations

1. INTRODUCTION

The air gauges are the excellent tools for accurate non-contact measurement (Schuetz, 2015). The merits of the air gauging are commonly known: cleaning of the measured surface during the measurement and hence indifference to the dirt and technological liquids, as well as insensitivity to the vibrations. That was the reason of wide implementation of the air gauging in the in-process measurement, especially during the grinding and honing processes (Vacharunukul, Mekid, 2005). There are, however, some limitations in the air gauge applications, imposed by relatively short measuring range and average dynamical characteristics (Jermak, Rucki, 2016).

Metrological characteristics could be influences by modification of geometry (dimensions and shape) of the flow-through channels (Jermak, 2010). It is possible because of the gasodynamic and thermodynamic phenomena that take place when the air stream passes through the nozzles, measuring chamber, and eventually expands in the measuring slot. In fact, some of those phenomena have got a negative impact worsening metrological characteristics of the air gauge. Thus it is crucial to examine those phenomena and to undertake proper actions to reduce or eliminate their negative impact.

2. AIR GAUGING PRINCIPLE

The main principle of air gauging has been described scientifically as early as in 1932 (Tanner, 1958), and it is based on the influence of the geometrical value (the slot between the jet and the measured surface) on the flow-through parameters. Perhaps the most common type of the air gauge applied today is the one-cascade device presented in the Fig. 1. It consists of inlet nozzle or restriction (1), measuring chamber (2) and measuring nozzle (3). Sometimes the measuring head may contain two or more measuring nozzles of equal geometry and dimensions. Multiple nozzle heads allow to perform measurement of several diameters or geometric conditions, e.g. two diameters and taper, squareness (perpendicularity) gauges, etc. (Schuetz, 2015).

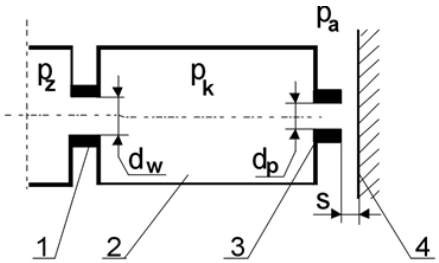

Fig. 1. Operating principle of one-cascade back-pressure open jet air gauge (Jermak and Rucki, 2012)

In open jet solutions, the outlet surface of the measuring nozzle is restricted with the surface of the measured detail (4), so the expansion of the air stream takes place in the slot s between the nozzle (3) and surface (4). The feeding air is cleaned and filtered according to the requirements of the second class air quality (Zelczak, 2002). The simple constructions require high accuracy of the feeding pressure p_z stabilization. The value of the back-pressure p_k in the measuring chamber depends on the actual slot width s (Bokov, 2011)and the pre-set dimensions of the inlet nozzle d_w and measuring nozzle d_p.

DOI 10.1515/ama-2017-0006

3. FLOW-THRUGH PHENOMENA IN THE AIR GAUGE ELEMENTS

3.1. Inlet nozzle

The inlet nozzle is the integral part of the air gauge which restricts the feeding air stream setting the basic metrological characteristics of the air gauge, namely sensitivity and measuring range. In case of the unchangeable restrictions, the inlet nozzles are typically of cylindrical orifice with lengthl_{dw}anddiameter $d_w \in <0.5 \div 2.0>$mm.

The inlet of the restriction may be shaped in different ways. In case of inexpensive nozzles, the hole may be simply drilled, a conical contraction or a simple roundings may be made (Tesar, 2010). More advanced curvature is applied in a supersonic nozzles (Tesar, 2008). Fig. 2presents the most typical solutions known and applied in air gauges for decades:

- sharp edge nozzle (perpendicular),
- conic edge nozzle,
- curved line (profiled nozzle).

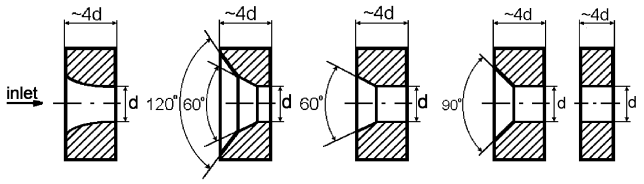

Fig. 2. Typical edges of the inlet nozzles applied in the air gauges, $L_{dw} \approx 4$d (Dejč, 1961)

It has been found decades ago that in any type of the nozzle, the actual airflow differs from the theoretical (ideal) one. It is so because the velocity distribution in the outlet intersection is unsteady, the friction consumes some energy, and the inlet edge shape has its impact on the flow (Dejč, 1961). To calculate the actual mass flow, the flow coefficient is commonly used which is to correct the isentropic flow:

$$\alpha_w = \frac{q_{mw}}{q_{m_t w}} \tag{1}$$

where:q_{mw} – mass flow,$q_{m_t w}$ – theoretical mass flow for the isentropic process (with no losses).

The flow coefficient α_w covers the influence of all factors which may cause the difference between the actual and theoretical mass flow, including variations of the velocity and density, stream contraction and friction in the flow channel. For any real element the flow coefficient is always $\alpha_w < 1$.

Sharp edge nozzles (Fig. 2) generate very large variety of the flow coefficient dependent on the mass flow. It is caused by the reduced actual flow intersection as a result of the stream contraction. Moreover, when the relative length of the nozzle $L_{dw} = l_{dw}/d_w$is large, the friction plays more important role (Lammel and Osiadacz, 1974; Idel'čik, 1960).

When the inlet edge is conical, the variation range of the actual stream diameter is smaller, and the value αw becomes stable in the large range of the mass flow values (Breitinger, 1969). In that case, contraction is substantially smaller and the stream fills in the channel, so the flow is more sensitive to the influence of the layers close to the orifice surface, especially when the length of the nozzle l_{dw} increases. The coefficient αw is dependent on the angle of the cone. If the orifice of the nozzle is very small ($d_w < < 1$ mm), the layer close to surface may block the entire flow through. Then the coefficient α_w is substantially decreased.

The most advantageous function of the α_w coefficient versus pressure ratio β_w could be achieved for the profiled nozzles (Fig. 3). Pressure ratio means the ratio of the absolute pressure before the restriction to the absolute pressure after it, which means for the inlet nozzle in the air gauge$\beta_w = p_k/p_z$. When the profile is very well and the losses are negligibly small (rapid expansion process could be approximated as adiabatic isentropic) (Dejč, 1961; Zalmanzon, 1971), then the maximal mass flow could be reached with the flow ratio close to the first critical one β_{kr1} = 0.528.

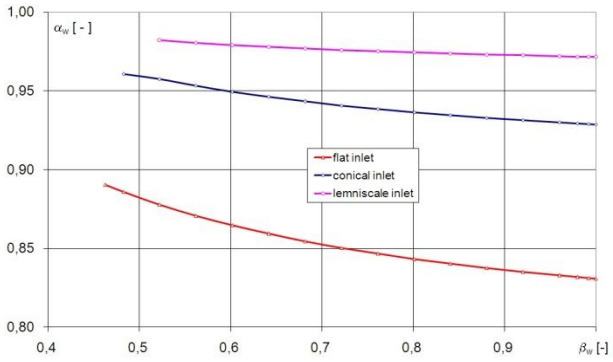

Fig. 3. Function of the αw coefficient versus pressure ratio $\beta_w = p_k/p_z$ for the inlet nozzles of the diameters: d_w= 1.002 mm – sharp edged; d_w = 0.984 mm – conic edge; d_w = 1.002 mm – Bernoulli's lemniscate

3.2. Flapper-nozzle area

In the air gauge, the flapper-nozzle area is the place where the measured dimension represented by the value s comes to interactions with the air gauge nozzle to convert the dimension into the flow parameter (Zelczak, 2002), which could be e.g. backpressure p_k or the volume q_v. The measuring nozzle could be analyzed only in interaction with the flapper surface, because those two elements determine the outflow surface and their cooperation effects with the restriction of the flow.

However, the flow through the flapper-nozzle area consists of two different stages: first the stream passes the jet with the diameter d_p and next it expands in the measuring slot s. The flow is very complicated, because of the rapid change of the stream direction and the way of expansion. In front of the jet, the stagnation point appears, and around it the boundary layer is formed. This layer thickness depends on many factors, mainly on the jet diameter d_p and Reynold's number. For the relative displacement $s/d_p \leq 4$ it is constant (Oleśkowicz-Popiel, 1981).

The boundary layer appears also close to the measuring nozzle front surface, which decreases the actual outlet surface. In this small area, large differences of pressure may appear causing supersonic local flows and even supersonic zones (Kazimierski and Krysiński, 1981). As a result, we deal with the thermodynamic flow process of the compressible medium, where along with sufficient velocity variety takes place highly diversified temperature distribution, where the air density is very difficult to be determined. The rapid change of the flow direction near the stagnation point provides highly complex mechanism of the energy transport,

DOI 10.1515/ama-2017-0006

because the kinetic energy of the stream falling on the flapper should be transformed into the rest enthalpy in the stagnation point, which in turn causes the increase of the local static pressure. On the other hand, the expansion of the air in the slot causes the radial flow and very large losses of the pressure. All the phenomena are very difficult to be described and visualized experimentally, and the measurement of the particular local vales is difficult because of the very small dimensions of the flow area. Both quality and quantity description of the flow in those conditions are very complicated.

In terms of pressure losses, there could be pointed out several zones in the flapper-nozzle area, where those losses are most evident (Lotze, 1965; Jermak and Rucki, 2012). These are shown in the Fig. 4 and included into the formula (3) below.

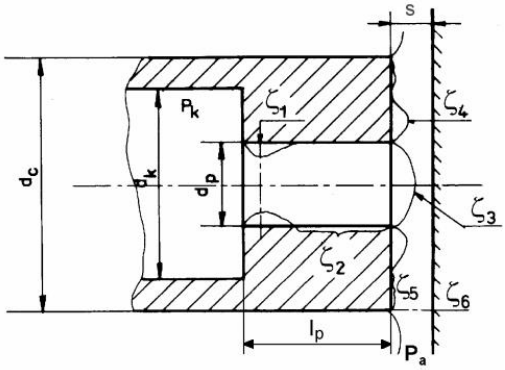

Fig. 4. Pressure losses in the flapper-nozzle area (Lotze, 1965)

The loss coefficient ζ has been defined by (Prosnak, 1971) as a ratio of the pressure difference caused by losses Δp_{str} divided by mean dynamic pressure in the analyzed point or intersection:

$$\zeta = \frac{2\Delta p_{str}}{\rho C^2}. \tag{2}$$

The negative impact of the loss of the pressure Δp_{str} on the sensitivity of the air gauge should be minimized. Different components of the coefficient ζ may affect the back-pressure p_k in different way and with different strength. So to express the overall pressure loss related to the mean pressure in the measuring slot s the following formula has been proposed (Lotze, 1965):

$$\zeta_c = 16\frac{d_c^2 s^2}{d_p^4}(\zeta_1 + \zeta_2 + \zeta_3) + \left(\left[\frac{d_c}{d_p}\right]^2 \zeta_4 + \zeta_5 + \zeta_6\right). \tag{3}$$

The first component of the formula (3) contains losses in the nozzle itself (see ζ_1, ζ_2 and ζ_3 in the Fig. 4), while the second is related to the slot between the measuring nozzle head and the flapper surface. The coefficient ζ_1 represents the stream contraction effect after the rapid decrease of the stream diameter. (Lotze, 1965) has proposed the formula to calculate its value:

$$\zeta_1 = \left(\frac{1}{\mu_k} - 1\right)^2 \tag{4}$$

where: μ_k– coefficient of contraction.

The variation range of the contraction coefficient μ_k depends on the profile of the inlet part of the nozzle. It lays in the range of <0.61÷0.99>, imposing the variety range of the loss coefficient: $\zeta_1 \in$<0.0001÷0.41>. Thus, it is possible to reduce ζ_1 applying profiled inlet area with large roundness.

Further pressure losses are the effect of the friction along the flow channel. The coefficient ζ_2 depends on the Reynolds number Re and on the length of the nozzle l_p. It is hardly expected the laminar flow in the working range of the slot widths s, so the following formula could be applied (Lotze, 1965):

$$\zeta_2 = \frac{0{,}316}{\sqrt[4]{Re}}\frac{l_p}{2s}. \tag{5}$$

The local losses described by the coefficient ζ_3 correspond with the expansion of the air leaving the jet. According to (Lotze, 1965), overall impact of those three components (ζ_1, ζ_2 and ζ_3) is rather small and do not exceed 8%.

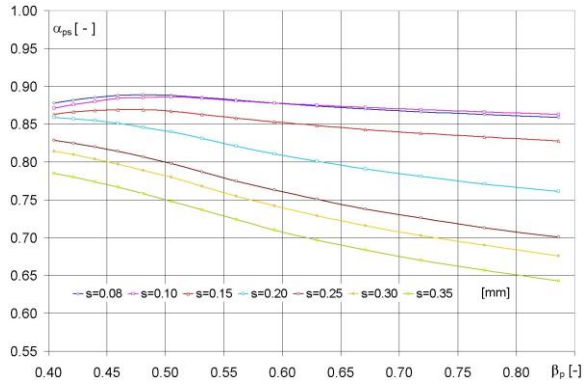

Fig.5. Graph of the flapper-nozzle flow coefficient α_{ps} versus flow ratio β_p for different slots s, the air gauge d_p=2.008 mm, D_c= 1.5

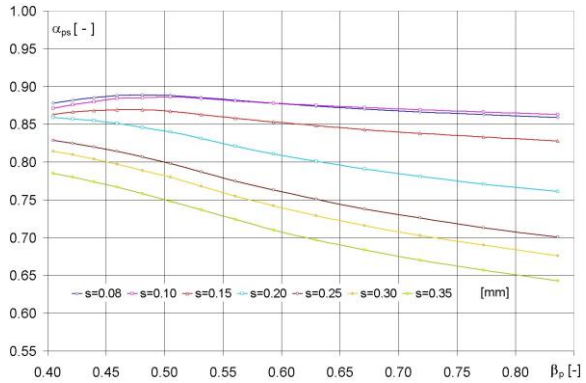

Fig. 6. Graph of the flapper-nozzle flow coefficient α_{ps} versus flow ratio β_p for different slots s, the air gauge d_p=2.008 mm, D_c= 3.0

Like in case of the stream contraction and coefficient ζ_1, rapid change of the flow direction after the nozzle edge causes the appearance of a "bubble ring" which results with the narrower than s actual flow. Coefficient ζ_4 is to represent that phenomenon, and when those "bubble rings" appear further at larger diameters as a result of the strike waves, additional pressure losses are described as ζ_5, covering friction losses as well.

Finally, when the stream of expanding air reaches the outer edge of the nozzle d_c, it is no more restricted by the slot. Here takes place the last pressure loss ζ_6 down to the atmospheric pressure pa, but its value is relatively small compared to ζ_4 and ζ_5.

To determine exact losses in the slot area (ζ_4, ζ_5 and ζ_6), the flow should be precisely characterized in all the crucial zones. It is a difficult task, thus the flow coefficient for the flapper-nozzle area αps appears to gain very different values. It should be noted that it varies not only for different slot widths s (and, hence, relative

DOI 10.1515/ama-2017-0006

pressure $\beta_p = p_a/p_k$), but also for different outer diameters of nozzle, expressed by relative value $D_c = d_c/d_p$. Figs. 5 and 6 show the corresponding graphs.

a)

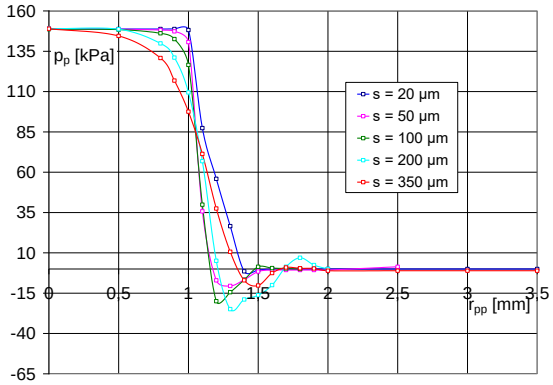

b)

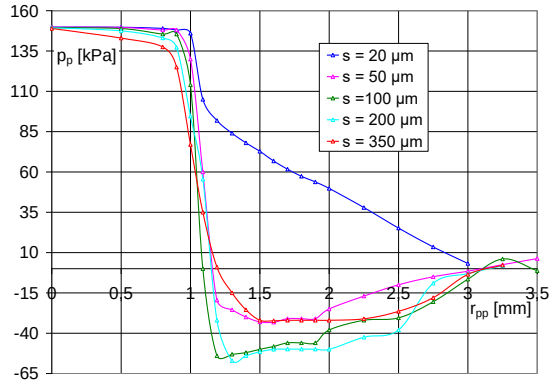

c)

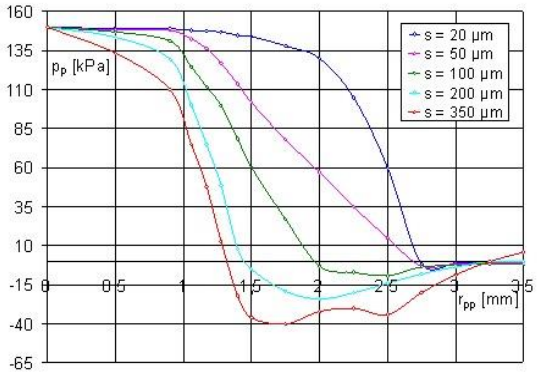

Fig. 7. Pressure distribution on the flapper surface for different measuring nozzles: a) flat narrow, D_c= 1.25; b) flat wide, D_c= 3; c) profiled, d_p= 2.008 mm, d_w= 0.802 mm

The experimentally obtained values of the local pressure on the flapper surface provide some additional information on the phenomena in the measuring slot. Following air gauges underwent examinations:

- inlet nozzle d_w: 0.802 mm,
- measuring nozzle d_p = 2.005 mm,
- feeding pressure p_z = 150 kPa,
- the measuring nozzle head surfaces: flat narrow (D_c = 1.25), flat wide (D_c = 3) and profiled according the lemniscate.

The results of the experiments led to the following conclusions:

- the local pressure p_p on the flapper surface measured on the radius r_{pp} could be described as:

$$p_p(r_{pp}) = f(p_z, s, d_p, d_p, D_c) = \text{const}, \quad (6)$$

- relatively large variations of the pressure appear in the flow area between outer and inner diameters of the nozzle head ($d_c - d_p$); it is there where "bubble rings" could be found, which are generated by sharp edge of the nozzle, rapid change of the flow direction and high velocity of the stream;
- large pressure gradients take place close to the inner edge of the nozzle, especially when the slot s is small;
- nozzles of narrow head surface generate rapid pressure change in the area of the orifice and relatively small sub-atmospheric pressure on the flapper surface (Fig. 7a). Large pressure gradient causes the expansion, which leads to maximal velocity with minimal pressure. It is highly probable that in this very area the air velocity reaches supersonic values. Further the velocity quickly decreases and the pressure on the flapper surface comes close to the atmospheric one.
- in case of the wide head nozzles no sub-atmospheric pressure was noted on the flapper surface for the slots smaller than s = 20 μm (Fig. 7b), and the pressure gradient along the head was small.
- the outlet edge of the profiled nozzle is placed higher than the outer edge. That is why the stagnation zone is much larger. As a result, the stream changes its direction smoothly, and the sub-atmospheric pressure on the flapper surface appears only for slots larger than 150 μm (Fig. 7c). For the larger slots, the phenomenon of the local stream slowdown effected with the appearance of the zones with higher pressure.
- in the area larger than restricted with the nozzle head, some pressure could be noted on the flapper surface, which may prove the dynamic effect of the stream slowdown.
- in all examined cases, the radius r_{pp} of the maximal sub-atmospheric pressure was close to (0.60÷0.70) d_p.

3.3. Pressure distribution in the measuring chamber

The air gauge's measuring chamber is the area between the inlet and measuring nozzles. Its task, on the one hand, is to dissipate the energy of the air stream leaving the inlet nozzle, and on the other hand, to provide the conditions for proper back-pressure measurement. It is required to ensure the minimal fluctuation of the pressure in the measuring point. If the chamber did not provide full expansion of the air stream, it would cause dynamical effects in its end part close to the measuring nozzle. When this requirement is met, the overall pressure in the area is equalized and could be measured in the point placed on the side surface. Theoretical (hypothetic) structure of the flow through the measuring chamber is shown in the Fig. 8.

The most complicated is the description of the flow in the measuring chamber area close to the inlet nozzle outlet surface. The expanding stream generates here some whirls and backflows caused by the small pressure with gradient both along the stream line, and perpendicular to it.

The velocity field in the perpendicular cross-section of the stream consists of the constant velocity segments and the transitional zone (turbulent boundary layer). The flow characteristic, in particular, is the variation of the velocity along the axis of the

DOI 10.1515/ama-2017-0006

circulation area. The boundary layer gradually widens from the outlet orifice surface, and at the certain distance l_s reaches its maximal width. The pressure distribution changes accordingly, as it is shown in the Fig. 8. When the stream leaves the nozzle, its pressure is $p_{1'}$, and in the minimal intersection (p_{min}), there is the minimal pressure $p_{1'min}$.

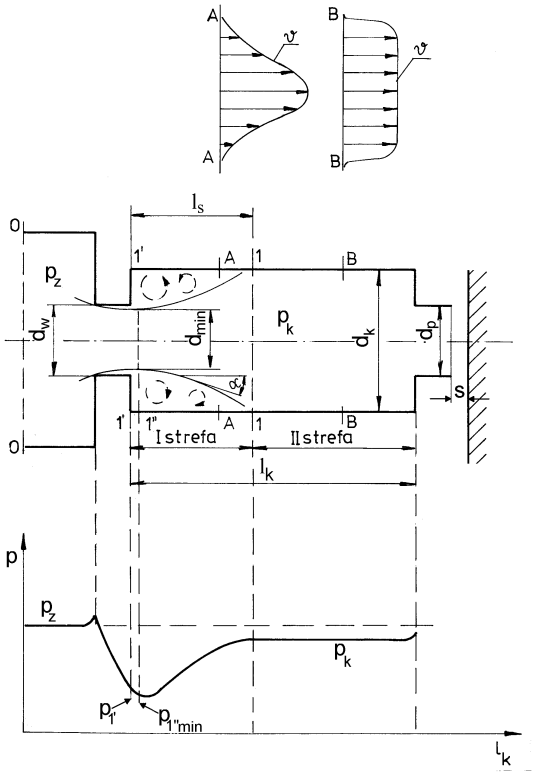

Fig. 8. Hypothetical structure of the stream expansion in the measuring chamber of length $l_k$and diameter d_k

Contraction of the stream d_{min}/d_w is dependent on the geometry of the inlet nozzle and its dimensions, and in case of the profiled jets it could be close to 1. After the minimal cross-section marked in the Fig 8 as 1′′–1′′, the increase of the pressure could be observed up to the maximal pressure in the cross-section 1-1. Further from the minimal cross-section, the pressure varies not much revealing weak trend to decrease, which can be explained with the friction inside the chamber. The distribution of the velocity and pressure in the chamber depend on the feeding pressure p_z, thus on the mass flow q_m, too. Of course, dimensions of the measuring chamber are of significant importance as well.

The most important form the designer's perspective is to know the dimensionless values that determine the geometry of the chamber: d_k/d_w and l_k/d_k. The minimal length of the measuring chamber is restricted by the relation $l_s < l_k$ for the assumed ratio d_k/d_w. This way the minimal dimensions of the measuring chamber could be estimated. Then it could be assumed that the dynamical effects near the measuring nozzle are negligibly small, and the mean velocity here is no larger than 15% of the velocity close to the inlet nozzle. Under such conditions, the authors Dejč (1961) and Zalmanzon (1961) recommend the following dimensions:

$$l_k \approx (4 \div 5)d_k;\ d_k \approx 7d_w \tag{7}$$

For the experimental research it was assumed to investigate the chambers of the diameter d_k = 10 mm and length l_k = 20, 40 and 80 mm. The measured values were: overall pressure pc measured along the axis of the chamber, and the loss of the pressure Δp_k on the chamber sides. The reference value was the back-pressure measured on the chamber side 0.5 mm far from the inlet nozzle edge. The experiments were repeated for the mass flow rates q_m of 6×10^{-4} kg/s and 14×10^{-4} kg/s, which correspond with the air gauge work at the slot width s = 50 μm and 350 μm, respectively. The results of experimental measurements are shown in the Fig. 9a and b.

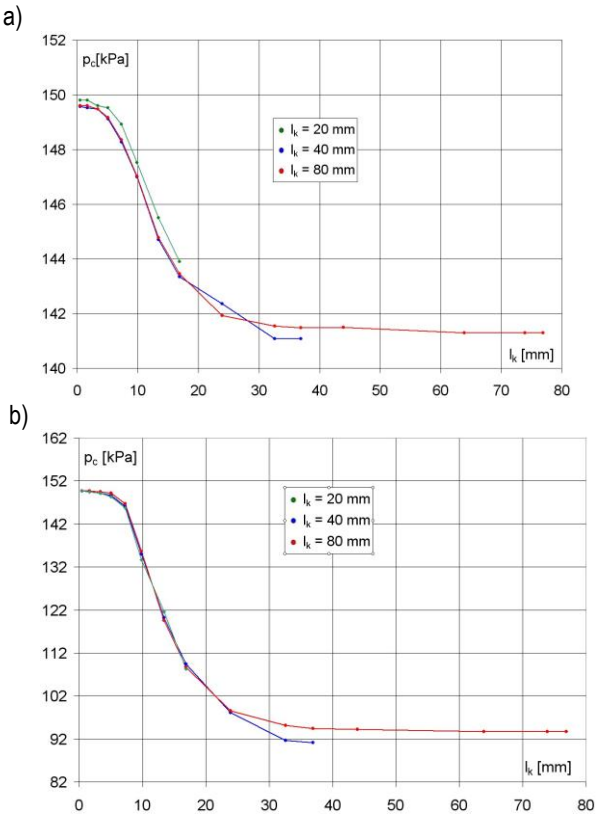

Fig. 9. Measurement results for the overall pressure pc versus chamber length l_k for different mass flow rates: a) q_m = 6×10^{-4} kg/s, b) q_m = 14×10^{-4} kg/s

Analysis of the above graphs leads to the conclusion that the overall pressure is dependent on the mass flow rate and on the distance from the inlet nozzle edge. Regardless what is the mass flow rate, in the chambers of the length l_k = 20 mm the overall pressure got never stabilized. That means high flow velocity and incomplete expansion of the stream across the chamber volume. Completely different result is seen for the chamber of length l_k = 40 mm and 80 mm. In both cases, the overall pressure reached its stabilized value dependent on the mass flow at the length ca. $0.8l_k$. The pressure decrease in both cases corresponded with ca. 0.45 kPa per 1 mm of the chamber length for the mass flow q_m = 6×10^{-4} kg/s and ca. 4.0 kPa per 1 mm of the chamber length for the mass flow q_m = 14×10^{-4} kg/s.

The changes of the pressure Δp_{st} on the chamber sides versus distance from the inlet nozzle varied from +25 Pa (l_k = 40 and 80 mm) down to −480 Pa (l_k = 80 mm) for the mass flow q_m = 6×10^{-4} kg/s and from +250 Pa (l_k = 20 mm) down to −3000 Pa (l_k = 80 mm) for q_m = 14×10^{-4} kg/s (see Fig. 10a, b).

DOI 10.1515/ama-2017-0006

a)

b)

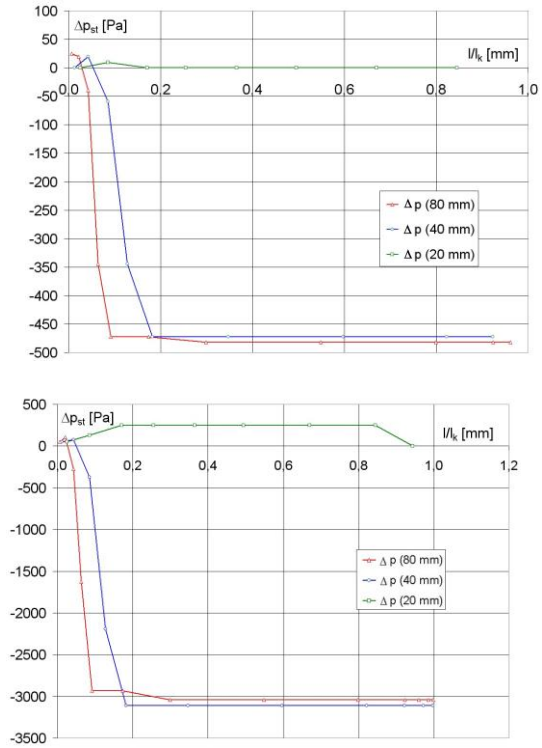

Fig. 10. The results of measurement of the back-pressure Δp_{st} versus the relative length from the inlet nozzle edge l_i/l_k for different mass flow rates: a) q_m = 6×10-4 kg/s, b) q_m = 14×10-4 kg/s

It could be stated that in the chambers of the length l_k = 20 mm took place the dynamic phenomenon with various intensity, but always resulting with back-pressure value Δp_{st} = 0 (for q_m = 6×10-4 kg/s) or Δp_{st}> 0 (for q_m = 14×10-4 kg/s). Initial recommendation could be made that it is reasonable to place there the measuring point for the back-pressure p_k.

In the longer chambers, the rapid fall of the back-pressure takes place in the area from 0.1 to 0.2 l_k. It is assumed that this particular point should not be chosen for the back-pressure measurement.

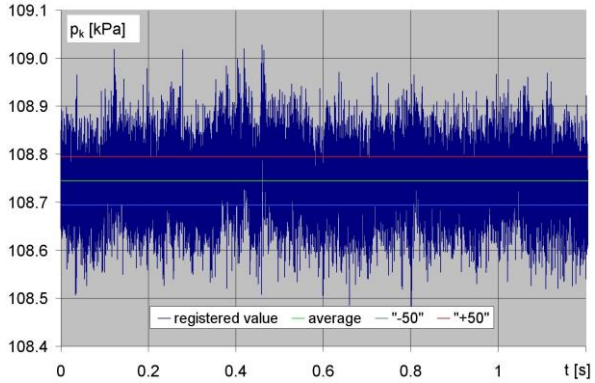

Fig. 11. Registered values of the back-pressure p_k in the point A; d_p = 2.005 mm, d_{kw} = 1.210 mm, D_c = 3, s = 170 µm; red and blue lins correspond with the acceptable fluctuations of ± 50 Pa

During the outflow process from the inlet nozzle to the chamber, strong turbulences take place. Thus, the back-pressure p_k measured both in static and dynamic conditions never achieves stable constant value, but is a subject of strong fluctuations shown in the Fig. 11. This way the reliability of the dimensional measurement result is under question both in the adjustment process and in the inspection, because the pressure fluctuations reveal themselves in changes of the dimension indication (Rucki, 2009).

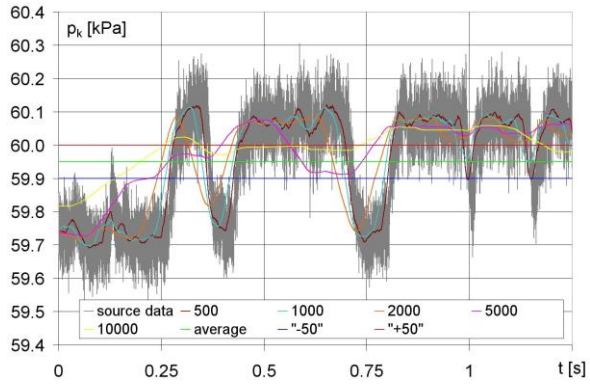

Fig.12. Fluctuations of the back-pressure p_k in the "jump" area; the air gauge parameters: d_p = 2.005 mm, d_w = 1.210 mm, D_c= 3

a)

b)

c)

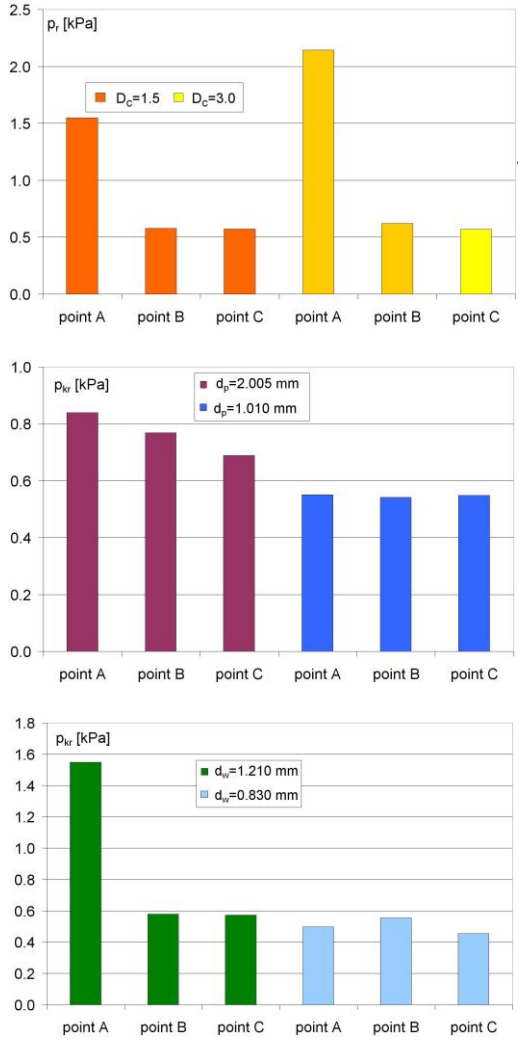

Fig. 13. Maximal range ($p_r = p_{kmax} - p_{kmin}$) of the back-pressure fluctuation dependent on: a) head surface D_c(d_p= 2.005 mm, d_w = 1.210 mm), b) diameter d_p (d_w = 1.210 mm, D_c = 1.5), c) diameter d_w (for d_p = 2.005 mm, D_c = 1.5)

DOI 10.1515/ama-2017-0006

The dimensions of the nozzles used in the investigations, the measuring one (diameter d_p = 2.008 mm and head surface D_c = 1.5 and 3.0) and the inlet one (d_w = 0.830 mm and 1.210 mm) provided the variations of the metrological characteristics in the range that corresponded with the working conditions of the industrial air gauges.

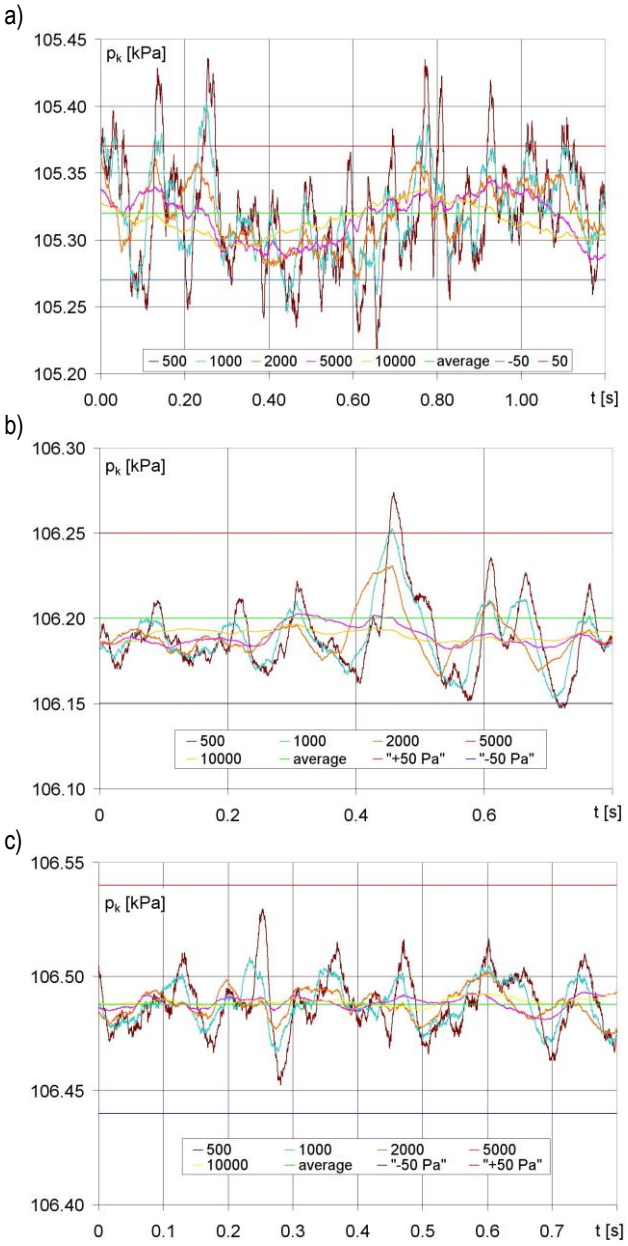

Fig. 14. The averaged signals of the back-pressure p_k in the points: a) A, b) B, c) C for the air gauge of d_p = 2.005 mm, d_w = 1.210 mm

The dimensions of the examined chambers were following: diameter d_k= 10 mm and length l_k= 70 mm. The probing points A, B and C were placed at the distance from the inlet nozzle edge l_{kA} = 10 mm, l_{kB} = 40 mm and l_{kC} = 68 mm, respectively. During the measurement, it could be noted that the back-pressure varied with the substantial amplitude, and two periods could be distinguished – longer ones of amplitude ca. 0.5 kPa and high frequency ones of smaller amplitude ca. 0.3 kPa (Fig. 12).

When those two waves are superposed, the resulting range of fluctuation of the back-pressure p_k reaches R = 0.7÷0.8 kPa. Along the walls of the chamber this process is occurring with various intensity, and reaches its peak close to the inlet nozzle (point A). To evaluate the range of the fluctuations $p_r = p_{kmax} - p_{kmin}$, the investigations were repeated for 64,000 samples with sampling interval t_p = 0.0004 s. It was noted that the fluctuations are dependent on the geometrical parameters of the nozzles: the head surface D_c, as well as the diameters d_p and d_w.

The analysis of the registered fluctuations, like shown in the Fig. 11, confirmed the earlier statement that there are significant turbulences in the area close to the inlet nozzle. It is particularly obvious in case of the air gauges with large diameters of the nozzles. The example shown in the Fig. 13 suggests also that the increase of the head surface D_c from 1.5 up to 3.0 could cause large fluctuation of the back-pressure in the point A. In other probing points of p_{kr}, the fluctuation level got stabilized and reached the value dependent on the measuring and inlet nozzles diameters. Certainly the best reduction of the fluctuations was achieved for the air gauge with the measuring nozzle d_p = 2 mm and inlet nozzles smaller than 1 mm. The localization of the measuring point was then of secondary importance.

However, the recommended localization of the measuring point is not enough to achieve the signal of possibly minimal fluctuation. The signal has to be averaged in order to make the amplitude fit the required range. Considering the high requirements on the uncertainty of the slot width determination, the maximal acceptable deviation of the back-pressure signal was assumed to lay in the range ± 50 Pa. In the graphs (Fig. 14), those upper and lower limits are represented with red and blue lines, respectively. The green line corresponds with the mean value.

Fig. 14 presents the graphs for the registered back-pressure in the measuring points A, B and C, obtained for different numbers of samples (from 500 up to 10,000) intended to be averaged. For the sampling time of t_p = 0.0004 s the time span t_u for the averaging process is from 0.2 s to 4 s.

Again, the dependence of the point localization and the fluctuation level is clearly seen. Certainly the largest range of fluctuations take place close to the inlet nozzle. When the acceptable fluctuation must not exceed ± 50 Pa, in the point A the averaging time must be t_u = 0.8 s, while in the point C some 500 samples is enough (t_u = 0.2 s).

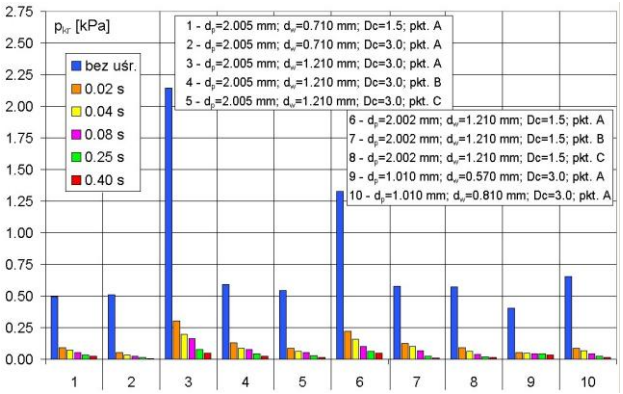

Fig. 15. Averaging time and the fluctuation amplitude p_r for different configurations of the air gauges and probing points localization (numbers 1−10 correspond with particular configurations)

The dimensions of the nozzles in air gauges also have their impact on the fluctuations. The earlier conclusion against the

DOI 10.1515/ama-2017-0006

nozzles of large diameters found its confirmation also in case of the configuration #3 shown in the Fig. 15. That comes to be true both in case of the rough measuring signals and the averaged ones. In the extremes, the range of the fluctuations reached values over 2 kPa, which corresponded with the slot width ca. 5 μm, or 5% of the measuring range. The decrease of the head surface down to D_c = 1.5 and the change of the probing point localization allowed to decrease fluctuations down to 25% of maximal value. However, the averaging process appears to be necessary anyway.

4. DISCUSSION ON THE DISCONTINUITY OF THE AIR GAUGES CHARACTERISTICS

The main metrological properties of the air gauge are described by its static characteristics which describes the function of the back-pressure $\mathrm{p_k}$ versus slot widths. This function is influenced by many geometrical parameters, as well as thermodynamic and flow-through conditions. From the metrological perspective, the changes in the multiplication (sensitivity) can provide much important information on the air gauge. In the article, the module of sensitivity $|K| = f(s)$ is considered.

Typically, the sensitivity of an air gauge is defined as following:

$$K = \lim_{\Delta s \to 0} \left(\Delta p_k / \Delta s\right) \approx \frac{dp_k}{ds} \tag{8}$$

where: $\Delta \mathrm{p_k}$ – increase of the back-pressure caused by the increase of the slot width, Δs – increase of the slot width in the linear area of the function.

In many cases, it was found that the actual static characteristics reveal discontinuity of the back-pressure $\mathrm{p_k}$, which affects the metrological properties of the air gauge shortening its measuring range. Fig. 16 provides the example of the phenomenon, where around the slot width s = 280 μm one can see the huge "jump" of the sensitivity and the hysteresis in the $\mathrm{p_k} = f(s)$ function. Perhaps the first scholar who paid attention to the phenomenon was (Markow, 1971).

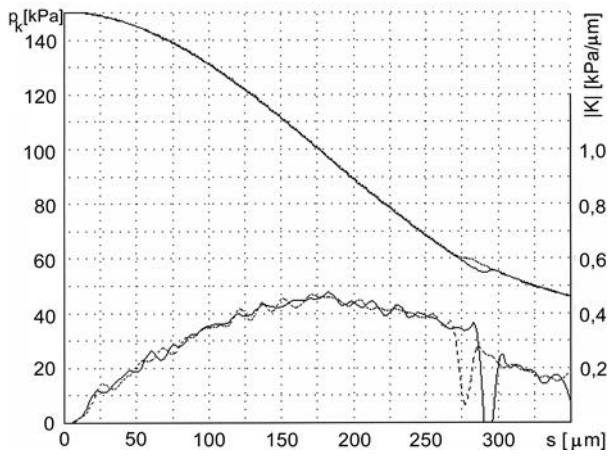

Fig. 16. Static characteristic $sp_k = f(s)$ and sensitivity graph $|K| = f(s)$ of the air gauge with d_w = 2.002 mm, d_p = 1.210 mm, and D_c = 3

The discontinuity provides some problem which may be solved in two different terms. The first term is the understanding of the phenomena that cause the problem and identification of the main sources. The second term is the practical elimination of the discontinuity or removal it from the linear area of the function. To do it, one must choose proper dimensions and shape of the air gauge elements.

The authors (Crnojevic et al., 1997) suggested that the discontinuity was caused by the diagonal strike wave that appeared in the outlet area of the measuring nozzle close to the flapper surface. As a result, the pressure losses increased and hence the airflow decreased. Similar explanations were proposed by other researchers (Breitinger, 1969; Zelczak, 2002).

It can be stated that the discontinuity is caused by many factors like feeding pressure p_z, relation between nozzle dimensions d_w/d_p, measuring slot width s and the outer diameter of the measuring nozzle d_c. It seems reasonable to look at the phenomenon from such a practical perspective.

Fig. 16 above presents the results of the investigations on the air gauge of following dimensions: d_p = 2.002 mm, d_w = 1.210 mm and D_c = 3 (Project Report, 2001). In the sensitivity graph $|K| = f(s)$ a series of areas can be pointed, where different kinds of the airflow take place. The laminar flow turns to the turbulent one in the inlet nozzle when the slot width is s = 20÷25 μm, which results with some "jump" in the sensitivity graph. Further fluctuations of the sensitivity, especially the ones around the slot widths sca. 55 μm and 70 μm, correspond with the similar changes of the flow in the measuring nozzle orifice and in the slot, respectively (Breitinger, 1969). When laminar flow turns into the turbulent one, some decrease of the sensitivity could be seen. In the range of the slots s = 275÷300 μm take place contractions of the air stream that lead to the disturbance of the static characteristics. Rapid increase and then decrease of the back-pressure form a hysteresis. High dynamics of the phenomenon attracts attention (Fig. 17): the "jump" lasts ca. 0.005 s, which corresponds with the ratio of 600 kPa/s.

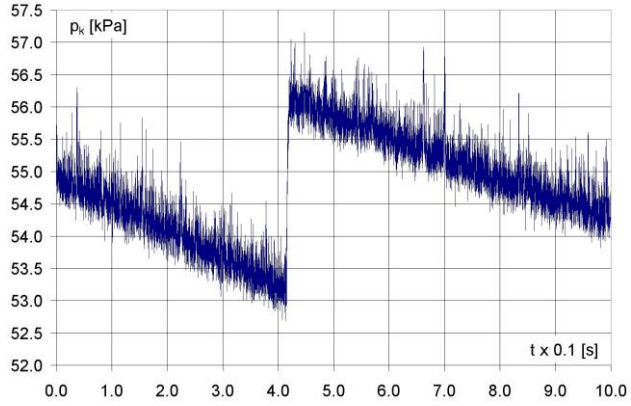

Fig. 17. Fragment of the static characteristics from the Fig. 16 close to s = 290 μm obtained when the slot was increased

The graphs presented in the Fig. 16 and 17 were obtained through slow controlled movement of the flapper surface in front of the measuring nozzle (see Jermak and Rucki, 2012). The direction of the "jump" between 275 μm and 300 μm depends on the condition, is the flapper surface moving towards or away from the nozzle. Since the discontinuity appearance depends on the slot width s, static characteristics become ambiguous which leads to the decrease of the measuring range.

DOI 10.1515/ama-2017-0006

5. CONCLUSIONS

Metrological characteristics of the air gauges are formed by the range of the thermodynamic and gasodynamic phenomena that take place in the flow-through elements like nozzles, measuring chamber or flapper-nozzle area. In every element some losses of energy and pressure occur, which may be expressed with the flow coefficient. The coefficient is dependent among others on the dimensions and shape of the nozzle. In case of the inlet nozzles, it is recommended to form the inlet surface with curved profile, which could cause some change in the flow coefficient.

The source of the main disturbances of the static characteristics, however, lays in the phenomena located in the flapper-nozzle area. The airflow here is very complicated because of the flow direction change around a stagnation point. Large differences of the local pressures may lead to the supersonic local flow. On the flapper surface, the areas with pressure substantially below the atmospheric pressure appear, temperature falls and the phenomenon of the transition of the flow from the surface of nozzle to the flapper surface and back again.

In the measuring chamber, the flow is mainly characterized by the pressure distribution. The pressure on the chamber walls reaches its minimal value in the maximal cross-section of the air stream. In the area close to the inlet nozzle edge, recirculation area appears where strong turbulences take place. Hence, the back-pressure measuring point is recommended to be placed at some distance from the inlet nozzle edge. It also appears advantageous to apply the nozzles of the diameters smaller than 2 mm, and the measuring nozzle with narrower surface $D_c \leq 1.5$.

The measurement with digital devices proved to require the averaging of the obtained signal because of substantial fluctuations of the back-pressure. The averaging effectiveness is dependent highly on the localization of the measuring point. Assuming the maximal fluctuation of ± 50 Pa and proper localization of the probing point, it is possible to obtain a reliable signal every 0.2 s.

REFERENCES

1. **Bokov V.B.** (2011), Pneumatic gauge steady-statemodelling by theoretical and empirical methods, *Measurement*, 44,303-311.
2. **Breitinger R.** (1971), New Pneumatic Measuring Gauges, *Fertigungtechnik*,61, 225–227, (in German)
3. **Crnojevic C, Roy G, Bettahar A, Florent P.** (1997), The Influence of the Regulator Diameter and Injection Nozzle Geometry on the Flow Structure in Pneumatic Dimensional Control Systems, *Journal of Fluids Engineering*, 119, 609–615.
4. **Dejč M.E.** (1961), *Technical, Gosènergoizdat*, Moskva–Leningrad, (in Russian)
5. **Idel'čik I.E.** (1960), Hydraulic Resistances Directory, Gosènergoizdat, Moskva, (in Russian)
6. **Jermak Cz.J, Rucki M.** (2016) Dynamics of the non-contac troundness measurement with air gages, *Acta Mechanica et Automatica*, 10(3),227-232.
7. **Jermak Cz.J.** (2010), Methods of Shaping the Metrological Characteristics of Air Gages, *Journal of Mechanical Engineering*, 56(6), 385-390.
8. **Jermak Cz.J.** (2012), Theoretical and Practical Aspects of Shaping of Static Metrological Properties of Length Air Gauges Wyd. Politechniki Poznańskiej, Seria Rozprawy, nr 476, (in Polish)
9. **Jermak Cz.J., Rucki M.** (2012),*Air Gauging: Static and Dynamic Characteristics*, IFSA, Barcelona.
10. **Kazimierski Z., Krysiński J.** (1981), *Gas Bearing Arrangement and Microturbine Drives*, WNT, Warszawa, (in Polish)
11. **Lammel L., Osiadacz A.** (1974), Pneumatic Signals in Automation, WNT, Warszawa, (in Polish)
12. **Lotze W.** (1971), *Design of Pneumatic Air Gauges*, Feingerätetechnik, 29(9), 389–394, (in German)
13. **MinaevA.N.** (1987), *Mechanics of Liquid and Gas*, Metallurgiâ, Moskva, (in Russian)
14. **Oleśkiewicz-Popiel Cz.** (1981), Axial-symmetric Free and Striking Stream, Wyd. Politechniki Poznańskiej, Poznań. (in Polish)
15. **Project Report** (2001), Design of Metodology of Improving of Properties of Pneumatic Lenght-measurement Gauges. Project Report KBN 1253/T07/00/18. (in Polish)
16. **Prosnak W.J.** (1971), *Fluid Mechanics – Gas Dynamics*, t. 2, PWN, Warszawa, (in Polish)
17. **Rucki M.** (2009), Reduction of Uncertainty in Air Gauge Adjustment Process, *IEEE Transactions on Instrumentation and Measurement*, 58(1), 52-57.
18. **Schuetz G.** (2015), Pushing the Limits of Air Gaging—And Keeping Them There, *Quality Magazine*, 54(7),22-26.
19. **Tanner C.J.** (1958), Air gauging – history and future developments, *Institution of Production Engineers Journal*, 37(7),448-462.
20. Theory of Pneumatic Sensors Integrated with Piezoceramical Pressure Transducer (1986-1990), Annual Research Report.CPBP 02.20, Nr III.02, Poznań–Warszawa. (in Polish)
21. **Tesar V.** (2008), Characterisation of subsonic axisymmetric nozzles, *Chemical Engineering Research and Design*, 86,1253–1262.
22. **Tesar V.** (2010), Characterisation of inexpensive, simplyshaped nozzles, *Chemical Engineering Research and Design*, 88, 1433-1444.
23. **Vacharanukul K., Mekid S.** (2005), In-Process Dimensional Inspection Sensors, *Measurement*, 38(3),204-218.
24. **Zalmanzon L.A.** (1961), *Flowing Elements of Pneumatic Control Appliances*, Izd. Akademii Nauk SSSR, Moskva. (in Russian)
25. **Zelczak A.** (2002), *Pneumatic Length Measurements*, WKŁ, Warszawa, (in Polish)

Acknowledgement: The investigations had been performed in frames of the projects CPBP 02.20 and KBN 1253/T07/00/18 financed by Polish Government.

DE GRUYTER
OPEN

DOI 10.1515/ama-2017-0007

acta mechanica et automatica, vol.11 no.1 (2017)

VERIFICATION OF RAM-PRESS PIPE BENDING PROCESS USING ELASTO-PLASTIC FEM MODEL

Paweł SIDUN*, Andrzej ŁUKASZEWICZ*

*Faculty of Mechanical Engineering, Bialystok University of Technology, 45C Wiejska Street, 15-351 Bialystok, Poland

pawel.sidun@gmail.com, a.lukaszewicz@pb.edu.pl

received 6 February 2016, revised 27 February 2017, accepted 6 March 2017

Abstract: In this paper selected aspects of numerical modelling of bending pipes process are described. Elasto-plastic material model was used in COMSOL FEM environment. The results of numerical analyses of two kinds of steel were presented. The correctness of the proposed model was verified based on comparison shapes of deformed pipe profile obtained at the ending step of bending both from numerical simulations and experiment.

Key words: Pipe Bending, FEM Analysis

1. INTRODUCTION

Bending pipe technology is used in many branches of industry. Development of Computer Aided Engineering (CAE) systems allows for numerical analysis of bending pipe phenomena in many different approaches. The research work (Kuanget al., 2015) presented numerical analysis of thermoplastic pipes under external pressure and bending moment. The research paper (Dong et al., 2015) showed analytical and numerical approach of biaxial dynamic unbounded flexible pipe bending process. Some analytical and numerical aspects of plastic limit loads for pipe under combined loading condition presented Haoet al. (2016) and Li et al. (2015). Problem of wrinkling carbon steel pipes using a numerical approach was solved by Vasilikis and Karamanos (2012). Effect of using different boundary conditions for bending pipe process in finite elements modelling was presented by Guarracino et al. (2008). Stress analysis of composite pipes during bending process in analytical approach presented Menshykova et al. (2014). Dong et al. (2015) reported another analytical approach for unbounded flexible pipe during bending process.

Presented short literature review shows many different approaches for modelling bending pipe process. Industry still needs easy way to evaluate many factors of bending process like ovalization and degree of bending after springback of material for optimization bending process (e.g. in CNC bending pipe machines). The aim of this paper is to present a 3D elasto-plastic FEM model of ram-press bending process, created in COMSOL software, and its verification by compare shapes of deformed cross-sections of pipe obtained from numerical analysis and experimental tests.

2. FINITE ELEMENT ANALYSIS OF RAM-PRESS BENDING PROCESS

In this paper numerical analysis of ram-press bending process (Korzemski, 1971) was presented (Fig. 1). Finite Element Method (FEM) analysis with elasto-plastic model, using COMSOL Multiphysic environment, was used. Experimental test of bending was done for pipe with dimension ϕ16x2 made of structural steel E235+N. Total displacement of pattern for bending process used in experiment was 120mm, the direction of pattern determines force P and the same value was applied in numerical analysis (Sidun, 2015). FEM analysis was based on data of stress-stain curve for three types of steel (stainless steel 1.4313, structural steel Kodur 260MC and E235+N). These was obtained from tension test of specimens cut from pipe and next implemented to elasto-plastic model in FEM system (Fig. 2, 3, 4).

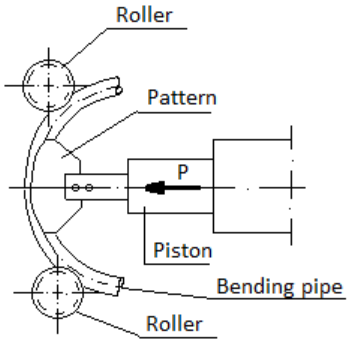

Fig. 1. Scheme of analysed bending process

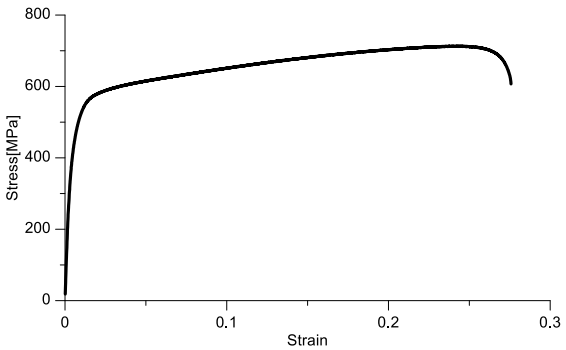

Fig. 2. Stress-strain curve from tension test for steel 1.4313

DOI 10.1515/ama-2017-0007

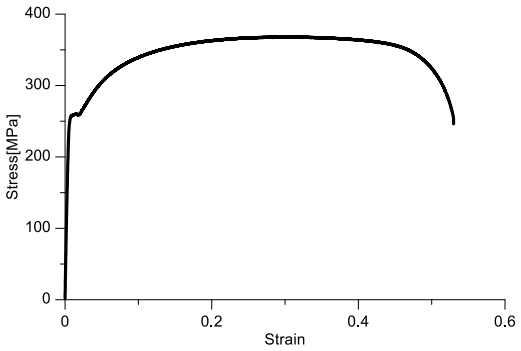

Fig. 3. Stress-strain curve from tension test for Kodur 260MC steel

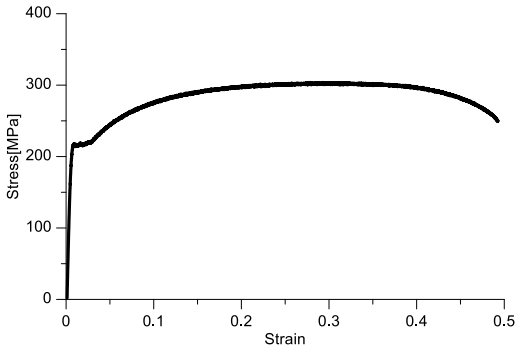

Fig. 4. Stress-strain curve from tension test for steel E235+N

Elasto-plastic FEM model was based on Huber-Mises yield criterion and isotropic hardening model of material (Ottosen and Ristinmaa, 2005). Contact between elements in FEM analysis was defined in following way: the roller and the pattern are rigid, the pipe has elasto-plastic behaviour, contact for pairs (roller-pipe and pattern-pipe) is assumed without friction coefficient.

In FEM system symmetry conditions (Fig. 5) were applied. Following boundary conditions (see coordinate system) were used (Fig. 5).

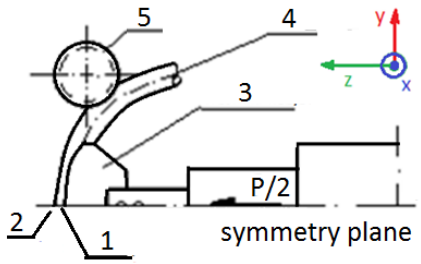

Fig. 5. Definition of boundary conditions (1 – face of pipe in symmetry line has u_y = 0; 2 – external point of pipe in symmetry line has u_x = 0; 3 – pattern can only move in z axis; 4 – pipe, have all degree of freedom, 5 – roller can only rotate about x axis)

Discrete model of ram-press bending components was made using quad elements to build the pattern and the pipe and tetra elements to build the roller (Fig. 6). Number degree of freedom brought 434723.

The main advantage of application FEM analysis in bending pipe process is faster implementation time of new series of products. Numerical analysis of bending pipe process allows for continuous productions process with reason of preparation initial bending parameters to obtain good quality of final product. It is very important because eliminates errors of bending radius due to springback and allows to predict good results of shape deformations.

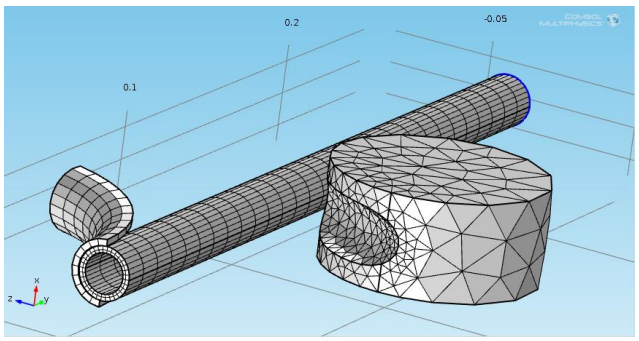

Fig 6. 3D mesh of ram-press bending FEM model in COMSOL Multyphysics

3. MAP OF EFFECTIVE PLASITC STRAIN FOR DIFFERENT MATERIALS

Analysis was executed for three materials: 1 – stainless steel 1.4313 (SS) designated for manufacture of parts and components for machines such as parts of pumps, compressors and turbines, 2 – steel Kodur 260MC used to produce welding constructions, pressure tank, pipelines, chassis of car, 3 – structural steel E235+N used to produce pipes, chassis of car, pumps compressors. The results of numerical analysis of ram-press bending pipe process show dependency between material plastic behaviour (strain-stress curve) and received deformation (effective plastic strain).

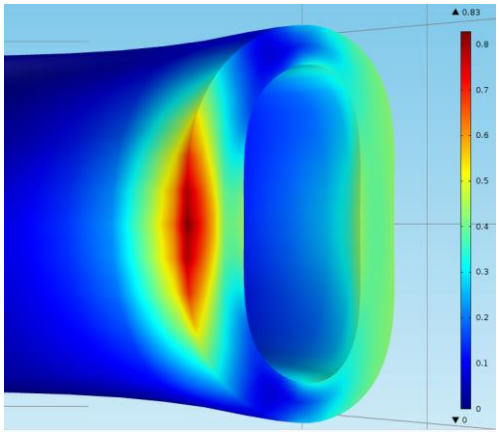

Fig. 7. Map of effective plastic strain for steel 1.4313

Figures 7, 8 and 9 present deformations of profile in the symmetry plane at the ending step of loading. Structural steel Kodur 260MC (Fig. 8) and E235+N (Fig. 9) steel demonstrate almost exactly the same deformation of bending profile. Stainless steel 1.4313 (Fig. 7) has flatten of pipe profile what is unacceptable in pipe bending process. In this case obtained value of effective plastic strain is much greater than real maximum strain (0,25) before plastic fracture (Fig. 2). It means, for this steel, fracture can occur after the strain exceeded limit value about 0,25. In computational process a real behaviour of material including fracture mechanism was not defined. FEM system continues calculations,

DOI 10.1515/ama-2017-0007

for the maximum stress value declared in strain-stress curve, to the end step of bending. That initial analysis of deformation profile helps in preliminary analysis of suitability materials for the bending process.

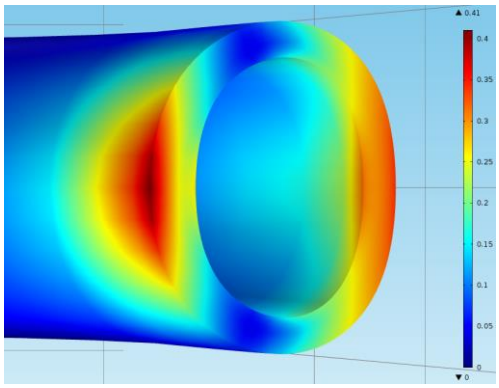

Fig. 8. Map of effective plastic strain for Kodur260MC steel

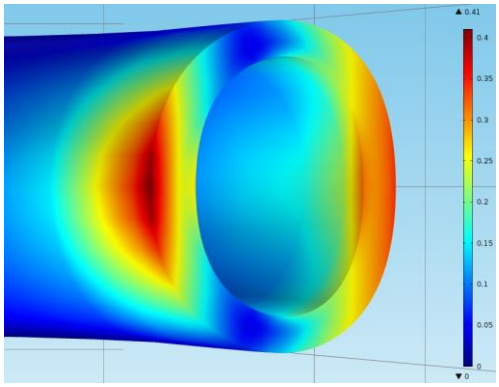

Fig. 9. Map of effective plastic strain for steel E235+N

4. EVOLUTION OF STRESS AND STRAIN DURING BENDING PROCESS

During ram-press bending process pipe zones were subjected to different stress conditions. The most loaded points of pipe presents Fig. 10.

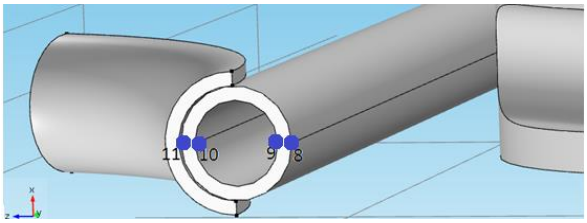

Fig. 10. Points of measure stress and strain during bending process

Pipe was under two different state of loading: compression - line 10 and 11, tension - 8 and 9, for stainless steel 1.4313 (Fig. 11, 12), Kodur 260MC steel (Fig. 13, 14) and E235+N (Fig. 15, 16).

Graphs (Fig. 11, 13, 15) show that material was subjected almost the same compressive stress in points 11 and 10. Points 8 and 9 shows that material was more loaded in inside part of pipe. Difference in Huber-Von-Misses stress for steel Kodur260MC and E235+N is very small, what is caused by almost exactly the same characteristic of strain-stress curve. Steel 1.4313 has very big difference in stress between points 9 and 8, what is caused by thinning of inside part of pipe.

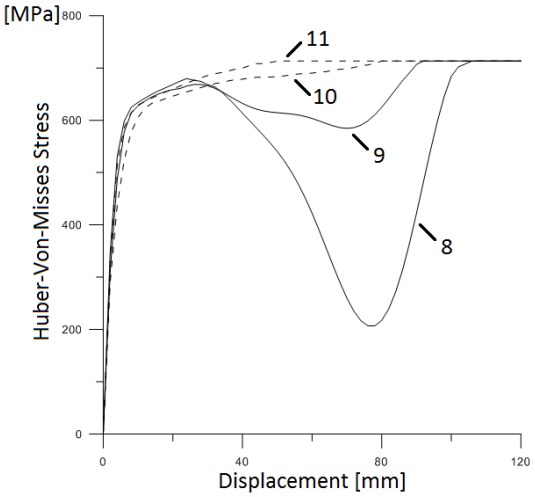

Fig. 11. Evolution of Huber-Von-Misses stress during bending process for stainless steel 1.4313

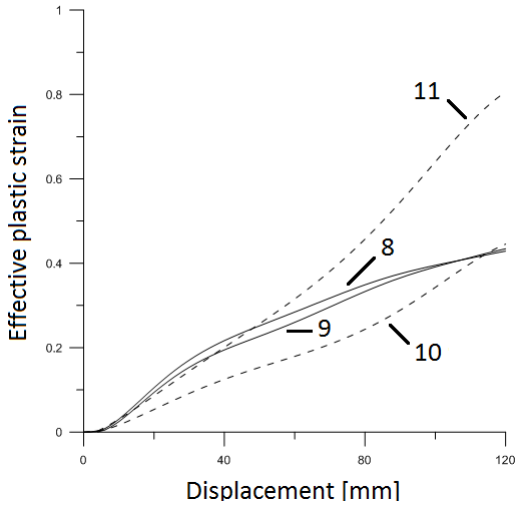

Fig. 12. Evolution of effective plastic strain during bending process for stainless steel 1.4313

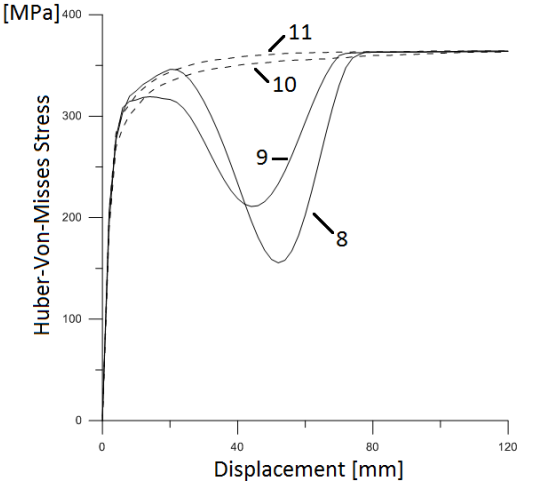

Fig. 13. Evolution of Huber-Von-Misses stress during bending process for Kodur 260MC steel

DOI 10.1515/ama-2017-0007

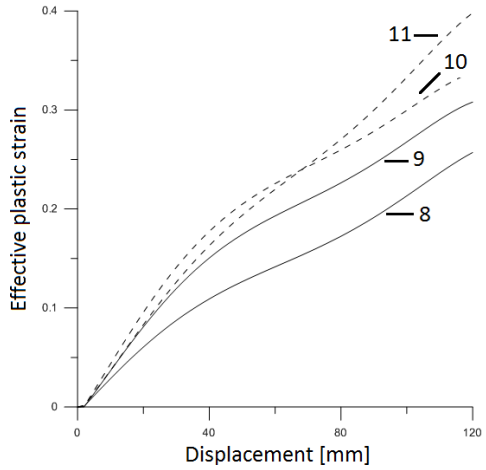

Fig. 14. Evolution of effective plastic strain during bending process for Kodur 260MC steel

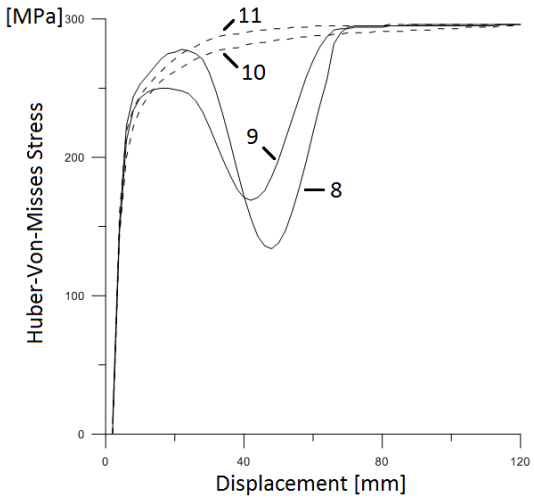

Fig. 15. Evolution of Huber-Von-Misses stress during bending process for steel E235+N

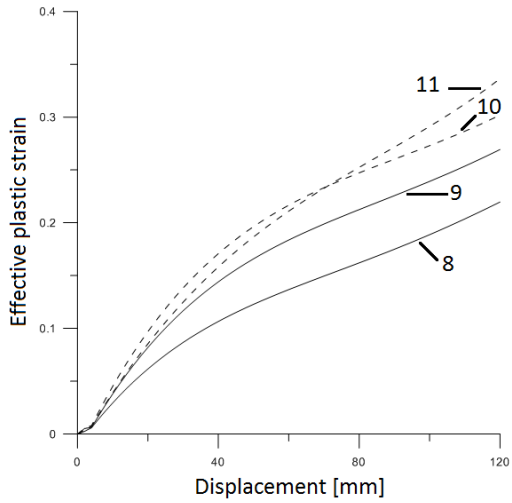

Fig. 16. Evolution of effective plastic strain during bending process for steel E235+N

Fig. 12 presents evolution of effective plastic strain during bending process for steel 1.4313. Lines 8 and 9 show that tensioned points of pipe have similar behaviour of plastic strain. Lines 10 and 11 demonstrate that outside part (point 10) of the pipe was more compressed that inside (point 11).

Fig.14 shows evolution of effective plastic strain for Kodur 260MC steel. Line 10, 9 and 8 have similar characteristic of growth strain. Character of line 11 is different what can be caused by thickening of inside wall of pipe.

Fig. 16 presents evolution of effective plastic strain for steel E235+N with similar characteristic of growth strain with Fig. 14. Different between this two graph is that for steel E235+N extreme compressed and tensile fibers was load with the same force. Received deformation of profile presents Fig 9.

Summarize received results, small change of characteristic strain-stress curve in FEM analysis cause very significant course of evolution effective plastic strain. In Huber-Von-Misses stress that effect not observed. Also for steel 1.4313 observed exceed of maximal value stress and strain. Based on Fig 11 and 12 we can establish maximal protrusion of pattern what not cause undulation in point of largest compressive stress concentration.

5. RESULTS OF VERIFICATION

The results of deformed shapes obtained from experiment and simulation for steel E235+N are presented in Fig. 17. Planar profile from Fig. 17 was created using 2D CAD tools and compared (Fig. 18). Fig. 19 presents radius of bending R and bending angle α.

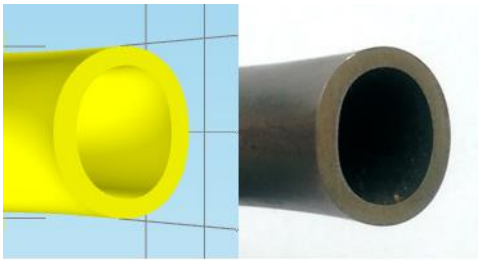

Fig. 17. Results of deformed shapes of pipe obtained from numerical and experimental analyses

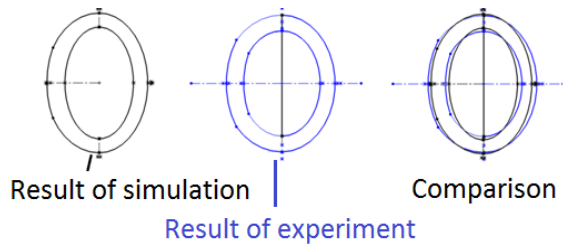

Fig. 18. Results of numerical and experimental analyses

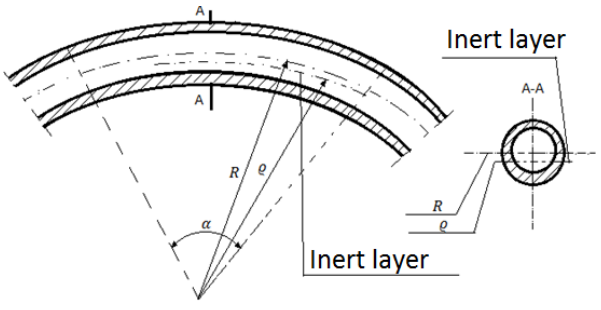

Fig. 19. Bending values during bending pipe process

DOI 10.1515/ama-2017-0007

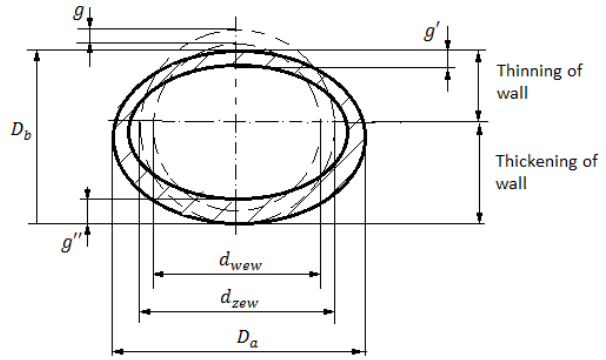

Fig. 20. Deformation of the pipe cross-section during bending

Parameters of deformations during bending pipe process presents Fig. 20. Based on bending parameters from Fig. 20 we can compute two most important parameters of bending pipe process, roundness (1) and relative bending radius (2).

Roundness:

$$e = \frac{D_a - D_b}{d_{zew}} . \quad (1)$$

Relative bending radius:

$$r = \frac{R}{d_{zew}} . \quad (2)$$

This two parameters of bending pipes are normalized for pipes transporting different medium. Small roundness and well matched relative bending radius cause less flow of liquid. Normally this two parameters are selected based on preliminary test bending. The new approach for determination that parameters is FEM analysis of bending pipe process. Comparison of shape parameters obtained from experimental and numerical tests presents Tab. 1.

Tab. 1. Values of numerical and experimental analyses

Parameter of bending	Value of parameter received experimentally	Value of parameter received form simulation	Relative error [%]
D_a major axis of the ellipse [mm]	17	17.5	2.8
D_b minor axis of the ellipse [mm]	14	13.5	3.5
Roundness [%]	18.7	25	25.2
Thinning of wall [mm]	1.8	1.7	5.5
Thickening of wall [mm]	2.1	2.2	4.5

Analysing values of shape parameters show that in four cases the relative error of parameters don't exceed 10%. This four results testifies about that Comsol elasto-plastic module is a good tool for analysing bending pipe process. Roundness normally don't exceed 10% but in this case, main idea was to show deformation seen with naked eye, so received results are out of values in accepted standards. In normal conditions of bending pipes process, roundness is very important parameter for pipes working in higher pressure because determines corrosion resistance in grain boundaries caused by micro-cracks in places of thickening wall emerging under bending pipe process.

6. SPRINGBACK OF PIPE AFTER BENDING PROCESS

The most important problem in CNC bending pipe process is still springback after bending. There is many approach to solve that problem. The scientific papers (Zhao et al., 2011; Zhao et al., 2014) present some analytical and numerical solutions for springback in bending plate and pipe processes. The hot bending pipe process is also solved (Hu,1998) using an analytical approach. The simple idea of solving this problems FEM analysis in Comsol environment which deal with that problem with very good results. Received results taken from experiment of bending angle after springback was about 70º. Results of simulations present Fig. 21, 22 and 23.

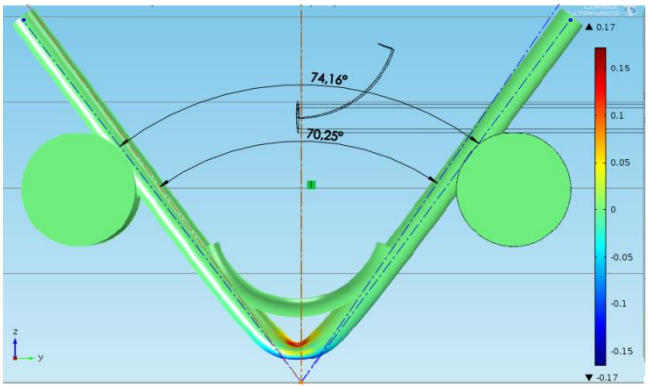

Fig. 21. Springback after bending pipe for steel 1.4313

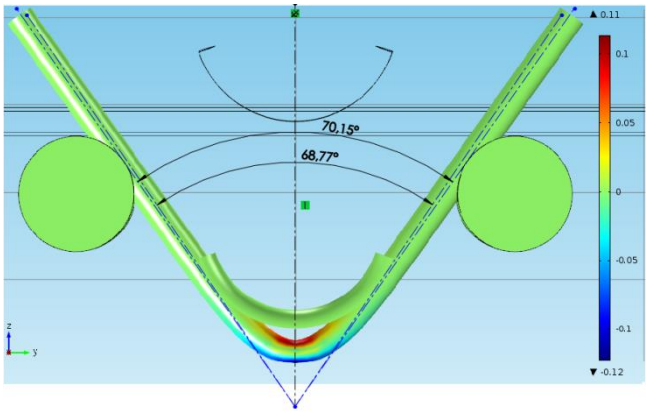

Fig. 22. Springback after bending pipe for steel Kodur 260MC

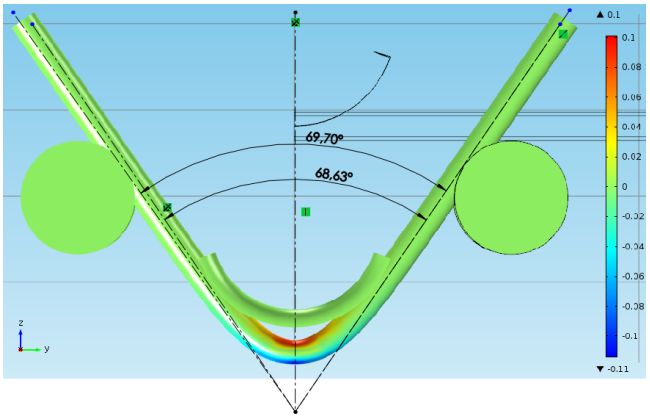

Fig. 23. Springback after bending pipe for steel E235+N

DOI 10.1515/ama-2017-0007

The results of simulation shows Tab. 2. Degree of bending was measured between two axes of symmetry bending pipe.

Tab. 2. Values of numerical analyses of springback

Material of pipe	Value of bending angle at the end of bending [º]	Value of bending angle after springback [º]	Relative difference [%]
E235+N	68.63	69.70	1.5
Kodur 260MC	68.77	70.15	2
Steel 1.4313	70.25	74.16	5.3

Results shown relationship between elasto-plastic material characteristic (type of strain-stress curve) and values of springback If characteristic of strain-stress curve is more steep (Fig. 2) then springback is bigger (steel 1.4313). When characteristic of strain-stress curve is shallow (Fig. 3, 4) springback is lower (steel Kodur 260MC and E235+N). This behaviour of elasto-plastic material during elastic return after unloading is obvious, but determination of springback after bending pipe process using analytical method is very difficult and time-consuming. Numerical results prove that FEM analysis of pipe bending process is a good tool to predict final degree of bending. It is important especially for precise bending process in mass production.

Difference between received results of bending angle from experiment and numerical analysis for steel E235+N is lower than 1%.

7. CONSLUSIONS

Properly selected values of bending process using numerical simulations reduce preparation time and costs. FEM analysis of bending processes require of knowledge a stress-strain characteristic of material. Experimental verification of numerical results based on shape errors comparison gave good results. Expected behavior of elasto-plastic material depending on stress-strain curve character was numerically confirmed. Values of bending angle after springback obtained from experiment and numerical simulation are very close. These conclusions confirm that worked-out FEM model can be used in engineering applications for simulation of ram-press pipe bending process for different kinds of steel.

REFERENCES

1. **Dong L., Huang Y., Dong G.,Zhang Q., Liu G.** (2015), Bending behavior modeling of unbonded flexible pipes considering tangential compliance of interlayer contact interfaces and shear deformations*, Marine Structures,* 42, 154-174.
2. **Dong L., Tu S., Huang Y., Dong G., Zhang Q.** (2015), A model for the biaxial dynamic bending of unbonded flexible pipes*, Marine Structures*, 43, 125-137.
3. **Guarracino F., Walker A.C., Giordano A.** (2008), Effects of boundary conditions on testing of pipes and finite element modeling, *International Journal of Pressure Vessels and Piping*, 86, 196-206.
4. **Hao Y., Jinyuan Q., Sunting Y., Chenghang J., Lin W., Zhi-jiang J.** (2016), Limit bending moment for pipes with two circumferential flaws under combined internal pressure and bending, *International Journal of Mechanical Sciences,* 106, 319-330.
5. **Hu Z.** (1998), Elasto-plastic solutions for spring-back angle of pipe bending using local induction heating, *Journal of Materials Processing Technology,* 102,103-108.
6. **Korzemski J.W. (**1971), *Bending of thin-walled pipes (*in Polish), Wydawnictwo Naukowo-Techniczne,Warszawa
7. **Kuang Y., MorozovE.V., Ashraf M.A., ShankarK.** (2015), Numerical analysis of the mechanical behaviour of reinforced thermoplastic pipes under combined external pressure and bending, *Composite Structures,* 131 453-461.
8. **Li J., Zhou Ch., Cui P., He X**. (2015), Plastic limit loads for pipe bends under combined bending and torsion moment, Int. J. of *Mech. Sciences,* 92, 133-145.
9. **Menshykova M.,Guz I.A.** (2014), Stress analysis of layered thick-walled composite pipes subjected to bending loading*, International Journal of Mechanical Sciences*, 88, 289-299.
10. **Ottosen N.S., Ristinmaa M.** (2005), T*he mechanics of constitutive modeling*, Lund University, Sweden.
11. **Sidun P.** (2015), *Modeling of plastic deformation during bending process at several levels* (in Polish), MSC diploma work, supervisor A. Łukaszewicz, Bialystok University of Technology.
12. **Vasilikis D., Karamanos S.A.** (2012), Mechanical behavior and wrinkling of lined pipes, *International Journal of Solids and Structures,* 49, 3432-3446.
13. **Xue J., Wang Y., Yuan D.**(2015**)** A shear deformation theory for bending and buckling of undersea sandwich pipes, *Composite Structures*, 132, 633-643.
14. **Zhao J., Yin J., Ma R., Ma L.X.** (2011) Springback equation of small curvature plane bending, *Sci China Technol Sci*, 54(9), 2386–2396.
15. **Zhao J.**, **Zhan P., Ma R., Zhai R.** (2014) Prediction and control of springback in setting round process for pipe-end of large pipe, *International Journal of Pressure Vessels and Piping,* 116, 58-62.

This paper was performed within a framework of S/WM/2/2013 realised in Bialystok University of Technology.

DE GRUYTER
OPEN

DOI 10.1515/ama-2017-0008 acta mechanica et automatica, vol.11 no.1 (2017)

FATIGUE TESTING OF DENTAL BRIDGES ON SELECTED EXAMPLES

Dariusz URBAN[*], Marek JAŁBRZYKOWSKI[**], Maria GOŁĘBIEWSKA[*]

[*]Medical University of Bialystok, Faculty of Medicine with the Division of Dentistry, ul. Jana Kilinskiego 1, 15-089 Bialystok, Poland
[**]Faculty of Mechanical Engineering, Department of Engineering of Materials and Manufacturing, Bialystok University of Technology, ul. Wiejska 45C, 15-351 Białystok, Poland,

darurb18@wp.pl, m.jalbrzykowski@pb.edu.pl, protetyk@umb.edu.pl

received 6 June 2016, revised 10 March 2017, accepted 13 March 2017

Abstract: The paper presents example tests of the functional quality of selected designs of dental bridges. These were: porcelain bridges on a metal base (cobalt based alloy), porcelain bridges on a zirconia base (zirconia ceramic – Zirkon Zahn), and full zirconia bridges (Zirkon Zahn). For the purpose of the study, durability of bridges in cyclic fatigue testing was adopted as a measure of their quality. The tests were carried out on a Zwick Roell Z010 universal testing machine. They consisted in cyclic loading and unloading of dental bridges mounted on gypsum models at a loading force of F= 400 [N] and a frequency of load of f= 1 [Hz]. Each bridge was subjected to a cycle of 7200 loads. The results show that there are no significant differences in the functional quality of the bridges.

Key words: Dental Bridges, Ceramics, Durability

1. INTRODUCTION

Many types of materials are used in dental practice, starting from metallic materials, which currently constitute the largest group, through resins and thermoplastic materials, to ceramic materials (Bińczyk, 2003; Craig et al., 2000). Metallic materials are understood as metals and metal alloys, commonly described as dental or prosthetic alloys. The reason for the widespread use of dental alloys is, among others, the fact that they exhibit the highest mechanical strength among all prosthetic materials (Craig et al., 2000; Surowska, 2009). Metal biomaterials and metal-ceramics]. Prosthetic alloys are used for the construction of supporting structures of dental restorations, e.g. skeletons of dentures, which has a decisive influence on their strength. Ceramic materials, used to construct full structures, e.g. zirconia ceramic bridges (Craig et al., 2000; Surowska, 2009; Zhang et al., 2016; Bachhav and Aras, 2011), are currently growing in popularity. Restorations of this kind are characterized by much more beneficial aesthetic qualities in comparison with similar metal-based designs. It should be noted, however, that full ceramic dental restorations are unfortunately characterized by significantly worse mechanical properties, e.g. brittleness, in comparison with metallic designs (Chruściel-Nogalska et al., 2002; Tanasić et al., 2014; Ritzberger et al., 2010; Höland et al., 2009; Höland et al., 2008). Thus, the question arises whether real values of load and deformation of denture structures pose a hazard to the use of ceramic restorations, or there are certain areas in which these states are still safe for structures of this kind. It is also possible that biomechanics and kinematics of micromovements of these structures has an impact on their behaviour in the oral cavity, and for this reason their use is expanding. In this context, in the selection process of the appropriate alloy or dental material (metallic and non-metallic) for constructing the dental restoration, the type and complexity of denture structure should be taken into consideration, as well as the loads that the structure will be subjected to during use. Depending on whether the material is intended for the bridge, crown, or skeleton, it must meet different requirements, pertaining to, for instance, mechanical strength, elasticity, or hardness (Eisenburger and Addy, 2002; Gajdus et al., 2002; Jałbrzykowski, 2016; Żmudzki, 2012; Jałbrzykowski and Kovalova, 2009; Coray et al., 2016; Shemtov-Yona and Rittel, 2016; Shemtov-Yona and Rittel, 2014). Considering the above, this paper presents model durability tests of selected types of dental bridges. The tested bridges were based on metal, zirconia, and full ceramic prosthetic bridges.

2. MATERIALS AND METHODOLOGY OF RESEARCH

Metallic and ceramic dental materials were used for the tests. Own dental bridges constructed in various configurations were prepared to be used as samples for the tests. These were: porcelain bridges on a metal base (cobalt based alloy), porcelain bridges on a zirconia base (zirconia ceramic – Zirkon Zahn), and full zirconia bridges (Zirkon Zahn). Fig. 1 shows examples of the designs used for the tests.

The model durability tests were carried out by means of a Zwick Roell Z010 universal testing machine. They consisted in cyclic loading and unloading of dental bridges mounted on gypsum models (Fig. 2). The bridges were fixed to supporting pillars by means of bone cement. The bridge loading force was F= 400 [N], while the frequency of load was f = 1 [Hz]. Each bridge was subjected to a cycle of 7200 loads. It was assumed that such a cycle roughly corresponds to a year of denture use, during which period each denture is assessed by a dentist, whatever the case.

DOI 10.1515/ama-2017-0008

a)

b)

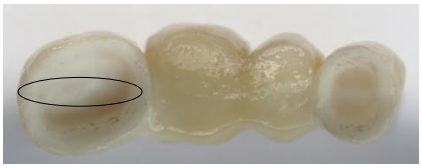

c)

Fig. 1. Prepared dental bridges: a) on a metal base, b) on a zirconia base, c) full zirconia; on the Fig 1a and 1b marked the area of analysis presented in Fig. 4 and Fig. 6.

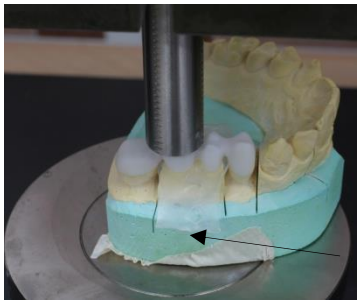

Fig. 2. Method of mounting of bridges for durability tests (full zirconia bridge; the arrow shows the silicone insert)

In case of any irregularities, if they occur at all, the denture is sent for repair (if possible), or constructed again. Before commencing the tests, a thin silicone foil (thickness of approx. 1 [mm]) was placed on the gypsum model, between the supporting pillars ('on toothless bed'), which would model the soft surface under the denture. In addition, after the durability tests, microscope observations of the working surfaces of the bridges were made, in order to look for possible damage. The microscope observations were performed by means of a Hitachi S-3000N scanning microscope.

3. TEST RESULTS

General observations of the experiment showed that the method of load application to the bridge, the value of the loading force, and the cyclical character of the process did not have a significant impact on the behaviour of bridges during their use. Fig. 3 shows example results of the performed measurements.

The data shown in Fig. 3 represent two situations. In the first case, the bridge was mounted directly on the gypsum model. In the second one, i.e. 'on toothless bed', the silicone insert was placed beforehand (Fig. 2). The obtained results show that in the case of the bridge placed directly on the gypsum model (without the silicone insert), it becomes anchored to a lesser extent than in the case of bridges anchored on the silicone insert. This situation seems obvious. It was also noticed that in the case of bridges without the silicone insert, anchoring of the bridge was more stable. In fact, the first cycles led to its natural fit under the load, then they "docked" until the maximum value of anchoring of approx. 0.5 [mm] (Fig. 3a) was reached. In the case of the bridge with the silicon insert, on the other hand, two-stage anchoring occurred. The first stage took place in steps, following a specific hysteresis loop, until a natural fit under the load was achieved. In the second stage, slow "docking" until the maximum value of anchoring of approx. 0.8 [mm] was reached occurred (Fig. 3b).

a)

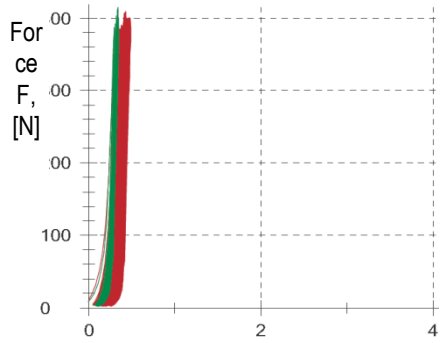

b)

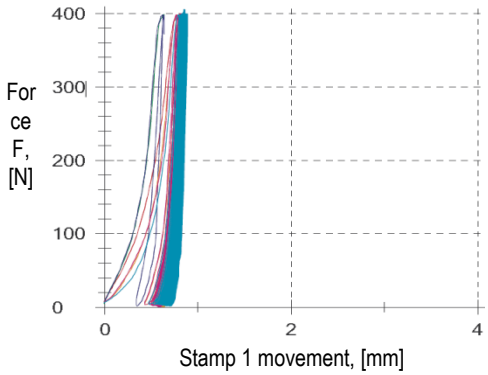

Fig. 3. Results of the test of cyclical loading of bridges a) without silicon insert, b) with the use of silicon insert

In all the analysed cases of bridges, no damage was observed that would render the bridges unfit for further use. All the bridges passed the test successfully and, as far as the tests performed within the framework of this paper are concerned, no differences in the functional quality of the prepared bridges were observed.

After carrying out the durability tests, microscope observations of the working surfaces of the bridges were performed. Fig. 4 shows selected photographs from the microscope analysis of the porcelain bridge on a metal base.

The performed analysis suggests a generally good adhesion of porcelain to the metallic surface (Fig. 4 a-c). However, porous spots and local lack of layer adhesion can be observed, which significantly reduces its properties (Fig. 4 d). Tab. 1 shows the results of x-ray microanalysis of areas shown in Fig. 4.

The chemical composition presented above apply to the metallic surface – Point 1, and the porcelain surface – Point 2. Obviously the contents and proportions of alloy elements vary as

DOI 10.1515/ama-2017-0008

they pertain to two completely different surfaces. However, an analysis of base surfaces was performed in this particular spot, as transition structures of the metallic-porcelain type were sought. With this in mind, an x-ray analysis for the interface area was performed. Its results are shown in Fig. 5.

a)

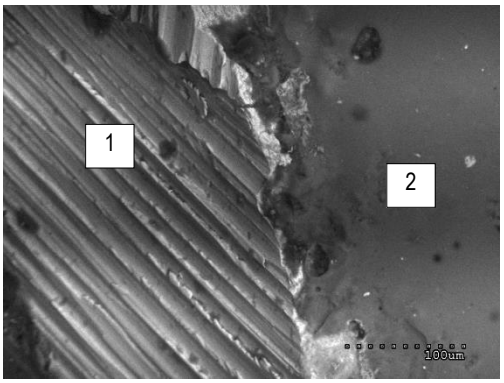

b)

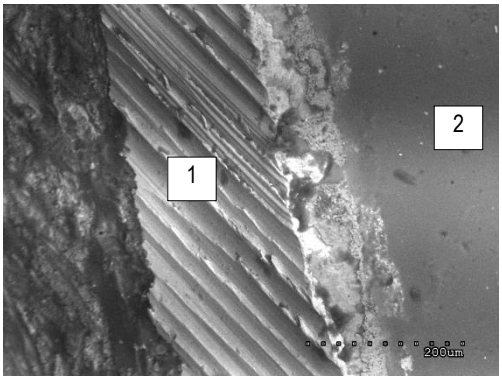

c)

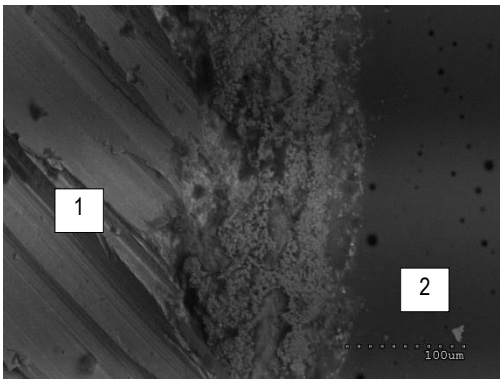

d)

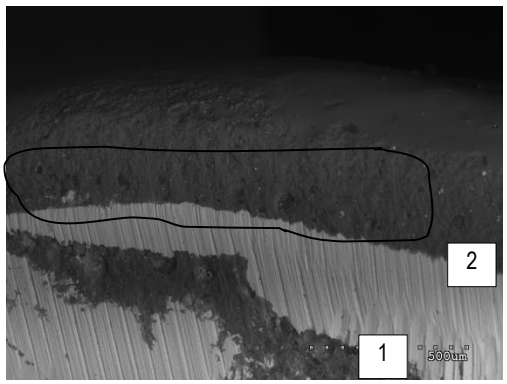

Fig. 4. Microphotographs of a porcelain bridge on a metal base: a) – c) view of the lateral surface on the metal-porcelain interface, d) view of the lateral surface; 1- metal, 2- porcelain

Tab. 1. Results of x-ray microanalysis of a bridge on a metallic base

Alloy elem. cont. [% mass] / Place of analysis	O	Na	Al	Si	K	Ca	V	Cr	Co	W
Point 1	-	-	1.24	2.28	0.73	-	1.96	21.53	55.97	8.42
Point 2	40.22	3.98	6.09	27/64	9.97	1.63	-	0.83	2.74	-
Alloy elem. cont. [% mass] / Place of analysis	**O**	**Na**	**Al**	**Si**	**K**	**Ca**	**V**	**Cr**	**Co**	**W**
The marked square area	29.47	1.90	3.24	12.67	1.93	0.83	0.63	5.84	37.08	3.85

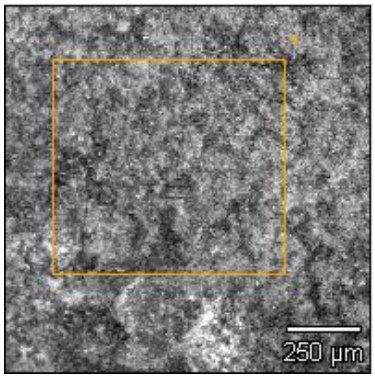

Fig. 5. Results of x-ray microanalysis at the metal-non-metal interface

The results of x-ray analysis from the metal-non-metal interface shown in Fig. 5 indicate the presence of all the elements, both from the metallic and the porcelain areas. This may indicate 'mixing' of the materials and the appearance of new transition structures. It is possible that these new structures acquire the structure of a 'composite' with aggregated properties and this is why the tested dental bridges behave so well in durability tests. It is also possible that the transition structure that appears is an excellent dampener of dynamic actions and through the specific mechanical properties, it allows the structure to work safely in the adopted biokinematic system. A detailed analysis in this area, however, was not performed.

Similar effects were obtained during the analysis of porcelain bridges on a zirconia base. Fig. 6 shows selected photographs of the analysed areas of bridges of this type. Fig. 6a-6c show the surface structure of a bridge at the interface. It can be observed that the rough structure of the zirconia base (Fig. 6b, area marked as 1) is probably a good base for the top porcelain layer (retention through porosity). Moreover, some few pores in the upper porcelain layer were noticed (Fig. 6d). This may be the result of careless porcelain preparation, a faulty porcelain firing process, or other reasons. It should be added that a porous structure of porcelain was also noticed in the case of bridges on a metallic base (Fig. 4d).

Tab. 2 compiles the results of analyses of the chemical composition for the zirconia and porcelain layers.

In the case of the zirconia surface, the main alloy elements are: Zr, O and N. In the case of the porcelain structure, on the other hand, these are: Si, O, K, Al, Na. Knowing what the main alloy elements for these phases are, transition areas were looked for, similarly to the case of the bridge on a metallic base. To achieve this, an analysis of the areas marked in Fig. 7 were performed.

DOI 10.1515/ama-2017-0008

a)

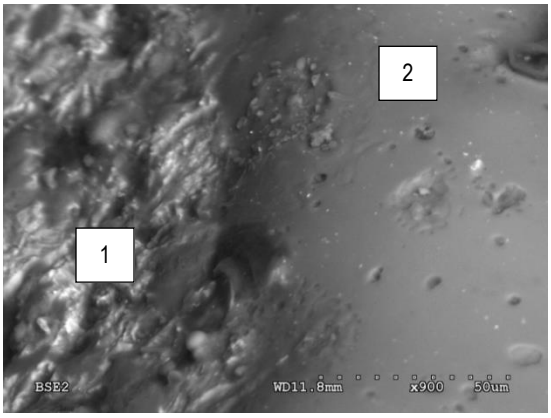

b)

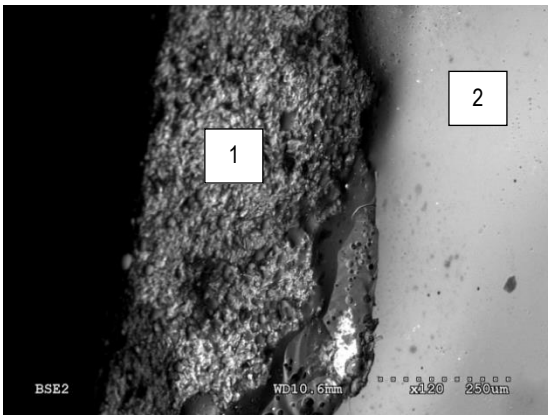

c)

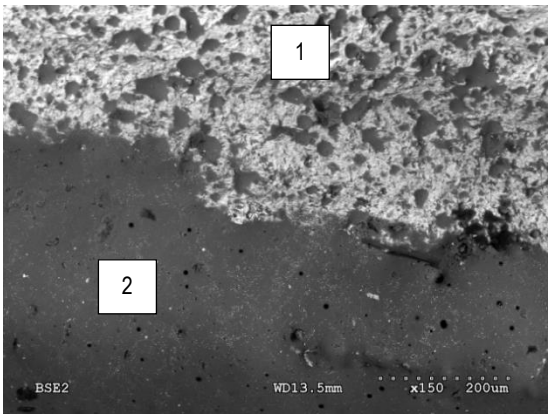

d)

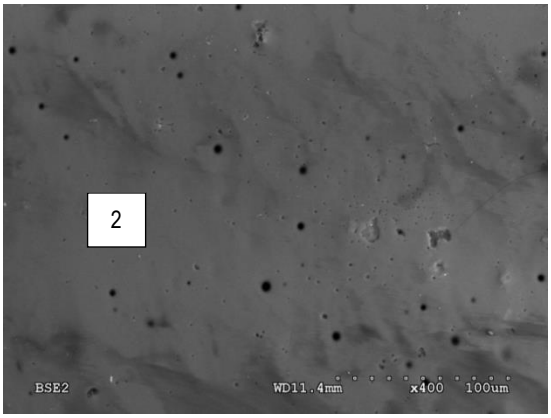

Fig. 6. Selected microphotographs of the surface of a porcelain bridge on a zirconia base: a)-c) pictures at the zirconia-porcelain interface, d) porous surface of the porcelain phase; 1 – zirconia phase, 2 – porcelain phase

Tab. 2. Results of chemical composition analysis

Alloy elem. cont. [% mass] / Place of analysis	N	O	Al	K	Ca	Y	Zr
Zirconia surface	4.98	29.01	1.22	0.20	0.22	2.51	51.81
Alloy elem. cont. [% mass] / Place of analysis	O	Na	Al	K	Ca	Si	Ba
Porcelain surface	41.45	6.41	5.85	9.29	2.86	28.74	3.12

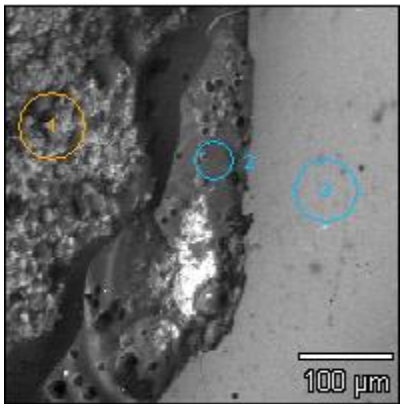

Fig. 7. Places of analysis of chemical composition – porcelain bridge on a zirconia base

Tab. 3 shows the results of analyses for the areas marked in Fig. 7. Analysing the results in Tab. 3, mixing of chemical compositions of the basic structures can generally be noted, probably caused by harmonizing porcelain penetrating micropores of the zirconia base. A curious issue, however, is the total absence of signal from the presence of the zirconia phase. It is possible that porcelain covers the zirconia layer very tightly. In order to better understand the issue of creation of transition structures, transverse metallographic specimens cutting through two phases perpendicular to the increase of their thickness should have been prepared. A detailed analysis at this stage, however, was omitted.

Tab. 3. Results of tests of chemical composition of areas from Fig. 7

Alloy elem. cont. [% mass] / Place of analysis	O	Na	Al	Si	P	Cl	K	Ca	Ti	Ba
Area "1"	44.95	3.46	4.56	15.59	8.52	0.29	3.70	2.69	-	-
Area "2"	45.80	7.75	5.69	25.03	0.92	0.21	5.57	1.90	0.07	1.28
Area "3"	33.13	7.48	4.36	27.48	0.88	1.04	7.79	2.01	0.45	3.39

4. CONCLUSIONS

The performed tests and their analysis allowed to formulate the following general conclusions:

– Results of the model durability tests did not reveal significant differences in the behaviour of the tested dental bridges. All designs (on metal, zirconia, and full zirconia bases) passed the test successfully with no discernible damage

DOI 10.1515/ama-2017-0008

- When performing the tests attention was paid to the dual character of bridge anchoring. In the first case, slow constant anchoring of the bridge until the maximum value of approx. 0.5 [mm]. In the second case, anchoring occurred at two stages. First, anchoring in steps that followed a hysteresis loop down to approx. 0.6 [mm] took place. Then, similarly to the first case, slow constant anchoring occurred until the value of. 0.8 [mm] was achieved.
- The character of anchoring probably depends on susceptibility of the bed on which the bridge is anchored.
- Analysis of the chemical composition of selected areas of bridges indicates the presence of regions with a chemical composition that comprises elements from the metallic and the non-metallic phases. This may indicate the creation of transition structures which contain both phases. It is possible the newly formed structure acquires the character of a composite with combined properties and has a beneficial impact on the behaviour of brittle porcelain on a susceptible metallic base. This issue, however, was not analysed.
- Microporosity of the top layer of porcelain was noted, both on metal- and zirconia-based bridges. This may be the result of careless porcelain preparation, a faulty porcelain firing process, or other reasons, however, this is not was analyzed.

REFERENCES

1. **Bachhav, V.C., Aras, M.A.** (2011), Zirconia-based fixed partial dentures: a clinical review, *Quintessence International*, 42 (2), 173-182
2. **Bińczyk F.** (2003), *Structural cast alloys*, Wydawnictwo Politechniki Śląskiej, Gliwice.
3. **Chruściel-Nogalska M., Światłowska M., Uchacz H.** (2002), Analysis of the reasons for damage of removable mucous-borne dentures anchored on the basis of clinical material, *Protetyka Stomatologiczna*, LII, 3, 62-166.
4. **Coray, R., Zeltner, M., Özcan, M.** (2016), Fracture strength of implant abutments after fatigue testing: A systematic review and a meta-analysis, *Journal of the Mechanical Behavior of Biomedical Materials*, 62(1), 333-346.
5. **Craig R. G., Powers J. M., Wataha J. C.** (2000), *Dental Materials*, Wydawnictwo Urban&Partner, Wrocław.
6. **Eisenburger M., Addy M.** (2002), Radiological examination of dental castings – a review of the method and comparisons of the equipment, *Journal of Oral Rehabilitation*, 29(7), 609-614.
7. **Gajdus P., Hędzelek W., Joniak S.** (2002), Assessment of mechanical strength of palatal plates – cast cobalt chrome and acrylic reinforced with steel mesh, *Protetyka Stomatologiczna*, LII, 6, 362-367.
8. **Höland, W., Rheinberger, V., Apel, E., Ritzberger, C., Rothbrust, F., Kappert, H., Krumeich, F., Nesper, R.** (2009), Future perspectives of biomaterials for dental restoration, *Journal of the European Ceramic Society*, 29 (7), 1291-1297.
9. **Höland, W., Schweiger, M., Watzke, R., Peschke, A., Kappert, H.** (2008), Ceramics as biomaterials for dental restoration, *Expert Review of Medical Devices*, 5(6), 729-745.
10. **Jałbrzykowski M.** (2016), The influence of type and design of denture attachment on its efficiency of operation in model tests, *Key. Eng. Mater.*, 687, 185-190.
11. **Jałbrzykowski M., Kovalova E.** (2009), The problems of exploitation reliability estimation of dental prosthetics elements, *Solid State Phenomena*, 147-149, 794-800.
12. **Ritzberger, C., Apel, E., Höland, W., Peschke, A., Rheinberger, V.M.** (2010), Properties and clinical application of three types of dental glass-ceramics and ceramics for CAD-CAM technologies, *Materials*, 3(6), 3700-3713.
13. **Shemtov-Yona, K., Rittel, D.** (2016), Random spectrum loading of dental implants: An alternative approach to functional performance assessment, *Journal of the Mechanical Behavior of Biomedical Materials*, 62(1), 1-9.
14. **Shemtov-Yona, K., Rittel, D.** (2014), Identification of failure mechanisms in retrieved fractured dental implants , *Engineering Failure Analysis,* 38, 58-65.
15. **Surowska B.** (2009), *Metal biomaterials and metal-ceramics connections in dental applications*, Wydawnictwo Politechniki Lubelskiej, Lublin, 9-13.
16. **Tanasić, I., Šojić, L.T., Lemić, A.M.** (2014), Biomechanical interactions between bone and metal-ceramic bridges composed of different types of non-noble alloys under vertical loading conditions, *Materiali in Tehnologije*, 48(3), 337-341.
17. **Zhang, Z., Chen, J., Li, E., Li, W., Swain, M., Li, Q.** (2016), Topological design of all-ceramic dental bridges for enhancing fracture resistance, *International Journal for Numerical Methods in Biomedical Engineering*, 32(6), 1, 1-13.
18. **Żmudzki J.** (2012), *Material conditionings of functional efficiency of mucous-borne complete denture, Open Access Library, Volume 4/10, 1-176.*

This research was realized from 123-08 839L and statutory activity S/WM/1/14 financed by MSHE

DOI 10.1515/ama-2017-0009

DETERMINATION OF CUTTING FORCES IN GRINDING WITH CROSSED AXES OF TOOL AND WORKPIECE

Volodimyr KALCHENKO*, Andrij YEROSHENKO*, Sergiy BOYKO*, Nataliia SIRA*

*Chernihiv National University of Technology, Mechanical Engineering Department, 95 Shevchenko street, Chernihiv, Ukraine

vvkalchenko74@gmail.com, yeroshenkoam@gmail.com, svboyko.cstu@gmail.com, nnseraya@ukr.net

received 6 May 2016, revised 10 March 2017, accepted 13 March 2017

Abstract: In the work the analysis of existent methods of determination of local and general forces of cutting at polishing of surfaces with a type as the arc of circumference is given. The dependence for determination of speed polishing and method for determination of thickness of the cut away layer on condition of equality of the tricked into and taken off volumes of material are offered. The method of determination of cutting forces, which takes into account cutting and deforming grain, is suggested. The method of determining the thickness of a cutting layer of one of the cutting edge, from the condition that the volume of material that is brought and is cut in each local point of contact spots has been proposed. The proposed method takes into account the compliance of the processing system and the discontinuity of the abrasive surface of the tool. By experimental way upper limits of thickness cutting layer when using different abrasive materials for a wide range of cutting speeds have been obtained.

Keywords: Cutting Forces, Grinding, Deforming Grain, Cutting Edge, Abrasive Surface, Abrasive Materials, Crossed Axes, Abrasive Grain, Cut Volumes, Grinding Wheel

1. INTRODUCTION

Application in manufacturing of the new methods of grinding requires the development of more accurate methods for calculating of cutting forces. There are two methods of determining the constituents of cutting forces: an empirical and calculated-experimental. The first method is based on measuring the cutting force by dynamometers, when grinding samples with the following obtaining empirical relationships. However, empirical relationships can only be used for calculations in the conditions close to the experimental, that limits their use. Calculation-experimental method defines a single force acting on the one cutting edge. After that the number of cutting edges, which are located in the contact zone of the abrasive wheel with the workpiece are determined, and then the resulting cutting force is calculated (Chang et al., 2008; Hecker, Rogelio, 2007).

Existing methods of determining of cutting forces (Malkin and Guo, 2008; Yeroshenko, 2009) do not take into account the influence of deforming grains, the oscillation power in the local areas of the contact patch, the rigidity of the processing system and intermittent surface of the wheel. The calculated volume of material that is removed by the cutting edge does not conform the volume which is fed to the cutting zone(Yeroshenko, 2009; Chen et al., 2007; Chee Keong Ng, 2006). This is explained by the fact that when determining of cutting forces the average value of a cut off volume is calculated and thus a material that is removed at the local site of the contact patch is not considered.

Thus, the aim of the work is the determination of local and total cutting forces based on the equality of supplied and cutting volumes, taking into account static compliances of processing systems and discontinuous of the tool surfaces.

2. DETERMINATION OF THE CUTTING LAYER THICKNESS

For reaching of the set goal, it is necessary to determine the layer thickness a_z, which is cut by one edge. The equation for determining the thickness of a cut off layer is the fundamental equation of grinding. The layer thickness determines the load on the grain, resistance and maximum cutting ability of the abrasive tool, the wear of the abrasive grains, the quality and depth of scratches on the workpiece. By experimental way upper limits azmax of thickness cutting layer when using different abrasive materials for a wide range of cutting speeds have been obtained. The slice thickness and their shape are determined by the kinematics of the process, the number and shape of the edges, that take part in the work of grinding (Kalchenko and Yeroshenko, 2009;Yeroshenko, 2008).

The main kinematic indicators that characterizes the process of cutting in the local point of contact patch is the ratio of V_n/V_s, where $V_n = \vec{V} \cdot \vec{n}$ – the projection of the relative speed of $\vec{V}$ on the normal $\vec{n}$ to the surface of the tool; V_g – grinding speed (the projection of relative speed $\vec{V}$ on the surface of instrument).

It must be noted that, while processing of parts with a profile in the form of a circular arc, the grinding speed along generatrix of profile is variable. The oscillation of speed along the profile becomes significant with a reduction ratio R_t/ρ_t (Fig. 1). Based on Fig. 1, the rate of grinding in the j-th point can be determined by the formula:

$$V_{gj} = \frac{2\pi(R_t+\rho_t \cdot cos\varphi_{tj})\cdot n}{1000} \quad (1)$$

where: n – rotational speed of wheel; R_t – radius of the center of the circle profile; ρ_t – the radius of the circle profile; φ_{tj} – the

DOI 10.1515/ama-2017-0009

angular coordinate of the tool.

There are two approaches to the definition of cutting layer thickness:

- a kinematic approach considers the cut geometry in the plane normal to the cutting surface (Yeroshenko, 2009; Stepien, 2007), asking the average distance between the cutting edges;
- a volumetric approach involves determining of the average volume of the slice and taking its shape and the average number of cutting edges on one surface of the wheel, finding its thickness (Yeroshenko, 2009;Kalchenko et al., 2012).

When calculating the cutting layer thickness it is necessary to provide cutting of all material that is fed into the processing zone. Since the location of the grain on the tool surface is chaotic, and they have a different shape, you must use a volume approach. The shape of the cutting edge (Fig. 2) has the shape of a cone with an apex angle α = 90-160° and a radius of curvature ρ(Yeroshenko, 2009; Chae et al., 2006).

The slice area equals the cross sectional area of abrasive grains and depends on the thickness of slice a_z, the radius of curvature ρ of the cutting edge and the selected variant of the slice form (Yeroshenko, 2009; Chae et al., 2006). Fig. 3 shows this dependence for ρ = 0 (curve 1) and ρ = 80 microns (curve 2).

At scoping, which is cut off by a cutting blade it is necessary to take into account the stiffness of the treated system, since the elastic deformation of the system machine-detail lead to additional errors. The stiffness of the treated system can be taken into account through pliability $y_s = f(\varphi_{tj}, K_s)$, which is a function of the angular position of a point on the profile φ and coefficient static compliance K_s.

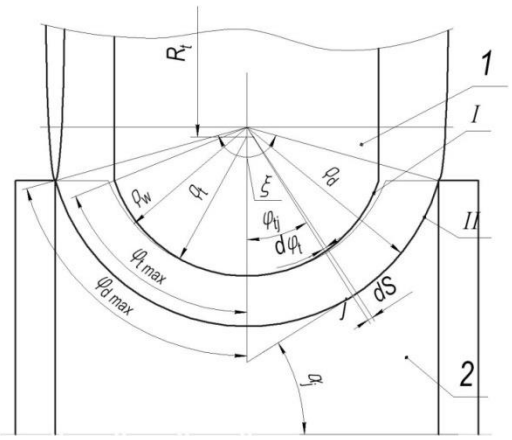

Fig. 1. Processing with crossed axes tool and workpiece with a profile in the form of a circular arc (ρ_d – radius of the detail profile; ξ – the central angle of the detail profile; ρ_w – radius of the workpiece profile; φ_{tmax} – the max angular coordinate of the tool; φ_{dmax} – the max angular coordinate of the detail; α_j – tilt angle of the tangent to the circle surface at the point j; $d_{\varphi t}$ – angular coordinate increment; 1 – wheel; 2 – detail; I - starting position of the wheel; II - final position of the wheel)

In passing from one cutting edge to the elementary portion of wheel dS one must considere the nonuniformity surface of an abrasive tool. It is possible to take into account the discontinuity surface of the wheel, by the usage of coefficient: $\left[1 - \exp\left(-\frac{\Sigma b(t,\theta)}{b_0}\right)\right]$ (Yeroshenko, 2009).

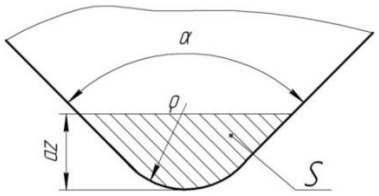

Fig. 2. The shape of the abrasive grain

Thus, in the grinding on the elementary area dS (Fig. 4) per unit time it is fed $(V_n - y_s) - \left[1 - exp\left(-\frac{\Sigma b(t,\theta)}{b_0}\right)\right] dS$ of the material. During the same time dSarea, the surface of which has $N_z(a_z)$ cutting edges, removes $N_z(a_z) \cdot V_s(\varphi_{tj}) \cdot S(a_z, \rho)$ of material. Based on the condition of the equality of the removed and cut volumes, you can create an expression:

$$(V_n - y_s) \cdot \left[1 - exp\left(-\frac{\Sigma b(t,\theta)}{b_0}\right)\right] \cdot dS = N_z(a_z) \cdot V_s(\phi_{tj}) \cdot S(a_z, \rho) \quad (2)$$

where: $N_z(a_z)$ – number of cutting edges on a given level a_z and disposed on the unit area of a wheel, which participate in the cutting of metal; $S(a_z, \rho)$ – sectional area of the abrasive grain. From the expression (2) it is determined the generalized equation of the shear layer:

$$\frac{(V_n - y_s)}{V_s(\phi_{tj})} = \frac{N_z(a_z) \cdot S(a_z, \rho)}{\left[1 - exp\left(-\frac{\Sigma b(t,\theta)}{b_0}\right)\right] \cdot dS}. \quad (3)$$

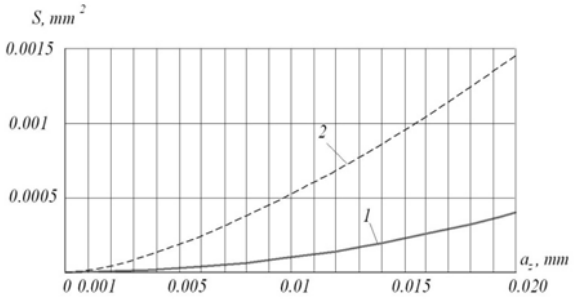

Fig. 3. The dependence of a cut off layer area from the slice thickness and the radius of edge curvature

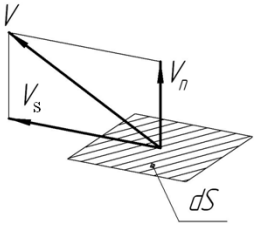

Fig. 4. The scheme for determining the thickness of a cut off layer

The abrasive grain, which is located on the working surface of the wheel, it is accepted to characterize by a number of parameters. Thus, according to modern concepts (Heinzel and Bleil, 2007;Yan and Lan, 2009), it is necessary to specify:

- The location of the top level of the grain regarding the level of the most protruding grains;
- Corner radius grain ρ.

DOI 10.1515/ama-2017-0009

The density of the probability location of the cutting edge fN(x), at the level z from the outer surface of the wheel, can be described by the law beta distribution (Yeroshenko, 2009):

$$f_N(x) = A \cdot t^{\gamma-1} \cdot (1-t)^{\eta-1} \quad (4)$$

where: $x = \frac{z}{h_n}$ – equivalent level of the grinding wheel, on which it is determined $f_N(x)$; A, n, γ, η – the parameters of the beta distribution; h_n – the total height of the profile of the grinding wheel.

The total number of cutting edges on level x can be determined (Yeroshenko, 2009; 2008):

$$N_z(x) = N_n \cdot A \cdot \int_0^{z/h_n} t^{\gamma-1}(1-t)^{\eta-1}\mathrm{dt}, \quad (5)$$

where:$N_z(x)$ – the number of cutting edges on a unit area on the level x; N_n – total number of cutting edges along the entire height $\mathrm{h_n}$ profile on the unit area.

Similarly we define the probability density of the radii distribution of the cutting edges curvature ρ:

$$f_\rho(x) = A \cdot t^{\gamma-1} \cdot (1-t)^{\eta-1} \quad (6)$$

where: $x = \rho/\rho_{max}$ – relative radius of curvature of the cutting edge; ρ_{max} – the maximum radius of the cutting edge.

Dependence 5 for grinding wheel AA-70-K7-V35 is shown in Fig. 5.

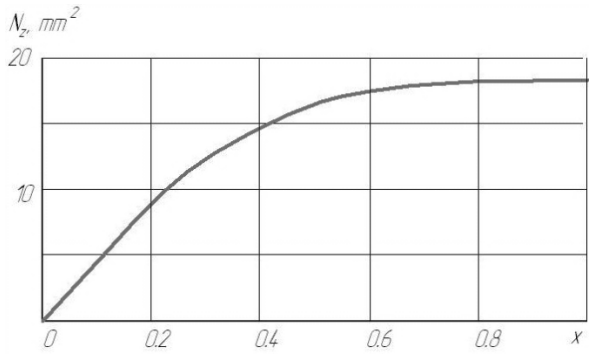

Fig. 5. The distribution of the number of cutting edges and fillet radii

However, not all cutting edges remove metal themselves. Some of them deform the metal elastically or plastically. It is considered (Ng and Chee Keong, 2006; Oliveira, 2009) that the criterion for cutting is the ratio z/ρ. To determine the minimum value of this ratio it is used experimental dependence (Ng and Chee Keong, 2006; Oliveira, 2009), which describes the minimum thickness of the cut layer, depending on the radius of curvature of the top of the grain and the cutting speed. In this case the minimum value of the ratio the cutting process is still going on. By approximating the experimental dependence by the exponential function (Yeroshenko, 2009; 2008), you can record it in the general form:

$$\frac{z}{\rho} = B \cdot \rho^{-\alpha} \cdot V_s^{-\beta}(\phi_{\mathrm{tj}}) \quad (7)$$

where:B, α, β – empirical coefficients determined depending on the material, the material of tool and workpiece.

Taking into account (7), you can obtain the dependence that will serve as a lower limit of the determination of the probability of cutting grain at depth *z* in the *j*-th point (Fig. 6):

$$z = B \cdot \rho^{1-\alpha} \cdot V_s^{-\beta}(\phi_{\mathrm{tj}}). \quad (8)$$

As the grinding speed $V_s(\varphi_{tj})$ is in a function at dependence of the angular position of point j, it will vary within the generatrix profile and thus it will change the depth z in the range of z_{min} to z_{max}, which correspond $V_s(\varphi_t = 0)$ and $V_s(\varphi_{tmax})$. Changing of the depth z along generatrix length of a profile will lie within area bounded by two curves in Fig. 6.

Statistical research of the work surface parameters (Yeroshenko, 2009; Nguyen and Butler, 2005; Brinksmeire, 2006) based on the density distribution found that the grains which deform metal in the cutting area is significantly greater than those that cut (area under the graph in Fig. 6).

Edges which are disposed below the metal level of penetration z in the grinding wheel, are involved in metal processing. Level z depends on the attitude and takes different values for each point of the contact patch. That's why, this scheme is given for a specific point of a contact patch, but rather for a specific relationship $\frac{(V_n - y_s)}{V_s(\varphi_{tj})}$. Lines $z(\rho, V_s)$ divide the edge of the abrasive grains to the cutting and deforming.

Graph analysis allows to state that while an increase of cutting speed the minimum thickness of cutting layer decreases. Since certain values of the depth z, the proportion of grains, which are involved in metal cutting, increases considerably. At shallow depths of cut the grain particle that is involved in cutting, should have only the smallest values of the radius of curvature of the cutting edge. After some time of operation, due to the occurrence of wear areas this share is shrinking.

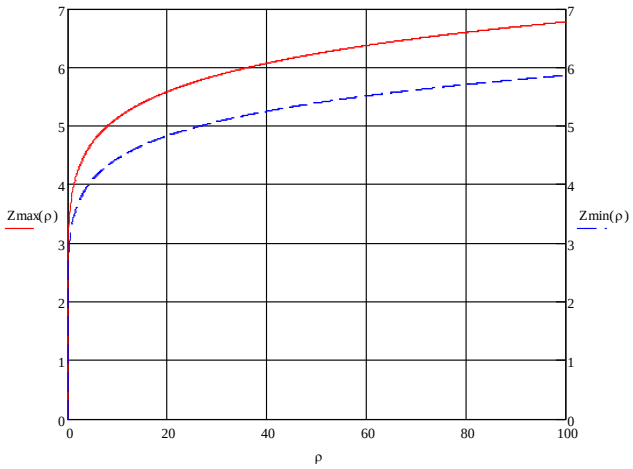

Fig. 6. Graph of the dependence of depth z, which defines the beginning of the cutting process by the edge of the abrasive tool

3. THE NUMBER OF CUTTING AND DEFORMING EDGES

The number of cutting and deforming edges which fall on the surface of the wheel unit can be determined by the following relationships (Yeroshenko, 2009):

$$N_z^p = \iint_{S_c} N_n \cdot f_N(z) \cdot f_\rho(\rho) \cdot \mathrm{ds}, \quad (9)$$

$$N_z^D = \iint_{S_d} N_n \cdot f_N(z) \cdot f_\rho(\rho) \cdot \mathrm{ds}, \quad (10)$$

where: S_c and S_d – the area in Fig. 7 which correspond to the cutting and deforming edges respectively.

DOI 10.1515/ama-2017-0009

Removal of metal provides exactly cutting edge, so it is of their number will depend on the thickness ofa cut off layer. Therefore, the equation (3) must be written in the form:

$$\frac{(V_n - y_s)}{V_s(\phi_{tj})} = \frac{N_z^p(a_z)\cdot S(a_z,\rho)}{\left[1-\exp\left(-\frac{\Sigma b(t,\theta)}{b_0}\right)\right]\cdot dS}. \quad (11)$$

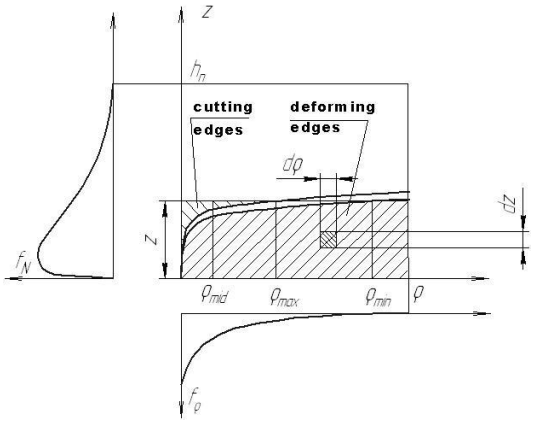

Fig. 7. Distribution of cutting and deforming edges in the contact patch

To determine the thickness of a cut off layer it is necessary to know the average radius of curvature of the grain edges, which take part in cutting at a given point in the contact patch. To simplify the calculations we assume:

$$\rho_{\text{mid}} = \frac{\rho'}{3} \quad (12)$$

where: ρ'- the coordinate of the intersection of levels with a line-level $z(\rho, V_s)$, or ρ_{max} when $\rho' > \rho_{max}$.

The dependence of a cut off layer thickness a_z on the ratio $\frac{(V_n - y_s)}{V_s(\varphi_{ij})}$ can be determined by joint decision of 4,6,8,9,11,12 equations. The graph of this dependence is shown in Fig. 8.

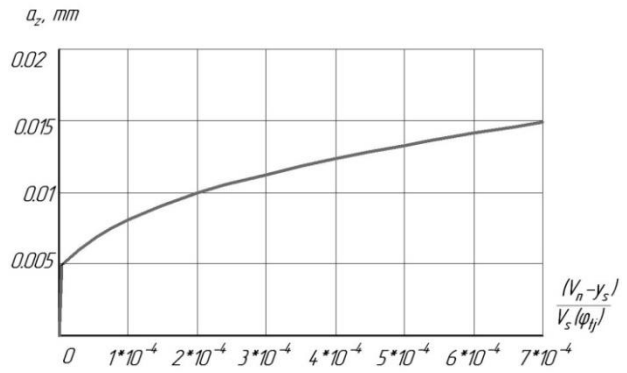

Fig. 8. The dependence of the thickness of a cut off layer a_z on the ratio $\frac{(V_n - y_s)}{V_s(\varphi_{ij})}$

Knowing the dependence $az\frac{(V_n - y_s)}{V_s(\varphi_{tj})}$ can obtain from the formulas (9) and (10) dependences $N_z^c\left(\frac{(V_n - y_s)}{V_s(\varphi_{ij})}\right)$ and $N_z^d\left(\frac{(V_n - y_s)}{V_s(\varphi_{ij})}\right)$, which graphs are shown in Fig. 9.

4. DETERMITATION OF THE CUTTING FORCES

It is considered (Yeroshenko, 2009) that the separate cutting edge is under action of the shear force P_{sd}, friction P_f and inertia P_{in}. Dependence to determine the normal and tangential forces acting on the cutting edge, taking into consideration these components are given in work of Yeroshenko, 2009. Total cutting force is determined by integrating of the microcutting forces on the contact patch surface based on cutting and deforming grains.

From the foregoing, the total tangential $P_z^{\Sigma}$and normal P_n^{Σ}cutting force can be determined by dependencies:

$$P_z^{\Sigma} = \iint_s P_z^c \cdot n_c(z,\rho)\cdot dS + \iint_s P_z^d \cdot n_d(z,\rho)\cdot dS, \quad (13)$$

$$P_n^{\Sigma} = \iint_s P_n^c \cdot n_c(z,\rho)\cdot dS + \iint_s P_n^d \cdot n_d(z,\rho)\cdot dS \quad (14)$$

where:P_z^c, P_z^d – forces which act in the tangential direction, respectively, on the cutting edge and deforming; n_c, n_d – number, respectively, of cutting and deforming edges on the elementary area dS; P_n^c, P_n^d – forces that operate in the normal direction, respectively, on the cutting edge and deforming; S – the spot of the contact area of the wheel and the parts.

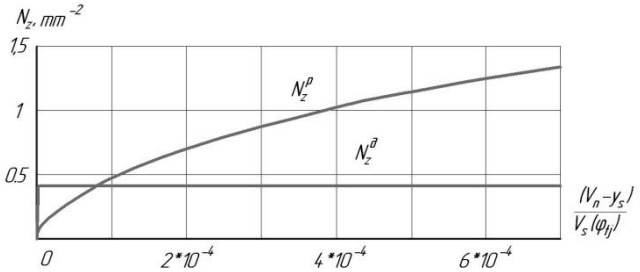

Fig. 9. The dependence of the number of cutting and deforming edges from the ratio $\frac{(V_n - y_s)}{V_s(\phi_{tj})}$

The shape and size of the contact area depends on the surface treatment process with a profile in the form of a circular arc. The calculation of the contact line of a part and a grinding wheel carried out by the method described in work of Yeroshenko (2009). Spot contact is the region bounded by the contact line and the cross-section of the grinding wheel, shifted by the amount of feed, the workpiece. In the traditional infeed grinding (Yeroshenko, 2009), when the radius of the tool ρ_t equals the profile radius of the machined workpiecepw and processing is done only with cross feed, the form of contact area will be almost a rectangle projected on the treated surface (Fig. 10). Contact area is bounded by a line contact 1, along which the shaping surface of the workpiece is done and on which the length $V_n = 0$, and the output line of the grinding wheel 2, a maximum value V_n. On each side the contact area is limited to links section of the grinding wheel with the workpiece with outer cylinder 3, and 4.

When processing with crossed axes tool and workpiece with a profile in the form of circular arcs machining is produced by a spiral of Archimedes. Permanent of Archimedean spiral, in which the relative motion moves the wheel with renting of allowance $\delta_{is}a = \frac{t}{2\pi}$. The line and the contact area of the spot with this method of processing have a spatial form (Fig. 10), and the radius of the line projection on the axial of the plane of contact during final shaping surface of a part is equal to the radius profile of a part.

Volodimyr Kalchenko, Andrij Yeroshenko, Sergiy Boyko, Nataliia Sira
DOI 10.1515/ama-2017-0009

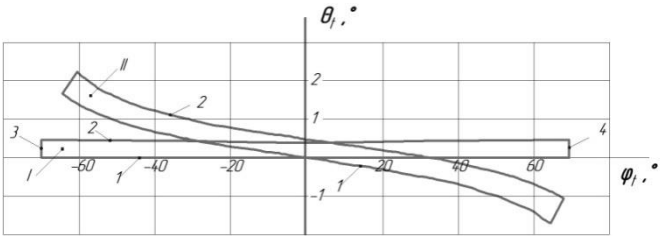

Fig. 10. The contact spots (I) with traditional and the new (II) methods of surface treatment with a profile in the form of a circular arc

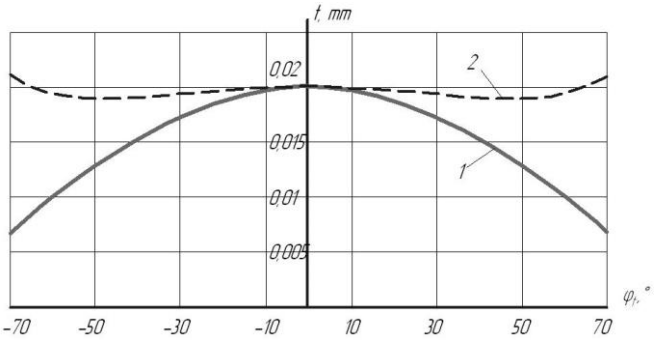

Fig. 11. Allocation of machining allowance that is cut off in one revolution of the workpiece, on the arc chute

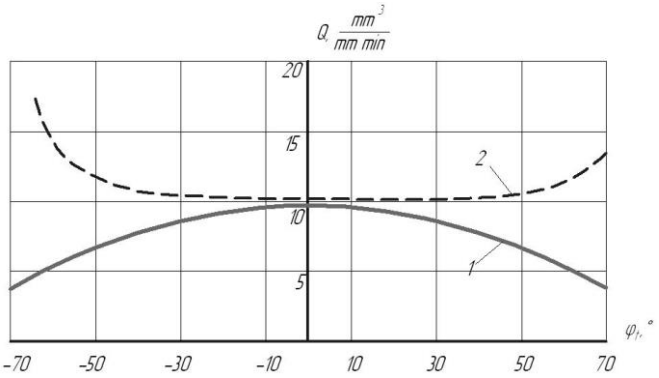

Fig. 12. Distribution of specific grinding performance on the arc chute

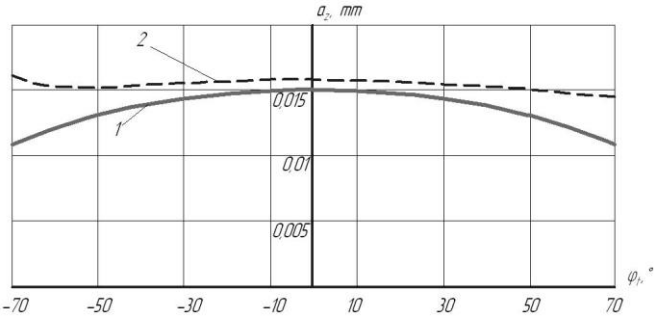

Fig. 13. Distribution of a cut off layer thickness by a cutting edge on the output line of the grinding wheel of the machining allowance

The allowance, cut in one revolution of the workpiece (Fig. 11) is defined as the distance between the workpiece and the part surface. Curve 1 illustrates the processing of the traditional way, curve 2 – processing with crossed axes of a tool and workpiece.

Immediate grinding performance that describes the volume of material which is removed by the contact line is defined by the expression:

$$Q = \int_{-\phi_{tmax}}^{+\phi_{tmax}} \left(\int_{\theta_{1kj}}^{\theta_{2kj}} (\overline{V}_j \overline{n}_j - y_s) \cdot (R_t + (\rho_t - W_j) cos\varphi_{tj} \left[1 - exp\left(-\frac{\Sigma b(t,\theta)}{b_0} \right) \right] \cdot d\theta_k \right) \cdot \sqrt{\left(\frac{dR_{\varphi_{tj}}}{dj}\right)^2 + \left(\frac{d\varphi_{tj}}{dj}\right)^2} \cdot d\varphi_t \quad (15)$$

where: $\pm\,\varphi_{tmax}$ – limiting value of angular position φ_{tj} of point j of the wheel profile; $\theta_{1kj}, \theta_{2kj}$ – angular coordinates of the contact patch on the radius $(R_t + \rho_t \cdot cos\phi\varphi_{tj}) - W_j \cdot cos\varphi_{tj} = R_t + (\rho_t - W_j) \cdot cos\varphi_{tj}$ – volumetric wear wheel at the point j; $\bar{V}_j, \bar{n}_j$ – vectors of the cutting speed and the normal to the j-th point of the wheel; $y_s = f(\varphi_{tj}, K_s)$ - compliance of the processing system; K_s – the value of the static compliance; R_t – the distance from the axis of rotation of the wheel to the center of its profile $\rho_t$radius; $R_{\varphi_{tj}} = R_t + \rho_t cos\varphi_{tj}$ – radius of rotation j-th point.

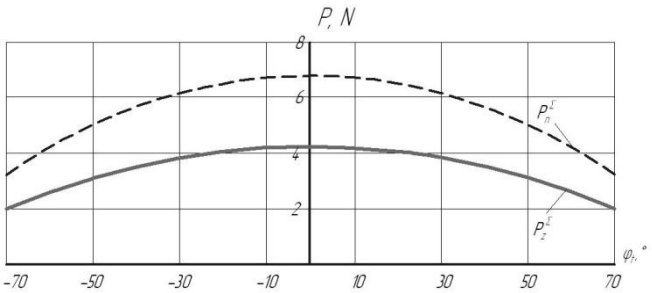

Fig. 14. Distribution of specific grinding force on the arc of the profile of the grinding wheel for the traditional method of processing

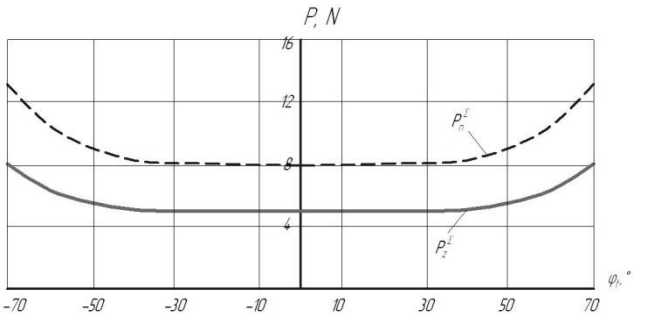

Fig. 15. Distribution of specific grinding force in an profile arc of wheel

Distribution of specific grinding performance, which is described by the inner integral of expression (15) in an arc chute for a traditional processing (curve 1) and the new method (curve 2) are shown in Fig. 12.

As, each cutting edge deforms a metal, the thickness of the shear layer of one of the cutting edge increases gradually from zero to a maximum value at the exit point of the wheel from machining allowance and can be determined from equation (11). The distribution of the shear layer thickness of one cutting edge on the output line of the grinding wheel of the machining allowance for grinding the two methods are shown in Fig. 13.

The specific grinding force i.e. a force that falls on the unit

DOI 10.1515/ama-2017-0009

of the wheel height is determined by integrating the forces of microcutting (9, 10) along the contact patch of the entrance point to the exit point of the range of machining allowance. The distribution of normal P_n and tangential P_z cutting forces along the arc profile of the grinding wheel, for traditional and new methods are shown in Figs. 14 and 15, respectively.

5. CONCLUSIONS

For the first time it has been proposed a method of determining the thickness of a cutting layer of one of the cutting edge, from the condition that the volume of material that is brought and is cut in each local point of contact spots. The proposed method takes into account the compliance of the processing system and the discontinuity of the abrasive surface of the tool.

According to calculations performance of grinding with crossed axes tool and workpiece is higher by reducing the value of infeed, which in this way is equal to the machining allowances. With this method of grinding allowance is cut by equidistant curves, which provides a constant cutting depth. In the traditional method of processing the cutting depth decreases from the center to the edges of the trough (Fig. 11).

The specific grinding performance remains substantially constant within a central angle of 100º, whereas in the traditional method it decreases from the center to the edges of the trough (Fig.12). This provides more uniform volume tool wear generatrix length of a profile.

Processing with crossed axes tool and parts with a profile in the form of a circular arc is especially effective in processing of precise parts, such as rings of ball screw with a central angle of up to 100º.

It is also possible to use a new method for grinding rollers for cold rolling of tubes in which the profile of the central angle exceeds 100º. From the Fig. 13 the thickness a cutting layer of one cutting edge remains virtually constant, which ensures consistent load on the grain. The increase in the specific performance on the edges of the trough is explained by the increase of contact area along the axis θ_t (Fig. 10).

REFERENCES

1. **BrinksmeireE.** (2006),Advances in modeling and simulation of grinding processes,*Annals of the CIRP*, 55,667-696.
2. **ChaeJ., ParkS.S., Freiheit T.** (2006),Investigation of micro-cutting operations. *International Journal of Machine Tools & Manufacture*, 46,313-332.
3. **Chang, H.-C., Junz Wang, J.-J.**(2008),A stochastic grinding force model considering random grit distribution,*International Journal of Machine Tools & Manufacture*, 48, 1335-1344.
4. **Chee Keong Ng , Shreyes N. Melkote, M. Rahman, A. Senthil Kumar.**(2006), Experimental study of micro- and nano-scale cutting of aluminum 7075-T6,*International Journal of Machine Tools & Manufacture*, 46, 929-936.
5. **Chen M., LiX., Yang, P.** (2007),Study on surface grinding-hardening of SKD11 hardened steel,*International Journal of Manufacturing Technology and Management,* 12, 236-245.
6. **HeckerRogelio L.** (2007),Grinding force and power modeling based on chip thickness analysis,*International Journal of Advanced Manufacturing Technology*, 33, 449-459.
7. **HeinzelC., BleilN.** (2007),The use of the size effect in grinding for work-hardening. *Annals of the CIRP*, 56, 327-330.
8. **Kalchenko V.V., YeroshenkoA.M.** (2009),Determination of the efficiency of grinding with crossed axes tool and workpiece with a circular profile, *Journal of The National Technical University 'Kharkiv Polytechnic Institute', technologies.*– Kharkiv, 1, 52-56.
9. **Kalchenko V.I.,KalchenkoV.V.,Pohiba N.N.** (2012),Determination of cutting forces in the process of deep grinding surfaces of rotation by oriented elbor wheel, *Journal "Super hard materials,* 2, 58-73.
10. **Lan Yan, Xuekun Li, Feng Jiang, Zhixiong Zhou, Yiming (Kevin) Rong.**(2009), Research on microscopic grain-workpiece interaction in grinding, Part 2 – Factorial Analysis. *Advanced Materials Research*, 76-78, 15-20.
11. **MalkinS., GuoC.** (2008),Grinding technology – Theory and applications of machining with abrasives, *New York: Industrial Press.*
12. **Nguyen,T. A., Butler, D. L.** (2005),Simulation of precision grinding process, part 1: generation of the grinding wheel surface,*International Journal of Machine Tools & Manufacture*, 45,1321-1328.
13. **Oliveira, J.F.G.** (2009),Industrial challenges in grinding,*Annals of the CIRP*,1-18.
14. **Stepien P.** (2007),Grinding forces in regular surface texture generation*, International Journal of Machine Tools & Manufacture*, 47, 2098-2110.
15. **Yeroshenko A.M.** (2008),Theoretical and experimental studies of the grinding process with crossed axes tool and the part of the profile curves in a circle, *Journal of Chernihiv State Technological University*, 35,5-24.
16. **Yeroshenko A.M.** (2009),*Increase of efficiency of polishing with the crossing axes ofinstrument and detail with a type as the arc of circumference*, The thesis for a scientific degree in specialty – machining processes, machines and tool, National Technical University.

DE GRUYTER
OPEN

DOI 10.1515/ama-2017-0010

ANALYSIS OF FORCE IN MR FLUIDS DURING OSCILLATORY COMPRESSION SQUEEZE

Wojciech HORAK[*], Bogdan SAPIŃSKI[**], Marcin SZCZĘCH[*]

[*]AGH University of Science and Technology Faculty of Mechanical Engineering and Robotics, Department Department of Machine Design and Technology, al. Mickiewicza 30, 30-059 Kraków, Poland
[**]AGH University of Science and Technology, Faculty of Mechanical Engineering and Robotics, Department of Process Control, al. Mickiewicza 30, 30-059 Kraków, Poland

horak@agh.edu.pl, deep@agh.edu.pl, szczech@agh.edu

received 19 April 2016, revised 10 March 2017, accepted 13 March 2017

Abstract: This study investigates the behaviour of MR fluids in the oscillatory compression squeeze mode. Experiments were performed on commercially available MR fluids in the purpose-built experimental set-up. The influence of MR fluid's properties and magnetic flux density on the force generated during the squeeze mode was investigated.

Key words: Mr Fluid, Oscillatory Squeeze Mode, Force, Experiment

1. INTRODUCTION

Magnetorheological (MR) fluids are categorised as smart materials whose properties vary under the influence of external magnetic fields. MR fluids contain ferromagnetic particles 0.1 to 10 μm in diameter suspended in a carrier fluid. In most engineering applications the carrier fluid is a mineral or synthetic oil. Additionally MR fluid particles are covered with a surfactant to enhance the sediment stability and to prevent particle aggregation.

In the absence of magnetic field MR fluids display rheological properties that are typical of non-homogeneous suspensions. In the presence of magnetic field, the structure of MR fluid gets changed and its rheological characteristics will change as well (Wang and Liao, 2011; Zubieta et al., 2009).

The direction of the fluid flow and that of magnetic field action are interrelated, hence several modes of MR fluid operation can be distinguished: the flowing mode, the sheer mode, squeeze mode and the gradient pinch mode (Gołdasz and Sapiński, 2015). So far only the flow-mode and shear-mode devices have been successfully commercialised. To the author's best knowledge, there are few studies exploring the behaviour of MR fluids in the squeeze mode and the involved phenomena (Farjoud et al., 2009; 2011; Chaoyang et al., 2013; Kuzhir et al., 2008; Mazlan et al., 2007). Moreover, no hardware handling the squeeze mode operation has been reported beyond the academia so far, with just one exception (Kim, 2014).

In the squeeze mode the working gap height varies in the direction parallel to that of the magnetic field. As the distance between the opposing surfaces changes, the fluid is squeezed out. The model of MR fluid behaviour in the squeeze mode is shown in Fig. 1. In the absence of magnetic field, the magnetic moments of particles have haphazard directions and the fluid will not exhibit any magnetic properties. In the presence of magnetic field and at the constant gap height h, magnetic moments of particles are arranged along the magnetic field lines H. That happens as a result of particles' rotating in the carrier fluid (Brownian mechanism) or due to the moment being rotated within the particle structure (Neel mechanism) (Kuzhir et al., 2008). Particles in the carrier fluid are arranged in column-like structures. When squeezed (displacement Δh, see Fig. 1c) the structures get deformed whilst their thickness are increased (Horak, 2013; Tao, 2001). Thus MR fluid provides increased resistance to compressive loading and its yield stress tends to increase (Sapiński and Szczęch, 2013; Tao, 2011).

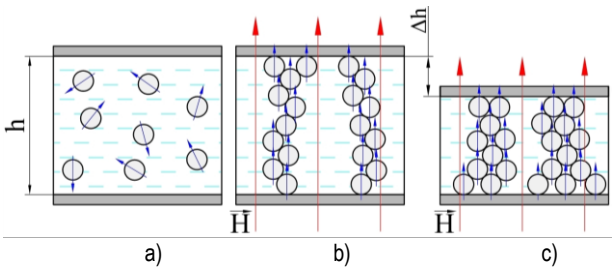

Fig. 1. MR fluid behaviour: a) in the absence of magnetic field; b) under magnetic field; c) in squeeze mode

In the oscillatory compression squeeze mode, MR fluids may tend to exhibit the clumping behaviour (Farjoud et al., 2008; 2011), and the carrier fluid between the particles tends to precipitate (Sapiński et al., 2014). The clumping behaviour consists in particles' being aggregated. In the case of fluid precipitation beyond the squeeze zone, the particles are retained in the zone exposed to magnetic field. Both effects are manifested in the macro scale by an increase in the squeeze resistance in the repeated load cycles.

Due to complexity of phenomena involved in the squeeze mode the analysis of this mode of MR fluid operation is fraught with difficulties. No mathematical model has been developed yet providing a comprehensive description of the MR fluid behaviour in the squeeze mode. There are two distinct approaches to the

DOI 10.1515/ama-2017-0010

modelling of MR fluid behaviour in the squeeze mode: that associated with the quasi-static input (Farjoud et al., 2008; Horak, 2013; Sapiński et al., 2013) and dynamic input (Chen et al., 2016).

The parameter that is of primary importance in investigations of the MR fluid behaviour in the squeeze mode is the compression force. Major determinants of this force include the volumetric fraction of particles, compression rate, magnetic flux density, particle shape and their magnetic properties (particularly the saturation magnetisation). Viscosity of the carrier fluid is of great importance too as it affects the resistance to the ferromagnetic particles' motion. Further, the presence of a surfactant covering the particles affects the magnitude of the friction force between the particles.

This study summarises the results of investigations of selected MR fluids during the oscillatory compression squeeze with the constant contact surface. No MR fluids are available on the market dedicated for squeeze mode operation exclusively, hence the testing was done on samples of MR fluids recommended by manufacturers for use in vibration dampers. This study is the continuation of the authors' research work (Sapiński et al., 2013). The purpose of the study was to find out how the force acting during the oscillatory quasi-static squeeze should vary in time. Furthermore, the behaviours of various MR fluids operated in that mode were compared and analysed.

2. INVESTIGATED FLUIDS

Testing was done on three MR fluids: Basonetic 2040, Basonetic 4035 and MRF-122EG. Basonetic fluids were manufactured by the BASF (http://www.basonetic.com/) company and MRF-122EG by the LORD Corporation (http://www.lord.com/). Properties of those fluids are compiled in Tab. 1.

Tab. 1. Properties of investigated MR fluids

No	MR fluid	Density	Dynamic viscosity B=0 mT, $\dot{\gamma}$=100 1/s, t=25°C	Saturation magnetization
		g/cm^3	mPa·s	kA/m
1	Basonetic 4035	2.68	106	417
2	Basonetic 2040	2.47	956	418
3	MRF-122EG	2.38	127	359

MR fluids Basonetic 4035 and MRF-122EG have a similar zero-field dynamic viscosity (indicating the similar viscosity of the carrier fluid) but differ significantly in the level of saturation magnetisation. Basonetic 4035 and Basonetic 2040 display a similar level of saturation magnetisation, however, Basonetic 2040 features a higher dynamic viscosity than Basonetic 4035.

3. EXPERIMENTAL SET-UP

Tests were performed in the experimental set-up described in Salwiński et al. (2014). Device and incorporating a test cell, and shown schematically in Fig. 2. The key component is a frame (Fig. 2a) supporting a linear servo motor 1 enabling the position of the measuring plate to be altered with the accuracy of 1 μm. A force sensor 2 is attached to the motor, used for measuring the tensile and compression forces. The sample of the MR fluid was placed inside the test cell 3.

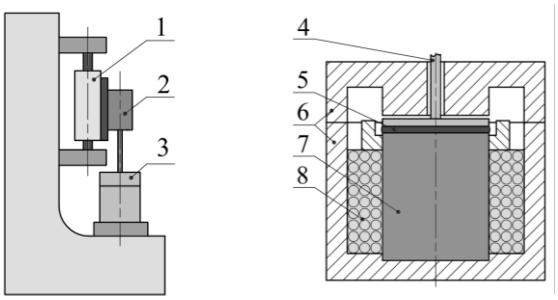

Fig. 2. Schematic diagram: a) experimental set-up; b) test cell

The investigated sample of MR fluid 5 was placed between the electromagnet cores 7 and a mobile plate made of a paramagnetic material 4. The magnetic circuit is closed by the cell housing 6. The magnetic flux density is altered by varying the current intensity in the electromagnet coil 8. Grooves are provided in the electromagnet core and in the housing to allow the flow of the cooling agent, which ensures the temperature stabilisation of the system. All experiments were conducted at the temperature 25°C. A PC with the dedicated software LabView enables the control of position and speed of the linear motor and steering of the electromagnet power supply, as well as data acquisition.

The test geometry is shown in Fig. 3. A mobile plate with the diameter 45 mm was placed between the electromagnet core and the cell housing, having identical diameter. The height of the gap between the core 7 and the cover 6 is g=10 mm. The initial height of the gap is h_0= 1 mm, and the volume of sample V_s=1.6 ml. The maximal plate displacement during compression is Δh=0.2 mm.

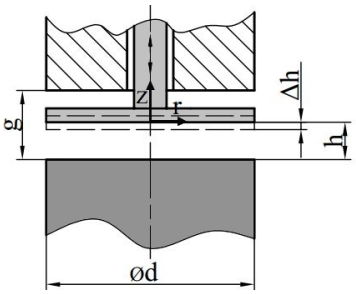

Fig. 3. Schematic of test geometry

Experiments were performed in the presence of the magnetic field with the flux density B: 70, 100, 140, 200 and 270 mT. The kinematic input was applied through the control of plate displacement Δh. The displacement pattern was taken to be trapezoidal, with the frequency f=0.1 Hz, corresponding to the velocity of the plate motion v= 0.04 mm/s. In accordance with the reference system (Fig. 3) the compressing force registered during the squeeze is assumed to have the negative sign.

4. RESULTS

In order to directly compared the plots of force registered at varied levels of magnetic flux density, the measurement data had to be corrected accordingly. For the given value of flux density, the constant force component was determined, expressed as the force acting when the plate was in its initial position (Δh=0 mm). The result correction consisted in subtracting thus deter-

DOI 10.1515/ama-2017-0010

mined constant component from the force registered in time.

The constant force components values are summarised in Fig. 4. Higher values are registered for MR fluids that exhibit higher saturation magnetisation. This issue is described in more detail elsewhere (Horak, 2013; Salwiński and Horak, 2012).

Fig. 5 summarises force measurement data for Basonetic 4035, corrected accordingly. Variations of the plate positions Δh are indicated on the plot. After correction, the measured force becomes F=0 N for t=0 s, regardless of the actual value of flux density.

For clarity, the force variation cycle is divided into 5 intervals (Fig. 5): A-B- compression squeeze; B-C- the mobile plate being stopped in its bottommost position Δh=0.2 mm (fluid being maximally compressed); C-D- returning to the plate's initial position. This interval is further sub-divided into: C-F0- time interval between the onset of the plate's upward movement and the instant the force value becomes zero for at least one of the fluids (the mobile plate moves and the gap becomes larger), F0-D- the time required for the plate to return to its initial position Δh=0 mm. The last interval D-A'- the plate being stopped in its initial position. Starting from the point A', the squeezing cycle is repeated.

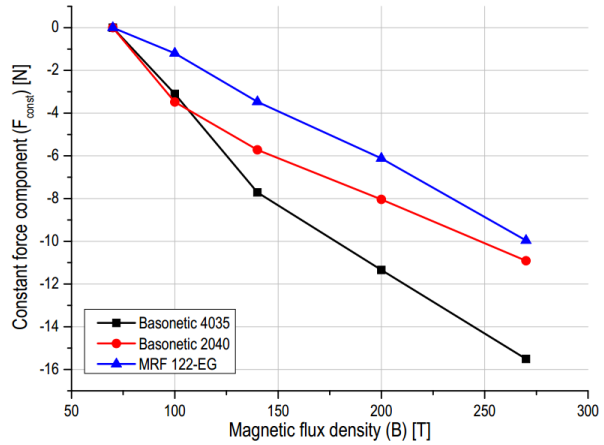

Fig. 4. Constant force component vs magnetic flux density

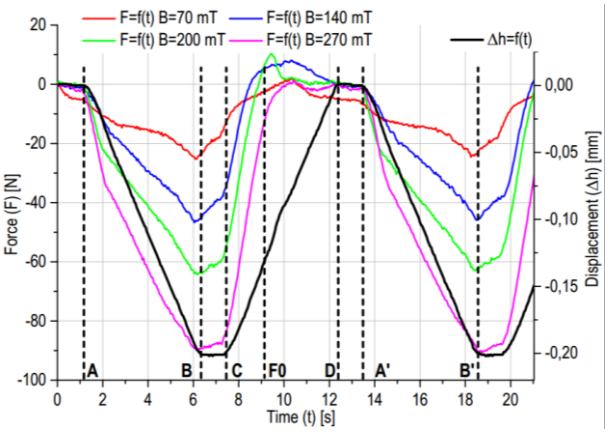

Fig. 5. Selected force plots (Basonetic 4035)

To adequately describe the force variability range in particular intervals, the force gradient value was determined expressed as the slope of the linear function approximating the force variability pattern.

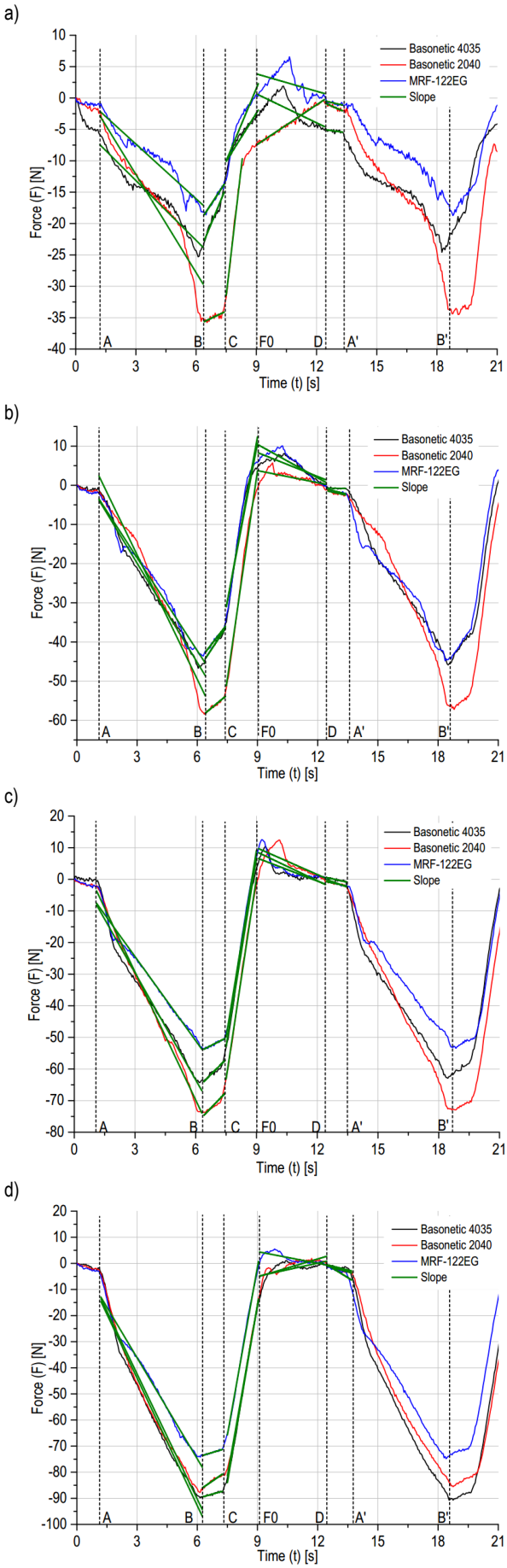

Fig. 6. Force vs time: a) 70 mT; b) 140 mT; c) 200 mT; d) 270 mT

DOI 10.1515/ama-2017-0010

Plots of force registered in particular intervals and the indicated sections of approximating linear functions are shown in Fig. 6a-d. Graphic representation of the slope values is given in Fig. 7.
During the compression squeeze (interval A-B) the compressing force increases nonlinearly (Fig. 6). The highest value of the force gradient for all magnetic flux density levels is registered for the fluid Basonetic 2040. Similar to Basonetic 4035, this fluid features the high saturation magnetisation, yet unlike Basonetic 4035, its zero field viscosity is much higher. For the flux density B=270 mT a slightly higher force gradient is registered for the fluid having a similar saturation magnetisation yet featuring a lower zero-field viscosity- Basonetic 4035 (Fig. 7d).

In the time interval corresponding to the plate being stopped in its bottommost position (B-C) and at the lowest level of magnetic flux density, the smallest force gradient is registered for Basonetic 2040.

a)

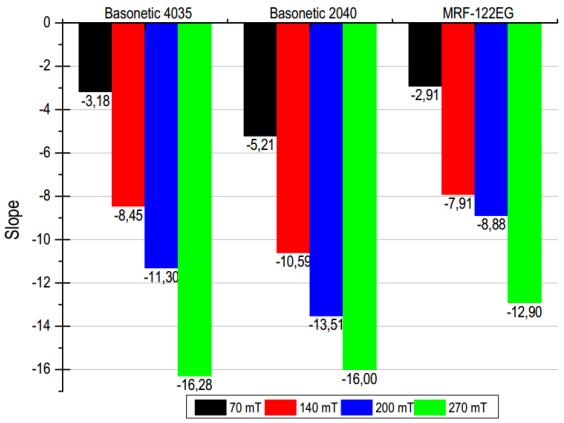

b)

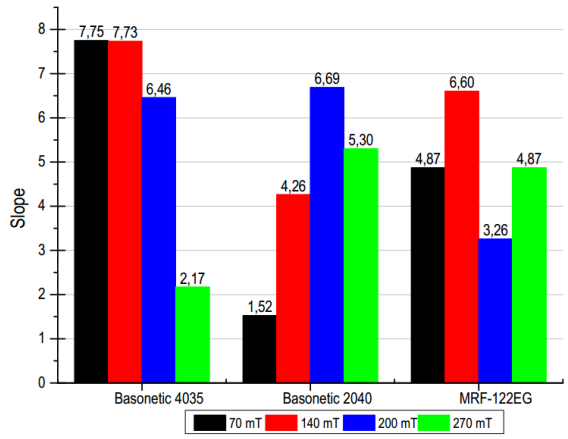

c)

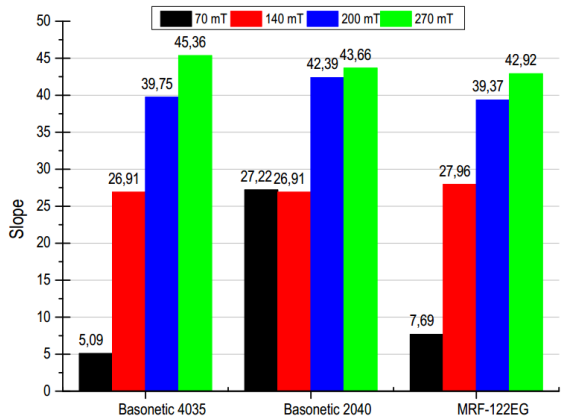

d)

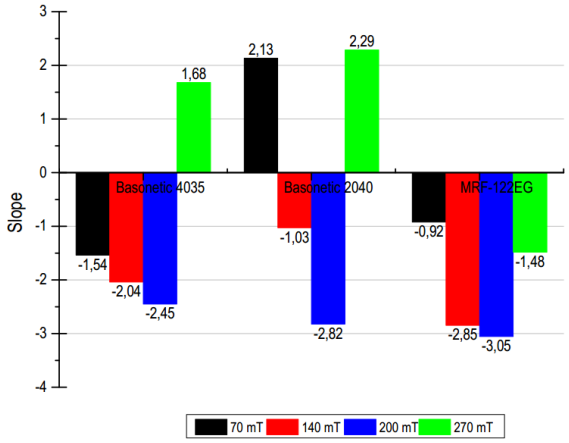

e)

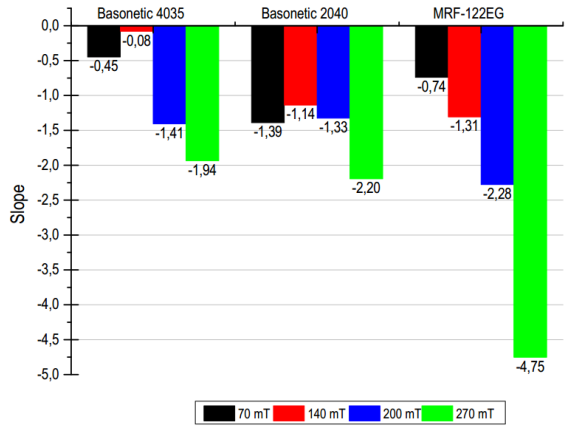

Fig. 7. Slope of force plots in the ranges: a) A-B; b)B-C; c) C-F0; d) F0-D; e) D-A'

When the magnetic flux density is the highest, the smallest gradient of force is registered for Basonetic 4035 (Fig. 7b). It is worthwhile to mention that the force gradient in the interval B-C ranges from 1.5 to more than 7.5 N/s, which implies force reduction by as much as 10% of its maximal value per second.

The gradient of compressing force during the phase when the plate moves upwards to its initial position (C-F0) is significantly higher than the force increase during compression squeeze. The higher the magnetic flux density, the greater this difference in force (Fig. 7 a, c).

The force pattern registered in the interval F0-D is the most complex. Whilst the plate moves upwards, the tensile force arises (the positive sense of the force vector) whose magnitude will then decrease (Fig. 6a-d).

One has to bear in mind that interpolating the force plot in this interval with a straight line section leads to a major simplification, yet giving us an insight into a general trend of force variations.

At flux density B=140 and 200 mT all investigated fluids would exhibit a similar pattern of force variability. In the interval F0-D (Fig. 6b,d) there is a decrease in the tensile force. The higher the magnetic flux density, the greater the force gradient (Fig. 7d).

The experiment performed at the lowest flux density level (B=70 mT) revealed that in the entire sample tension interval, the value of the compressing force in the fluid of highest initial viscosity (Basonetic 2040) would decrease (Fig 6a).

During the experiments taken at B=270 mT the compressing force decreased for the two Basonetic fluids whilst for MRF-122EG it was the tensile force that decreased.

DOI 10.1515/ama-2017-0010

In the interval D-A' the compressing force increased for all investigated fluids. The higher the magnetic flux density, the faster the rate of force increase (Fig 7e).

5. CONCLUSIONS

To a certain extent, the changes of force measured in all investigated cases follow a similar pattern. In the first interval (A-B) there is a nonlinear increase of the compressing force. The highest gradient of the compressing force is registered for the fluid featuring the highest saturation magnetisation and highest zero-field viscosity (Basonetic 2040). An exception is the measurement taken at 270 mT, in this case the highest value is registered for Basonetic 4035.

When the plate is retained in its bottommost position (interval B-C), the compressing force will decrease in all investigated cases. In the case of fluid displaying low zero-field viscosity and high magnetisation (Basonetic 4035) decrease of the force value was more intensive for lower magnetic field strength through a reverse trend is revealed in the case of Basonetic 2040 which has a similar saturation magnetisation but is based on a high-viscosity carrier fluid (Fig. 6a).

During the return motion of the plate (C-D), the compressing force falls rapidly in the first phase (C-F0). For the investigated fluids, the compressing force during the return movement of the plate changes 2 or 3 times faster than the force increase during the squeeze. The higher the magnetic flux density, the faster the force decrease proceeds (Fig. 7c). In all cases considered in the study, during the further stage of the return motion (F0-D), the tensile force will arise and its value tends to decrease while the plate is approaching its initial position. This force can be partly caused by the fluid being sucked back, due to negative pressure produced during the upward movement. Most probably this force is also attributed to the fluid moving in the radial direction with respect to the plate axis during the tensile phase whilst the field gradient in the area of MR fluid application causes the fluid to move beyond the compression zone, due to the presence of an opening in the upper chamber.

In the last interval (D-A'), the compressing force increases when the plate is stopped in its initial position. The higher the magnetic flux density, the faster the force increase (Fig. 7e). The force which pushes the plates away from one another may be attributed to rebuild of column-like structures of particles contained in MR fluids.

REFERENCES

1. **Chaoyang G., Xinglong G., Shouhu X., Lijun Q., Qifan Y.** (2013), Compression behaviors of magnetorheological fluids under nonuniform magnetic field, *Rheologica Acta*, 52(2), 165–176.
2. **Chen, Peng and Bai, Xian-Xu and Qian, Li-Jun** (2016), Magnetorheological fluid behavior in high-frequency oscillatory squeeze mode: Experimental tests and modelling, *Journal of Applied Physics*, 119, 105101.
3. **Farjoud A., Cavey R., Ahmadian M., Craft M.** (2009) Magneto-rheological fluid behaviour in squeeze mode, *Smart Materials and Structures*, 18, 095001.
4. **Farjoud A., Craft M., Burke W., Ahmadian M.** (2011), Experimental investigation of MR squeeze mounts, *Journal of Intelligent Material Systems and Structures*, 22, 1645–1652.
5. **Farjoud A., Vahdati N., Fah Y.** (2008), MR-fluid yield surface determination in disc-type MR rotary brakes, *Smart Materials and Structures*, 17(3), 1-8.
6. **Gołdasz J., Sapiński B.** (2015), *Insight into Magnetorheological Shock Absorbers*, Springer International Publishing, Switzerland.
7. **Horak W.** (2013), *Theoretical and experimental analysis of magnetorheological fluid squeeze flow*, PhD Thesis (in Polish), AGH University of science and Technology, Krakow.
8. **Kim J. H.** (2014), *Damping force control filled with magnetorheological fluids and engine mount having the same*, US Patent, No. US 8,672,105 B2.
9. **Kuzhir P., Lopez-Lopez M. T., Vertelov G., Pradille Ch., Bossis G.** (2008), Oscillatory squeeze flow of suspensions of magnetic polymerized chains, *Journal of Physics: Condensed Matter*, 20(1), 1-5.
10. **López-López M.T, Kuzhir P**., et al. (2011), Normal stresses in a shear flow of magnetorheological suspensions: viscoelastic versus Maxwell stresses, *Journal of Rheology*, 54, 1119.
11. **Mazlan S. A., Ekreem, N.B., Olabi A.G.,** (2007) The performance of magnetorheological fluid in squeeze mode, *Smart Mater. Struct.*,16 1678–1682.
12. **Odenbach S., Pop L. M., Zubarev A. Yu**. (2007), Rheological properties of magnetic fluids and their microstructural background, GAMM-Mitteilungen, 30(1), 195-204.
13. **Salwiński J., Horak W**. (2012), Measurement of Normal Force in Magnetorheological and Ferrofluid Lubricated Bearings, *Key Engineering Materials*, 490, 25-32.
14. **Salwiński J., Horak W., Szczęch M.** (2014), Experimental apparatus for examination of magnetic fluid lubricated thrust bearing, *Scientific Papers of Silesian University of Technology*, 83, 243-249.
15. **Sapiński B., Horak W. Sioma A.** (2014), Experiments of MR fluid behaviour in the squeeze mode using the vision method, *Control Conference (ICCC), 15th International Carpathian*, Velke Karlovice, 513–516.
16. **Sapiński B., Horak W. Szczęch M.** (2013), Investigation of MR fluids in the oscillatory squeeze mode, *Acta Mechanica et Automatica*, 7(2), 111-116.
17. **Sapiński B., Szczęch M.** (2013), CFD model of a magnetorheological fluid in squeeze mode, *Acta Mechanica et Automatica*, 7(3), 180-183.
18. **Tao R.** (2001), Super-strong magnetorheological fluids, *Journal of Physics: Condensed Matter*, 13(50), 979–999.
19. **Wang, D.H., Liao, W.H**. (2011), Magnetorheological fluid dampers: a review of parametric modelling, *Smart Mater. Struct.*, 20, 023001.
20. **Zubieta M., Eceolaza S., Elejabarrieta M.J., Bou-Ali M. M.** (2009) Magnetorheological fluids: characterization and modeling of magnetization, *Smart Mater. Struct.*, 18, 095019.
21. BASF The Chemical Company, http://www.basonetic.com/.
22. LORD Corporation, http://www.lord.com/.

Acknowledgement: This work is supported by AGH University of Science and Technology under research program No. 11.11.130.958.

DE GRUYTER
OPEN

DOI 10.1515/ama-2017-0011

acta mechanica et automatica, vol.11 no.1 (2017)

TRANSIENT TORSIONAL ANALYSIS OF A BELT CONVEYOR DRIVE WITH PNEUMATIC FLEXIBLE SHAFT COUPLING

Peter KAŠŠAY*, Jaroslav HOMIŠIN*, Matej URBANSKÝ*, Robert GREGA*

*Faculty of Mechanical Engineering, Technical University of Košice, Letná 9, 040 01, Košice, Slovakia

Peter.Kassay@tuke.sk, Jaroslav.Homisin@tuke.sk, Matej.Urbansky@tuke.sk, Robert.Grega@tuke.sk

received 14 April 2016, revised 13 March 2017, accepted 15 March 2017

Abstract: Development and application of pneumatic flexible shaft couplings have been in the center of our department research activities for a long time. These couplings are able to change torsional stiffness by changing pressure in their flexible elements – air bel-lows. Until now we have dealt with the use of pneumatic flexible shaft couplings for tuning mechanical systems working with periodically alternating load torque at steady state. Some mechanical systems, however, operate with a static load torque at constant speed (e.g. hoists, elevators, etc.), where it is necessary to consider the suitability of shaft coupling in terms of load torque at transient conditions (run-up and braking). Therefore we decided to analyze the use of pneumatic flexible shaft couplings also in this type of mechanical systems on an example of conveyor belt drive.

Key words: Transient Torsional Vibration, Optimization, Torsional Analysis, Belt Conveyor, Pneumatic Flexible Shaft Coupling

1. INTRODUCTION

Development and application of pneumatic flexible shaft couplings has been in the center of our department research activities for a long time (Homišin, 1984, 2002, 2003, 2013, 2014, 2015). These couplings are able to change torsional stiffness by changing pressure in their flexible elements – air bellows. Mechanical drives with periodically alternating load torque (reciprocating engines and compressors) are prone to resonance (Czech, 2012a, 2012b, 2014; Czech et al. 2014), pneumatic flexible shaft coupling are ideal device for protecting them from excessive torsional vibration (Kaššay et al., 2015). Some mechanical systems, however, operate with a static load torque at constant speed (e.g. hoists, elevators, etc.), where it is necessary to consider the suitability of shaft coupling in terms of load torque at transient conditions (run-up and braking). Therefore we decided to analyze the use of pneumatic flexible shaft couplings also in this type of mechanical systems on an example of conveyor belt drive.

2. INVESTIGATED MECHANICAL SYSTEM

The proposed belt conveyor drive (Kaššay, 2014) is shown schematically in Fig. 1. Conveyor belt (1) is driven by a *SIEMENS 1LA7 133-4AA* three-phase quadrupole asynchronous electric motor (2) with nominal power of P_N = 7.5 kW and nominal speed n_N = 1455 rpm through a *MOTOVARIO B123* bevel helical gearbox (3) with gear ratio i = 59.36 The motor and the gearbox are connected by a *Periflex PTT 104R* rubber tire flexible shaft coupling (4). The gearbox and belt conveyor drive pulley are connected with a *4–1/250–T–C* pneumatic flexible shaft coupling developed by us (5) (Homišin, 2002). The *FENA 262 AHH* brake (6) is located before the gearbox. Conveyor capacity is Q_m = 180 [t·h^{-1}], horizontal length L_h = 41 m and height H = 12 m.

Ideally in this type of device the transmitted load torque during a steady state operation is constant. Therefore it is necessary to determine the maximum torque reached during run-up and braking and compare them with maximum allowed values. Since pneumatic shaft coupling is applied, we carried out this calculations for the whole operating pressure range p_{p0} = 100 to 600 kPa of used coupling. As operating pressure p_{p0} is meant the initial overpressure (to the atmospheric pressure) by zero twist angle.

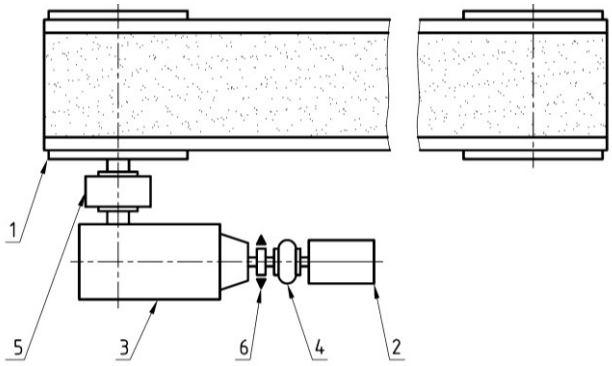

Fig. 1. Conveyor belt drive

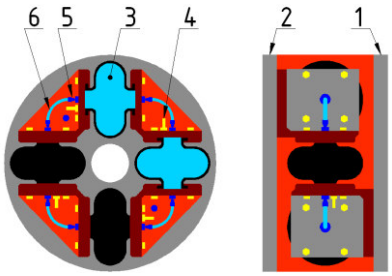

Fig. 2. Tangential pneumatic flexible shaft coupling

DOI 10.1515/ama-2017-0011

The applied pneumatic flexible shaft coupling is a tangential type pneumatic coupling (Fig. 2) (Homišin, 1984, 2003) consists of driving (1) and driven hub (2) connected by pneumatic flexible elements (3) filled with air under pressure. The compression volumes of elements are interconnected by tubes (6).

3. DYNAMIC MODEL OF THE MECHANICAL SYSTEM

The conveyor belt drive was modelled as four-mass torsional system (Fig. 3). The conveyor belt was replaced with two masses (I_3, I_4) to take viscoelastic properties of the belt into account. The resistances were equally divided between the masses.

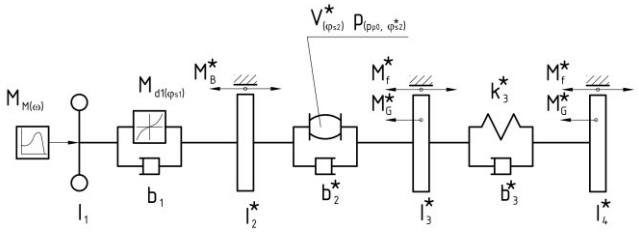

Fig. 3. Dynamic model of conveyor belt drive (reduced on motor shaft)

Basic parameters of torsional system are as follows:

- $I_1 = 2.475 \cdot 10^{-2}$ [kg·m^2] – mass moment of inertia of mass 1,
- $I_2^* = 1.950 \cdot 10^{-2}$ [kg·m^2] – mass moment of inertia of mass 2,
- $I_3^* = 5.282 \cdot 10^{-2}$ [kg·m^2] – mass moment of inertia of mass 3,
- $I_4^* = 4.969 \cdot 10^{-2}$ [kg·m^2] – mass moment of inertia of mass 4,
- $k_3^* = 9.104$ [Nm·rad^{-1}] – reduced torsional stiffness of conveyor belt,
- $b_2^* = 0.1036$ [Nm·rad^{-1}·s] – reduced coefficient of viscous damping of pneumatic coupling,
- $b_3^* = 2.243$ [Nm·rad^{-1}·s] – reduced coefficient of viscous damping of conveyor belt.

where all parameters labelled with * symbol are equivalent parameters reduced on the motor shaft of equivalent system.

The torque (M_M) speed (n) characteristics of electric motor is displayed in Fig. 4.

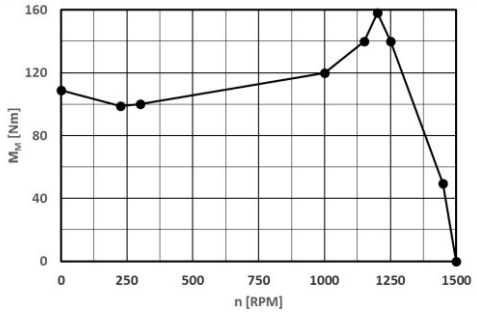

Fig. 4. Torque speed characteristics of electric motor

The dynamic load torque characteristic of *Periflex* coupling is defined by formula:

$$M_{d1} = 528454 \cdot \varphi_{s1}^5 + 1509.1 \cdot \varphi_{s1}^3 + 649.17 \cdot \varphi_{s1} \qquad (1)$$

where: M_{d1} – is the dynamic torque of coupling 1, φ_{S1} – twist angle of coupling 1 (*Periflex*).

Constant values of braking torque M_B = 75 Nm, reduced conveyor belt friction torque M_f *= 3.912 Nm and reduced torque from load's weight M_G* = 19.52 Nm were considered. We used a mathematical-physical model of pneumatic flexible shaft coupling based on air compression. We considered the air volume (V) dependency on coupling twist angle (φ_{s2}). The change of air pressure is adiabatic. In neutral position (by zero twist angle) the air pressure has a value of p_{p0}. The compression volume-twist angle graph is displayed in Fig.5.

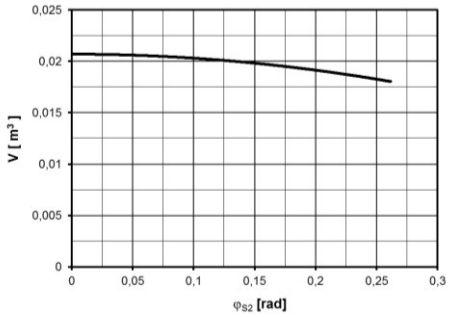

Fig. 5. Compression volume – twist angle graph

Static load characteristics of pneumatic coupling by different p_{p0} pressures are displayed in Fig. 6 (Homišin, 2002).

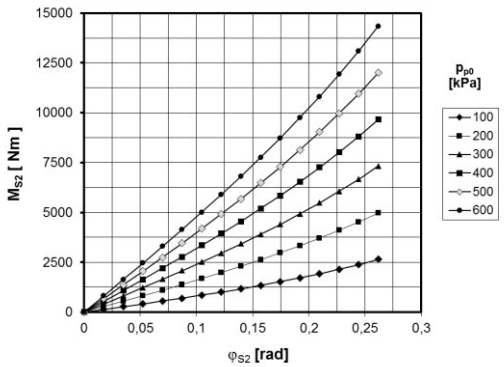

Fig. 6. Static load characteristics of pneumatic flexible shaft coupling by different air pressures

Viscous damping coefficient of *Periflex* coupling b_1 was computed for each pressure p_{p0} corresponding to relative damping coefficient $\Psi = 1.2$. The values of viscous damping coefficient b_1 are listed in Tab. 1.

Tab. 1. Viscous damping coefficient b_1 values

p_{p0} [kPa]	100	200	300	400	500	600
b_1 [Nm.rad^{-1}.s]	6.283	7.662	8.549	9.520	10.65	11.63

In the simulation we considered run-up, continuous operation and braking. In time t = 0 s the brake disengages and the motor starts, in time t = 5 s the motor shuts down and the brake engages.

In Fig. 7 is displayed the time course of *Periflex* coupling load torque by initial pressure p_{p0} = 400 kPa in the pneumatic coupling. In the graph is marked the maximum permissible torque of *Periflex* coupling by the horizontal line M_{K1P}.

DOI 10.1515/ama-2017-0011

In Fig. 8 are displayed the maximum and minimum values of *Periflex* coupling load torque reached during simulation by different pressures p_{p0} in the pneumatic coupling. It is evident, that *Periflex* coupling exceeded the permissible value of load torque by pressures p_{p0} = 100 and 200 kPa.

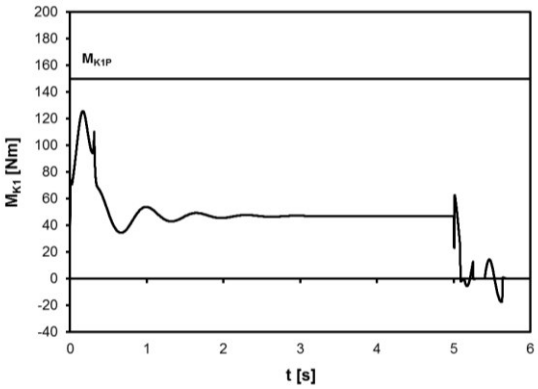

Fig. 7. Time course of the Periflex coupling load torque by pressure p_{p0} = 400 kPa in the pneumatic coupling

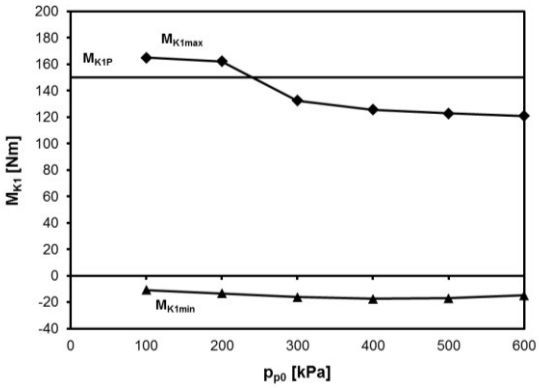

Fig. 8. Maximum and minimum load torque of Periflex coupling reached during simulation by different pressures in pneumatic coupling

In Fig. 9 the time course of pneumatic coupling load torque by pressure p_{p0} = 400 kPa is displayed.

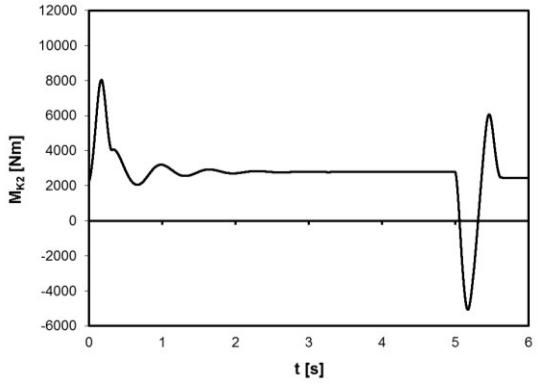

Fig. 9. Time course of pneumatic coupling load torque by pressure p_{p0} = 400 kPa

In Fig. 10 are displayed the maximum and minimum values of pneumatic coupling load torques reached during simulation by different pressures p_{p0}. The maximum torque M_{K2max} decreases with pressure, while the minimum absolute values M_{K2min} increases. But to determine the suitability of pneumatic coupling, the twist angle derived from pneumatic elements permissible compression is decisive.

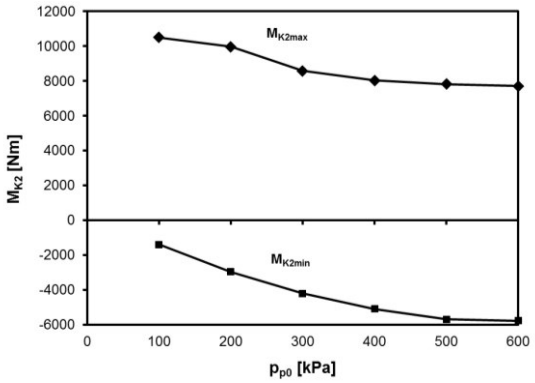

Fig. 10. Maximum and minimum load torque of pneumatic coupling during simulation by it's different pressures

In Fig. 11 the time course of pneumatic coupling twist angle by pressure p_{p0} = 400 kPa is displayed.

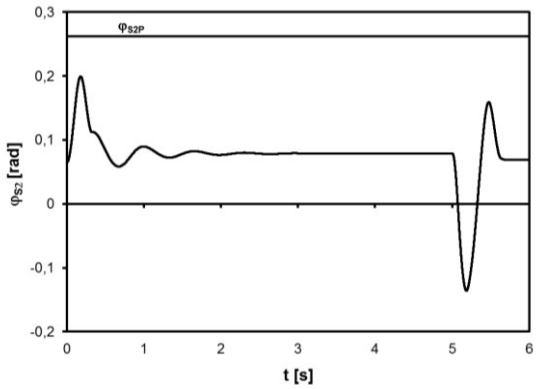

Fig. 11. Time course of pneumatic coupling twist angle by pressure p_{p0} = 400 kPa

In Fig. 12 are displayed the maximum and minimum values of pneumatic coupling twist angle reached during simulation by different pressures p_{p0}. The maximum permissible twist angle φ_{S2P} is exceeded by pressures p_{p0} = 100 and 200 kPa.

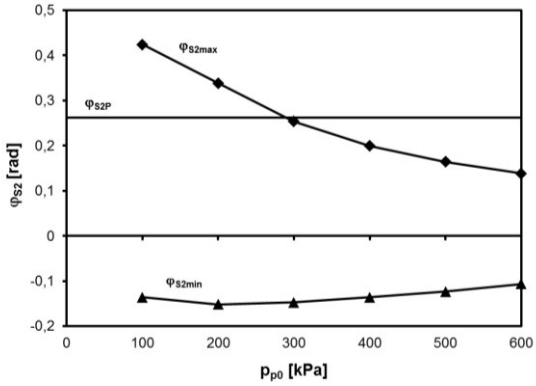

Fig. 12. Maximum and minimum twist angle of pneumatic coupling reached during simulation by it's different pressures

DOI 10.1515/ama-2017-0011

4. CONCLUSIONS

From the simulation results it is possible to say that using different initial pressures in pneumatic flexible coupling influences the limit values of load torque in both couplings. Generally it is necessary to select proper value of air pressure in coupling with focus on minimizing torsional vibration and load of multiple drive components. In this specific case the given mechanical system can operate by pressure p_{p0} = 300 kPa and above. For the examined system it is best to inflate the pneumatic coupling on the maximum pressure p_{p0} = 600 kPa.

REFERENCES

1. **Ankarali A., Mecitoğlu Z., Diken H.** (2012), Response spectrum of a coupled flexible shaft-flexible beam system for cycloidal input motion, *Mechanism and Machine Theory*, 47, 89–102.
2. **Binglin Lv., Huajiang O., Wanyou L., Zhijun S., Gang W.** (2016), An indirect torsional vibration receptance measurement method for shaft structures, *Journal of Sound and Vibration*, 372, 11–30.
3. **Bulut G.** (2014), Dynamic stability analysis of torsional vibrations of a shaft system connected by a Hooke‘s joint through a continuous system model, *Journal of Sound and Vibration*, 333(16), 3691–3701.
4. **Curà F., Mura A.** (2013), Experimental procedure for the evaluation of tooth stiffness in spline coupling including angular misalignment, *Mechanical Systems and Signal Processing*, 40, 545–555.
5. **Czech P.** (2012a), Diagnosis of industrial gearboxes condition by vibration and time-frequency, scale-frequency, frequency-frequency analysis, *Metalurgija,* 51(4), 521–524.
6. **Czech P.** (2012b): Identification of Leakages in the Inlet System of an Internal Combustion Engine with the Use of Wigner-Ville Transform and RBF Neural Networks. *Communications in Computer and Information Science*, 329, 414-422.
7. **Czech P.** (2014), Conception of use vibroacoustic signals and neural networks for diagnosing of chosen elements of internal combustion engines in car vehicles*, Scientific Journal of Silesian University of Technology, Series Transport,* 82(1903), 51-58 (in Polish).
8. **Czech P., Wojnar G., Folęga P.** (2014), Vibroacoustic diagnosing of disturbances in the car ignition system by amplitude estimates, *Scientific Journal of Silesian University of Technology, Series Transport,* 83(1904), 59-64 (in Polish).
9. **El-Sayed A. T., Bauomy H. S.** (2015), Passive and active controlers for suppressing the torsional vibration of multiple-degree-of-freedom system, *Journal of Vibration and Control*, 21(13), 2616–2632.
10. **Figlusz T., Konieczny Ł., Burdzik R., Czech P.** (2015a), Assessment of diagnostic usefulness of vibration of the common rail system in the diesel engine, *Vibroengineering Procedia*, 6, 185-189.
11. **Figlusz T., Konieczny Ł., Burdzik R., Czech P.** (2015b), The effect of damage to the fuel injector on changes of the vibroactivity of the diesel engine during its starting, *Vibroengineering Procedia*, 6, 180-184.
12. **Folęga P., Wojnar G., Czech P.** (2014), Influence of housing ribbing modification on frequencies and shapes of vibrations, *Scientific Journal of Silesian University of Technology, Series Transport,* 82(1903), 81-86 (in Polish).
13. **Gao W., Hao Z.** (2010), Active control and simulation test study on torsional vibration of large turbo-generator rotor shaft, *Mechanism and Machine Theory*, 45, 1326 – 1336.
14. **Handrik, M., Vaško M., Kopas P., Sága M.** (2014), Effective Finite Element Solution and Post-processing for Wide Load Spectrum, *Communications*, (16)3A, 19-26.
15. **Homišin J.** (1984), *Pneumatic flexible shaft coupling*, IPO CZ Praha, Patent No 254180 (in Slovak).
16. **Homišin J.** (2002), *New types of flexible shaft couplings: development, research, application*, *Vienala, Košice* (in Slovak).
17. **Homišin J.** (2003), *Axial pneumatic flexible shaft coupling*, IPO SK Banská Bystrica, Patent No 275867 (in Slovak).
18. **Homišin J.** (2013), New Ways of Controlling Dangerous Torsional Vibration in Mechanical Systems, *Transactions on Electrical Engineering*, 2(3), 70-76.
19. **Homišin J.** (2014), New Methods for Tuning of Mechanical Systems During Operation in Steady State, *Scientific Journal of Silesian University of Technology, Series Transport,* 85(1925), 49-55.
20. **Homišin J.** (2015), Partial results of the grant project: „research and application of universal regulation system in order to master the source of mechanical systems excitation”, *Scientific Journal of Silesian University of Technology, Series Transport,* 89, 27-36.
21. **James D., Van de Ven , Cusack J.** (2014). Synthesis and baseline testing of a digital pulse-width-modulated clutch, *Mechanism and Machine Theor,* 78, 81–91.
22. **Kaššay P.** (2014), *Modeling, analysis and optimization of torsional oscillating mechanical systems*, Habilitation thesis, Technical University of Košice, Košice (in Slovak).
23. **Kaššay P., Urbanský M.** (2015), Torsional natural frequency tuning by means of pneumatic flexible shaft couplings, *Scientific Journal of Silesian University of Technology, Series Transport*, 89, 57-60.
24. **Konieczny Ł., Burdzik R., Warczek J., Czech P., Wojnar G., Młyńczak J.** (2015), Determination of the effect of tire stiffness on wheel accelerations by the forced vibration test method, *Journal of Vibroengineering*, 17(8), 4469-4477.
25. **Kopas, P., Vaško, M., Handrik, M.** (2014) Computational Modeling of the Microplasticization State in the Nodular Cast Iron, *Applied Mechanics and Materials*, 474, 285-290.
26. **Madej, H., Czech, P.** (2010), Discrete Wavelet Transform and Probabilistic Neural Network in IC Engine Fault Diagnosis, *Maintenance and reliability*, 4, 47-54.
27. **Moravič M.** (2016), Stiffness change as means of dangerous vibrations elimination, *Novus Scientia 2016 – conference proceedings*, 125-128 (in Slovak).
28. **Ondrouch J., Ferfecki P., Poruba Z.** (2010), Active vibration reduction of rigid rotor by kinematic excitation of bushes of journal bearings, *Metalurgija,* 49(2), 107–110.
29. **Sága M., Bednár R., Vaško M.** (2011) Contribution to Modal and Spectral Interval Finite Element Analysis, *Vibration Problems ICOVP 2011*, *The 10th International Conference on Vibration Problems*: Liberec, Czech Republic, 269–274.
30. **Sága M., Vaško M., Pecháč P.** (2014) Chosen Numerical Algorithms for Interval Finite Element Analysis, *Procedia Engineering*, 96, 400-409.
31. **Sapietová A., Dekýš V.** (2016) Dynamic Analysis of Rotating Machines in MSC.ADAMS, *Procedia Engineering*, 136, 143-149.
32. **Wang Ch., Xie X., Chen Y., Zhang Z.** (2016) Investigation on active vibration isolation of a Stewart platform with piezoelectric actuators, *Journal of Sound and Vibration,* 383, 1-19.
33. **Wojnar G., Czech P., Stanik Z.** (2011), Use of amplitude estimates and nondimensional discriminants of vibroacoustic signal for detection of operational wear of rolling bearings, *Scientific Journal of Silesian University of Technology. Series Transport,* 72 (1860), 107-112 (in Polish).
34. **Wojnar G., Homik W.** (2015), Reduction of the amplitudes of selected components of the frequency spectrum of momentary velocity of the crankshaft of the internal combustion engine piston through the use of torsional vibration dampers, *Vibroengineering Procedia,* 6, 83-86.
35. **Žmindák M., Dekýš V., Novák P.** (2014) Fracture Mechanics Approach for Analysis of Delamination in Composite Plates, *Advanced Materials Research*, 969, 176-181.

This paper was written in the framework of Grant Project VEGA: „1/0688/12 – Research and application of universal regulation system in order to master the source of mechanical systems excitation.

DE GRUYTER
OPEN

DOI 10.1515/ama-2017-0012 acta mechanica et automatica, vol.11 no.1 (2017)

MEASUREMENT APPROACH OF MEAN HEAT TRANSFER COEFFICIENT FOR PACKED BED OF VEGETABLES

Adam ŁAPIŃSKI[*], Dariusz BUTRYMOWICZ[**], Mirosława KOŁODZIEJCZYK[***]

[*]Department of Thermal Engineering and Refrigeration, Faculty of Mechanical Engineering, Bialystok University of Technology, ul. Wiejska 45c, 15-351 Białystok, Poland

a.lapinski@doktoranci.pb.edu.pl, d.butrymowicz@pb.edu.pl, m.kolodziejczyk@pb.edu.pl

received 26 October 2016, revised 13 March 2017, accepted 15 March 2017

Abstract: The non-invasive measurement approach of the mean heat transfer coefficient for the packed bed of vegetables may be thought as still open issue. There is a clear need for the assessment of heat transfer conditions for various types of fruits and vegetables in order to accurately predict the thermal load that is necessary to select refrigeration equipment for cold storage chamber. Additionally, there is significant development in numerical modelling of heat and mass transfer processes in cold storage chambers for fruits and vegetables which requires precise heat transfer prediction. The theoretical basis for the indirect measurement approach of mean heat transfer coefficient for the packed bed of vegetables that is based on single blow technique is presented and discussed in the paper. The approach based on the modified model of Liang and Yang was presented and discussed. The testing stand consisted of a dedicated experimental tunnel along with auxiliary equipment and measurement system are presented. The geometry of the tested vegetables bed were presented. Selected experimental results of heat transfer are presented and discussed for the packed bed of carrots. These results were presented as dimensionless relationship. The obtained results were compared with the existing dimensionless relationships developed for the packed bed consisting of elements of various regular shapes.

Key words: Heat Transfer Coefficient, Packed Bed, Carrot, Single Blow Technique

1. INTRODUCTION

The paper deals with approach of the measurement of heat transfer and flow resistance in packed bed of vegetables. The knowledge of heat transfer conditions during cooling of vegetables is necessary for the reliable design of the cold storage chamber.

Usually measurement of the flow resistance in packed bed of vegetables or fruits is not very difficult. However, the measurement of the heat transfer coefficient may be thought as a challenge in most cases due to very complicated geometry of the packed bed elements. This is the reason why it is impossible to apply the simplest direct methods of the measurement of the heat transfer coefficient that are based on the direct measurement of the mean temperature of the vegetables surfaces, gas temperature distribution as well as heat flux density. This means that in this case an indirect method must be applied. The methodology of such measurement is proposed in this paper.

2. INDIRECT MEASUREMENT METHODS

The methods or techniques that can be applied to measure of the mean heat transfer coefficient in the packed bed can be classified in many ways. One of the possible classification approach that can be found in the literature is the classification proposed by Achenbach (2006) that is as follows:

- heat transfer measurement for a single spherical element located in the tested packed through which blows electrically heated air;
- techniques using the measurements of the mass transfer and the analogy between heat and mass transfer is applied;
- simultaneous exchange of heat and mass transfer approach;
- measurements involving the regenerative heating;
- semi-empirical method.

According to Achenbach (1995) a method using a blast of hot air flow involves determining temperature difference between the wall of the probe and its environment. Probe used in this method should be made in the form of a copper or brass sphere. Filling ambient probe should be characterized by a very low thermal conductivity. To eliminate the measurement error associated with the radiation of the probe surface is done by means of polishing of the sphere surface.

The technique of using of heat and mass transfer analogy is based on the measurement of weight loss with beads of naphthalene which sublimate during air flow in a specific period of timeΔt. According to Achenbach (1995) the boundary condition in this technique is the substance concentration on the walls surface of the tested spheres.

Measurements using a simultaneous heat and mass transfer consists of placing the porous balls soaked with a liquid in air stream. In this method mass transfer is measured by loss in mass of the balls and the balls surface temperature which strongly depends on the process of evaporation. However, determination of the balls surface temperature causes considerable problems with application of this approach, Achenbach (1995).

Another method described by Achenbach (1995) is a regenerative heat technique. This technique involves simultaneous heat-

DOI 10.1515/ama-2017-0012

ing and cooling of the tested packed bed. Temperature distribution is measured in this method which provides indirect information about heat transfer coefficient. The disadvantage of this technique is considerable technical and calculation efforts which strongly reduces the efficiency and accuracy of the measurement.

The last discussed method is a semi-empirical approach. It consists in determination of mean heat transfer on a single element of the regular shape for which the experimental correlations were obtained are transferred to the entire packed bed. Gnielinski (1978) successfully applied and described semi-empirical method for the first time. He used the asymptotic solutions with laminar flow around a flat plate:

$$Nu_l = 0{,}664 Pr^{1/3} \left(\frac{Re}{\epsilon}\right)^{1/2} \quad (1)$$

while for turbulent flow:

$$Nu_t = \frac{0{,}037 Pr^{1/3} \left(\frac{Re}{\varepsilon}\right)^{0,8} Pr}{1 - 2{,}443 \left(\frac{Re}{\varepsilon}\right)^{-0,1} \left(Pr^{2/3} - 1\right)} \quad (2)$$

where: Nu_l, Nu_t is Nusselt number for laminar and turbulent flow, respectively; Pr is Prandtl number; Re is Reynolds number; ε is porosity of the packed bed.

Using eq. (1) and (2) are received the following correlation for Nusselt number Nu_{sp} for a single sphere:

$$Nu_{sp} = 2 + (Nu_l^2 + Nu_t^2)^{1/2}. \quad (3)$$

Another classification of the experimental methods of mean heat transfer in the packed bed was proposed by Fricke and Becker (2004). They classified methods as follows:

- the measurements at constant temperature;
- the measurement at a variable temperatures;
- heat flux measurements.

According to Becker and Fricke (2004) the most popular way to determine heat transfer coefficient is the measurement at variable temperatures. The measurement at variable temperatures consists on the determination of heat transfer coefficient during heating or cooling of the product. During the measurements two cases are possible: low Biot number ($Bi \leq 0.1$), and h$igh\ Biot\ number$ ($Bi > 0.1$).

The Biot number, Bi, can be defined as the ratio of external heat transfer resistance to internal heat transfer resistance, and is defined as follows:

$$Bi = \frac{\alpha Z}{\lambda}. \quad (4)$$

The first case, i.e. small Bi number means negligible internal thermal resistance, i.e. in all of the tested elements temperature is very uniform at a given point in time. For a case of high Biot Number the thermal resistance affects temperature distribution in the tested element, i.e. at the same time in the tested objects temperature gradient will appear. During cooling process by cold air flow the typical range of Biot number is $0.2 < Bi < 20$. Therefore internal thermal resistance is important during cooling or freezing of foodstuff. A method involving the internal temperature gradient of food products is useful to determine heat transfer coefficient in the case of elements of a simple regular shape, e.g. flat plate-shaped elements, cylinders or spheres (Becker and Fricke 2004).

A different approach for measurement of heat transfer coefficient was proposed by Alvarez et al. (1999a, b). They conducted the measurement of transfer coefficient using non-steady methods. They heated balls made of aluminium inside which were placed thermocouples. Such constructed spheres first were heated up to 60°C and then placed in the boxes, and finally are cooled in an air stream. The authors (Alvarez et al. 1999b), defined the heat transfer coefficient of the balance sheet:

$$\alpha A(T - T_0) = \rho V c_p \frac{dT}{dt} \quad (5)$$

where: T – temperature of the ball; T_0 – air temperature; ρ – density of the ball; c_p – specific heat of the ball material; t – time; V – volume of the ball; A – surface area of the ball; α – heat transfer coefficient.

For the case of bed consisted of balls, Alvarez et al. (1999a,b)proposed the following empirical correlation:

$$Nu = 2 + 3{,}78 Re^{0,44} Tu^{0,33} Pr^{0,33} \quad (6)$$

where: Tu is turbulence intensity.

Studies on the heat transfer in the bed are also carried out by Laguerre et al. (2006, 2008). In both cases, tests were performed with use of the spherical objects. The investigations of Laguerre et al. (2006) were performed to study of heat transfer between of the bed and the container wall. They used balls made of aluminium and steel in the measurements. Balls were additionally coated with chrome in order to eliminate the effect of radiation. Additionallythey put in the bed two balls: heating and the heated in order to determine of heat conduction in the bed. Laguerre et al. (2008) studied heat transfer for the case of natural convection in the bed of balls made of PVC filled with gel.

Detailed overview and summary of the heat transfer coefficients for food products, along with the existing correlations, helpful in determining the value of transfer coefficients includes ASHRAE Handbook - Refrigeration (2010).

All of the above approaches may be thought as unsuitable for measurement of mean heat transfer coefficient of the packed bed of vegetables since in most of these techniques the various shapes of the vegetables could not be taken into account as well as there is possible significant change of the vegetables thermo-kinetic properties during the measurement procedure. The above disadvantages may be omitted by means of application of the purely indirect method, i.e. single blow technique. To the knowledge of the authors this technique has never been applied for the measurement of the mean heat transfer coefficient of the packed bed of vegetables. Therefore the application of this technique as well as preparation of the appropriate methodology dedicated for the packed bed of vegetables is the motivation of the authors for present investigations reported in this paper.

3. SINGLE BLOW METHOD

The so-called single blow technique is thought to be an efficient method used to experimentally determine the average heat transfer coefficient α in the packed bed. This method was also effectively applied for investigations of heat transfer in compact heat exchangers: Shaji and Das (2010), Krishnakumar et al. (2011), Ranganayakulu et al. (2017). Heat transfer coefficient is based on the actual surface area of the bed elements and takes into account convective heat transfer between gas and the packed bed element surface. In the discussed method the average heat transfer coefficient α to be found is determined by means of the comparison of the actual temperature profile of gas (that is heated or cooled in the tested packed bed) measured at the outlet of the tested packed bed with the predicted one on the basis of the

DOI 10.1515/ama-2017-0012

theoretical model, Butrymowicz et al. (2016). The agreement between the experimental temperature profiles and theoretical prediction depends on the heat transfer coefficient α that is applied in the theoretical model of heat transfer. Various theoretical approaches may be applied in order to predict temperature profile at the outlet for given inlet conditions and the vegetables geometry. Below short review of theoretical models which may be applied in the single blow method is presented.

The measurement in the single blow method is to record the time variability of gas temperature profile directly at the inlet and outlet of the tested packed bed which is caused by switching the heating section on or off is of key importance for the discussed method. The following conditions need to be met before the measurement:

- gas flow is steady state (constant velocity);
- the temperature in the measurement section is constant and equal in the axial and radial directions.

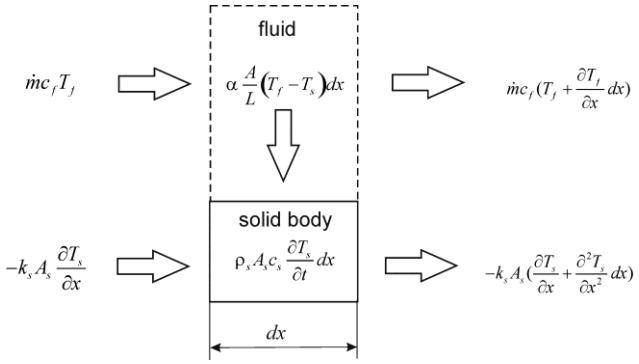

Fig. 1. Energy balance for fluid (f) and solid body (s) for the packed bed element

Temperature profiles should be measured for different velocities, involving the whole range of Reynolds numbers expected in the range of the operating conditions of the packed bed.

Temperature profiles recorded during the single blow technique measurements are used when solving equations modelling heat exchange in the tested packed bed. The measured temperature leap or profile at the inlet to the test section is the boundary condition for the model equations. The measured temperature profile at the outlet of the test section should be predicted on the basis of the model. However, the theoretical and the measured outlet temperature profiles may be compared in several ways that may be thought as equivalent.

The most basic one-dimensional model of transient heat transfer between a porous body and a fluid flowing through it is the model proposed by Anzelius (1926). This model became the basis for many further modifications and is still being developed by removing the numerous simplifications assumed by the author in order to obtain analytical solution of the model equations. Anzelius (1926) model is based on the energy balance for a solid body element (porous or perforated packing of the exchanger) in the situation presented in Fig. 1.

The following assumptions were made:

- the physical properties of fluid are independent of temperature;
- gas flow is steady state (m= const);
- the solid has a homogeneous structure;
- the thermal conductivity perpendicular to the flow direction is infinite (both for the fluid and for the solid body);
- the thermal conductivity of the fluid in the flow direction equals to zero;
- the external casing of the packed bed is adiabatic;
- initially the temperature in the exchanger is uniform (T_s = T_f = T_i);
- initially the fluid temperature leaps from T_i to T_{f1} and then it remains steady.

Balance equations of the element of fluid and solid body are as follows:

$$\frac{\partial T_f}{\partial z} = T_s - T_f, \tag{7}$$

$$\frac{\partial T_S}{\partial \tau} = \lambda NTU \frac{\partial^2 T_S}{\partial z^2} + \left(T_f - T_s\right) \tag{8}$$

where: non-dimensional time is defined as follows:

$$\tau = t\frac{\alpha A}{m_s c_s} \tag{9}$$

and non-dimensional coordinate is defined as:

$$z = NTU\frac{x}{L}. \tag{10}$$

After the transformation of the above equations, two new coefficients appear in the energy balance for the solid body, namely the number of heat transfer units:

$$NTU = \frac{\alpha A}{\dot{m}c_f} \tag{11}$$

and a parameter connected with solid body thermal conductivity $k_s$in the direction θ is parallel to the flow direction:

$$\lambda = \frac{k_S A_S}{\dot{m}c_f L}. \tag{12}$$

If the conductivity can be ignored, the above equations have analytical solutions developed by Schumann (1929) in the form:

$$\theta_z = 1 - e^{-(z+\tau)} \sum_{n=0}^{\infty} z^n \frac{d^n}{d(z\tau)^n}\left(J_0\left(2i\sqrt{z\tau}\right)\right), \tag{13}$$

$$\theta_f = 1 - e^{-(z+\tau)} \sum_{n=1}^{\infty} z^n \frac{d^n}{d(z\tau)^n}\left(J_0\left(2i\sqrt{z\tau}\right)\right) \tag{14}$$

where: θ is non-dimensional temperature defined as follows

$$\theta = \frac{T - T_i}{T_{f1} - T_i}. \tag{15}$$

The distributions of temperatures obtained from the above Schumann analytical solution can be used to determine the heat transfer coefficient α if the experiment well agrees with the boundary and initial conditions assumed in the model. Then, comparing the measured temperature distribution $T_f(t)$ at the packed bed outlet with the theoretical temperature distribution the spot $z = NTU$, the best fit will be achieved if the value α specific for the tested exchanger is used (Furnas, 1932).

Instead of comparing the temperature profiles, their derivatives can be used, and in particular their maximum values. Locke (1950) differentiated the solution for the outlet temperature $T_{f2} = T_f(\tau, z = NTU)$ at constant NTU and obtained the relationship for the slope S of the curve describing evolution of temperature T_{fa} in dimensionless coordinates. This makes it possible to determine the derivative from the experimental profile of outlet temperature $T_{f2}(t)$ and the experimental value S_{max}. For that value it is possible to obtain the corresponding NTU value, and then find the needed value of coefficient α.

Solving the model equations taking into consideration heat

DOI 10.1515/ama-2017-0012

conductivity along the solid body is only possible with numerical methods. The necessary calculations were done e.g. by Howard (1964), and his findings in the form of tables and graphs of function $NTU = f(S_{max})$ for selected values λ within the range of [0.005 …10, ∞] are also included in the paper presented by Pucci et al. (1967). The effect of the parameter λ on the determination of NTU is significant, especially when $NTU > 10$. Due to the considerable slope of the curve $NTU = f(S_{max})$ this approach of determination of α with the use of maximum slope S_{max} involves considerable error for certain combinations of parameters $S_{max}\ and\ \lambda$.

The accuracy of determining of heat transfer coefficient using the single blow method can be improved by extending the Anzelius model, providing that:

- the leap of the inlet temperature of the fluid occurs not immediately;
- heat conductivity in the solid body occurs not only in the axial direction but also in the radial direction;
- the external wall of the packed bed (packed bed) is not adiabatic; consequently there is a radial temperature gradient in the packed bed;
- pressure drop of the fluid flowing through the packed bed (packed bed) causes change of its temperature due to Joule-Thomson effect;
- the distribution of fluid velocity in the axial direction is heterogeneous due to disturbances of gas flow occurring at the elements of the packed bed (packed bed).

The modification of the initial conditions of Schumann solution proposed by Liang and Yang (1975) minimizes the problems connected with experimental realization of the non-immediate temperature leap at the tested exchanger inlet. Liang and Yang model was further extended by Cai et al. (1984) by taking into consideration also the conductivity of the solid body in the axial direction. The solution of this model could be obtained by numerical procedure, however. In this case the temperature profile at the exchanger inlet can be any function of time. Chen and Chang (1996) added to the model an equation describing the heat transfer between fluid and the casing. They also took into account the Joule-Thomson effect (Chen and Chang, 1997), and finally also radial conductivity (Chang et al., 1999). Luo et al., 2001, highlighted the impact of disturbances of fluid flow caused by the elements of exchanger packing (so-called axial dispersion). Taking into consideration that the usually the measurements cover large number of test runs then the most useful will be the analytical solution of the temperature profile at the outlet of the tested packed bed, however.

One of the sources of inaccuracy of the heat transfer coefficient α determined by means of the single blow method is the difficulty of the realization of the immediate temperature leap at the exchanger inlet. Due to the thermal capacity of the heater any temperature changes always occur at a certain time span. Liang and Yang (1975) proposed the dimensionless inlet temperature profiles obtained in the discussed test method after switching the heater on or off as the exponential function:

$$\theta_f(\tau, 0) = 1 - e^{-\tau/\tau^*} \tag{16}$$

where: τ^* is an experimentally determined dimensionless constant.

The above temperature profile as the boundary condition for modified Anzelius model equations (Liang and Yang, 1975). In the equation for fluid energy balance its thermal capacity was taken into consideration so the equation for gas energy balance was obtained as follows:

$$\frac{\partial \theta_f}{\partial \tau} + b_1 \frac{\partial \theta_f}{\partial z} = b_2\left(\theta_s - \theta_f\right) \tag{17}$$

The thermal conductivity in the solid body was ignored. In the dimensionless form energy balance equation for solid body can be presented as follows:

$$\frac{\partial \theta_s}{\partial \tau} = \theta_f - \theta_s. \tag{18}$$

The coefficients b_1 and b_2 in Eq. (17) are constant and defined as follows:

$$b_1 = b_2 \frac{v_f}{A_{f,min}}, \quad b_2 = \frac{m_s m_s}{m_f m_f} \tag{19}$$

where: v_f is the volume of fluid inside the packed bed per length in the flow direction and $A_{f,min}$ is the smallest cross-section surface area of the packed bed available for the flowing fluid. It must be remembered that temperature T_{f1}, necessary to calculate θ should be the value settled at the inlet after a sufficiently long time after switching the heater on or off. Equations (17) and (18) with boundary condition Eq. (16) and the following initial conditions:

$$\theta_z(0, z) = \theta_f(0, z) = 0 \tag{20}$$

were solved (Liang and Yang, 1975) with the use of the Laplace transform which gave a set of equations:

$$p\bar{\theta}_f + b_1 \frac{d\bar{\theta}_f}{dz} = b_2\left(\bar{\theta}_s - \bar{\theta}_f\right), \tag{21}$$

$$p\bar{\theta}_s = \bar{\theta}_f - \bar{\theta}_s, \tag{22}$$

$$\bar{\theta}_f(p, 0) = \frac{1}{\tau^* p\left(p + \frac{1}{\tau^*}\right)} \tag{23}$$

where: $\bar{\theta}$ denotes the transform, and p is its argument. The solution to the set of Eqs. (21)–(23) in relation to $\bar{\theta}_f$ is as follows (Liang and Yang, 1975):

$$\bar{\theta}_f = \frac{exp\left(-\frac{p}{b_1}\left(1 + \frac{b_2}{1+p}\right)z\right)}{\tau^* p\left(p + \frac{1}{\tau^*}\right)}. \tag{24}$$

Finding the inverse Laplace transform for Eq. (25) at $z = NTU$, the following relationships describing the profile of dimensionless temperature at the packed bed outlet are obtained:

- if $\tau < t^*$ (i.e.: $t < L/w_f$):

$$\theta_f(\tau, NTU) = 0, \tag{25}$$

- b) when $\tau \geq t^*$ (i.e. $t \geq L/w_f$):

$$\theta_f(\tau, NTU) = \frac{1}{\tau^*}\int_{\tau^*}^{\tau} e^{-(\tau-\eta)/\tau^* - b_2\tau^*}\left\{e^{-(\eta-\tau^*)} I_0\left(2\sqrt{b_2 t^*(\eta - t^*)}\right) + \int_0^{\eta - t^*} e^{-\xi} I_0\left(2\sqrt{b_2 t^* \xi}\right) d\xi\right\} d\eta. \tag{26}$$

In the above relationships the symbol t^* denotes dimensionless time defined as follows:

$$t^* = \frac{NTU}{b_1} \tag{27}$$

and w_f is the mean velocity of fluid in the packed bed.

Provided the relatively high numerical cost connected with the application of more complex mathematical models of heat transfer

DOI 10.1515/ama-2017-0012

in regenerators, the authors decided that the use the above modified Liang and Yang model (Liang and Yang, 1975). The key element in this model is the consideration of the exponential character of the inlet temperature profile which allows to avoid a considerable error resulting from the impossibility to execute an immediate leap of temperature at the inlet of the tested packed bed. It is recognized that the accuracy of this model should be satisfactory for indirect measurement of the heat transfer coefficient.

4. TEST APPARATUS

The experimental part of the single blow method is carried out in a wind tunnel. Temperature and pressure measurement points are placed at the inlet and outlet of the tested packed bed. Static pressure difference is measured in order to determine the frictional flow resistance. In addition, the velocity of gas flow through the packed bed should be also measured. It may be suggested that the temperature of gas flowing through the packed bed should be raised above the ambient temperature by approximately 5–10 K. An electrical heating coil made of resistance wires may be applied for this purpose. Due to the required velocity homogeneity, the heating coil should disturb the flow as little as possible. The structure of the coil also affects the gas temperature profile obtained after switching it on or off which is important from the point of view of the theoretical model applied to draw up the results of the measurements. The simplest models offer the analytical solutions for which an immediate temperature leap at the measurement section inlet is assumed. Some of the theoretical models assume the inlet temperature profile that is described by an exponential function achieved in the experiment. In more complicated numerical models there is no limitation concerning the profile of inlet temperature so the restrictions concerning the heating section (mainly its length in the direction of gas flow) are less important. Due to the homogeneity of velocity profiles required in the case of the theoretical models, it is recommended to place a flow straightened (in the form of a honeycomb packed bed) before the test section. In order to eliminate the influence of disturbances generated at the tunnel outlet geometry, a similar flow straightened should be also placed at the outlet of the test section. Reduction of the channel hydraulic diameter between the tunnel inlet and the test section is required in order to reduce turbulence level in the flow.

The test tunnel consists of three sections as it is show in Fig. 2. Air flow rate in the tunnel was controlled by means of change of the centrifugal exhaust fan rotational speed. The electric heater capacity was adapted to current operating conditions in order to produce the required air temperature jump. The electric heater capacity was fixed during the test run. The test stand consists of three parts:

- the inlet section with an electrical heater;
- the measurement section with the tested packed bed of vegetables;
- an exhaust fan with a diffuser.

The schematic of the test section is show in Fig. 3. The temperature distribution at the inlet and outlet to the test section were measured by means of thermocouples nets. Based on these measurements the average temperature of air at the inlet and outlet were obtained under transient operating conditions.

The following basic parameters are measured on the test stand:

- air temperature at the tunnel inlet;
- air temperature at the tested bed inlet ;
- air temperature at the tested bed outlet;
- static pressure drop at the tested bed;
- dynamic pressure at the tunnel inlet;
- air humidity at the channel inlet and outlet;
- electric heater on/off signal.

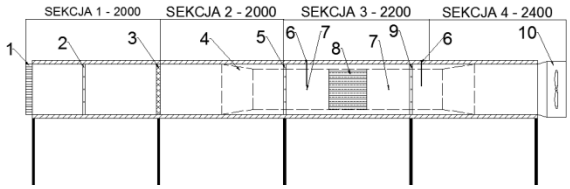

Fig. 2. Schematic diagram of the test tunnel: 1 – flow rectifier; 2 – air flow rate and temperature sensors; 3 – electric air heater; 4 – confusor/diffuser; 5 – thermocouples net at the tested bed inlet; 6 – moisture sensors; 7 – pressure gauges; 8 – tested packed bed of vegetables; 9 – thermocouples net at the tested bed outlet; 10 –exhaust fan

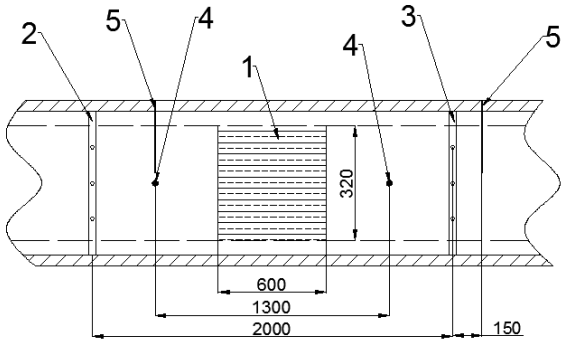

Fig. 3. Schematic of the test section: 1 – tested packed bed; 2 – thermocouples net at the bed inlet; 3 – thermocouples net at the bed outlet; 4 – pressure gauges; 5 – air moisture sensors

Thermocouples of the type of TP201 J of the diameter 0.5 mm were placed. The thermocouples of the open junction type were applied which enabled low thermal inertia. The thermocouples were calibrated for three temperature levels with use of the calibrated Pt100 sensor. The maximum difference between calibration sensor readings and thermocouples readings were not exceed ±0.15 K.

The reported measurements were carried out for the case of carrot. The prepared packed bed of carrot before insertion in the test tunnel were show in Fig. 4 and Fig. 5. The tested carrot was inserted in the gauze container.

The dimensions of the prepared packed bed were as follows: width 0.320 m; height 0.320 m; length 0.600 m.

The parameters of tested carrots placed in the bed are reported in Tab. 1. Carrots in this table have been classified by weight every 5 g.

Parameters of the tested bed of carrot:

- average mass: m_b = 32.27 kg;
- average heat transfer surface area: A_p = 4.8 m2;
- average volume: V = 0.0363 m3;
- average density: ρ = 1.007 kg/dm3.

DOI 10.1515/ama-2017-0012

Fig. 4. The packed bed of carrot (inlet bed)

Fig. 5. The packed bed of carrot (view from above)

Tab. 1. Parameters carrots in bed

Range weight [g]	Amount	Average mass [g]	Average volume [dm^3]	Average surface area [dm^2]	Average density [kg/dm^3]
55-60	15	57	0.056	1.036	1.005
60-65	18	61	0.060	1.110	1.020
65-70	21	67	0.065	1.066	1.030
70-75	25	72	0.071	1.191	1.014
75-80	27	78	0.076	1.247	1.018
80-85	23	83	0.080	1.272	1.038
85-90	19	87	0.085	1.408	1.024
90-95	23	92	0.093	1.480	0.989
95-100	15	97	0.099	1.444	0.987
100-105	15	102	0.100	1.527	1.014
105-110	15	107	0.107	1.597	1.002
110-115	20	112	0.110	1.573	1.010
115-120	17	118	0.112	1.675	1.053
120-125	11	121	0.124	1.684	0.979
125-130	13	127	0.126	1.657	1.012
130-135	12	133	0.152	1.892	0.874
135-140	7	136	0.137	1.735	0.988
140-145	6	142	0.141	1.866	1.006
145-150	9	147	0.141	1.967	1.037
150-155	10	152	0.148	1.950	1.026
155-160	3	157	0.159	2.100	0.986
160-165	5	163	0.164	2.019	0.996

The average hydraulic diameter of the packed bed d_h may be assessed on the basic of porosity:

$$d_h = \frac{4A_{pwl}}{U_p} = \frac{4V_p}{A_p} \tag{28}$$

where: A_{pwl}– surface area of the free space inlet; U_p – perimeter of the free space inlet; V_p $(A_{pwl} \cdot L)$ – volume of free space; A_p $(U_p \cdot L)$ – surface area of free space; L – length of the bed.

Knowing that the porosity (ε) and specific surface area (a) the following relationship may be applied:

$$\epsilon = \frac{V_p}{V}\,;\, a = \frac{A_p}{V}, \tag{29}$$

where: V – total volume of the bed. Substituting equation (29) to (28) it may be obtained:

$$d_h = 4\frac{\epsilon}{a}. \tag{30}$$

5. TEST RESULTS

The obtained results based on the application of the described single blow technique for the packed bed of carrots were presented in Tab. 2. It should be noted that Reynolds number Re was based on flow parameters in the equivalent channel inside the packed bed and w is velocity at the tested bed inlet. On the basis of the obtained experimental results the following correlation describing heat transfer in packed bed of carrots may be proposed:

$$Nu = 0{,}308Re^{0{,}56}Pr^{0{,}012} \tag{31}$$

Tab. 2. Results of heat transfer measurements

w [m/s]	Δp [Pa]	Re	α [W/m^{2}K]	Nu	Pr	j	f_D
0.096	0.545	268.304	11.2	6.55	0.524	0.03	0.9
0.138	1.763	384.063	13.7	8.048	0.527	0.026	1.445
0.19	2.083	531.895	18	10.673	0.532	0.025	0.874
0.23	3.297	641.719	17.7	10.566	0.535	0.02	0.953
0.283	4.302	791.88	20.6	12.206	0.531	0.019	0.812
0.335	5.826	936.08	24	14.259	0.533	0.019	0.786
0.397	7.407	1109	27.1	16.044	0.531	0.018	0.71
0.437	9.065	1221	28.3	16.642	0.527	0.017	0.718
0.49	10.866	1369	29.9	17.402	0.522	0.016	0.684
0.556	12.862	1552	33	19.114	0.519	0.015	0.631
0.599	14.982	1673	34.7	20.563	0.531	0.015	0.633
0.638	17.319	1783	35	20.524	0.524	0.014	0.646
0.684	19.492	1911	36	21.281	0.53	0.014	0.634
0.74	21.949	2066	36.8	21.594	0.526	0.013	0.611
0.798	24.621	2229	39.7	23.23	0.525	0.013	0.589
0.838	27.277	2340	40.6	23.46	0.518	0.012	0.591
0.892	30.209	2487	42	24.028	0.513	0.012	0.578
0.938	33.328	2619	43	24.81	0.517	0.012	0.575
0.992	36.775	2768	43.7	25.436	0.522	0.011	0.568
1.029	40.341	2872	45.2	26.375	0.523	0.011	0.58

The comparison of the measurement results with proposed dimensionless relationship eq. (31) is presented in Fig. 6.

Heat transfer coefficient (α) used in the measurement method, was presented as a heat transfer coefficient Colburn, which can be written as:

$$j = \frac{Nu}{RePr^{1/3}}, \tag{32}$$

DOI 10.1515/ama-2017-0012

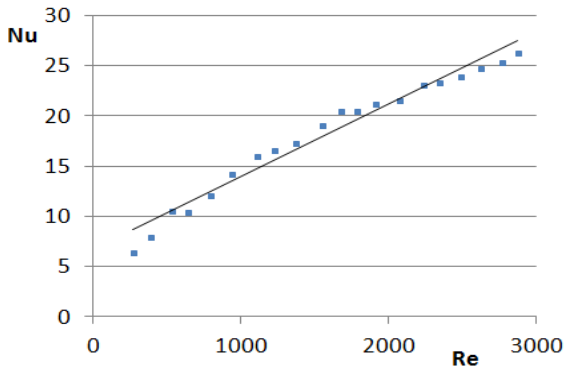

Fig. 6. Comparison of measured Nusselt number Nu with proposed correlation eq. (31)

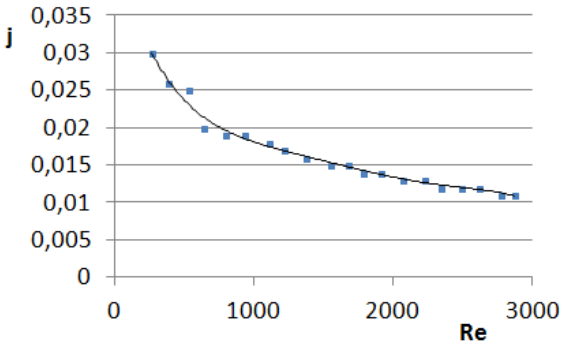

Fig. 7. Comparison of measured Colburn heat transfer factor j with proposed correlation eq. (31) for the whole range of Reynolds number Re

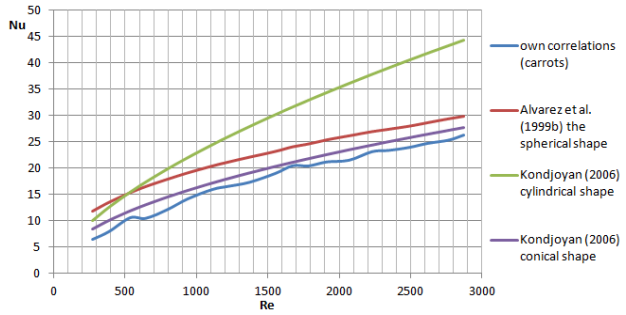

Fig. 8. Comparison of own correlation, eq. (31) for carrots with other correlations for regular shapes, eq. (33) ÷ eq. (35)

Relationship between Colburn heat transfer factor versus Reynolds number is shown in Fig. 7.

The proposed own correlation may be compared with literature available correlations developed for the cases of the packed bed consisted of the elements of the regular shape:

– correlation proposed by Alvarez et al.(1999b) for the case of spherical shape:

$$Nu = 2 + 3{,}78Re^{0{,}44}Tu^{0{,}33}Pr^{0{,}33}, \quad (33)$$

– correlation proposed by Kondjoyan (2006) for the case of the cylindrical shape:

$$Nu = 0{,}31Re^{0{,}62}(1 + 0{,}9TuRe^{0{,}04}), \quad (34)$$

– correlation proposed by Kondjoyan (2006) for the case of the conical shape:

$$Nu = 0{,}5Re^{0{,}5}(1 + 0{,}87TuRe^{0{,}09}). \quad (35)$$

The comparison between own correlation eq. (31) and other correlations developed for the packed bed consisted of the elements of the regular shape, eq. (33) ÷ eq. (35) is presented in Fig. 8. It was assumed turbulence intensity Tu = 0,02 which corresponds to conditions of the test tunnel air flow. As it can be seen the analysed correlations eq. (33) ÷ eq. (35) slightly over predicts own experimental correlation for Nusselt number for the whole range of Reynolds number except for the relationship eq. (34) developed for the cylindrical shape which strongly over predicts own results for higher Reynolds number range. However, it may be thought that the agreement between own correlation, eq. (31) and correlation developed for the conical shape, eq. (35) may be thought as reasonable good. Since the conical shape may be thought as the best geometry for the case of tested carrots the obtained results may be thought as the positive evaluation of the proposed measurement methodology of mean heat transfer coefficient for the packed bed of the vegetables.

6. SUMMARY

This paper presents the methodology of the measurement of heat transfer coefficients for packed bed composed of the vegetables. The reported measurements were carried out for the case of carrots. It is necessary to emphasize the necessity to develop an indirect method of measurement of the heat transfer coefficient by means of single blow technique. The current results involve the modification of this method proposed by Liang and Yang (Liang and Yang, 1975). The authors believe that the proposed methodology proved to be useful and produced reliable values of coefficients given by relationship eq. (30) for the tested packed bed of carrots. Further development of the proposed methodology may be proposed for the case of the other vegetables.

REFERENCES

1. **Achenbach E.** (1995), Heat and flow characteristics of packed beds, *Experimental Thermal and Fluid Science*, 10, 17-27.
2. **Alvarez G., Bournet P.-E., Flick D.** (2003). Two-dimensional simulation of turbulent flow and transfer through stacked spheres, *International Journal of Heat and Mass Transfer*, 46, 2459-2469.
3. **Alvarez G., Flick D.** (1999a), On heterogeneous cooling of agricultural products inside bins. Part I: aerodynamic study, *Journal of Food Engineering*, 39, 227-237
4. **Alvarez G., Flick D.** (1999b). On heterogeneous cooling of agricultural products inside bins. Part II: thermal study, *Journal of Food Engineering*, 39, 239-245,
5. **ANSYS FLUENT 14.5** Theory Guide, 2012.
6. **Anzelius A.** (1926), On heating of bodies by flowing media, *Zeitschrift für Angewandte Mathematik und Mechanik*, 6(4), 291–294 (in German).
7. **ASHRAE Handbook – Refrigeration** (2010), chapter 19, page 19.1-19.31.
8. **Becker B. R., Fricke B. A.** (2004),Heat transfer coefficients for forced-air cooling and freezing of selected foods, *International Journal of Refrigeration*, 27, 540-551.
9. **Ben Amara S., Laguerre O., Flick D.** (2004). Experimental study of convective heat transfer during cooling with low air velocity in a stack of objects, *International Journal of Thermal Science*, 43, 1213-1221.

DOI 10.1515/ama-2017-0012

10. **Butrymowicz D., Karwacki J., Kwidziński R., Śmierciew K., Gagan J., Przybyliński T., Skiepko T., Łapin M.,** (2016), Methodology of heat transfer and flow resistance measurement for matrices of rotating regenerative heat exchangers, *Chemical and Process Engineering*, 37 (3), 341-358.
11. **Cai Z.H., Li M.L., Wu Y.W., Ren H.S.** (1984), A modified selected point matching technique for testing compact packed bed surfaces,*International Journal of Heat and Mass Transfer*, 27(7), 971-978.
12. **Chang Z.-Ch., Hung M.-Sh., Ding P.-P., Chen P.-H.** (1999), Experimental evaluation of thermal performance of Gifford–McMahon regenerator using an improved single-blow model with radial conduction, International Journal of Heat and Mass Transfer, 42, 405-413.
13. **Chen P.-H., Chang Z.-Ch.** (1996), An improved model for the single-blow measurement including the non-adiabatic side wall effect, International Communications in Heat and Mass Transfer, 23(1), 55-68.
14. **Chen P.-H., Chang Z.-Ch.** (1997), Measurements of thermal performance of cryocooler regenerators using an improved single-blow method, International Journal of Heat and Mass Transfer, 40(10), 2341-2349.
15. **Defraeye T., Blocken B., Derome D., Nicolai B., Carmeliet J.** (2012), Convective heat and mass transfer modelling at air-porous material interfaces: Overview of existing methods and relevance. *Chemical Engineering Science*, 74, 49-58.
16. **Gnielinski E.** (1978), Equations for calculation of heat and mass transfer in flow-through static ball beds with medium and large Peclet number**,** *Verfahrenstechnik*, 12(6), 63-366, (in German).
17. **Howard C.P.** (1964),*The single blow problem including the effects of longitudinal conduction*, ASME Paper No. 64-GTP-11, presented at Gas Turbine Conference and Product Show, Houston TX, USA.
18. **Kays W.M., London A.L.** (1997), *Compact packed beds*, McGraw-Hill.
19. **Kondjoyan A.** (2006), A review on surface heat and mass transfer coefficients during air chilling and storage of food products, *International Journal of Refrigeration*, 29, 863-875.
20. **Krishnakumar K., John A.K., Venkatarathnam G.** (2011), A review on transient test techniques for obtaining heat transfer design data of compact heat exchanger surfaces, *Experimental Thermal and Fluid Science*, 35, 738–743.
21. **Laguerre O., Ben Amara S., Alvarez G., Flick D.,** (2008), Transient heat transfer by free convection in a packed bed of spheres: Comparison between two modelling approaches and experimental results, *Applied Thermal Engineering*, 28, 14-24
22. **Laguerre O., Ben Amara S., Flick D.,** (2006),Heat transfer between wall and packed bed crossed by low velocity airflow, *Applied Thermal Engineering*, 26, 1951-1960
23. **Liang C.Y., Yang. W.-J.** (1975), Modified single-blow technique for performance evaluation on heat transfer surfaces, Transactions of the ASME Series C, *Journal of Heat Transfer*, 97, 16-21.
24. **Locke G.L.** (1950),*Heat transfer and flow friction characteristics of porous solids*, Technical Report No. 10, Department of Mechanical Engineering, Stanford University, Stanford CA, USA.
25. **Luo X., Roetzel W., Lüdersen U.** (2001),The single-blow transient testing technique considering longitudinal core conduction and fluid dispersion, *International Journal of Heat and Mass Transfer*, 44, 121-129.
26. **Pucci P.F., Howard C.P., Piersall C.H. Jr.** (1967), The single-blow transient testing technique for compact packed bed surfaces, Trans. ASME,*Journal of Engineering for Power*, 89, 29-40.
27. **Ranganayakulu C., Luo X., Kabelac S.** (2017), The single-blow transient testing technique for offset and wavy fins of compact plate-fin heat exchangers, *Applied Thermal Engineering*, 111, 1588–1595.
28. **Schumann T.E.W.** (1929). Heat transfer: a liquid flowing through porous prism,*J. Franklin Inst.*, 208(3), 405-416.
29. **Shaji K., Das S.K.** (2010),The effect of flow maldistribution on the evaluation of axial dispersion and thermal performance during the single-blow testing of plate heat exchangers, *International Journal of Heat and Mass Transfer*, 53, 1591–1602.
30. **Verboven P., Datta A.K., Anh N.T., Scheerlinck N., Nikolai B.M.** (2003), Computation of airflow effects on heat and mass transfer in a microwave oven, *Journal of Food Engineering*, 59, 181-190.

Acknowledgement: Research was performed as a part of projects MB/WM/9/2016and financed with use of funds for science of MNiSW.

ABSTRACTS

Jan Slota, Ivan Gajdos, Emil Spišák, Marek Šiser
Springback Prediction of Stretching Process using Finite Element Analysis for DP600 Steel Sheet

Springback phenomenon is well predicted for some mild steel materials, but not for steels with higher strength. One of the most used tools to stamping optimization is usage of finite element analysis. In order to accurate describe the real behaviour of the materials for stamping of vehicle panels, the application of proper hardening rule seems to be crucial. Due to higher accuracy of predicted results, high strength steel sheets are usually modelled by means of kinematic or mixed isotropic-kinematic hardening models. In this paper the springback prediction of advanced high strength steel DP600 by numerical simulation was investigated. Through cyclic tension-compression tests, the material characterization has been performed for DP600 steel sheet. Different hardening models (isotropic, kinematic and mixed isotropic-kinematic) used in the simulations were compared with expreriment. The Yoshida–Uemori model succesfully describe the kinematic behaviour of the material and provided more accurate results than others.

Tadeusz Pała, Ihor Dzioba, Jarosław Gałkiewicz
Verification of Strength of the Welded Joints by using of the Aramis Video System

In the paper are presented the results of strength analysis for the two types of the welded joints made according to conventional and laser technologies of high-strength steel S960QC. The hardness distributions, tensile properties and fracture toughness were determined for the weld material and heat affect zone material for both types of the welded joints. Tests results shown on advantage the laser welded joints in comparison to the convention ones. Tensile properties and fracture toughness in all areas of the laser joints have a higher level than in the conventional one. The heat affect zone of the conventional welded joints is a weakness area, where the tensile properties are lower in comparison to the base material. Verification of the tensile tests, which carried out by using the Aramis video system, confirmed this assumption. The highest level of strains was observed in HAZ material and the destruction process occurred also in HAZ of the conventional welded joint.

Ryszard Sygulski, Michał Guminiak, Łukasz Polus
Stability of a Steel Welded Girder with Bending and Shear Forces Included

The stability of the element of a steel welded girder subjected to bending and shear forces is considered. The considered element is a rectangular plate supported on boundary. The type of a plate boundary conditions depend on the types (thickness) of the stiffeners. Considered plate is loaded by in-plane forces causing bending and shear effects. The Finite Element Method was applied to carry out the analysis. Additionally the Boundary Element Method in terms of boundary-domain integral equation was applied to evaluate the critical shear loading.

Najeeb Alam Khan, Shahnila Aziz, Saif Ullah
Entropy Generation on MHD Flow of Powell-Eyring Fluid Between Radially Stretching Rotating Disk with Diffusion-Thermo and Thermo-Diffusion Effects

An investigation is performed for an alyzing the effect of entropy generation on the steady, laminar, axisymmetric flow of an in-compressible Powell-Eyring fluid. The flow is considered in the presence of vertically applied magnetic field between radially stretching rotating disks. The Energy and concentration equation is taking into account to investigate the heat dissipation, Soret, Dufour and Joule heating effects. To describe the considered flow non-dimensionalized equations, an exact similarity function is used to reduce a set of the partial differential equation into a system of non-linear coupled ordinary differential equation with the associated boundary conditions. Using homotopy analysis method (HAM), an analytic solution for velocity, temperature and concentration profiles are obtained over the entire range of the imperative parameters. The velocity components, concentration and temperature field are used to determine the entropy generation. Plots illustrate important results on the effect of physical flow parameters. Results obtained by means of HAM are then compared with the results obtained by using optimized homotopy analysis method (OHAM). They are in very good agreement.

Maciej Słowik, Daniel Ołdziej, Zdzisław Gosiewski
Integration and In-Field Gains Selection of Flight and Navigation Controller for Remotely Piloted Aircraft System

In the paper the implementation process of commercial flight and navigational controller in own aircraft is shown. The process of autopilot integration were performed for the fixed-wing type of unmanned aerial vehicle designed in high-wing and pull configuration of the drive. The above equipment were integrated and proper software control algorithms were chosen. The correctness of chosen hardware and software solution were verified in ground tests and experimental flights. The PID controllers for longitude and latitude controller channels were selected. The proper deflections of control surfaces and stabilization of roll, pitch and yaw angles were tested. In the next stage operation of telecommunication link and flight stabilization were verified. In the last part of investigations the preliminary control gains and configuration parameters for roll angle control loop were chosen. This enable better behavior of UAV during turns. Also it affected other modes of flight such as loiter (circle around designated point) and auto mode where the plane executed a pre-programmed mission.

Czesław Janusz Jermak
Discussion on Flow-Through Phenomena in the Air Gauge Cascade

In the paper, the flow-through phenomena in the air gauge are under discussion form the thermodynamic and gasodynamic perspective. The main elements of the cascade are considered the inlet nozzle (restriction), measuring chamber and the measuring nozzle with the measuring slot (displacement between the nozzle head and measured surface). The purpose of the analysis was to point out the impact on the metrological characteristics of the air gauge. In particular, attention was paid to the airflow through the measuring slot. Here, the complex phenomena take place, among others the supersonic areas and a “bubble ring,” which cause discontinuity and hysteresis in the static characteristic. On the other hand, the air stream expansion after the restriction (inlet nozzle) is observed in the measuring chamber. The point of the above discussion was to work out some recommendation on the nozzles geometry and the localization of the back-pressure measuring point in the chamber.

Paweł Sidun, Andrzej Łukaszewicz
Verification of Ram-Press Pipe Bending Prosses using Elasto-Plastic FEM Model

In this paper selected aspects of numerical modelling of bending pipes process are described. Elasto-plastic material model was used in COMSOL FEM environment. The results of numerical analyses of two kinds of steel were presented. The correctness of the proposed model was verified based on comparison shapes of deformed pipe profile obtained at the ending step of bending both from numerical simulations and experiment.

Dariusz Urban, Marek Jałbrzykowski, Maria Gołębiewska
Fatigue Testing of Dental Bridges on Selected Examples

The paper presents example tests of the functional quality of selected designs of dental bridges. These were: porcelain bridges on a metal base (cobalt based alloy), porcelain bridges on a zirconia base (zirconia ceramic – Zirkon Zahn), and full zirconia bridges (Zirkon Zahn). For the purpose of the study, durability of bridges in cyclic fatigue testing was adopted as a measure of their quality. The tests were carried out on a Zwick Roell Z010 universal testing machine. They consisted in cyclic loading and unloading of dental bridges mounted on gypsum models at a loading force of F= 400 [N] and a frequency of load of f= 1 [Hz]. Each bridge was subjected to a cycle of 7200 loads. The results show that there are no significant differences in the functional quality of the bridges.

Volodimyr Kalchenko, Andrij Yeroshenko, Sergiy Boyko, Nataliia Sira
Determination Of Cutting Forces In Grinding With Crossed Axes Of Tool And Workpiece

In the work the analysis of existent methods of determination of local and general forces of cutting at polishing of surfaces with a type as the arc of circumference is given. The dependence for determination of speed polishing and method for determination of thickness of the cut away layer on condition of equality of the tricked into and taken off volumes of material are offered. The method of determination of cutting forces, which takes into account cutting and deforming grain, is suggested. The method of determining the thickness of a cutting layer of one of the cutting edge, from the condition that the volume of material that is brought and is cut in each local point of contact spots has been proposed. The proposed method takes into account the compliance of the processing system and the discontinuity of the abrasive surface of the tool. By experimental way upper limits of thickness cutting layer when using different abrasive materials for a wide range of cutting speeds have been obtained.

Wojciech Horak, Bogdan Sapiński, Marcin Szczęch
Analysis of Force in MR Fluids during Oscillatory Compression Squeeze

This study investigates the behaviour of MR fluids in the oscillatory compression squeeze mode. Experiments were performed on commercially available MR fluids in the purpose-built experimental set-up. The influence of MR fluid's properties and magnetic flux density on the force generated during the squeeze mode was investigated.

Peter Kaššay, Jaroslav Homišin, Matej Urbanský, Robert Grega
Transient Torsional Analysis of a Belt Conveyor Drive with Pneumatic Flexible Shaft Coupling

Development and application of pneumatic flexible shaft couplings have been in the center of our department research activities for a long time. These couplings are able to change torsional stiffness by changing pressure in their flexible elements – air bel-lows. Until now we have dealt with the use of pneumatic flexible shaft couplings for tuning mechanical systems working with periodically alternating load torque at steady state. Some mechanical systems, however, operate with a static load torque at constant speed (e.g. hoists, elevators, etc.), where it is necessary to consider the suitability of shaft coupling in terms of load torque at transient conditions (run-up and braking). Therefore we decided to analyze the use of pneumatic flexible shaft couplings also in this type of mechanical systems on an example of conveyor belt drive.

Adam Łapiński, Dariusz Butrymowicz, Mirosława Kołodziejczyk
Measurement Approach of Mean Heat Transfer Coefficient for Packed Bed of Vegetables

The non-invasive measurement approach of the mean heat transfer coefficient for the packed bed of vegetables may be thought as still open issue. There is a clear need for the assessment of heat transfer conditions for various types of fruits and vegetables in order to accurately predict the thermal load that is necessary to select refrigeration equipment for cold storage chamber. Additionally, there is significant development in numerical modelling of heat and mass transfer processes in cold storage chambers for fruits and vegetables which requires precise heat transfer prediction. The theoretical basis for the indirect measurement approach of mean heat transfer coefficient for the packed bed of vegetables that is based on single blow technique is presented and discussed in the paper. The approach based on the modified model of Liang and Yang was presented and discussed. The testing stand consisted of a dedicated experimental tunnel along with auxiliary equipment and measurement system are presented. The geometry of the tested vegetables bed were presented. Selected experimental results of heat transfer are presented and discussed for the packed bed of carrots. These results were presented as dimensionless relationship. The obtained results were compared with the existing dimensionless relationships developed for the packed bed consisting of elements of various regular shapes.